Commande et commande tolérante aux fautes par modes glissants : application à une mission de rendez-vous en orbite circulaire

Jazmin Zenteno Torres

université de BORDEAUX

THÈSE

présentée pour obtenir le grade de

Docteur de l'Université de Bordeaux

ÉCOLE DOCTORALE DES SCIENCES PHYSIQUES ET DE L'INGÉNIEUR
SPÉCIALITÉ AUTOMATIQUE, PRODUCTIQUE, SIGNAL ET IMAGE,
INGÉGNERIE COGNITIQUE

par

Jazmín ZENTENO TORRES

Sliding mode control with fault tolerance capacities: application to a rendezvous mission in a circular orbit

---

Soutenue le 3 Juillet 2020

Membres du jury:

Didier THEILLIOL	Professeur des Universités	Université de Lorraine	Rapporteur et Président
Christophe LOUEMBET	Maître de Conférences	Université de Toulouse	Rapporteur
Jorge DÁVILA	Professeur des Universités	Instituto Politécnico Nacional	Examinateur
Mickael RODRIGUES	Maître de Conférences	Université Claude Bernard	Examinateur
Jérôme CIESLAK	Maître de Conférences	Université de Bordeaux	Examinateur
David HENRY	Professeur des Universités	Université de Bordeaux	Directeur

- 2020 -

Titre : Commande et commande tolérante aux fautes par modes glissants: application à une mission de rendezvous en orbite circulaire

Résumé : De nombreux travaux de recherche ont été conduits dans le domaine de synthèse de lois de commande par modes glissants. Différentes approches de commande été proposées dans la litérature, telles que l'algorithme Super-Twisting (STA) et sa version récente, l'algorithme généralisé Super-Twisting (GSTA). Les travaux de recherche présentés dans ce mémoire de thèse s'inscrivent dans ces méthodes pour résoudre le problème de commande et de commande tolérante aux fautes, pour une mission spatiale. La mission considère une cible passive et un chasseur. L'objectif visé est de synthétiser les lois de contrôle d'attitude et de mouvement relatif, tolérantes aux pannes. Les approches proposées abordent la problématique des modes flexibles des panneaux solaires et des phénomènes de ballottement du carburant dans les réservoirs.
Dans un premier travail, une loi de commande de type STA est proposée dans une configuration dite de backstepping. Dans un second travail, une loi de commande tolérante aux fautes basée sur les modes glissants du second ordre, est proposée. La solution est basée sur l'algorithme GSTA ,placé en boucle externe de compensation de défauts utilisant un estimateur de défauts non linéaire. Le problème de saturation des actionneurs est également abordé et une solution basée sur la géométrie polytopique, est proposée. Les éléments clés de l'approche tolérante aux pannes sont, i) d'une part la solution ne nécessite pas de diagnostiquer les fautes et donc n'utilise pas d'algorithme de détection et de localisation de défauts, et ii), d'autre part, l'approche est basée sur le formalisme du quaternion dual qui permet de tenir compte des effets de couplage attitude/mouvement relatif. Des critères orientés mission, illustrent les résultats obtenus au travers d'une campagne de simulation réaliste.

Mots clés : Modes glissants, commande tolérante aux fautes, quaternion dual, mission spatiale.

Title : Sliding mode control with fault tolerance capacities: application to a rendezvous mission in a circular orbit

Abstract : Increasing attention has grown with regards to Sliding Mode Controllers (SMC). In order to reduce the so-called chattering effect, the Super-Twisting Algorithm (STA) has been proposed, recently. In this work, a controller based on the STA in a backstepping setup, is proposed for spacecraft rendezvous in a circular orbit. A key feature is that the chaser is not treated as a point mass, given that the effects of the flexible modes and propellant sloshing phenomena are considered. The results obtained are taken further, given that the guarantee of robustness against perturbations is not enough when it comes to critical systems, through the second order sliding mode controllers technique. It is shown that the technique enables to solve to problem of fault tolerant control. The solution is based on the Generalized Super-Twisting Algorithm (GSTA) with an anti-windup strategy and a nonlinear observer and the dual quaternion formalism. The main reason of employing a GSTA is because it offers more robustness against state dependent perturbations (sloshing phenomena and flexible modes) than the STA. In addition, with the help of the anti-windup strategy, the control law does not saturate the thrusters, avoiding instablity when faults occur. The proposed solution is evaluated through a simulation campaign in a high-fidelity non-linear simulator, and mission oriented criteria demonstrate its potential.

Keywords : Sliding modes, fault tolerant control, dual quaternion, aerospace application.

IMS - UMR n.5218 - Bat A31 - Université de Bordeaux - 351 cours de la libération - 33405 Talence cédex

"Nothing of me is original.
I am the combined effort of
everyone I've ever known."

Chuck Palahniuk,
Invisible Monsters

Extended Abstract

Sliding mode control with fault tolerance capacities: application to a rendezvous mission in a circular orbit

With the growing complexity of control systems, researchers have focused their work on the development of robust control laws. Increasing attention has grown with regards to Sliding Mode Controllers due to its attractive properties: finite time convergence and robustness against matched disturbances (i.e. disturbances that act on the input channels). It is known that its main drawback is the chattering effect. In order to reduce this effect, different modifications to the original technique have been proposed, take for instance the Super-Twisting Algorithm (STA). In this work, a controller based on the STA in a backstepping setup, is proposed for spacecraft rendezvous in circular orbit. The rendezvous takes place between a passive (no sensors or actuators) and an active spacecraft (has sensors, actuators and a Guidance Navigation and Control (GNC) unit). Along this work, the passive spacecraft is called the target and the active spacecraft is called the chaser. In addition, the chaser is not treated as a point mass, given that the effects of the flexible modes and the sloshing phenomena are considered. Furthermore, it has a Control Allocation (CA) unit, which distributes the control signal into the thrusters. No measurement noise is considered. The potential of the proposed solution is shown with a high-fidelity nonlinear simulator that considers the most dimensioning space disturbances (e.g. second zonal harmonic J_2, atmospheric drag, magnetic disturbance).

The results obtained are taken further, given that the guarantee of robustness against perturbations is not enough when it comes to critical systems. In other words, it is now considered that not only disturbances can affect the performance of the system, but also faults. Then, the capability of second order sliding mode controllers to compensate for both, disturbances and faults, is analyzed. A control that is capable of maintaining an acceptable performance despite the occurrence of faults is called Fault Tolerant Control (FTC). It is known that certain type of thruster faults can be modelled in an additive form, i.e. as matched disturbances. From this premise, the work in this thesis proposes a solution that consists of Generalized Super-Twisting Algorithm (GSTA) with an anti-windup strategy and a nonlinear observer. The main reason of employing a GSTA is because it offers more robustness against state dependent perturbations (sloshing phenomena and flexible modes) than the STA. In addition, with the help of the anti-windup strategy, the control law does not saturate the thrusters. The proposed solution does not assume the existence of a Fault Detection and Identification (FDI) unit, i.e. the system is not aware of the occurrence of a fault. Therefore, the CA unit does not play an active role in the proposed FTC solution. The considered faults are stuck open and stuck close thruster. The capability of the proposed solution to compensate against both types of faults, is shown with simulations in the high-fidelity non-linear benchmark.

Finally, considering that the accuracy of the control solution depends on the model, the proposed FTC solution is based on a coupled model. This model is expressed in Dual Quaternion formalism, which is the combination of dual numbers and quaternions. Dual quaternions have similar properties to quaternions and this allows to extend the control techniques applied to quaternions into dual quaternions.

Acknowledgements

I would like to start my acknowledgements by thanking CONACyT (Consejo Nacional de Ciencia y Tecnología) for the financial support. It is thanks to this organization that my dream of pursuing a PhD degree in France, became true.

I have been fortunate to work four years in the pleasant atmosphere of the IMS (laboratoire de l'Intégration du Matériau au Système) laboratory at the University of Bordeaux. Therefore, I would like to thank all the members and staff of the lab for their support. Especially, Prof. D. Henry is acknowledged for letting me join his ARIA (Approche Robuste et Intégrée de l'Automatique) research team and for making me feel welcomed since day one. I would like to highlight that this thesis wouldn't have been possible without his guidance and support. Thank you David for not losing your patience with me while explaining the same things over and over again; for your valuable time and for sharing your knowledge. In the same manner, I would also like to thank Jérôme Cieslak for his support, availability and valuable feedback. Thank you Jérôme for always making time for helping me.

I am also grateful to my external supervisor Prof. Jorge Dávila, who has been the only constant throughout my career. It is thanks to his enthusiasm towards research and his encouragement, that I pursued a Masters and a PhD degree. I cannot thank him enough for the life changing opportunities he gave me, for allowing me to learn from him, for his patience and support. Dr. Jorge, de corazón, muchas gracias.

In addition, I would like to thank the members of the jury for taking the time to read my work and for their very valuable comments to help me improve. Special thanks for Prof. D. Theilliol for serving as the president of the thesis examination committee.

Agradezco mucho a mi familia por siempre estar conmigo, porque nunca los sentí lejos. Gracias papás, por enseñarnos con el ejemplo, que el trabajo duro trae recompensas. Gracias por siempre apoyarme, por sus consejos, por impulsarme a ir por más y por creer en mí. Gracias a mis hermanas Rebeca y Nancy por compartir mis alegrias y mis tristezas, por siempre tener tiempo para escucharme y aconsejarme. Esto es para ustedes, los amo.

I must specially thank you Valentin, meeting you brought so much happiness and goodness to my life. Thank you for all the teaching, for all the selfless advice, for cooking delicious food for me and for the "very excellent" experiences we've shared. I wouldn't have been able to finish this without you. Mulțumesc.

I am thankful that this journey allowed me to meet awesome people that very quickly became friends. Thank you guys (Elodie, Andrei, Salma, Massoud, Nicolas, Alejandro and many more) for all the nice moments we shared.

Contents

List of Figures

List of Tables

List of Acronyms

ASMC Adaptive Sliding Mode Controllers. 20

ATV Automated Transfer Vehicle. 1

CA Control Allocation. 3, 4, 22–25, 30, 31, 37, 38, 56, 59, 63

CNSMA Continuous Nested Sliding Mode Controllers. 19, 20

CoM Center of Mass. 2, 26–30, 51

DCM Direction Cosine Matrix. 2

DoF degrees of freedom. 2, 4, 25, 45, 76

ESA European Space Agency. 1

FDI Fault Detection and Isolation. 3–5, 22, 23, 76

FES Functional Engineering Simulator. 26, 50, 67

FOSMC First Order Sliding Mode Control. 13, 16, 19, 24, 25, 32, 36–38, 40, 75

FTC Fault Tolerant Control. 1–4, 21–24, 45, 46, 50, 51, 57, 59, 63, 66, 67, 70, 73, 75, 76

GNC Guidance and Navigation Control. 2, 25

GSTA Generalized Super-Twisting Algorithm. 4, 15, 17, 24, 45, 57, 59, 63, 73, 75, 76

HCW Hill-Clohessy-Wiltshire. 4, 25

IMU Inertial Measurement Unit. 2, 26, 35

ISMC Integral Sliding Mode Control. 13, 14

ISS International Space Station. 1

LIDAR Light Detection and Ranging. 2, 26, 35

LISA Laser Interferometer Space Antenna. 1

LPV Linear Parameter Varying. 22, 24

LTI Linear Time-Invariant. 9, 14, 16, 22

LVLH Local Vertical Local Horizontal. 25, 26, 29, 51, 63

MIMO Multi-input/Multi-output. 7

MPC Model Predictive Control. 23, 24

NASA National Aeronautics and Space Administration. 1

PRISMA Hyperspectral PRecursor of the Application Mission. 1

SFF Satellite Formation Flying. 1

SMC Sliding Mode Control. 1, 3–5, 7, 9, 12–14, 18–20, 23–25, 37, 42, 57, 75, 76

SMO Sliding Mode Observers. 3, 20, 23

SOSMC Second Order Sliding Mode Controller. 15, 16, 19, 75

STA Super-twisting Algorithm. 15–18, 20, 24, 25, 32, 34, 36, 39, 40, 75

TA Twisting Algorithm. 15, 20

TSM Terminal Sliding Mode. 15, 20

VGSTA Variable Gain Super-Twisting Algorithm. 17

VSC Variable Structure Control. 7, 8

List of Publications of the Author

Conferences

[1] Jazmín Zenteno Torres, Jérôme Cieslak, David Henry, and Jorge Dávila. Fault compensability criteria with application to a rendezvous mission around mars. In *14th International Workshop on Advanced Control and Diagnosis*, 2017.

[2] Jazmín Zenteno-Torres, Jérôme Cieslak, David Henry, and Jorge Dávila. A tracking backstepping sliding-mode control for spacecraft rendezvous with a passive target. In *2018 UKACC 12th International Conference on Control (CONTROL)*, pages 69–74. IEEE, 2018.

[3] Jazmín Zenteno Torres, Jérôme Cieslak, David Henry, and Jorge Dávila. A super-twisting sliding mode control in a backstepping setup for rendezvous with a passive target. *IFAC-PapersOnLine*, 52(12):25–30, 2019.

[4] Jazmín Zenteno Torres, Jérôme Cieslak, David Henry, and Jorge Dávila. A sliding mode control in a backstepping setup for rendezvous mission on a circular orbit. In *8th European Conference for Aeronautics and Aerospace Sciences*, 2019.

[5] Jazmín Zenteno Torres, Jérôme Cieslak, David Henry, and Jorge Dávila. A super-twisting fault-tolerant control based on dual-quaternion formalism for spacecraft rendezvous. In *15th European workshop on advanced control and diagnosis*, 2019.

[6] David Henry, Jérôme Cieslak, J Zenteno Torres, Pablo Colmenarejo, João Branco, Nuno Santos, Pedro Serra, J Telaard, Hans Strauch, Alessandro Massimo Giordano, et al. Model-based fault diagnosis and tolerant control: the esa's e. deorbit mission. In *2019 18th European Control Conference (ECC)*, pages 4356–4361. IEEE, 2019.

Journals

[1] Luis F Ramírez Jerónimo, Jazmín Zenteno Torres, Belem Saldivar, Jorge Dávila, and Juan Carlos Ávila Vilchis. Robust stabilisation of linear time-invariant time-delay systems via first order and super-twisting sliding mode controllers. *IET Control Theory & Applications*, 14(1):175–186, 2019.

[2] David Henry, Jazmín Zenteno Torres, Jérôme Cieslak, Jorge Dávila, and Alejandra Ferreira De Loza. A dual quaternion sliding mode fault tolerant control solution for spacecraft rendezvous. *Submitted for Review to AIAA Journal of Guidance, Control, and Dynamics*, 2020.

Resumé en Français

R.1 Contexte

Le travail de recherche présenté dans ce mémoire de thèse, résulte d'une collaboration initiée il y a une dixaine d'année, entre l'équipe ARIA (Approche Robuste et Intégrée de l'Automatique) du laboratoire IMS (Intégration du Matériau au Système) de l'université de Bordeaux et L'IPN (Instituto Politecnico Nacional) de Mexico. Les travaux menés au sein de cette collaboration visent à développer de nouvelles méthodes de commande tolérante aux fautes, basées sur les techniques de commande par modes glissants.

Beaucoup de futures missions spatiales requerront des opérations de proximité autonomes dans lesquelles la détection des défauts, la localisation et les mesures de tolérance des défauts qui en découlent, sont d'une importance cruciale. Les missions de rendez-vous et d'amarrage/capture, comme pour la mission Mars Sample Return (MSR), le Project for On-Board Autonomy No.3 (PROBA 3) ou encore la mission e.Deorbit qui vise à capturer en orbite, le satelitte mort ENVISAT, sont aussi intrinsèquement liés aux conditions de fonctionnement et à la sécurité des engins spatiaux. Les rendez-vous autonomes et les tolérances de défauts ont été reconnus par l'ESA comme un élément clé des futures missions spatiales, ce qui nécessitera un système de Guidage Navigation Control (GNC) hautement sophistiqué. Cette thèse porte sur la conception et la validation d'un système de commande de tolérance de défauts actif, capable d'accommoder des défauts de tuyère qui affectent un vaisseau spatial chasseur lors d'un rendez-vous avec un vaisseau spatial cible passif sur une orbite circulaire. Les méthodologies proposées sont développées dans un contexte modes glissants.

Nous présentons donc dans les paragraphes suivant, les résultats importants des contributions de nos travaux de recherche.

R.2 Description de la mission spatiale support de nos travaux

La mission spatiale support de nos travaux de recherche, est une mission de rendez-vous entre deux engins spatiaux, en orbite terrestre, circulaire. La problématique abordée, se concentre sur la séquence terminale du rendez-vous de la mission, qui correspond aux derniers cent mètres, jusqu'à la capture.

L'un des engins (la cible) est un véhicule spatial considéré sphérique, sans aucun système embarqué, c'est à dire qu'il n'est pas équipé ni de capteurs, ni d'actionneurs, ni de système de télémétrie embarqué. A l'inverse, le deuxième (le chasseur) est équipé de systèmes embarqués lui permettant de contrôler son attitude et sa position, et donc d'effectuer n'importe quelle trajectoire dans l'espace et mouvements de rotation. Le mécanisme de capture est un panier avec une ouverture cylindrique, adaptée à la géométrie sphérique de la cible. Il est orienté selon l'axe de déplacement du chasseur. L'objectif est de réaliser la capture avec une précision inférieure à quelques centimètres. Le chasseur est supposé équipé:

- d'un panneau solaire à deux modes flexibles, localisés à $0.1 rad/s$ et $0.5 rad/s$, chaque mode ayant un facteur d'amortissement de 0.003;
- de deux réservoirs de carburant, partiellement remplis, de telle sorte que tout mouvement du chasseur produit des phénomènes de ballottement du carburant, dont les fréquences sont supposées localisées à $0.4 rad/s$, $0.8 rad/s$ et 1 rad/s, avec un facteur d'amortissement fixé à 0.1.

Les données relatives aux paramètres physiques de la mission, sont données dans le tableau 1.

Sous-systèmes	Paramètres
MCI	Masse: $m = 300\,\text{kg}$
	Inertie: $\boldsymbol{J} = \begin{bmatrix} 30 & 1 & 1 \\ 1 & 40 & 1 \\ 1 & 1 & 15 \end{bmatrix} \text{kg m}^2$
	CoM (centre de masse): [1.5 0.2 0.15]m
Réservoir 1	Facteur d'amortissement: 0.1
	Fréquence du mode 1: 0.4 rad/s
	Fréquence du mode 2: 0.8 rad/s
	Fréquence du mode 3: 1 rad/s
	Masse du carburant: 10 kg
Réservoir 2	Facteur d'amortissement: 0.1
	Fréquence du mode 1: 0.4 rad/s
	Fréquence du mode 2: 0.8 rad/s
	Fréquence du mode 3: 1 rad/s
	Masse du carburant: 20 kg
Panneau solaire	Facteur d'amortissement: 3e-3
	Fréquence du mode 1: 0.1 rad/s
	Fréquence du mode 2: 0.5 rad/s
	Inertie: $\boldsymbol{J}_{SA}$ =diag$(10, 1, 10)\text{kg m}^2$
	Masse: $m_{SA} = 40\,\text{kg}$
	ΔCoM chasseur - SA: $d = [0 \;\; 2 \;\; 0]\text{m}$
	Angle d'orientation des panneaux: $\beta = 0°$
	Matrice de participation modale en rotation: $\boldsymbol{B}_R$: $\begin{bmatrix} 36.64 & 0 \\ 0 & 0.06 \\ 0 & -37 \end{bmatrix}$
	Matrice de participation modale en translation: $\boldsymbol{B}_T$: $\begin{bmatrix} 0 & 6.8 \\ -0.01 & 0 \\ 6.54 & 0 \end{bmatrix}$

Table 1: Caractéristiques physiques du chasseur

Pendant le rendez-vous terminal, le contrôle d'attitude et de position du chasseur est continu, et supposé réalisé à l'aide de tuyères. En début de phase de rendez-vous, le guidage est modifié afin d'aligner le mécanisme de capture avec la cible (profil de guidage d'attitude correspondant à la phase dite d'acquisition de la cible). Puis, la position est contrôlée afin de se rapprocher de la cible, le long de son axe de vitesse (profil de guidage en translation relative dit translation forcée), tout en maintenant l'attitude du chasseur alignée avec la cible.

La figure 1 illustre les trajectoires du chasseur et de la cible, autour de la terre, ainsi que la trajectoire de rendez-vous. Les figures présentées sont tirées du simulateur haute-fidélité utilisé dans nos travaux de thèse. Le tableau 2 donne les paramètres orbitaux caractérisant la trajectoire

de rendez-vous.

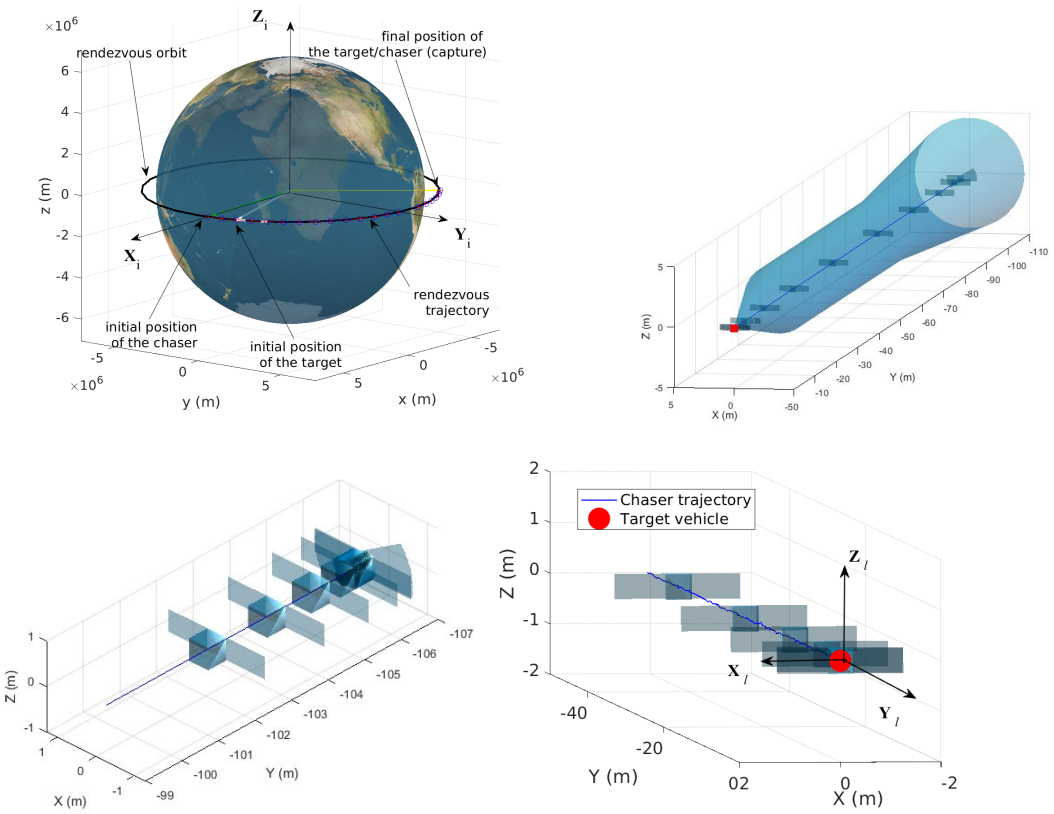

Figure 1: Mission spatiale considérée dans les travaux de thèse

Paramètres orbitaux:	Cible	Chasseur
Rayon orbital (a)	$7068km$	$7068km$
Excentricité (e)	0	0
Inclinaison (i)	$0rad$	$0rad$
Longitude du nœud ascendant (Ω)	$0rad$	$0rad$
Argument du périgée (ω)	$0rad$	$0rad$
Anomalie vraie (ν: $\dot{\nu} = n$)	$\nu(0) = 1,5.10^{-5}rad$	$\nu(0) = 0rad$

Table 2: Caractéristiques de l'orbite de rendez-vous

Niveau système de mesure, le chasseur est supposé équipé d'une centrale inertielle IMU (Inertial Measurement Units) et d'un viseur d'étoiles, de telle sorte que l'on suppose que tout l'état en attitude (position angulaire, vitesse angulaire et accélération angulaire) est accessible, via un module de navigation. On suppose également que le chasseur est équipé d'un système de mesure de type LIDAR, de telle sorte que tout l'état en position relative (position relative, vitesse relative et accélaration relative) est supposé accessible, via un module de navigation. Les modules de navigation étant pratiquement composés d'estimateurs, ces mesures ne peuvent être considérées parfaites. Aussi, les caractéristiques suivantes sont-elles considérées:

- des précisions de $0.1deg$, $0.01deg/s$ et $0.01deg/s^2$ sont considérées pour les mesures d'attitude, de vitesse angulaire et d'accélération angulaire, selon les trois axes;
- des précisions de $2mm$, $0.2mm/s$ et $0.2mm/s^2$ sont considérées pour les positions relatives

3D, les vitesses relatives 3D et les accélérations relatives 3D.

Au niveau du système d'actionneurs, deux jeux de tuyères différents sont considérés dans nos travaux de thèse.

- Dans un premier temps, on considère un jeu de 12 tuyères de $4N$, disposées et orientées comme illustré sur la figure 2 de gauche. Cette configuration de tuyères est utilisée dans les travaux présentés dans le chapitre 3.

- Une étude de capacité de tolérance aux pannes sur la configuration 12 tuyères, montre que cette configuration ne permet pas d'atteindre les objectifs de tolérance aux pannes, voir chapitre 4. Cette problématique est connue sous la terminologie *"fault recoverability property"*. Ainsi, dans un deuxième temps, on considère un jeu de 24 tuyères de $2N$, disposées et orientées comme illustré sur la figure 2 de droite.

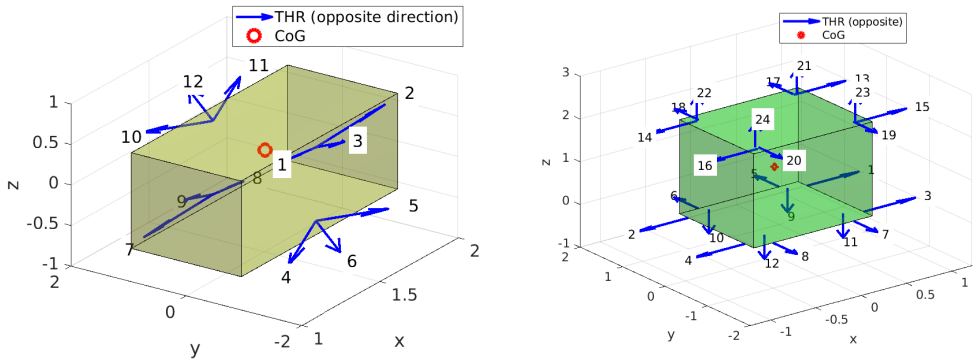

Figure 2: Configurations des tuyères utilisées dans le chapitre 3 (gauche) et 4 (droite)

La mission complète avec toutes les caractéristiques précédemment explicitées, est implantée dans un simulateur haute-fidélité appelé FES (Functional Engineering Simulator), développé sous Matlab/Simulink. FES est un acronyme utilisé dans l'industrie du spatial pour désigner un simulateur très haute-fidélité, permettant de jouer (et donc de valider en simulation), une mission spatiale complète. C'est une phase cruciale dans le développement d'une mission spatiale, car elle précède la mission réelle. Un environnement FES est utilisé pour déterminer les spécifications de mission, dimensionner les engins spatiaux, vérifier les performances des systèmes et sous-systèmes, etc. L'environnement FES utilisé prend en compte les perturbations spatiales les plus dimensionnantes, telles que le deuxième harmonique zonale J2, la traînée atmosphérique, le champ magnétique terrestre, le gradient de gravité terrestre, la pression solaire et albédo-terrestre.

La phase terminale du rendez-vous est très critique, car toute défaillance pourrait conduire à un échec de la mission. Il est évident, que si, par exemple, une défaillance ouvrant entièrement une tuyère se produit (une tuyère coincée en position entièrement ouverte), des conséquences dramatiques peuvent survenir. Les lois de contrôle peuvent devenir instables, ce qui peut alors conduire le chasseur à perdre l'attitude et/ou la position de la cible, ou pire entrer en collision avec la cible. Le problème devient particulièrement critique au cours des 20 derniers mètres de la phase de rendez-vous.

L'objectif des travaux de recherche présentés dans ce mémoire, vise à apporter des solutions à cette problématique.

R.3 Commande placée dans une configuration backstepping

La première contribution de nos travaux de thèse est abordée dans le chapitre 3. Nous y présentons une approche de commande par modes glissants, placée dans une configuration dite de "boucles imbriquées", connue sous le terme "backstepping". L'objectif visé est de synthétiser les lois de contrôle d'attitude et de mouvement relatif du chasseur, de façon à satisfaire aux spécifications de la mission de rendez-vous. Il est important de souligner ici que la partie tolérance aux fautes n'est pas abordée, et que le module de navigation est supposé délivré des mesures parfaites (pas de d'erreur de mesures). Ces hypothèses sont relaxées dans le chapitre 4.

R.3.1 Modélisation

Dans ce chapitre, la dynamique de translation relative est exprimée à l'aide des équations de Clohessy-Wiltshire, aussi appelées équations de Hill [Wie98, MG12]. Ces équations sont basées sur l'hypothèse que la distance relative entre les deux engins est très petite devant l'orbite, ce qui est réaliste pratiquement. Ces équations sont données dans un repère particulier appelé le repère LVLH (Local Vertical Local Horizontal), identifié par la notation vectorielle $\bullet^{(l)}$ (voir paragraphe 3.1 pour la définition de ce repère). Le modèle est donné par

$$\begin{bmatrix} \dot{\boldsymbol{\rho}} \\ \ddot{\boldsymbol{\rho}} \end{bmatrix} = \begin{bmatrix} 0 & 0 & 0 & 1 & 0 & 0 \\ 0 & 0 & 0 & 0 & 1 & 0 \\ 0 & 0 & 0 & 0 & 0 & 1 \\ 3n^2 & 0 & 0 & 0 & 2n & 0 \\ 0 & 0 & 0 & -2n & 0 & 0 \\ 0 & 0 & -n^2 & 0 & 0 & 0 \end{bmatrix} \begin{bmatrix} \boldsymbol{\rho} \\ \dot{\boldsymbol{\rho}} \end{bmatrix} + \begin{bmatrix} 0_3 \\ \mathbb{I}_3 \end{bmatrix} \left(\frac{1}{m} \boldsymbol{F}_u^{(l)} + \boldsymbol{\gamma}_v^{(l)} \right) \tag{1}$$

où $\boldsymbol{\rho} \in \mathbb{R}^3$ et $\dot{\boldsymbol{\rho}} \in \mathbb{R}^3$ représentent les distances et vitesses relatives tridimensionnelles entre les deux véhicules, dans le repère LVLH. $\boldsymbol{F}_u^{(l)} \in \mathbb{R}^3$ représente le vecteur de forces tridimensionnelles causé par le système de tuyères (système de propulsion). $\boldsymbol{\gamma}_v^{(l)}$ représente une accélération tridimensionnelle généralisée qui modélise les accélérations sous forme additive, des modes souples du panneau solaire, des ballottements du carburant et des perturbations spatiales, i.e. le deuxième harmonique zonale J2, la traînée atmosphérique, le champ magnétique terrestre, le gradient de gravité terrestre, la pression solaire et albédo-terrestre. m est la masse totale du chasseur et $n = \sqrt{\mu a^3}$ où $\mu = 3.9860044.10^{14} m^3/s^2$ est la constante gravitationnelle de la Terre.

Le modèle dynamique d'attitude est déduit de la seconde loi de Newton, exprimée dans le repère chasseur (on parle de repère *"body"*, identifiée par la notation vectorielle $\bullet^{(b)}$) et linéarisée autour d'une attitude et d'une vitesse angulaire de référence nulle, soit:

$$\begin{bmatrix} \dot{\boldsymbol{\Theta}} \\ \dot{\boldsymbol{\omega}} \end{bmatrix} = \begin{bmatrix} \mathbf{0}_3 & \mathbb{I}_3 \\ \mathbf{0}_3 & \mathbf{0}_3 \end{bmatrix} \begin{bmatrix} \boldsymbol{\Theta} \\ \boldsymbol{\omega} \end{bmatrix} + \begin{bmatrix} \mathbf{0}_3 \\ \boldsymbol{J}^{-1} \end{bmatrix} (\boldsymbol{T}_u^{(b)} + \boldsymbol{T}_v^{(b)}) \tag{2}$$

$\boldsymbol{\Theta} \in \mathbb{R}^3$ et $\boldsymbol{\omega} \in \mathbb{R}^3$ représentent l'attitude et la vitesse angulaire du chasseur. $\boldsymbol{T}_u^{(b)} \in \mathbb{R}^3$ représente le vecteur de couples tridimensionnelles causé par le système de propulsion et $\boldsymbol{T}_v^{(b)}$ représente un couple tridimensionnel généralisé qui modélise les couples de perturbations sous forme additive, des modes souples du panneau solaire, des ballottements du carburant et des perturbations spatiales.

Dans cette partie de nos travaux, le couplage entre les modèles d'attitude et de position relative, provient du système de propulsion illustré sur la figure 2 de gauche, puisque la commande des tuyères $\boldsymbol{u}_T$ génère simultanément les forces $\boldsymbol{F}_u^{(b)} = \mathcal{R}_l^{(b)}(\boldsymbol{\Theta}) \boldsymbol{F}_u^{(l)}$ et les couples $\boldsymbol{T}_u^{(b)}$. Ici, $\mathcal{R}_l^{(b)}(\boldsymbol{\Theta})$ est la matrice de changement de repère $\bullet^{(l)} \rightarrow \bullet^{(b)}$. On montre en effet dans nos travaux que la

commande $\boldsymbol{u}_T$ des 12 tuyères est liée à $\boldsymbol{F}_u^{(b)}$ et $\boldsymbol{T}_u^{(b)}$ par la relation mathématique

$$\begin{aligned}\boldsymbol{F}_u^{(l)} &= \mathcal{R}_b^{(l)}(\boldsymbol{\Theta})\boldsymbol{F}_u^{(b)} = \mathcal{R}_b^{(l)}(\boldsymbol{\Theta})[R_{f_1}\dots R_{f_{12}}]\boldsymbol{u}_T \\ &= \mathcal{R}_b^{(l)}(\boldsymbol{\Theta})\mathbf{R}_f\boldsymbol{u}_T \qquad (3)\\ \boldsymbol{T}_u^{(b)} &= [R_{\tau_1}\dots R_{\tau_{12}}]\boldsymbol{u}_T = \mathbf{R}_\tau\boldsymbol{u}_T,\ \mathbf{R} = \left[\mathbf{R}_\tau^\intercal\ \mathbf{R}_f^\intercal\right]^\intercal \qquad (4)\end{aligned}$$

où les colonnes de $\mathbf{R}$ sont les coefficients de participation des tuyères, qui définissent comment chaque tuyère affecte chaque composante des vecteurs $\boldsymbol{F}_u^{(b)}$ et $\boldsymbol{T}_u^{(b)}$. Dans cette équation, $\mathcal{R}_b^{(l)}(\boldsymbol{\Theta})$ est la matrice de changement de repère $\bullet^{(b)} \rightarrow \bullet^{(l)}$. Inverser cette équation à chaque instant t, permet de calculer la commande $\boldsymbol{u}_T(t)$ des 12 tuyères, connaissant $\boldsymbol{F}_u^{(l)}(t)$ et $\boldsymbol{T}_u^{(b)}(t)$. On parle de module d'allocation, noté CA pour Control Allocation. Dans nos travaux, ce problème est posé comme le problème d'optimisation suivant:

$$\mathbf{u}_c^{(b)}(t) = \underset{\mathbf{u}_c^{(b)}\in\mathcal{U}=\{u_{ck}^{(b)}:0\le u_{ck}^{(b)}\le u_{kmax}\}}{argmin} \left\|\mathbf{W}_v(\mathbf{R}\mathbf{u}_c^{(b)}(t) - \mathbf{v}_r)\right\|_p \qquad (5)$$

$\mathbf{v}_r$ est le torseur des couples/forces de commande et $u_{kmax} = 4N$ est la valeur max de poussée des tuyères.

R.3.2 Solution de commande par modes glissants et backstepping

On montre alors que les modèles (1) et (2) admettent la forme générique suivante dite commandable par bloc [DILU90]:

$$\begin{aligned}\dot{x}_1 &= A_1x_1 + B_1x_2 \qquad (6)\\ \dot{x}_i &= A_i\overline{x}_i + B_ix_{i+1} \qquad (7)\\ \dot{x}_r &= A_r\overline{x}_r + B_r(u+v) \qquad (8)\end{aligned}$$

avec $i = \overline{2, r-1}$. $x = [x_1^\intercal, x_2^\intercal, \dots, x_r^\intercal]^\intercal \in \mathbb{R}^n$, $u \in \mathbb{R}^m$ et $v \in \mathbb{R}^m$ font référence à l'état, à la commande et aux entrées de perturbations, associés aux modèles (1) et (2). $\overline{x}_i$ est défini tel que $\overline{x}_i = [x_1^\intercal, x_2^\intercal, \dots, x_i^\intercal]^\intercal, x_i \in \mathbb{R}^{n_i}$ où $n_i = \text{rank}(B_i)$, $\sum_{i=1}^r n_i = n$. Le sous-système (6)-(7) pour $i = \overline{2, r-1}$ représente la dynamique sous-actionnée du système et (8) corresponds à la dynamique actionnée. Ainsi, $x_r \in \mathbb{R}^m$. Les matrices A_i, B_i sont déduites de (1) et (2).

Sous certaines hypothèses, notamment sous l'hypothèse de bornitude des perturbations au sens l_∞, on montre que la structure de commande par backstepping (boucles imbriquées récursives) et modes glissants (termes u_l et u_n) illustrée sur la figure 3, permet de résoudre le problème de contrôle en attitude et en position relative du chasseur.

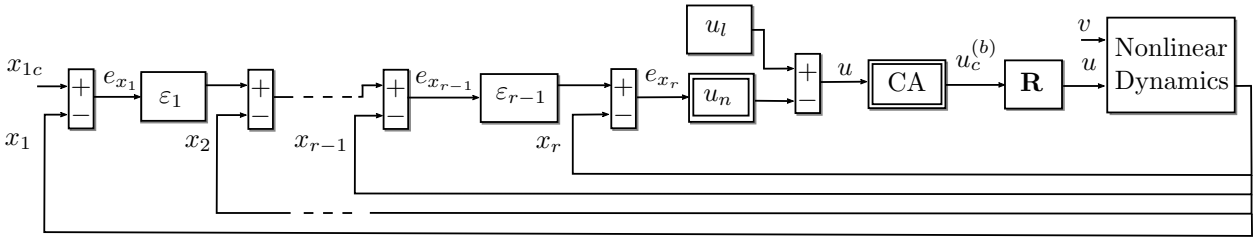

Figure 3: Commande par backstepping et modes glissants

Deux types de commande par modes glissants sont alors proposés:

1) Une commande par mode glissant du premier ordre. L'approche proposée se résume en la succession des étapes suivantes.

Step 1. Soit l'erreur de consigne $e_{x_1} = x_{1c} - x_1$. On utilise x_2 comme commande virtuelle telle que $x_2 := \varepsilon_1$ où

$$\varepsilon_1 = B_1^{\dagger}(\dot{x}_{1c} - A_1 x_1 - \hat{A}_1 e_{x_1}) \tag{9}$$

où $\hat{A}_1 < 0$ permet de fixer les performances de suivi de trajectoire. $B_i^{\dagger} = B_i^{\intercal}(B_i B_i^{\intercal})^{-1}$ est l'inverse à droite de la matrice B_i.

Step i, $\mathbf{i = \overline{2, r-1}}$. Soit l'erreur $e_{x_i} = \varepsilon_{i-1} - x_i$ et la commande virtuelle

$$\varepsilon_i = B_i^{\dagger}(\dot{\varepsilon}_{i-1} - A_i \bar{x}_i - \hat{A}_i e_{x_i} + B_{i-1}^{\intercal} e_{x_{i-1}}) \tag{10}$$

où $\hat{A}_i < 0$, $i = \overline{2, r-1}$.

Step r. Soit la surface de glissement $e_{x_r} = \varepsilon_{r-1} - x_r$ et la commande

$$u = \underbrace{B_r^{\dagger}(\dot{\varepsilon}_{r-1} - A_r \bar{x}_r + B_{r-1}^{\intercal} e_{x_{r-1}})}_{u_l} - u_n \tag{11}$$

où $u_n \in \mathbb{R}^m$ est la partie non linéaire de la commande par modes glissants du premier ordre, définie telle que

$$u_n = \alpha \operatorname{sign}(e_{x_r}) \tag{12}$$

On montre alors à l'aide de la théorie de Lyapunov, que cette commande est stable et rejette les perturbations considérées. Malheureusement, ce type de solution conduit à un effet de broutement du signal de commande (dit "chattering"), effet bien connu de la communauté de la commande par mode glissant.

2) Pour palier le problème de broutement du signal de commande, nous proposons une solution basée sur l'algorithme Super-Twisting (STA). Cette solution consiste à définir la commande u_n dans la *rième* étape précédente, de la façon suivante:

$$u_n = K_1 \Psi_1 + K_2 \int_{t_0}^{t} \Psi_2 d\tau \tag{13}$$

où les matrices $K_1 = \operatorname{diag}(k_{11}, \dots k_{1m})$, $K_2 = \operatorname{diag}(k_{21}, \dots k_{2m})$, $\Psi_1 = \operatorname{diag}(\Psi_{11}, \dots, \Psi_{1m})$ et $\Psi_2 = \operatorname{diag}(\Psi_{21}, \dots, \Psi_{2m})$ vérifient

$$\Psi_{1j} = |e_{x_{r_j}}|^{\frac{1}{2}} \operatorname{sign}(e_{x_{r_j}}),\ \Psi_{2j} = \operatorname{sign}(e_{x_{r_j}}), j = \overline{1, m} \tag{14}$$

et

$$k_{2j} > \tilde{\delta}_j, \quad k_{1j} > \sqrt{k_{2j} + \tilde{\delta}_j}, \quad j = \overline{1, m} \tag{15}$$

On montre alors à l'aide d'un théorème, que cette commande est stable et rejette les perturbations considérées, assurant *de facto* le suivi des trajectoires de référence. Le théorème établit également les conditions que doivent satisfaire les constantes $\tilde{\delta}_j, j = \overline{1, m}$, voir chapitre 3 pour de plus amples détails.

R.3.3 Résultats de simulation

Les deux types de commande par modes glissants sont implantés dans le simulateur FES. Nous ne présentons ici que les résultats les plus pertinents, qui correspondent à ceux obtenus avec la loi de commande STA, voir figures 4 et 5.

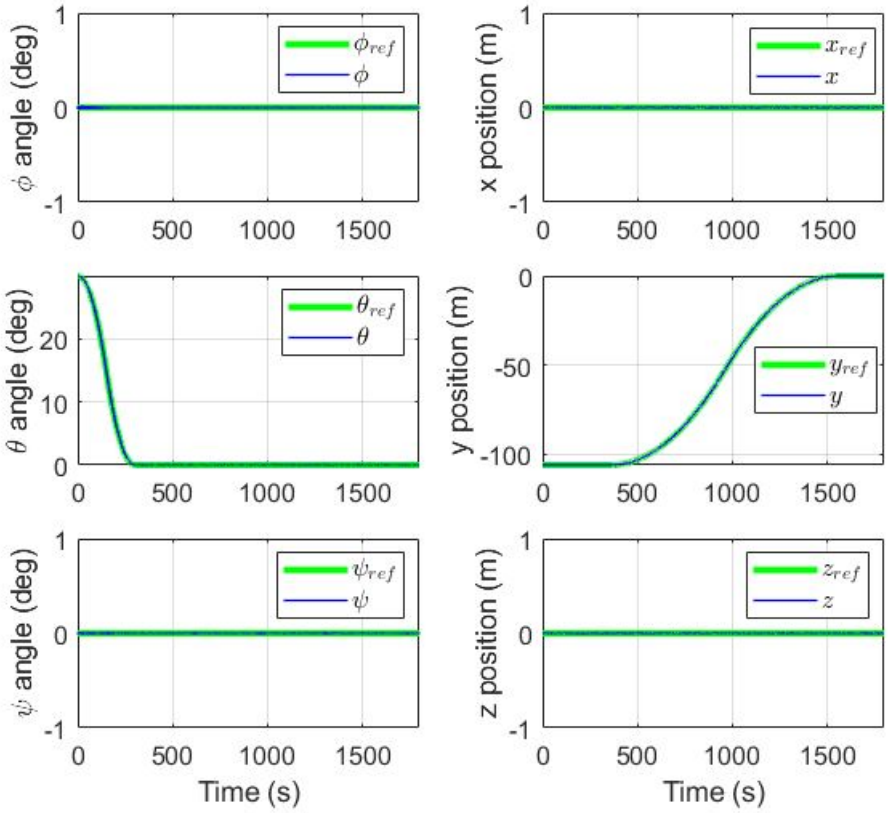

Figure 4: Attitudes et positions relatives selon les 3 axes x, y, z

Les résultats obtenus montrent que les profils d'attitude et de position relative, sont suivis par le chasseur avec des erreurs d'asservissement faibles, et ce malgré la présence des modes souples du panneau solaire, du ballottement du carburant dans les deux réservoirs et des perturbations spatiales que sont le deuxième harmonique zonale J2, la traînée atmosphérique, le champ magnétique terrestre, le gradient de gravité terrestre, la pression solaire et albédo-terrestre. De plus, la figure 5 de droite, montre des signaux de commande des tuyères dans leur plage de fonctionnement non saturé.

Les résultats obtenus illustrent donc que la solution de contrôle/commande proposée, permet de satisfaire aux objectifs de rendez-vous et de capture de la cible. Ces résultats sont confirmés par la représentation des mouvements du chasseur dans le corridor de rendez-vous, donnés sur la figure 6.

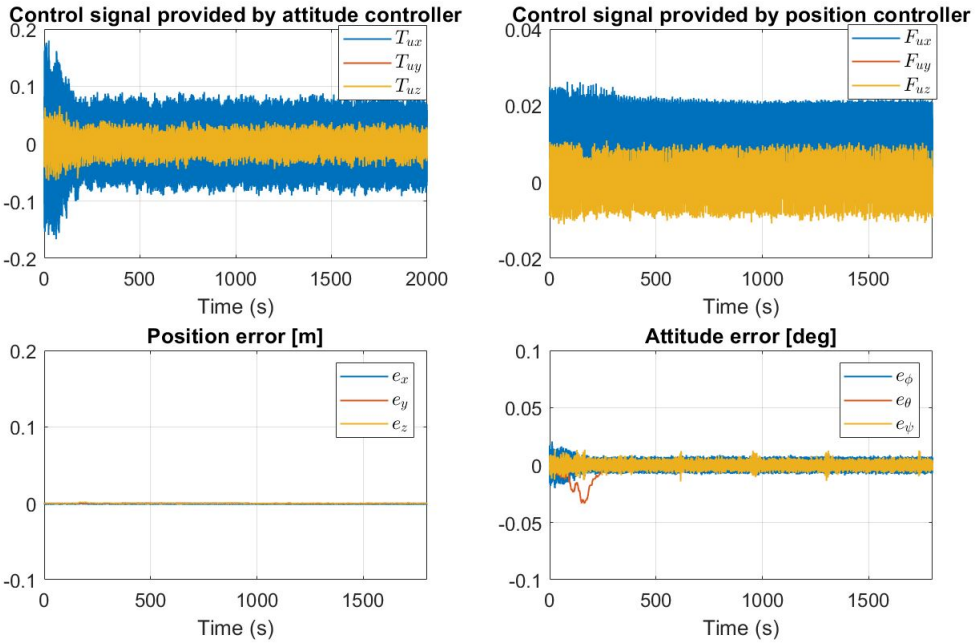

Figure 5: Erreurs d'asservissement et commande des tuyères

R.4 Commande tolérante aux fautes basée sur l'algorithme GSTA

La deuxième contribution de nos travaux de thèse est abordée dans le chapitre 4. Les résultats établis au chapitre 3 sont étendus au cas de la problématique de tolérance aux fautes, les défauts considérés étant ceux du système de propulsion par tuyères. Une solution est alors proposée sur la base des modes glissants du second ordre. L'élément clé de la démarche réside dans la modélisation des défauts actionneurs, qui sont exprimés comme des perturbations d'entrées, conjointement avec les perturbations spatiales, comme des perturbations d'état qui dépendent de l'état. En d'autres termes, et contrairement à l'approche précédente, les perturbations ne sont pas approximées. La démarche méthodologique vise alors à proposer une solution de commande tolérante aux fautes, basée sur l'algorithme "Generalized STA" (noté GSTA), placé en boucle externe de compensation de défauts utilisant un estimateur de défauts non linéaire. Le problème de saturation des actionneurs est également abordé et une solution basée sur la géométrie polytopique, est proposée. L'élément clé de l'approche tolérante aux pannes est que la solution ne nécessite pas de diagnostiquer les fautes et donc n'utilise pas d'algorithme de détection et de localisation de défauts.

R.4.1 Modélisation par l'algèbre du quaternion dual

Dans ce chapitre, les dynamiques de translation relative et de d'attitude du chasseur sont établies à l'aide du formalisme du quaternion dual, qui permet de tenir compte des effets de couplage [Cli82, Stu91, GV16]. Nous utilisons la notation $\bar{a} = a_r + \varepsilon a_d, \varepsilon \neq 0, \varepsilon^2 = 0$ pour un nombre dual, $a_r \in \mathbb{R}$ et $a_d \in \mathbb{R}$ étant la partie réelle et la partie duale du nombre dual. ε est le nombre dual unitaire [Cli82, Stu91].

La solution développée est une solution dite à six degrés de libertés (approche 6-DOF). Nous montrons ainsi que les équations suivantes, exprimées dans le repère chasseur noté $\bullet^{(c)}$, permettent de modéliser entièrement la mission de rendez-vous (la notation $\bullet^{(t)}$ indique un vecteur dans le repère cible):

$$\dot{\bar{\mathbf{q}}}_e = \frac{1}{2}\bar{\mathbf{q}}_e \circ \bar{\boldsymbol{\omega}}_e^{(c)} \tag{16}$$

$$\dot{\bar{\boldsymbol{\omega}}}_e^{(c)} = -\bar{\boldsymbol{M}}^{-1} \circ \left(\bar{\boldsymbol{\omega}}_c^{(c)} \times \bar{\boldsymbol{M}} \circ \bar{\boldsymbol{\omega}}_c^{(c)}\right) + \bar{\boldsymbol{M}}^{-1} \circ \bar{\boldsymbol{f}}_{ct}^{(c)} - \bar{\mathbf{q}}_e^* \circ \dot{\bar{\boldsymbol{\omega}}}_t^{(t)} \circ \bar{\mathbf{q}}_e + \bar{\boldsymbol{\omega}}_e^{(c)} \times \left(\bar{\mathbf{q}}_e^* \circ \bar{\boldsymbol{\omega}}_t^{(t)} \circ \bar{\mathbf{q}}_e\right) \tag{17}$$

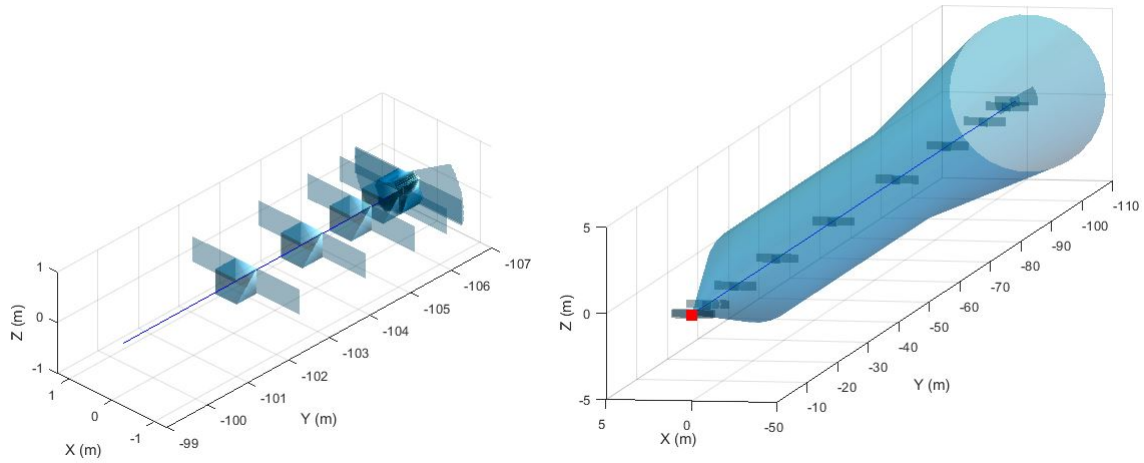

Figure 6: Mission de rendez-vous et de capture

Dans ces équations, $\bar{\mathbf{q}}_e, \bar{\boldsymbol{\omega}}_e^{(c)}, \bar{\boldsymbol{\omega}}_c^{(c)}, \bar{\boldsymbol{\omega}}_t^{(t)}$ et $\bar{\boldsymbol{f}}_{ct}^{(c)}$ représentent le quaternion dual des mouvements relatifs entre les deux véhicules, la vitesse de rotation duale relative, la vitesse de rotation duale du chasseur, la vitesse de rotation duale de la cible et la force duale totale, respectivement. $\bar{\mathbf{M}}$ est la matrice d'inertie duale définie telle que [WLS+12]

$$\begin{aligned}\bar{\mathbf{M}} &= m\frac{d}{d\varepsilon}\mathbf{I}_3 + \varepsilon \boldsymbol{J} \\ &= \begin{bmatrix} m\frac{d}{d\varepsilon} + \varepsilon J_{xx} & \varepsilon J_{xy} & \varepsilon J_{xz} \\ \varepsilon J_{xy} & m\frac{d}{d\varepsilon} + \varepsilon J_{yy} & \varepsilon J_{yz} \\ \varepsilon J_{xz} & \varepsilon J_{yz} & m\frac{d}{d\varepsilon} + \varepsilon J_{zz} \end{bmatrix}\end{aligned} \tag{18}$$

On montre alors que, compte tenu des caractéristiques particulières géométriques de la cible et du mécanisme de capture, ces équations se simplifient sous la forme:

$$\dot{\boldsymbol{\omega}}_e^{(c)} = -\boldsymbol{J}^{-1}\left(\boldsymbol{\omega}_e^{(c)} \times \boldsymbol{J}\boldsymbol{\omega}_e^{(c)}\right) + \boldsymbol{J}^{-1}\left(\boldsymbol{\tau}_{c_u}^{(c)} + \boldsymbol{\tau}_{ct_d}^{(c)} + \boldsymbol{\tau}_{c_f}^{(c)}\right) \tag{19}$$

qui traduit la dynamique de rotation du chasseur, et

$$\ddot{\boldsymbol{r}}_e^{(c)} = -\boldsymbol{\omega}_e^{(c)} \times \dot{\boldsymbol{r}}_e^{(c)} - \boldsymbol{\omega}_e^{(c)} \times \boldsymbol{\omega}_e^{(c)} \times \boldsymbol{r}_e^{(c)} + \frac{\boldsymbol{f}_{c_u}^{(c)}}{m} + \frac{\boldsymbol{f}_{ct_d}^{(c)}}{m} + \frac{\boldsymbol{f}_{c_f}^{(c)}}{m} \tag{20}$$

tel que $\boldsymbol{\omega}_e^{(c)} = \boldsymbol{\omega}_c^{(c)}$, pour la dynamique de translation relative. $\boldsymbol{\tau}_{c_u}^{(c)}, \boldsymbol{\tau}_{ct_d}^{(c)}, \boldsymbol{\tau}_{c_f}^{(c)}$ représentent les couples générés par le système de propulsion, les perturbations spatiales et les défauts actionneurs considérés, respectivement. $\boldsymbol{f}_{c_u}^{(c)}, \boldsymbol{f}_{ct_d}^{(c)}, \boldsymbol{f}_{c_f}^{(c)}$ représentent les forces générées par le système de propulsion, les perturbations spatiales et les défauts actionneurs considérés, respectivement.

Dans cette partie, les couples et forces de propulsion sont modélisés comme dans le chapitre 3, soit via la distribution d'une matrice de configuration des tuyères $\boldsymbol{R}$, i.e.

$$\begin{bmatrix} \boldsymbol{\tau}_{c_u}^{(c)}(t) \\ \boldsymbol{f}_{c_u}^{(c)}(t) \end{bmatrix} = \begin{bmatrix} \boldsymbol{R}_\tau \\ \boldsymbol{R}_f \end{bmatrix} \boldsymbol{u}_c^{(c)}(t) = \boldsymbol{R}\boldsymbol{u}_c^{(c)}(t), \quad \boldsymbol{R} \in \mathbb{R}^{6\times 24} \tag{21}$$

A l'inverse, les perturbations spatiales ainsi que les modes du panneau solaire et des ballottements du carburant, sont eux modélisés de façon mathématique, et on montre que le modèle obtenu, conduit à des couples et des forces qui dépendent de l'état, voir chapitre 4 pour de plus amples

détails.

Les défauts considérés sont de type *"embardée à vitesse maximale vers la position complètement ouverte ou fermée"* des tuyères. Inspirés des travaux [Hen08, HCT+19], nous montrons que ce type de défauts peut être mathématiquement exprimé de la façon suivante

$$\phi_k(t) = \begin{cases} \max\{u_k(t), 1\} & \text{tuyère ouverte} \\ 0 & \text{tuyère fermée} \end{cases} \tag{22}$$

où u_k fait référence à la commande en poussée de la *kième* tuyère. Il vient alors que l'effet de ces défauts peut être modélisé de façon multiplicative, tel que (la notation "$\tilde{\bullet}$" souligne le cas défaillant)

$$\tilde{u}_{c_k}^{(c)}(t) = \left(\mathbb{I}_{24} - \Psi(t)\right) u(t) \tag{23}$$

où $\Psi(t) = diag\left(\psi_1(t), ..., \psi_{24}(t)\right)$, $0 \leq \psi_k(t) \leq 1, k = \overline{1, 24}$ étant inconnu. ψ_k est donné par

$$\psi_k(t) = \begin{cases} 0 & \text{si non défaillant} \\ 1 - \phi_k(t)/u_{c_k}^{(c)}(t) & \text{si défaillant} \end{cases} \tag{24}$$

Ainsi, $\tilde{u}_{c_k}^{(c)}(t)$ n'est rien d'autre que la poussée réelle de la *kième* tuyère, à chaque instant t, qui est bien évidemment inconnue.

Nous montrons alors qu'il est possible d'approximer ces équations sous forme additive, ce qui conduit à exprimer les couples $\boldsymbol{\tau}_{c_f}^{(c)}(t)$ et les forces $\boldsymbol{f}_{c_f}^{(c)}(t)$ à l'aide des équations suivantes

$$\begin{bmatrix} \boldsymbol{\tau}_{c_f}^{(c)}(t) \\ \boldsymbol{f}_{c_f}^{(c)}(t) \end{bmatrix} = \sum_{k=1}^{24} \boldsymbol{K}_k f_k(t) \tag{25}$$

où f_k désigne la signature du *kième* défaut, $\boldsymbol{K}_k$ étant sa matrice de répartition qui se déduit de $\boldsymbol{R}$.

R.4.2 Solution de commande tolérante aux fautes

La solution de contrôle tolérant aux fautes qui est proposée dans nos travaux de thèse, est illustrée sur la figure 7.

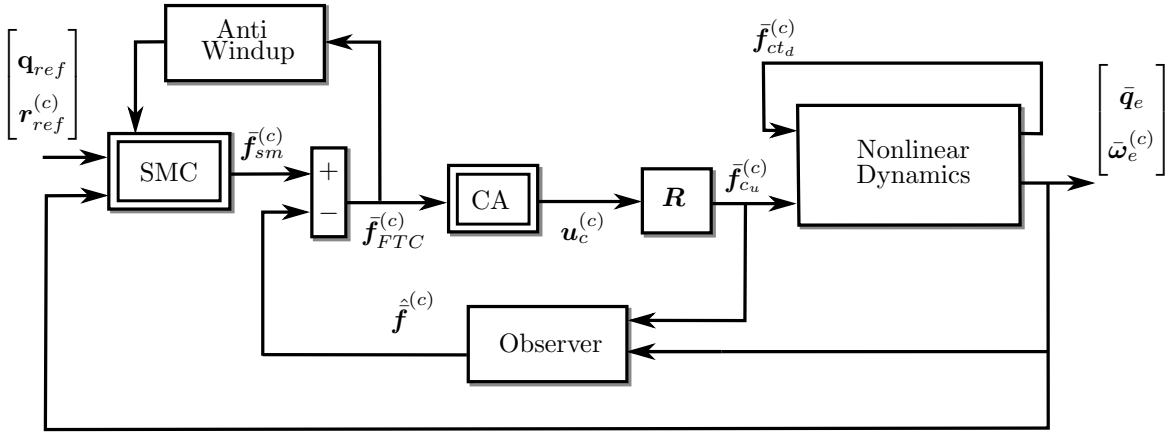

Figure 7: Control setup

La structure proposée consiste en une commande donnée par:

$$\bar{\boldsymbol{f}}_{FTC}^{(c)} = \bar{\boldsymbol{f}}_{sm}^{(c)} - \hat{\bar{\boldsymbol{f}}}^{(c)} = \underbrace{\boldsymbol{f}_{sm}^{(c)} - \hat{\boldsymbol{f}}^{(c)}}_{\boldsymbol{f}_{FTC}^{(c)}} + \varepsilon(\underbrace{\boldsymbol{\tau}_{sm}^{(c)} - \hat{\boldsymbol{\tau}}^{(c)}}_{\boldsymbol{\tau}_{FTC}^{(c)}}) \tag{26}$$

où $\boldsymbol{f}_{sm}^{(c)}$ et $\boldsymbol{\tau}_{sm}^{(c)}$ sont calculés à l'aide de l'algorithme GSTA. Les signaux $\hat{\boldsymbol{f}}^{(c)}$ et $\hat{\boldsymbol{\tau}}^{(c)}$ sont des estimations des parties réelle et duale des forces duales correspondantes aux perturbations spatiales et aux défauts. Due à le présence des saturations des tuyères, un système "anti-windup" est ajouté à la loi de commande.

La solution proposée repose donc sur la conjonction de trois sous-systèmes:

1) La partie estimation des parties réelle et duale des forces duales correspondantes aux perturbations spatiales et aux défauts. Cette dernière est réalisée à l'aide des estimateurs non linéaires suivant

$$\hat{\boldsymbol{\tau}}^{(c)} = \boldsymbol{J}\left(\dot{\boldsymbol{\omega}}_c^{(c)} - \hat{\dot{\boldsymbol{\omega}}}_c^{(c)}\right) = \boldsymbol{\tau}_{ct_d}^{(c)} + \boldsymbol{\tau}_{c_f}^{(c)} - \boldsymbol{\tau}_{\Delta} \tag{27}$$

$$\hat{\boldsymbol{f}}^{(c)} = m\left(\ddot{\boldsymbol{r}}_e^{(c)} - \hat{\ddot{\boldsymbol{r}}}_e^{(c)}\right) = \boldsymbol{f}_{ct_d}^{(c)} + \boldsymbol{f}_{c_f}^{(c)} - \boldsymbol{f}_{\Delta} \tag{28}$$

la partie gauche des égalités représentant la forme de calcul, et la partie droite, la forme d'évaluation. Ces équations montrent que ces estimations ne sont pas parfaites et qu'elles sont donc entachées des erreurs $\boldsymbol{\tau}_{\Delta}$ et $\boldsymbol{f}_{\Delta}$.

2) La boucle de commande par modes glissants GSTA, dont l'objectif sera de suivre les trajectoires d'attitude et de position relative de référence $\boldsymbol{q}_{ref}(t)$ et $\boldsymbol{r}_{ref}^{(c)}(t)$, tout en rejetant les termes d'erreurs $\boldsymbol{\tau}_{\Delta}$ et $\boldsymbol{f}_{\Delta}$.

Sous certaines hypothèses de bornitude relatives à $\boldsymbol{\tau}_{\Delta}$ et $\boldsymbol{f}_{\Delta}$, nous montrons dans nos travaux de thèse, que la structure suivante de l'algorithme GSTA permet de résoudre le problème:

$$\boldsymbol{\tau}_{sm}^{(c)} = \boldsymbol{J}\left(-\boldsymbol{F}_{\tau} - \boldsymbol{K}_{\tau}\left[\frac{1}{2}\left[(\mathbf{q}_{\epsilon})_s\boldsymbol{\omega}_c^{(c)} + (\mathbf{q}_{\epsilon})_v \times \boldsymbol{\omega}_c^{(c)}\right]\right] - \boldsymbol{\alpha}_{1\tau}\boldsymbol{\phi}_{1\tau}(\boldsymbol{s}_{\tau}) - \boldsymbol{\alpha}_{2\tau}\int_0^t \boldsymbol{\phi}_{2\tau}(\boldsymbol{s}_{\tau}(\chi))d\chi\right) \tag{29}$$

$$\boldsymbol{f}_{sm}^{(c)} = m\left(-\boldsymbol{F}_f - \boldsymbol{K}_f\dot{\boldsymbol{r}}_{\epsilon}^{(c)} - \boldsymbol{\alpha}_{1f}\boldsymbol{\phi}_{1f}(\boldsymbol{s}_f) - \boldsymbol{\alpha}_{2f}\int_0^t \boldsymbol{\phi}_{2f}(\boldsymbol{s}_f(\chi))d\chi\right) \tag{30}$$

avec $\boldsymbol{F}_{\tau} = -\boldsymbol{J}^{-1}\left(\boldsymbol{\omega}_c^{(c)} \times \boldsymbol{J}\boldsymbol{\omega}_c^{(c)}\right)$, $\boldsymbol{F}_f = -\boldsymbol{\omega}_c^{(c)} \times \dot{\boldsymbol{r}}_e^{(c)} - \boldsymbol{\omega}_c^{(c)} \times \boldsymbol{\omega}_c^{(c)} \times \boldsymbol{r}_e^{(c)}$.

Dans ces équations, $\mathbf{q}_{\epsilon} = \mathbf{q}_{ref}^{*} \circ \mathbf{q}_c$ et $\boldsymbol{r}_{\epsilon}^{(c)} = \boldsymbol{r}_{ref}^{(c)} - \boldsymbol{r}_e^{(c)}$ représentent les erreurs d'asservissement en attitude et en position relative. $(\mathbf{q}_{\epsilon})_s$ et $(\mathbf{q}_{\epsilon})_v$ sont les parties scalaires et vectorielles du quaternion $\mathbf{q}_{\epsilon}$, tels que

$$(\dot{\mathbf{q}}_{\epsilon})_s = -\frac{1}{2}(\mathbf{q}_{\epsilon})_v^{\intercal}\boldsymbol{\omega}_c^{(c)} \tag{31}$$

$$(\dot{\mathbf{q}}_{\epsilon})_v = \frac{1}{2}\left[(\mathbf{q}_{\epsilon})_s\boldsymbol{\omega}_c^{(c)} + (\mathbf{q}_{\epsilon})_v \times \boldsymbol{\omega}_c^{(c)}\right] \tag{32}$$

$\boldsymbol{\phi}_{1j}(\boldsymbol{s}_j) = \lfloor \boldsymbol{s}_j \rceil^{1/2} + \boldsymbol{\beta}_j\boldsymbol{s}_j$ and $\boldsymbol{\phi}_{2j}(\boldsymbol{s}_j) = \frac{1}{2}\lfloor \boldsymbol{s}_j \rceil^0 + \frac{3}{2}\boldsymbol{\beta}_j\lfloor \boldsymbol{s}_j \rceil^{1/2} + \boldsymbol{\beta}_j^2 s$ sont des matrices diagonales, où $\lfloor \boldsymbol{s}_j \rceil^q = |\boldsymbol{s}_j|^q \operatorname{sign}(\boldsymbol{s}_j)$, pour $j \in \{\tau, f\}$. $\boldsymbol{K}_j, \boldsymbol{\alpha}_{ij}, \boldsymbol{\beta}_j \in \mathbb{R}^3, i = 1, 2,\ j \in \{\tau, f\}$ sont des gains matriciels à déterminer, dont le choix permet de fixer les performances de la loi de commande. $\boldsymbol{s}_{\tau}$ and $\boldsymbol{s}_f$ sont les surfaces de glissement définies telles que:

$$\boldsymbol{s}_{\tau} = \boldsymbol{\omega}_c^{(c)} + \boldsymbol{K}_{\tau}(\mathbf{q}_{\epsilon})_v \tag{33}$$

$$\boldsymbol{s}_f = \dot{\boldsymbol{r}}_{\epsilon}^{(c)} + \boldsymbol{K}_f\boldsymbol{r}_{\epsilon}^{(c)} \tag{34}$$

On montre alors à l'aide d'un théorème, que cette commande est stable et rejette les perturbations considérées, assurant *de facto* le suivi des trajectoires des références $\boldsymbol{q}_{ref}(t)$ et $\boldsymbol{r}_{ref}^{(c)}(t)$. Le théorème établit également les conditions que doivent satisfaire les paramètres $\boldsymbol{K}_j, \boldsymbol{\alpha}_{ij}, \boldsymbol{\beta}_j \in \mathbb{R}^3, i = 1, 2,\ j \in \{\tau, f\}$.

3) La solution "anti-windup" proposée repose sur l'utilisation de coefficients de forme $e^{\lambda c_i}, \lambda < 0$, qui sont introduits dans la loi de commande comme suit:

$$\begin{aligned}\boldsymbol{\tau}_{sm}^{(c)} =& \boldsymbol{J}\left(-\boldsymbol{F}_\tau - \boldsymbol{K}_\tau\left[\frac{1}{2}\left[(\mathbf{q}_\epsilon)_s\boldsymbol{\omega}_c^{(c)} + (\mathbf{q}_\epsilon)_v \times \boldsymbol{\omega}_c^{(c)}\right]\right] - \boldsymbol{\alpha}_{1\tau}\boldsymbol{\phi}_{1\tau}(\boldsymbol{s}_\tau)\right. \\ & \left. -\boldsymbol{\alpha}_{2\tau}\mathrm{diag}(e^{\lambda\Delta_{\tau i}})\int_0^t \boldsymbol{\phi}_{2\tau}(\boldsymbol{s}_\tau(\chi))d\chi\right) \end{aligned} \tag{35}$$

$$\boldsymbol{f}_{sm}^{(c)} = m\left(-\boldsymbol{F}_f - \boldsymbol{K}_f\dot{\boldsymbol{r}}_\epsilon^{(c)} - \boldsymbol{\alpha}_{1f}\boldsymbol{\phi}_{1f}(\boldsymbol{s}_f)\ -\boldsymbol{\alpha}_{2f}\mathrm{diag}(e^{\lambda\Delta_{fi}})\int_0^t \boldsymbol{\phi}_{2f}(\boldsymbol{s}_f(\chi))d\chi\right) \quad i = \overline{1,3} \tag{36}$$

Sachant qu'en fonctionnement non saturé, les couples et forces engendrés par le système de propulsion évoluent dans des polytopes $\boldsymbol{\Pi}_\tau$ et $\boldsymbol{\Pi}_f$ respectivement, l'idée consiste à déterminer si les signaux de commande $\boldsymbol{\tau}_{FTC}^{(c)}$ et/ou $\boldsymbol{f}_{FTC}^{(c)}$ définissent des vecteurs appartenant ou non, aux polytopes associés. Si le vecteur couple et/ou le vecteur force n'appartient pas à son polytope associé, on cherche alors le vecteur couple $\boldsymbol{\tau}_0^{(c)}$ et/ou force $\boldsymbol{f}_0^{(c)}$ appartenant au polytope, le plus proche au sens des moindres carrés. On montre alors que ce problème se pose comme le problème d'optimisation suivant:

$$\begin{aligned} &\min_{\boldsymbol{\tau}_0^{(c)}} \left\|\boldsymbol{\tau}_{FTC}^{(c)} - \boldsymbol{\tau}_0^{(c)}\right\|_2 \quad \text{s.t.} \quad \boldsymbol{\tau}_0^{(c)} \in \boldsymbol{\Pi}_\tau \\ &\min_{\boldsymbol{f}_0^{(c)}} \left\|\boldsymbol{f}_{FTC}^{(c)} - \boldsymbol{f}_0^{(c)}\right\|_2 \quad \text{s.t.} \quad \boldsymbol{f}_0^{(c)} \in \boldsymbol{\Pi}_f \end{aligned} \tag{37}$$

La figure 8 illustre l'approche proposée.

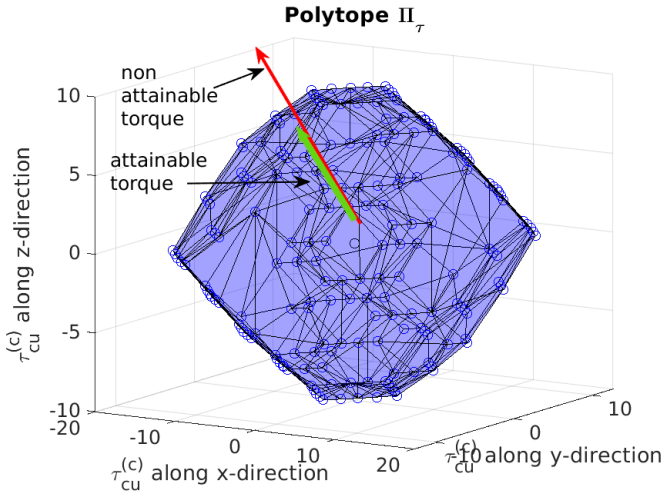

Figure 8: Principe du système "anti-windup"

Les termes $\Delta_{\tau i}, \Delta_{fi}$, $i = \overline{1,3}$ sont alors déterminés tels que

$$\begin{aligned} &\boldsymbol{\Delta}_\tau = \boldsymbol{\tau}_{FTC}^{(c)} - \boldsymbol{\tau}_0^{(c)} \quad \boldsymbol{\Delta}_f = \boldsymbol{f}_{FTC}^{(c)} - \boldsymbol{f}_0^{(c)} \\ &\boldsymbol{\Delta}_\tau = \mathrm{vec}(\Delta_{\tau i}),\ \boldsymbol{\Delta}_f = \mathrm{vec}(\Delta_{fi}),\ \Delta_{\tau i} \geq 0,,\ \Delta_{fi} \geq 0 \quad i = \overline{1,3} \end{aligned} \tag{38}$$

Ainsi, avec $\lambda < 0$, lorsque $\Delta_{\tau i}$ et/ou Δ_{fi} sont grands , $e^{\lambda\Delta_{\tau i}}$ et/ou $e^{\lambda\Delta_{fi}}$ sont proches de zéro, ce qui annule le terme intégral dans la commande GSTA, responsable du problème d'instabilité lié à la saturation des commandes des tuyères. *A contrario*, si la commande ne sature pas, $\boldsymbol{\tau}_0^{(c)} = \boldsymbol{\tau}_{FTC}^{(c)}$ et $\boldsymbol{f}_0^{(c)} = \boldsymbol{f}_{FTC}^{(c)}$. Alors les termes $e^{\lambda\Delta_{\tau i}}$ et $e^{\lambda\Delta_{fi}}$, $i = \overline{1,3}$ sont égaux à 1, et les termes intégrales de la commande GSTA opèrent normalement, malgré la présence de défauts tuyères.

R.4.3 Résultats de simulation

La loi de commande tolérante aux fautes développée, est implantée dans le simulateur FES. Nous présentons figure 9 les résultats obtenus, dans le cas d'un défaut "tuyère ouverte" pour la tuyère n. 1. Le défaut est injecté dans le système de propulsion à l'instant $t = 40s$ et est maintenu durant toute la durée de la simulation. Les figures présentent, de haut gauche à bas droite, l'attitude du chasseur et l'erreur d'asservissement associée, la position relative dans le repère LVLH et l'erreur d'asservissement associée, la force duale $\bar{\boldsymbol{f}}_{FTC}^{(c)}(t)$, la commande des tuyères $\boldsymbol{u}_c^{(c)}(t)$, l'estimée $\hat{\bar{\boldsymbol{f}}}^{(c)}$ et la commande délivrée par le contrôleur GSTA.

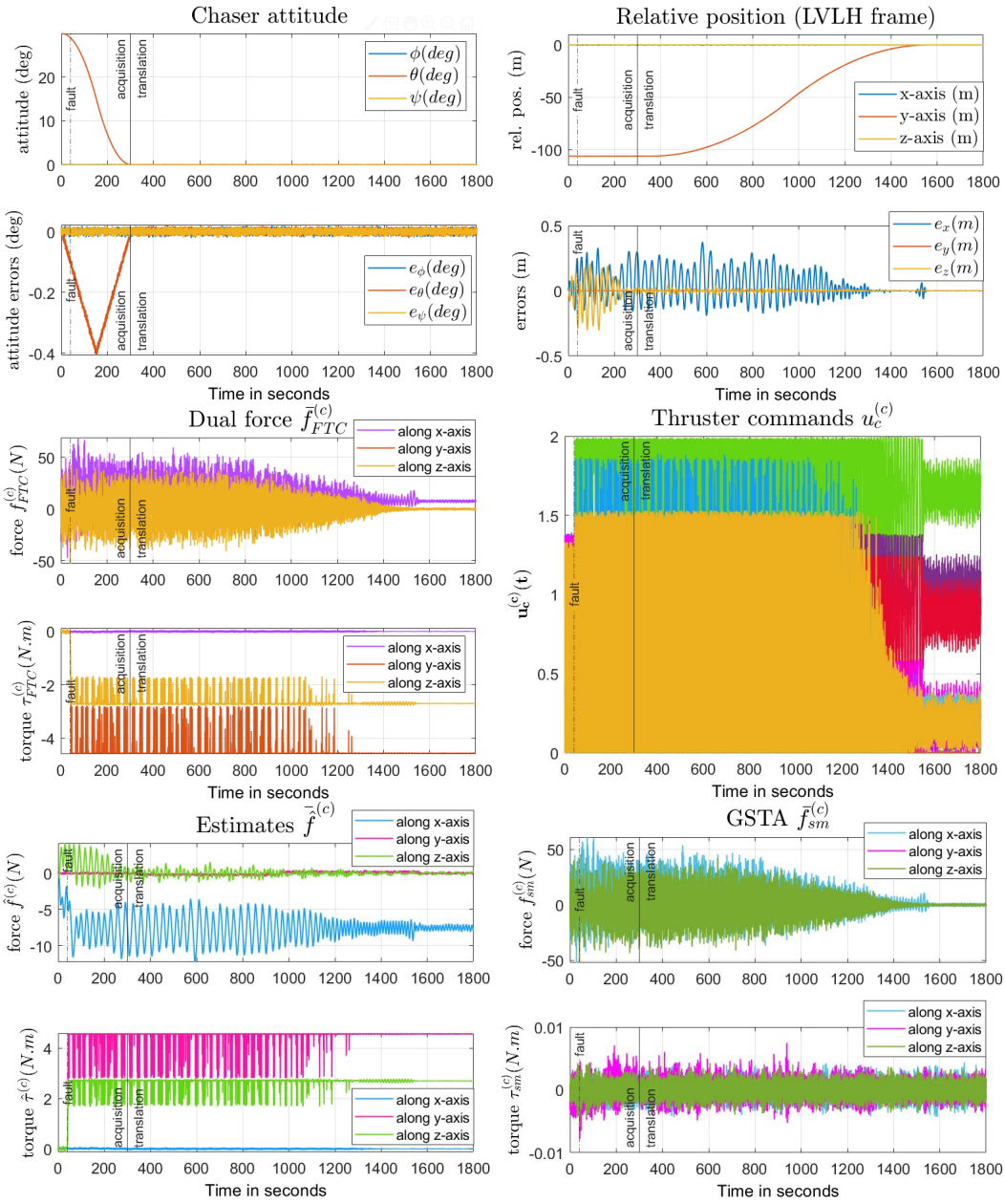

Figure 9: THR 1. Tuyère ouverte: a) Attitude du chasseur et erreur - b) Position relative dans le repère LVLH et erreur - c) force duales $\bar{\boldsymbol{f}}_{FTC}^{(c)}$ - d) commandes des tuyères $\boldsymbol{u}_c^{(c)}$ - e) force duale estimatée $\hat{\bar{\boldsymbol{f}}}^{(c)}$ - f) commande du contrôleur GSTA $\bar{\boldsymbol{f}}_{sm}^{(c)}$.

Une campagne de simulation est finalement réalisée à l'aide du FES. Les deux types de défaut (tuyère ouverte et tuyère fermée) sont injectés à chacune des 24 tuyères. Un total de 49 simulations (1 en fonctionnement normal et 48 en fonctionnement défaillant), est donc joué. Afin de

mesurer les performances obtenus, des critères orientés mission tels que l'alignement du système de capture versus la cible au point de capture, la position du chasseur dans le corridor de rendez-vous, les vitesses latérales et longitudinales du chasseur au point de contact, l'attitude et la vitesse de rotation du chasseur au point de contact, sont calculés puis reportés sur la figure **??**. Les résultats obtenus illustrent le potentiel de la solution développée, puisque les résultats montrent que dans chaque cas, la mission spatiale est un succès, malgré la présence d'un actionneur hors service.

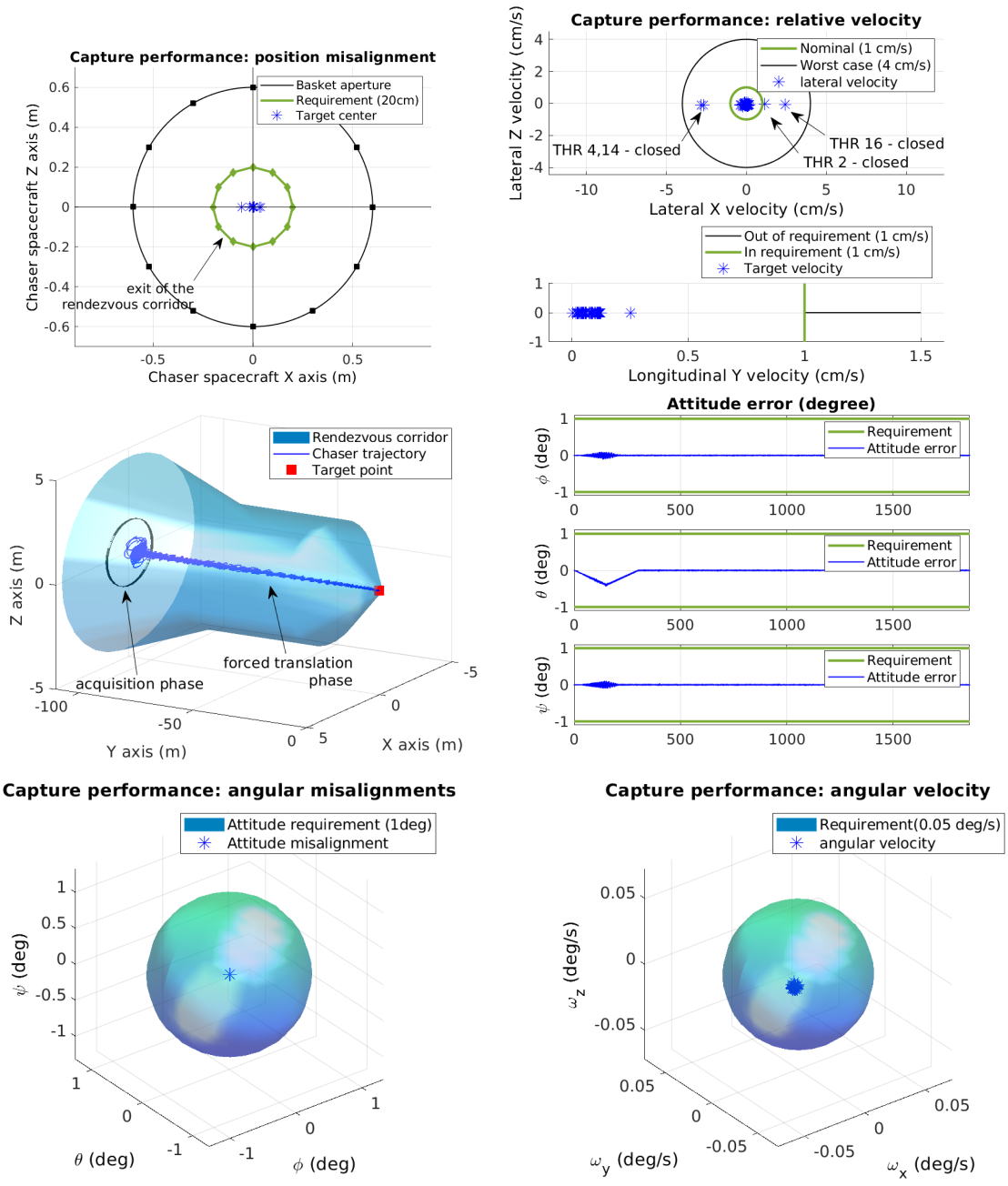

Figure 10: Campagne de simulation FES: a) alignement du système de capture versus la cible b) positions relatives au point de capture - c) Position relative versus le corridor de rendez-vous - d) attitude du chasseur - e) attitude au point d'impact f) vitesse angulaire au point d'impact.

1 Introduction

Nowadays, control systems can be found everywhere around us. With the advance of technology, their reliability and complexity has increased. As a consequence, many critical systems are supervised by control systems. A critical system is required to be safe and reliable, given that human lives depend on it. This is achieved by designing a controller which considers the possible occurrence of faults. A control that is capable of maintaining an acceptable system's performance is called Fault Tolerant Control (FTC). Different control design approaches have been applied for FTC purposes, an extensive study can be found in [JY12a, YJ15]. This work explores the capabilities of a specific control design approach called Sliding Mode Control (SMC). SMC has gained attention due to its robustness properties against matched disturbances, i.e disturbances that act in the control input channel. Given that some actuator faults can be modelled as matched disturbances, SMC has gained attention in the FTC community, see for example [FdLCH+15, AET11, AE08, RKFZ15, EAH18].

1.1 Context and motivation

With the current advance in space exploration, different missions involve the use of multiple spacecraft, also known as Satellite Formation Flying (SFF). This approach has gained popularity given that it is cost and time effective. Some space missions that use or consider SFF are New Millennium Program [FNG96, BBF+97], specifically for Earth Observing-1 mission developed by the National Aeronautics and Space Administration (NASA) and Cluster [Rou98], Orion [HTW+98] and Laser Interferometer Space Antenna (LISA) [Fol01] missions, developed by the European Space Agency (ESA). Besides maintaining the formation between vehicles, SFF may implicate rendezvous between two spacecraft. Rendezvous is defined in [Feh03] as a series of orbital maneuvers and controlled trajectories, which successively bring the active vehicle (chaser) into the vicinity of, and eventually into contact with the passive vehicle (target). In this work, it is considered that the rendezvous mission consists of two phases: the acquisition phase, where the chaser aligns with the target and the rendezvous phase, where the chaser translates to approach towards the target. The importance of the rendezvous mission relies on the different applications it may have, for instance for debris removal or on-orbit servicing.

Rendezvous between spacecraft was first done manually between the Gemini spacecraft and the unmanned Agena target vehicle, in 1966. The first automatic rendezvous then took place in 1967 between two Soviet spacecraft, Cosmos 186 and Cosmos 188. Several others followed after, mainly within american (US) and soviet (Russia) space programs like Apollo, Soyuz, Skylab, Salyute and Mir [Ank10]. Recently, ESA developed the unmanned Automated Transfer Vehicle (ATV) to re-supply the International Space Station (ISS); Hyperspectral PRecursor of the Application Mission (PRISMA) serves for on-orbit guidance testing of SFF and spacecraft rendezvous [ESA]; and docking between Northrop Grumman's satellite and an Intelsat communications [Nor].

Challenges in rendezvous mission

The success of the rendezvous mission depends on the control algorithm employed. Its robustness, defines the degree of autonomy that the spacecraft can have. Same level of importance relies on the development of accurate dynamic models, given that the control algorithm is designed based on it. A dynamic and kinematic model that accurately includes the characteristics of the system while having a reasonable level of complexity, is desired.

In this work, the rendezvous mission studied is performed in a circular orbit. In addition, in accordance with the definition given in [Feh03], the chaser refers to the active vehicle (equipped with sensors, actuators and a Guidance and Navigation Control (GNC) unit) while the target represents the passive vehicle (no sensor or actuator). Specifically, the sensors equipped in the chaser are a Light Detection and Ranging (LIDAR) which provides relative positions and velocities, an Inertial Measurement Unit (IMU) and a Star Tracker. With regards to actuators, it is first considered that the chaser is equipped with 12 thrusters of 4 N for both attitude and position control. It is assumed a perfect navigation unit, i.e. all measurements are assumed to be noise free. Then, a new thruster structure is proposed for FTC purposes which consists of 24 thrusters of 2 N. For this scenario, noise is taken into account in the navigation unit. Finally, the target is always considered to be a sphere.

Relative Models

Along this manuscript, relative motion is referred to the description of the chaser's state with respect to the target. Different approaches can be found in literature for the description of the 3 degrees of freedom (DoF) relative translational model. The work developed in [CW60], presented the first linear relative model for spacecraft rendezvous in circular orbit. This result was later extended to elliptical orbits and nonlinear models, see for example [Law63, CH87, YA02].

With regard to the attitude model, different researchers like Euler, Jacobi, Hamilton, Cayley, Klein, Rodrigues and Gibbs, devoted their work towards establishing the 3DoF rigid body orientation description [JS01]. In addition, there exist many parameters that can be employed for describing the orientation of a body, for instance Euler angles, Rodrigues Parameters, Rotation Matrices, quaternions, Direction Cosine Matrix (DCM), among others.

The works mentioned above, described the general motion of a rigid body in space in terms of a translation and a rotation, around the Center of Mass (CoM) of the body. In other words, their description of relative motion of a body is composed of the relative translational and rotational dynamics of arbitrary points on the body. When one of these points does not coincide with the CoM of the body, a kinematic coupling between the rotational and translational dynamics of these points is obtained. This coupling effect is independent of external perturbation, unlike the coupling effect induced by gravity torques [SG09]. For the case of two spacecraft in proximity, this effect is accentuated as the distance between them is reduced. Thus, in order to develop a controller with a higher degree of accuracy, both motions have to be model at the same time, i.e. a coupled model (6DoF) is needed.

On-orbit thruster failures

A fault occurrence during close proximity maneuvers like rendezvous, may threaten the success of the mission. Depending on the location and type of the fault, system's performance can be affected in different degrees of severity. Based on the study presented in [SBD18], thruster faults account for the largest percentage of failures in orbit. A summary of the causes of launch vehicle failures from 1980-2016 is shown in Figure 1.1.

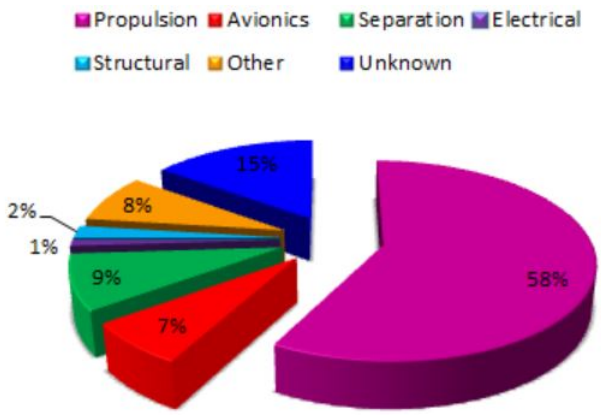

Figure 1.1: Causes of launch vehicle failures on systems 1980-2016 (adapted from [SBD18])

In addition, according to [Jia05], FTC is mainly concerned about dealing against actuator faults, given that they affect the system's behaviour directly. In this work, the occurrence of a thruster fault is considered. It is assumed that only one thruster fails at a time. Furthermore, the faults considered are a thruster open at its maximum value and a completely closed thruster. Several effects are possible in the case when the controller is incapable of compensating it. These faults can cause instability in the spacecraft, a collision against the target, lost of sight of the target, among others. Such faulty scenario can not be diagnosed by ground control given that other problems with regards to communication, arise. Thus, this motivates the study of control strategies that can cope against faults, specifically against thruster faults.

1.2 Approach and objectives

As mentioned before, the motivation for studying FTC methods is to increase the reliability and robustness of a critical system. The redundancy of components is the key element for FTC. In literature, different approaches for FTC purposes can be found, which can be classified in active or passive approaches. Passive approaches exploit the robustness properties of a specific controller, and thus, the type of faults that can be compensated is limited. On the other hand, active approaches can compensate a wider class of faults given that they reconfigure the controller based on the fault detected. This means, that there exists an interaction between the controller and the Fault Detection and Isolation (FDI) unit. As a consequence, is harder to guarantee stability of the closed-loop system given that any delay effect or imperfection in the FDI unit, may lead to instability. An example of how to address this issue can be found in [CEH15, ECH13, ZWT+16].

Among the different control design approaches, sliding mode techniques are attractive for FTC purposes due to its robustness properties against matched disturbances (i.e. disturbances that act on the input channels) and finite-time response. In literature, both active and passive approaches, with SMC, can be found. With regard to the active approaches, the existence of a FDI unit is frequently assumed, see for example [HEA11, XCW15, CEAS20, CAE19a, CEA19]. Another common approach employed in FTC, which allows to compensate a wider range of faults without the need of reconfiguration of the controller, is Control Allocation (CA) scheme. CA distributes the control signal into the available actuators. This means that it depends on an FDI unit to know which actuators are available. In the case study considered in this thesis, the actuators are a set of thrusters. On the other hand, passive approaches with SMC, mostly consider the case when an actuator can only actuate a percentage of the desired value, this is known as loss of effectiveness, see for example [SWZP15, MNB15, LJPZ19, LP17, LP16]. Furthermore, Sliding Mode Observers (SMO) are employed for fault estimation or detection, given that according to [ES98], SMO have better performance under several faulty scenarios in comparison with other methods in noise-free

environment.

In this work, the objective is to explore the capabilities of SMC for FTC purposes without the need of a FDI unit. In addition, unlike the other passive approaches with SMC, the faults considered along this thesis, are a thruster stuck open at its maximum value or a thruster stuck completely closed. It is worth noting that the level of severity of a stuck open or stuck closed fault is higher than a loss of effectiveness. In summary, the question to be answered with this research can be written as follows: *"is it possible to compensate for a stuck open or a stuck close thruster fault, without the knowledge of its occurrence?"*.

Furthermore, the importance of the development of an accurate model is implicit, given that the proposed solution is model-based. As mentioned above, a 6DoF model increases the accuracy of the controller. This thesis begins with the description of two 3DoF models, which are based on classical approaches for circular orbit, i.e. Hill-Clohessy-Wiltshire (HCW) for relative translational motion and Newton-Euler for rotational motion. In addition, a first approach towards the development of a robust controller is done based on these models. Then, in Chapter 4, the 6DoF model is obtained with dual quaternions. Dual quaternions are a combination of dual numbers and quaternions, which describe both translational and rotational dynamics in a compact form. A more detailed description of their properties and particular algebra can be found in Chapter 4. In addition, given that they have similar properties to quaternions, the control techniques employed for quaternions, can be extended to dual quaternions. It is at this stage that the capabilities of SMC for FTC purposes are explored, i.e the FTC is based on dual quaternion formalism. Although dual quaternions are applied in different fields (robotics, image processing, navigation, computer graphics, control), with regards to FTC, few works can be found, specifically FTC with SMC. Take for instance [DHM16, DLJS17, GdR17] where active FTC approaches with SMC are proposed. These works are proposed without an explicit design of FDI unit, leading to a closed-loop stability not guaranteed. To overcome this constraint, in this manuscript, a passive technique that consists of a Generalized Super-Twisting Algorithm (GSTA) with an anti-windup strategy is proposed for FTC purposes.

1.3 Overview of Chapter contents

This thesis comprises 5 chapters. The first chapter is the current introduction, and the content of the following chapters is described below:

- **Chapter 2** aims to be an introduction to SMC techniques. This chapter begins with the description of the operating principle and the definition of the basic concepts. Then, the control objective is described, followed by the design procedure. Likewise, the evolution of this control technique into different families is studied. Their respective design procedure, limitations and robustness properties are highlighted. Finally, an introduction to FTC concepts, classification and design approaches are revised.

- **Chapter 3** presents the development of a SMC applied to the rendezvous mission in circular orbit. This chapter begins with the description of the vehicles involved (i.e chaser and target) and the phases that comprise the rendezvous mission. Then, the development of the two 3DoF model for both dynamics, translational and rotational, is explained along with the frames and disturbances (e.g. second zonal harmonic, J_2, atmospheric drag, magnetic disturbance) considered. Two SMC in a backstepping setup, are designed in order to guarantee the tracking of the target despite the disturbances that affect both vehicles. The control effort computed by the designed controller is then distributed by a CA unit. It is worth noting that, in this work, the chaser is not studied as a point mass, given that it is considered that the chaser has a solar array and two half-filled fuel tanks. The stability of the designed controllers is analyzed with Lyapunov theory. Finally, the proposed solution is validated in a high fidelity

benchmark, that correctly simulates the rendezvous mission in a circular orbit.

- **Chapter 4** explores the capabilities of SMC for fault tolerance purposes. In this work, a stuck open and a stuck close thruster fault are considered. It is assumed that only one fault occurs at a time and that there is no fault detection and identification (FDI) unit. Furthermore, the relative dynamic model in Dual Quaternion formalism is introduced. Unlike the model developed in Chapter 3, this model takes into account the coupling between translational and rotational dynamics. Therefore, the controller designed also takes into account the coupling effects. Similar to Chapter 3, the stability of the designed controller is analyzed with Lyapunov theory. Finally, the proposed solution is validated in the high-fidelity benchmark used in the previous chapter.
- **Chapter 5** summarizes the results obtained from this research work, in the form of conclusions. Finally, recommendations for extending this research work are given.

2 Sliding Mode Control

2.1 Introduction

This chapter aims to be an introduction to sliding mode techniques. It begins with the description of their operating principle, and the definition of the main concepts. The design procedure and the requirements of the controller are described. The evolution of the Sliding Mode techniques into different families of controllers is reviewed. The design for each controller with their characteristics, is also mentioned. Finally, a short discussion about the potential of sliding mode controllers for fault-tolerant control purposes, is presented.

2.2 Sliding Mode Control

Variable Structure Control (VSC) was first proposed by Emelyanov [Eme63, Eme06] in the Soviet Union. It was only known outside Russia by means of Utkin [Utk77]. Its operating principle is based on the "switching" of the control signal depending on certain conditions, with the goal of keeping a desirable performance. According to [Eme06, Utk78], VSC properties are exemplified with a second order system as follows:

$$\begin{aligned} \dot{x} &= y \\ \dot{y} &= ax + by + u \end{aligned} \tag{2.1}$$

where x and y are the states; and a, b are system parameters. The main concept is illustrated in Fig. 2.1, where u refers to the control signal; r refers to the reference signal; x, y are the states (see (2.1)); k_1, k_2 are gains; e is the error and s is the switching condition function. VSC was originally applied to a second-order linear system and it was the basis for what it is now known as SMC. Nowadays, VSC has been extended to different types of systems like discrete-time and Multi-input/Multi-output (MIMO), to mention some. The main property of VSC is that it provides robustness, in the way of insensitivity against parametric uncertainties and external disturbances. Due to this property, VSC is applied to numerous fields like aeronautics, aerospace, robotics, electronics and chemistry, to name a few.

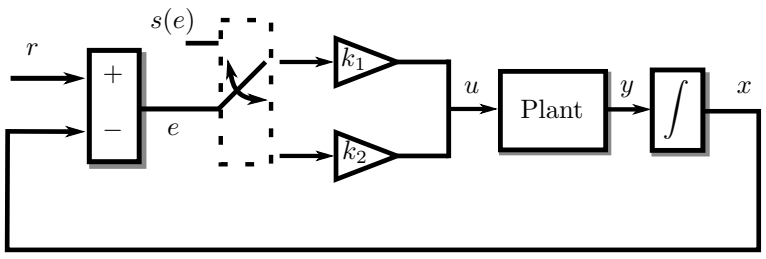

Figure 2.1: Structure of a variable structure control (VSC)

Consider that the control input is described by

$$u = -\gamma x \tag{2.2}$$

where γ is a variable that can take values between k_1 and k_2. Suppose that when γ is k_1, the system (2.1) has complex eigenvalues with positive real part. In addition, when γ is k_2, the system has real positive and negative eigenvalues. The behaviour of the system for each case, is analyzed with their phase plane in Fig. 2.2. The procedure to obtain this figure is explained in the Appendix A.1. Note that the origin of the phase plane represents the equilibrium point. For Fig. 2.2(a), the behaviour of system (2.1), with k_1, is shown as an unstable focus at the origin. The saddle point observed in Fig. 2.2(b), belongs to the systems response when γ is k_2.

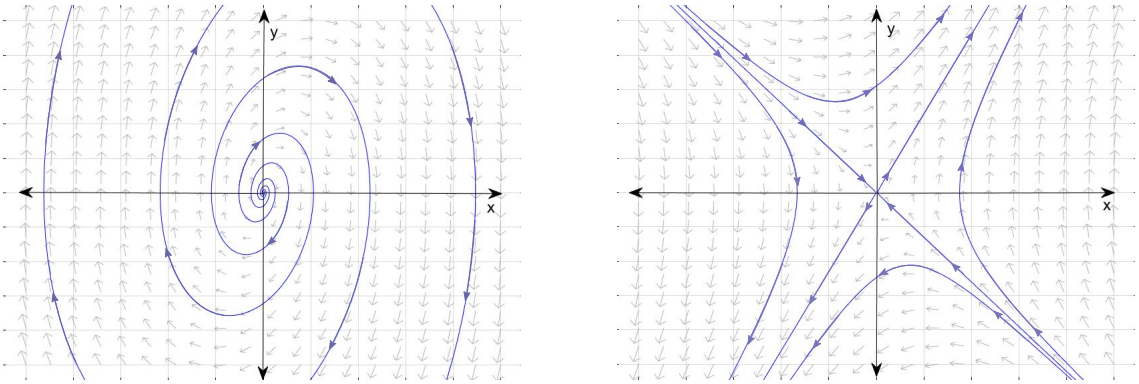

(a) Unstable focus at the origin (b) Saddle point

Figure 2.2: Phase plane of system (2.1) with two different control inputs

Although in Fig. 2.2 it is shown that both cases result in unstable systems, it can be seen that there are some regions of stability. See for example case (b) in Fig. 2.2, where the saddle point approaches the origin. In order to have the desired regions from both cases, a switching function is defined as:

$$s = s(x, y) = cx + y, \quad c > 0 \tag{2.3}$$

When the switching function is equal to zero, the sliding surface obeys to $s = cx + y = 0$. Then, γ changes its value according to the following expression:

$$\gamma = \begin{cases} k_1, & \text{when} \quad s(x, y) > 0 \\ k_2, & \text{when} \quad s(x, y) < 0 \end{cases} \tag{2.4}$$

As shown in (2.4), the structure of the control signal (2.2) is changed depending on the distance of the state trajectories to the equilibrium point. From its initial conditions, the state trajectories move firstly towards the sliding surface $s = 0$. This is known as the reaching phase. Then, they slide to the equilibrium point through the sliding surface. This is known as the sliding mode phase. Whenever the states move away from the sliding surface, the controller changes structure in order to make them come back to it. In other words, high switching between control structures is involved, also called chattering. When the state trajectories are sliding, the value of s is close to zero. Furthermore, when in the equilibrium point, $s = 0$. The concepts previously explained are illustrated in Fig. 2.3, where the resulting phase plane of the system under VSC is shown.

In literature, a common variable structure for the control signal u is defined as:

$$u = \begin{cases} -1, & \text{when} \quad s(x, y) > 0 \\ 1, & \text{when} \quad s(x, y) < 0 \end{cases} \tag{2.5}$$

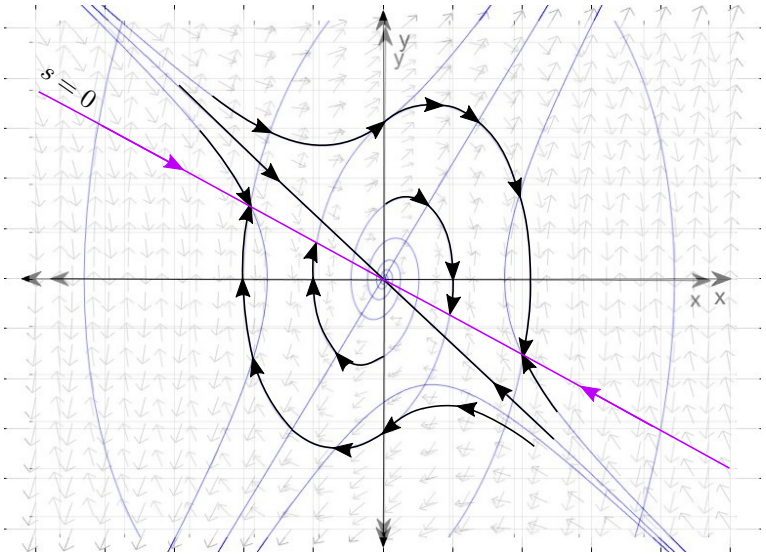

Figure 2.3: Resulting phase plane diagram of the system under VSC

where s is defined as in (2.3). It follows that (2.5) is rewritten as:

$$u = -\text{sign}(s(x, y)) \tag{2.6}$$

where sign$(\cdot)$ refers to the sign function, which has as property $s \cdot \text{sign}(s) = |s|$.

Variable structure control is usually known as sliding mode control given the importance of the sliding mode phase.

Remark 1. *In this chapter, the description of the properties and the design procedure of SMC is exemplified based on a Linear Time-Invariant (LTI) system. However, the reader must take into account that SMC theory is extended to nonlinear systems, see for example [FYH13, Dav13, DFPU09, YE07].*

2.3 Problem Statement

In this section, the design procedure is exemplified with the following LTI system defined as

$$\dot{x}(t) = Ax(t) + B\left[u(t) + f(t, x, u)\right] \tag{2.7}$$

where $A \in \mathbb{R}^{n\times n}$, $B \in \mathbb{R}^{n\times m}$. It is considered that rank$(B) = m$, $1 \leq m < n$ and the pair (A, B) is controllable. In (2.7), $f(t, x, u)$ may represent an unknown bounded disturbance or bounded model uncertainty acting on the input channel, i.e. matched disturbance/uncertainty. On the contrary, a disturbance/uncertainty that does not act on the input channel is called unmatched. The main purpose is to design a control law that ensures the convergence of the states despite model uncertainties or perturbations. The first step for the design of the robust control law is to define the sliding surface $\mathcal{S}$ as

$$\mathcal{S} = \{x : s(x) = 0\} \tag{2.8}$$

where the switching function $s(x) = Sx$ is a linear function, with $S \in \mathbb{R}^{m\times n}$ full rank.

To illustrate the concept of equivalent control, it is first considered that $f(t, x, u) = 0$ in (2.7). This leads to the nominal system description as:

$$\dot{x}(t) = Ax(t) + Bu(t) \tag{2.9}$$

An ideal sliding mode occurs when the state $x(t)$ converges to the sliding surface in finite-time t_r, i.e. the sliding phase begins at time $t \geq t_r$. It is mathematically expressed as:

$$s(t) = \dot{s}(t) = 0 \quad \text{for all} \quad t \geq t_r \tag{2.10}$$

By substituting for (2.9), the equation on sliding motion is described as:

$$\dot{s}(t) = S(Ax(t) + Bu(t)) = 0 \tag{2.11}$$

The necessary average value of the control signal to enforce and ideal sliding motion, i.e. $s(t) = \dot{s}(t) = 0$, is called equivalent control. It is obtained from (2.11) as:

$$u_{eq}(t) = -(SB)^{-1}(SAx(t)) \tag{2.12}$$

where (SB) is nonsingular. This condition guarantees the existence of a unique equivalent control [Utk13]. From (2.12), the equivalent control can be rewritten as a state feedback controller as:

$$u_{eq}(t) = -(SB)^{-1}(SAx(t)) = Kx(t) \tag{2.13}$$

It is worth noting that the equivalent control is not implementable, i.e. (2.13) would not induce a sliding motion. Instead, the concept of equivalent control should be thought as a tool to obtain a reduced order expression from which closed-loop stability can be analyzed. For (2.9), the closed-loop response is obtained from substituting (2.12) in (2.9) as:

$$\dot{x}(t) = Ax(t) + B\left(-(SB)^{-1}(SAx(t))\right) = \underbrace{\left(I - B(SB)^{-1}S\right)}_{P} Ax(t) \tag{2.14}$$

where I is the identity matrix and P is a projection operator that satisfies the following conditions [ES98]:

$$SP = 0 \quad PB = 0 \tag{2.15}$$

In the following, the definition of equivalent control for the perturbed case is shown. As mentioned before, when the states reach the sliding surface $s(t) = \dot{s}(t) = 0$. In order to find the equation on the sliding motion, the derivative of $s(t) = Sx(t)$ is analyzed by using (2.7) as follows:

$$\dot{s}(t) = S\dot{x}(t) = S\left[Ax(t) + B\left(u(t) + f(t, x, u)\right)\right] \tag{2.16}$$

The expression of the equivalent control, for the perturbed case, is obtained by equating (2.16) to zero, then the following expression is obtained

$$u_{eq}(t) = -(SB)^{-1}\left[SAx(t) + SBf(t, x, u)\right] \tag{2.17}$$

where (SB) is nonsingular. The idea of considering the equivalent control just as a tool is reinforced by the results obtained for the perturbed case, given that the equivalent control equation (2.17) is dependent on the disturbance. The expression obtained when substituting (2.17) in (2.7), gives the closed-loop response defined as:

$$\begin{aligned} \dot{x}(t) &= Ax(t) + B\left[-(SB)^{-1}\left(SAx(t) + SBf(t, x, u)\right)\right] + Bf(t, x, u) \\ &= Ax(t) - B(SB)^{-1}Ax(t) - B(SB)^{-1}SBf(t, x, u) + Bf(t, x, u) \\ &= \underbrace{\left(I_n - B(SB)^{-1}\right)}_{\text{P}} Ax(t) + \underbrace{\left(I_n - B(SB)^{-1}\right)}_{\text{P}} Bf(t, x, u) \end{aligned} \tag{2.18}$$

Based on the conditions expressed in (2.15), (2.18) can be rewritten as:

$$\dot{x}(t) = PAx(t) \tag{2.19}$$

From (2.19), it is shown that during sliding motion, the reduced order system motion is insensitive to matched disturbances. In addition, it can be seen that the design of the switching function $s(t)$ is independent of the disturbance, i.e. $s(t) = Sx(t)$ is applicable for both systems, (2.7) and (2.9). Furthermore, the reduced dynamics equations that describe the system in sliding motion, (2.14) and (2.19), show that there exists a dependency on the selection of the sliding surface. This effect is more visible when transforming the system into its canonical form, as explained in the following.

Given that by assumption B has full rank, there exists a transformation matrix $T \in \mathbb{R}^{n\times n}$ such that:

$$TB = \begin{bmatrix} 0 \\ B_2 \end{bmatrix} \tag{2.20}$$

where $B_2 \in \mathbb{R}^{m\times m}$ is nonsingular. Matrix T can be computed by using Gaussian elimination or QR decomposition, for example. The transformed state coordinates are obtained by employing the transformation matrix as $\tilde{x}(t) = Tx(t)$. Under this transformation, system (2.7) becomes:

$$\dot{\tilde{x}}_1(t) = \tilde{A}_{11}\tilde{x}_1(t) + \tilde{A}_{12}\tilde{x}_2(t) \tag{2.21}$$

$$\dot{\tilde{x}}_2(t) = \tilde{A}_{21}\tilde{x}_1(t) + \tilde{A}_{22}\tilde{x}_2(t) + B_2(u(t) + \tilde{f}(t, x, u)) \tag{2.22}$$

where $\tilde{x}_1 \in \mathbb{R}^{n-m}$ and $\tilde{x}_2 \in \mathbb{R}^m$. This is also known as a regular form, which also allows to separate the states that are directly affected by the disturbance.

The switching matrix of the transformed coordinate system is also partitioned as:

$$S = \begin{bmatrix} S_1 & S_2 \end{bmatrix} T \tag{2.23}$$

where $S_1 \in \mathbb{R}^{m\times(n-m)}$ and $S_2 \in \mathbb{R}^{m\times m}$. Then, the necessary condition for (SB) to be nonsingular comes from

$$\det(SB) = \det(S_2B_2) \tag{2.24}$$

where by design $B_2 \neq 0$, thus it follows that $S_2 \neq 0$ is needed. During the sliding mode phase, the sliding surface is defined as:

$$s(t) = S_1\tilde{x}_1 + S_2\tilde{x}_2 = 0 \quad \text{for all} \quad t \geq t_r \tag{2.25}$$

Given that S is full rank, one can express the states as a linear combination of the $n - m$ states. Based on this, $\tilde{x}_2(t)$ can be expressed in terms of $\tilde{x}_1(t)$ as:

$$\tilde{x}_2(t) = -S_2^{-1}S_1\tilde{x}_1(t) = -M\tilde{x}_1(t) \tag{2.26}$$

Substituting the definition of $\tilde{x}_2(t)$ in (2.26) for (2.21), it follows:

$$\dot{\tilde{x}}_1(t) = \left(\tilde{A}_{11} - \tilde{A}_{12}M\right)\tilde{x}_1(t) \tag{2.27}$$

This shows that the ideal sliding motion is described by the combination of (2.26) and (2.27). The selection of the surface $\mathcal{S}$ in (2.8), affects the dynamics in (2.27), given the definition of M in (2.26). In addition, the stability of (2.27) depends on the pair $\left(\tilde{A}_{11}, \tilde{A}_{12}\right)$. Consequently, the design of M depends on the controllability of the same pair. When the system (2.21)-(2.22) is controllable, any classical state feedback method (quadratic minimisation, robust or direct eigenstructure assignment, LMI methods) can be employed for the design of M. Then, the matrix S in (2.23) can be computed as:

$$S = \begin{bmatrix} S_2M & S_2 \end{bmatrix} T \tag{2.28}$$

S_2 is commonly chosen as I_m, but can be chosen arbitrarily. From (2.26) and (2.28), it can be seen that S_2 only acts as a scaling factor for the switching function and has no direct effect on the

dynamics of the sliding motion.

Furthermore, from the previous developments, one can notice that (2.14), (2.19) and (2.27) are independent of the control signal. This means that the systems response is only governed by the switching function; whilst the control signal is designed to guarantee that the state trajectories will converge to the sliding surface, i.e. $s(x) = 0$. This is called the reachablity condition, and for a single input system, it is expressed as

$$\lim_{s \to +0} \dot{s} < 0 \quad \text{and} \quad \lim_{s \to -0} \dot{s} > 0 \tag{2.29}$$

which can also be rewritten as:

$$s\dot{s} < 0 \tag{2.30}$$

Conditions (2.29) and (2.30) do not guarantee the existence of an ideal sliding motion. They only guarantee asymptotic reach to the sliding surface as shown from (2.30) [ES98]:

$$s(t) = s(0)e^{-t} \tag{2.31}$$

A stronger condition that guarantees an ideal sliding motion in finite time, is the η-reachability condition, expressed as

$$s\dot{s} \leq -\eta|s| \tag{2.32}$$

where η represents a positive design scalar and $|\cdot|$ represents the absolute value operator. By rewriting (2.32) as:

$$\frac{1}{2}\frac{d}{dt}s^2 \leq -\eta|s| \tag{2.33}$$

and integrating from 0 to t_s, it follows:

$$|s(t_s)| - |s(0)| \leq \eta t_s \tag{2.34}$$

where t_s represents the time taken to reach $s = 0$, which satisfies:

$$t_s \leq \frac{|s(0)|}{\eta} \tag{2.35}$$

For the case of multi inputs systems, the η-reachability condition is defined as

$$s^\intercal \dot{s} \leq -\eta\|s\| \tag{2.36}$$

with $\|\cdot\|$ as the norm operator. A designed control law is said to satisfy the reachability condition when the state trajectories are driven into the sliding surface and remain thereafter.

A sliding mode control law typically consists of two parts

$$u(t) = u_l(t) + u_n(t) \tag{2.37}$$

where u_l represents the linear part and u_n the nonlinear part of the controller. The linear part of the controller is in charge of maintaining the sliding motion. Moreover, the nonlinear part, is in charge of compensating the disturbances and inducing the sliding motion.

Typically, the nominal equivalent control or a state feedback are employed as u_l. They are designed based on the nominal system, that is with $f(t, x, u) = 0$. Moreover, the different families of SMC can be employed as u_n. In the following sections, their design procedure and characteristics are shortly explained.

2.4 First Order Sliding Mode

A generation classification of SMC can be found in [FMB+15], where it is stated that First Order Sliding Mode Control (FOSMC) belong to the first generation. In addition, the chattering effect; relative degree one of the switching function with respect to the output; and finite time-convergence of the sliding variables but only asymptotic convergence of the states, are highlighted as disadvantages. These disadvantages are targeted with the next generation of SMC.

The design of the following control law is based on (2.37). As mentioned before, the expression of the nominal system is employed for the design of u_l. Consider the system in (2.7), by equating $f(t,x,u)=0$ the following equation is derived:

$$\dot{x}(t) = Ax(t) + Bu(t) \tag{2.38}$$

The switching function is defined as $s = Sx$. Then, similar to (2.17), the equivalent control associated to (2.38) is defined as:

$$u_l(t) = u_{eq}(t) = -(SB)^{-1}(SAx(t)) \tag{2.39}$$

For a FOSMC, the discontinuous part is defined as

$$u_n(t) = -\rho(t,x)(SB)^{-1}\operatorname{sign}(s) \tag{2.40}$$

given that s is a vector, the sign function is applied element by element. The design gain $\rho(t,x)$ is a scalar in charge of enforcing the sliding motion. Substituting (2.39) and (2.40) in (2.37), the control law is:

$$u(t) = -(SB)^{-1}(SAx(t)) - \rho(t,x)(SB)^{-1}\operatorname{sign}(s) \tag{2.41}$$

In order to obtain the equation of the system in sliding motion, the derivative of the switching function is obtained by using (2.7) and (2.41) as:

$$\begin{aligned} \dot{s} = S\dot{x} &= SAx(t) + SB\left[-(SB)^{-1}(SAx(t)) - \rho(t,x)(SB)^{-1}\operatorname{sign}(s)\right] + Bf(t,x,u) \\ &= -\rho(t,x)\operatorname{sign}(s) + Bf(t,x,u) \end{aligned} \tag{2.42}$$

Following the η-reachability condition (2.36), by multiplying both sides of (2.42) by $s^\intercal$ and by using the property $s^\intercal \operatorname{sign}(s) = \|s\|$, it follows:

$$\begin{aligned} s^\intercal \dot{s} &= -\rho(t,x)s^\intercal \operatorname{sign}(s) + s^\intercal Bf(t,x,u) \\ &= -\rho(t,x)\|s\| + s^\intercal Bf(t,x,u) \\ &\leq \|s\|(-\rho(t,x) + \|Bf(t,x,u)\|) \end{aligned} \tag{2.43}$$

The condition for the value selection of the design gain ρ is:

$$\rho(t,x) \geq \|Bf(t,x,u)\| + \eta \tag{2.44}$$

Then, the following inequality is derived:

$$s^\intercal \dot{s} \leq -\eta\|s\| \tag{2.45}$$

Integral Sliding Modes

Although SMC has the insensitivity property against matched disturbances, it is only guaranteed after the reaching phase, i.e. when the system is in sliding motion. Integral Sliding Mode Control (ISMC) was proposed with the aim of eliminating the reaching phase. This implies that the insensitivity property is guaranteed since the beginning of the systems response.

The design procedure is similar to the one explained in Section 2.4. Consider the LTI system (2.7), the proposed control law follows the structure in (2.37) and is defined as

$$u(t) = u_l(t) + u_n(t) = -Kx - \rho(t,x)(GB)^{-1}\,\text{sign}(s) \tag{2.46}$$

where K represents a design matrix from the state feedback controller $u_l = -Kx$, see (2.13). For ISMC, it is considered that there exists a previously designed controller u_l, for the nominal system. The performance of the nominal system with u_l, is taken into account for the design of the switching function. The integral switching function is designed as:

$$s(t) = Gx(t) + z(t) \tag{2.47}$$

with $G \in \mathbb{R}^{m\times n}$ is a design matrix, which satisfies the condition $\det(GB) \neq 0$ considering that B has full rank. The derivative of the switching function is defined as

$$\begin{aligned} \dot{s} &= G\dot{x}(t) + \dot{z}(t) = G\left[Ax(t) + B\left(u(t) + f(t,x,u)\right)\right] + \dot{z}(t) \\ &= G\dot{x}(t) + \dot{z}(t) = G\left[Ax(t) + Bu_l(t) + Bu_n(t) + Bf(t,x,u)\right] + \dot{z}(t) \end{aligned} \tag{2.48}$$

where (2.7) was substituted in (2.48). During sliding motion, it is expected that the equivalent control u_{neq} compensates the perturbations, so that $s = \dot{s} = 0$. It follows that $\dot{z}(t)$ has the following form

$$\dot{z}(t) = -G\left(Ax(t) + Bu_l(t)\right) \quad z(0) = -Gx \tag{2.49}$$

by substituting (2.49) in (2.48) it follows:

$$\begin{aligned} \dot{s} &= G\left[Ax(t) + Bu_l(t) + Bu_n(t) + Bf(t,x,u)\right] - G\left(Ax(t) + Bu_l(t)\right) \\ &= GBu_n(t) + GBf(t,x,u) \end{aligned} \tag{2.50}$$

When equating (2.50) to zero, the expression of u_{neq} is defined as:

$$u_{neq} = -(GB)^{-1}(GBf(t,x,u)) = -f(t,x,u) \tag{2.51}$$

Then,by substituting (2.51) in (2.7) it follows:

$$\dot{x} = Ax(t) + Bu_l - Bf(t,x,u) + Bf(t,x,u) = Ax(t) + Bu_l \tag{2.52}$$

From (2.52), it can be seen that during sliding mode the disturbances are rejected and the system will be governed by (2.52).

The switching function that eliminates the reaching phase is defined based on (2.49) and (2.47) as:

$$s(t) = Gx(t) + z(t) = G\left(x(t) - x(0)\right) - G\int_0^t \left(Ax(\tau) + Bu_l(\tau)\right)d\tau \tag{2.53}$$

where the term $-Gx(0)$ ensures $s(0) = 0$. This means that the reaching phase is eliminated and thus, the sliding mode will exist from $t = 0$.

The analysis of the η-reachability condition follows the procedure shown in the previous sections. The capability of compensating unmatched disturbances with ISMC is studied in [SEFL14, HEA16]. Furthermore, it is worth noting that ISMC can be combined with other SMC techniques, see for example [CKB13, KCB+15].

2.5 Second order sliding modes

The second order sliding mode concept was firstly introduced in [Lev87]. These controllers were mainly created with the aim of reducing the chattering effect. This is accomplished by driving the sliding variable and its derivative to zero. Following the classification in [FMB+15], the Twisting Algorithm (TA) and Terminal Sliding Mode (TSM) belong to the second generation. Even though this generation reduced the chattering effect, this property was only guaranteed for systems with relative degree one. The third generation is composed by the Super-twisting Algorithm (STA), GSTA and the differentiator. The applicability of STA is limited to systems with relative degree one or two.

Remark 2. *In the following, the parameters of the controllers are described with inequalities. The reader must take into account that in practice, these parameters are never assigned according to their respective inequalities, as stated in [SEFL14, Lev03b]. This due to the fact that the real system is not exactly known and thus the model is not adequate, leading to an overestimation of the parameters K_M, K_m, C. Instead it is suggested to adjust the parameters during the simulation. This remark applies for the controllers described in this section (2.5).*

2.5.1 Twisting algorithm

The twisting algorithm was the simplest Second Order Sliding Mode Controller (SOSMC) proposed. Consider the following system:

$$\dot{x}(t) = a(t,x) + b(t,x)u \tag{2.54}$$

where for some positive constants C and K_m it follows that $|a(t,x)| \leq C$ and $0 \leq K_m \leq b(t,x)$. The TA is defined as:

$$u(t) = -r_1 \text{sign}(x) - r_2 \text{sign}(\dot{x}), \quad r_1 > r_2 > 0 \tag{2.55}$$

Let r_1 and r_2 satisfy the conditions $K_m(r_1 + r_2) - C > K_M(r_1 - r_2) + C$, $K_m(r_1 - r_2) > C$. The controller guarantees finite time convergence of the states $x_1 = x_2 = 0$ for all $t > 0$ when the parameters are chosen according to [Eme86]. The total convergence time is estimated as:

$$T \leq \sum \frac{|\dot{x}_i|}{[K_m(r_1 - r_2) - C]} \leq \frac{|\dot{x}_0|}{(1-q)\,[K_m(r_1 - r_2) - C]} \tag{2.56}$$

The interested reader can find the convergence proof in [Eme86, SEFL14].

2.5.2 Terminal Sliding Mode

TSM was first proposed in [VG93]. This controller is based on terminal attractors that guarantee finite-time convergence of the states. This is accomplished by adding a nonlinear term in the switching function as:

$$s(x) = x_2 + \beta \sqrt{|x_1|}\, \text{sign}(x_1) \tag{2.57}$$

where the value of $\beta > 0$. The Terminal Sliding Mode Control is given by:

$$u(x) = -\alpha\, \text{sign}(s(x)) \tag{2.58}$$

In [FMB+15], the derived behaviour of the system, due to the selection of β, is analyzed and classified on terminal and twisting mode. In addition, variations of TSM can be found in literature as Non-Singular TSM [FYM02] and Fast TSM [YZ02].

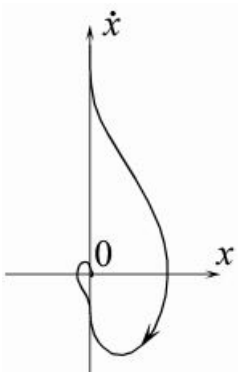

Figure 2.4: Phase plane of the STA controller [Lev03b]

2.5.3 Super-Twisting Controller

Given that the STA does not need the measurement of $\dot{s}$, it can be employed as an alternative for FOSMC. In addition, STA is known for reducing the chattering , this means that a continuous control signal is obtained. Consider the system (2.54), where for some positive constants C, K_M, K_m, U_M, q [Lev03b]:

$$|\dot{a}| + U_M|\dot{b}| \leq C, \quad 0 \leq K_m \leq b(t,x) \leq K_M, \quad |a/b| < qU_M \quad \text{and} \quad 0 < q < 1 \tag{2.59}$$

Then, the STA is described by the following equation:

$$u = -\lambda|x|^{\frac{1}{2}}\,\text{sign}(x) + u_1, \quad \dot{u}_1 = \begin{cases} -u, & |u| > U_M \\ -\alpha\,\text{sign}(x), & |u| \leq U_M \end{cases} \tag{2.60}$$

Lemma. *With $K_m\alpha > C$ and λ sufficiently large, the controller (2.59) guarantees the appearance of a SOSMC $x = \dot{x} = 0$ attaching the trajectories to $[-U_M, U_M]$ and stays there. It never leaves the segment if the initial value is inside at the beginning.*

The phase portrait of (2.59) is shown in Fig.2.4. A sufficient condition which validates the Lemma is:

$$\lambda > \sqrt{\frac{2}{(K_m\alpha - C)}}\frac{(K_m\alpha + C)K_M(1+q)}{K_m^2(1-q)} \tag{2.61}$$

The total convergence time can be estimated by [Lev03b, SEFL14]:

$$T \leq \sum |\dot{x}_i|/(K_m\alpha - C) \tag{2.62}$$

To illustrate its design procedure, one can consider the example of the LTI system (2.7), with the previously defined switching function (2.3) and the expression for u_l in (2.39). Then, the expression of u_n is defined as

$$\begin{aligned} u_n &= -k_1|x|^{\frac{1}{2}}\text{sign}(x) + v \\ \dot{v} &= -k_2\text{sign}(x) \end{aligned} \tag{2.63}$$

where $\lambda = k_1$ and $\alpha = k_2$. Following the structure in (2.37), the control law is defined as:

$$u(t) = -(SB)^{-1}\left[SAx(t) + k_1|x|^{\frac{1}{2}}\text{sign}(x) + \int_0^t k_2\text{sign}(x)d\tau\right] \tag{2.64}$$

where the gains k_1 and k_2 are selected according to [Lev98, MO12] as $k_1 = 1.5\sqrt{\Gamma_2}$ and $k_2 = 1.1\Gamma_2$, where it is assumed that $\left|\dot{f}(t,x,u)\right| < \Gamma_2$ is known. The control law (2.63) leads to $s = \dot{s} = 0$ in finite time, as a consequence $x = \dot{x} = 0$ converges asymptotically.

2.5.4 Generalized/Variable Gain Super-Twisting Algorithm

Variable Gain Super-Twisting Algorithm (VGSTA) is an extension of the STA that provides exact compensation against state dependent perturbations that can exponentially grow in time. Consider the system (2.7), which linear transformation is described as in (2.21) and (2.22). The switching function is described in the new coordinate system as:

$$s(t) = \tilde{x}_2 - K\tilde{x}_1 \tag{2.65}$$

The reduced order model is obtained when $s(t) = 0$, i.e. during sliding mode. It is obtained by equating (2.65) to zero and substituting it in (2.21) as :

$$\dot{\tilde{x}}_1 = \tilde{A}_{11}\tilde{x}_1 + \tilde{A}_{12}K\tilde{x}_1 = \left(\tilde{A}_{11} + \tilde{A}_{12}K\right)\tilde{x}_1 \tag{2.66}$$

where K can be designed employing any linear control design method for (2.66), given that the pair $(\tilde{A}_{11}, \tilde{A}_{12})$ is controllable. Following the procedure shown in [GMF11, SEFL14], by applying the control law defined as:

$$u = -\left(\tilde{A}_{21} + \tilde{A}_{22}K - K\left(\tilde{A}_{11} + \tilde{A}_{12}K\right)\right)\tilde{x}_1 - \left(\tilde{A}_{22} - K\tilde{A}_{12}\right)s + v \tag{2.67}$$

to (2.21) and (2.22), and considering $(\tilde{x}_1^\intercal, s)$ as state variables, the system takes the form:

$$\begin{aligned} \dot{\tilde{x}}_1 &= \left(\tilde{A}_{11} + \tilde{A}_{12}K\right)\tilde{x}_1 + \tilde{A}_{12}s \\ \dot{s} &= v + \tilde{f}\left(\tilde{x}_1, s + K\tilde{x}_1, t\right) \end{aligned} \tag{2.68}$$

The GSTA also known as VGSTA, has a similar definition to the STA, but with added terms [Mor09], as:

$$\begin{aligned} u_n &= -k_1\phi_1(x) + v \\ \dot{v} &= -k_2\phi_2(x) \end{aligned} \tag{2.69}$$

with

$$\phi_1(x) = |x|^{\frac{1}{2}}\operatorname{sign}(x) + k_3 x \quad \phi_2(x) = \frac{1}{2}\operatorname{sign}(x) + \frac{3}{2}k_3|x|^{\frac{1}{2}}\operatorname{sign}(x) + k_3^2 x \tag{2.70}$$

where k_3 ensures robustness against a wider class of uncertainty and perturbations than the STA, for instance in the presence of uncertain control coefficient and state dependent perturbations [CFM18]. The perturbations $\tilde{f}\left(\tilde{x}_1, s + K\tilde{x}_1, t\right)$ can also be rewritten as:

$$\tilde{f}\left(\tilde{x}_1, s + K\tilde{x}_1, t\right) = \underbrace{\left[\tilde{f}\left(\tilde{x}_1, s + K\tilde{x}_1, t\right) - \tilde{f}\left(\tilde{x}_1, K\tilde{x}_1, t\right)\right]}_{g_1(\tilde{x}_1, s, t)} + \underbrace{\tilde{f}\left(\tilde{x}_1, K\tilde{x}_1, t\right)}_{g_2(\tilde{x}_1, t)} \tag{2.71}$$

In order for $s(t)$ to be equal to zero it is required that $g_1(\tilde{x}_1, s, t) = 0$, whilst it is only necessary that $\dot{g}_2(\tilde{x}_1, t)$ is bounded by $\frac{1}{2}g_2(\tilde{x}_1, t)$ [Lev07]. Then, the disturbance is bounded by the known continuous functions $\varrho_1(t, x) \geq 0$ and $\varrho_2(t, x) \geq 0$ as:

$$\begin{aligned} g_1(\tilde{x}_1, s, t) &\leq \varrho_1(t, x)|\phi_1(x)| = \varrho_1(t, x)\left(1 + k_3|x|^{\frac{1}{2}}\right)|x|^{\frac{1}{2}} \\ \dot{g}_2(\tilde{x}_1, t) &\leq \varrho_2(t, x)|\phi_2(x)| = \frac{1}{2}\varrho_2(t, x) + k_3\varrho_2(t, x)\left(\frac{3}{2} + k_3|x|^{\frac{1}{2}}\right)|x|^{\frac{1}{2}} \end{aligned} \tag{2.72}$$

System (2.68) driven by (2.69) can be written as:

$$\begin{aligned} \dot{\tilde{x}}_1 &= \left(\tilde{A}_{11} + \tilde{A}_{12}K\right)\tilde{x}_1 + \tilde{A}_{12}s \\ \dot{s} &= -k_1\phi_1(x) + v + g_1(\tilde{x}_1, s, t) \\ \dot{v} &= -k_2\phi_2(x) + \dot{g}_2(\tilde{x}_1, t) \end{aligned} \tag{2.73}$$

Lemma. *Suppose that for some known continuous functions $\varrho_1(t,x) \geq 0$, $\varrho_2(t,x) \geq 0$ the inequalities (2.72) are satisfied. Then for any initial condition $(\tilde{x}_1^\intercal, s_0, v_0)$ the sliding surface $s = 0$ will be reached in finite time if the variable gains are selected as [SEFL14]:*

$$\begin{aligned} k_1 &= \delta + \frac{1}{\beta}\left\{\frac{1}{4\epsilon}[2\epsilon\varrho_1 + \varrho_2]^2\right\} a + 2\epsilon\varrho_2 + \epsilon + [2\epsilon + \varrho_1](\beta + 4\epsilon^2) \\ k_2 &= \beta + 4\epsilon^2 + 2\epsilon k_1 \end{aligned} \tag{2.74}$$

where $\beta > 0, \epsilon > 0, \delta > 0$ are arbitrary positive constants. The reaching time of the sliding surface can be estimated by

$$T = \frac{2}{\gamma_2} ln\left(\frac{\gamma_2}{\gamma_1} V^{\frac{1}{2}}(s_0, v_0) + 1\right) \tag{2.75}$$

where $V(s,v) = \xi^\intercal P \xi$, $\xi^\intercal = \left[|s|^{\frac{1}{2}}\,\mathrm{sign}(s) + k_3,\ v\right]$ and

$$\gamma_1 = \frac{\epsilon\lambda_{min}^{\frac{1}{2}}\{P\}}{\lambda_{max}\{P\}} \quad \gamma_2 = \frac{2\epsilon k_3}{\lambda_{max}\{P\}} \tag{2.76}$$

2.5.5 Observer/Differentiator

The sliding mode differentiator is employed for exact robust differentiation in the absence of measurement noise. For instance, it can be employed for controllers that need the measurements of $\dot{x}$, given that it offers finite-time convergence to the estimated derivative. Based on the STA algorithm, its operating principle is explained below.

Let $f(t)$ be a function to be differentiated. It is assumed that its second derivative is bounded by a known constant L, i.e. $|\ddot{f}(t)| < L$. Consider that $x_1 = f$ and $x_2 = \dot{f}$, then it can be rewritten as:

$$\begin{aligned} \dot{x}_1 &= x_2 \\ \dot{x}_2 &= \ddot{f} \\ y &= x_1 \end{aligned} \tag{2.77}$$

Similar to the definition of the STA controller defined in (2.63), the differentiator is defined as:

$$\begin{aligned} \dot{\hat{x}}_1 &= -k_1|\hat{x}_1 - y|^{\frac{1}{2}}\mathrm{sign}(\hat{x}_1 - y) + \hat{x}_2 \\ \dot{\hat{x}}_2 &= -k_2\mathrm{sign}(\hat{x}_1 - y) \end{aligned} \tag{2.78}$$

By appropriately selecting the gains k_1 and k_2 [Lev98], finite-time convergence of $(f - \hat{x}_1) = \left(\dot{f} - \hat{x}_2\right) = 0$ and the estimate of $\dot{f}$ can be found in $\hat{x}_2$.

2.6 Arbitrary Sliding Mode Controllers

Arbitrary Sliding Mode Controllers were developed with the aim of stabilizing arbitrary relative degree systems in finite-time, by using nested sliding mode controllers [Lev01]. Its recursion is dependent on the relative degree of the output. The main families of r-sliding controllers were: nested sliding and quasi-continuous sliding. Nested sliding and quasi-continuous sliding controllers belong to the fourth generation of SMC [FMB+15]. Although the quasi-continuous r-sliding controllers reduce the chattering effect, they do not reduce it to a great extent. A proposed solution to this problem is analyzed in the following section. The controller design is explained by considering the

system (2.7), where its output $y = Cx$ has a known relative degree. Then, the controller is defined as:

$$u = -\alpha \Psi_{r-1,r}\left(y, \dot{y}, \ldots, y^{r-1}\right) \tag{2.79}$$

where β_i can be fixed in advance for every relative degree r as positive large values. The design gain $\alpha > 0$ is more conveniently adjusted by simulations, as suggested in [SEFL14]. The value of $\Psi_{r-1,r}$ is defined in the following for each family of controllers.

Based on FOSMC, the nested r-sliding controllers are built with $\Psi_{0,r} = \text{sign}(y)$ and $\Psi_{i,r} = \text{sign}\left(y^{(i)} + \beta_i N_{i,r} \Psi_{i-1,r}\right)$. Let $q > 1$, it follows that $N_{i,r}$ is defined as:

$$N_{i,r} = \left(|y|^{\frac{q}{r}} + |\dot{y}|^{\frac{q}{r-1}} + \ldots + |y^{(i-1)}|^{\frac{q}{(r-i+1)}}\right)^{\frac{1}{q}} \tag{2.80}$$

Given that the quasi-continuous r-sliding controllers are based on SOSMC, a reduced chattering effect is observed in the control signal. Their structure consists of the following definitions:

$$\begin{aligned} &\varphi_{0,r} = y, \quad \varphi_{i,r} = y^{(i)} + \beta_i N_{i-1,r}^{(r-i)/(r-i+1)} \Psi_{i-1,r} \\ &\Psi_{0,r} = \frac{\varphi_{0,r}}{N_{0,r}} = \text{sign}(y), \quad \Psi_{i,r} = \frac{\varphi_{i,r}}{N_{i,r}} \\ &N_{i,r} = \left|y^{(i)}\right| + \beta_i N_{i-1,r}^{(r-i)/(r-i+1)} \end{aligned} \tag{2.81}$$

Arbitrary order Observer/Differentiator

In order for the previous controller (2.79) to be applicable, the r derivatives of y have to be available. Their computation is obtained by means of the arbitrary order differentiator [Lev03a] defined as

$$\begin{aligned} \dot{z}_0 &= v_0 = -\lambda_k L^{\frac{1}{k+1}} |z_0 - y|^{\frac{k}{k+1}} \text{sign}(z_0 - \sigma) + z_1 \\ \dot{z}_1 &= v_1 = -\lambda_{k-1} L^{\frac{1}{k}} |z_1 - v_0|^{\frac{k-1}{k}} \text{sign}(z_1 - v_0) + z_2 \\ &\vdots \\ \dot{z}_{k-1} &= v_{k-1} = -\lambda_1 L^{\frac{1}{2}} |z_{k-1} - v_{k-2}|^{\frac{1}{2}} \text{sign}(z_{k-1} - v_{k-2}) + z_k \\ \dot{z}_k &= -\lambda_0 L \text{sign}(z_k - v_{k-1}) \end{aligned} \tag{2.82}$$

where L represents the upper bound of $|y^{(k+1)}|$. According to [Dav13, SEFL14, FMB+15], by choosing the appropriate gains $\lambda_1, \lambda_2, \ldots, \lambda_k$, the following inequality is true in the absence of noise:

$$|z_i - y^{(i)}| = 0 \quad i = 1, 2, \ldots, k \tag{2.83}$$

Then, the estimated derivative of $y^{(i)}$ is obtained in finite-time in z_i.

Continuous Nested Sliding Mode Controllers

Continuous Nested Sliding Mode Controllers (CNSMA) were first proposed in [FMB+15]. They compose the fifth and last generation of SMC. The aim of the CNSMA was to have a continuous signal while keeping the properties of the arbitrary order sliding mode controllers. The generalized form of the Continuous Nested Terminal Sliding Mode Algorithm, for a system with relative degree r, is proposed as:

$$\begin{aligned} \dot{x}_1 &= x_2 \\ \dot{x}_2 &= x_3 \\ &\vdots \\ \dot{x}_{r-1} &= -k_1 |\phi_{r-2}|^{\frac{1}{2}} \text{sign}(\phi_{r-2}) + x_r \\ \dot{x}_r &= -k_r \text{sign}(\phi_{r-2}) + \rho \end{aligned} \tag{2.84}$$

It is assumed that the perturbation is bounded as $|\rho| \leq \Delta$. In (2.84), $x_1, x_2, \ldots, x_r$ represent the states and $\phi_{r-2} = s_{r-1,r-1}$, where for $i = 2, 3, \ldots, (r-1)$, the following is defined:

$$\begin{aligned} s_{0,r-1} &= x_1 \\ s_{1,r-1} &= x_2 + k_2 R_{1,r-1} \text{sign}(x_1) \\ s_{i,r-1} &= x_{i+1} + k_{i+1} R_{i,r-1} \text{sign}(s_{i-1,r-1}) \end{aligned} \tag{2.85}$$

with $R_{1,r-1} = |x_1|^{\frac{r}{r+1}}$, $R_{i,r-1} = \left| |x_1|^{r_1} + |x_2|^{r_2} + \ldots + |x_{i-2}|^{r_{i-2}} \right|^{q_i}$ and q_i represents a design parameter.

The main difference between the quasi-continuous $r-$sliding controllers and the CNSMA is that the quasi-continuous controller remains continuous until a 2-sliding mode takes place, unlike the TSM.

The work developed in [BPZ04] can be classified as a nested continuous SMC for relative degree systems. It is defined as simplex control methods and it is mainly employed for the control of systems with mono-directional actuators given that it reduces the number of control vectors.

2.7 Adaptive Sliding Mode Controllers

In the previous sections, the tunning of the described controllers was shown to be dependent on the bound of the disturbance, see for example (2.44). One may assume that when the bound of the disturbance is unknown or variable, the gains of the controllers can be selected with an overestimated bound. The consequence would be an increment in the chattering effect. Consider for instance, the case when a STA controller is designed with the aim of having a control signal with a reduced chattering effect. With an overestimated disturbance bound, its chattering attenuation property might be diminished. Adaptive Sliding Mode Controllers (ASMC) were developed with the aim of having a robust controller, even when the bound of the disturbance is unknown or in the case the disturbance is time-varying.

Their main design principle is to adjust the gains of the controller to maintain the sliding motion, depending only on the information that is available. In literature, different approaches towards applying adaptation to SMC can be found, see for example [HKC08, EUT+70] where the coefficients of the switching plane are varied without information of the plant with the aim of improving the systems response. Recent research in this field, is dedicated to the proposal of a solution that considers reducing the chattering effect, see for instance [SMP+10, HLC12, TLP13, GBDB17, HBHS20, EEZ16] were the adaptation principles are applied to the STA, TA, arbitrary order SMC, TSM and SMO, respectively.

2.8 Output Tracking

The output tracking problem refers to a control system that follows a specific trajectory in order to have a desired performance. It is commonly employed in practice, for example the attitude angles of a quadrotor follow reference profiles; to induce a specific trajectory in an autonomous robot or for the control of electric power systems.

For the output tracking problem, the control design procedure is the same as explained in the previous sections. The main difference is the definition of the switching function, given that it is based on the tracking error. Following the example shown in [SEFL14], consider the following

system:

$$\begin{aligned} \dot{x}_1 &= x_2 \\ \dot{x}_2 &= u + f(t, x, u) \\ y &= x_1 \end{aligned} \tag{2.86}$$

where $|f(x,t)| < \Gamma_1$ represents the bounded disturbances/uncertainties, and the bound f^+ is assumed to be known. The reference trajectory is defined as $y_c = x_{1c}$. The tracking error is then defined as $e = y - y_c = x_1 - x_{1c}$. The switching function is defined based on the tracking error as:

$$s = ce + \dot{e} \quad c > 0 \tag{2.87}$$

The design process of a control law that drives $s = 0$ and $e = 0$ in finite time, follows the specific procedure for each controller, as explained in the previous sections.

2.9 Fault Tolerance and Sliding Modes

Control systems have become part of our daily life. Initially, their evolution was mainly shaped by the need of reducing effort, costs and time. Progressively, their complexity increased, since not only they had to guarantee efficiency, but safety. This can be better understood when considering systems like chemical reactors, nuclear plants or even airplanes. Thus, the importance of considering faults during the design process of the controlled systems. A fault is defined in [IB97], as an unpermitted deviation of at least one characteristic property or parameter of the system from the acceptable/usual/standard condition. A control that has the capability of maintaining an acceptable performance despite the occurrence of a fault, is called FTC. It is achieved due to redundancy of actuators, sensors or other components on the system.

According to their location, faults can be classified as sensor, actuator or component faults, see Fig. 2.5. Sensor and actuator faults can present total or partial loss. A total loss on an actuator, represents a stuck actuator that does not generate the expected actuation, despite the applied input. For the case of a sensor, it means that the received measurements are incorrect. Furthermore, an actuator with partial loss produces a percentage of the expected actuation. In the sensor case, the measurements may be noisier, scaled or have an offset. Component faults represent changes in physical parameters which affect the dynamical behaviour of the system. Is hard to classify them since they can cover a wide variety of situations. Faults can also be classified according to their time behaviour as abrupt, incipient and intermittent, see Fig. 2.6. It can be seen that an abrupt fault behaves like a step signal; an incipient fault like a drifted signal and an intermittent fault as a signal with interrupts.

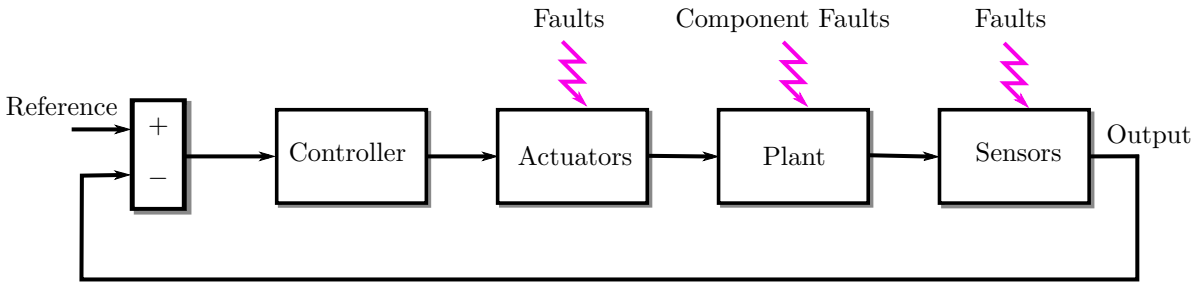

Figure 2.5: Classification of faults according to their location

Faults can be modelled as additive or multiplicative representations. For instance, an offset or drift in the control signal can be described as an additive fault as follows:

$$\boldsymbol{u}_f(t) = \boldsymbol{u}(t) + \boldsymbol{f}(t) \tag{2.88}$$

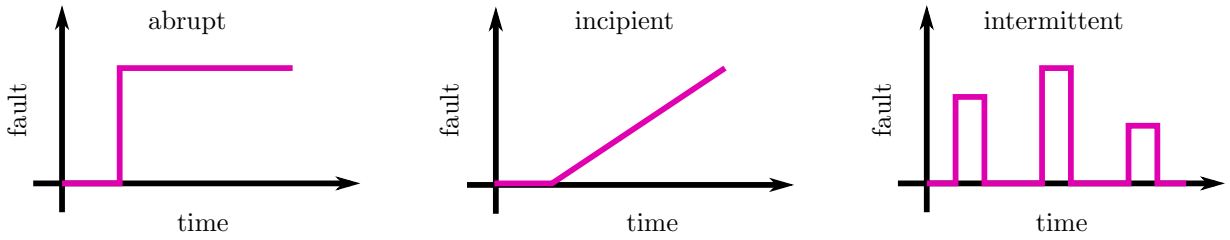

Figure 2.6: Classification of faults according to their time behaviour [Ise06]

where $\boldsymbol{f}(t) \in \mathbb{R}^n$ represents the fault actuator vector, $\boldsymbol{u}(t) \in \mathbb{R}^n$ is the control input and $\boldsymbol{u}_f(t) \in \mathbb{R}^n$ is the faulty control input. On the other hand, faults that cause changes in the parameters of the system are modelled as multiplicative faults. Following the model employed in [Hen10], $\boldsymbol{u}_f(t)$ is described as a multiplicative fault as

$$\boldsymbol{u}_f(t) = (\mathbb{I} - \boldsymbol{\Psi})\boldsymbol{u}(t) \tag{2.89}$$

where $\boldsymbol{\Psi} = \text{diag}[\psi_i, \ldots, \psi_n]$ is an unknown matrix that has values that range between $[0, 1]$. When $\psi_i = 1$, the i-th actuator is faulty; $\psi_i = 0$, represents normal actuation; and $\psi_i = \%x$ means a loss of efficiency.

Similar expressions are obtained for describing faulty output $\boldsymbol{y}_f(t)$, caused by faulty sensors. The difference relies on changing $\boldsymbol{u}(t)$ and $\boldsymbol{u}_f(t)$ for $\boldsymbol{y}(t)$ and $\boldsymbol{y}_f(t)$, respectively, in (2.88) and (2.89). Finally, the description of a component fault is translated to a modification on the system's matrix. For the LTI case, it is modelled as:

$$\dot{\boldsymbol{x}}(t) = \boldsymbol{A}_f\boldsymbol{x}(t) + \boldsymbol{B}\boldsymbol{u}(t) = (\boldsymbol{A} + \boldsymbol{\Delta A})\boldsymbol{x}(t) + \boldsymbol{B}\boldsymbol{u}(t) \tag{2.90}$$

where $\boldsymbol{\Delta A}$ represents a change in the system matrix $\boldsymbol{A}$.

Based on the use of the redundant components, FTC is classified in passive and active [JY12a, JY12b]:

- Passive techniques consider that possible system failures are known. Then, the control designed is developed considering the pre-specified faults. Given that the controller stays fixed during the systems operation, it is expected that it can overcome any component fault. This makes passive approaches less complex, considering that the robustness properties of a fixed controller are exploited, see Fig. 2.7. As a consequence, the type of faults that the robust controller can compensate is limited. However, their lack of complexity plays and advantage when implementing, given that they are more reliable and they have less requirements in software/hardware [ELS+10].

- Active techniques reconfigure the control parameters in the presence of a fault. They rely on a FDI unit, see Fig. 2.8. The FDI is in charge of the constant monitoring of the status of the system and its components. In this way, when the FDI detects a fault, a reconfiguration is carried out in the controller. As a result, a wider range of faults can be compensated. One limitation of this scheme is that it has limited time to perform FDI followed by control reconfiguration. In addition, the accuracy of the FDI affects the reconfiguration process. In other words, despite the existence of some stability and performance proofs for active FTC techniques, the main problem lies in guaranteeing stability and performances of the overall fault-tolerant scheme taking into account FDI performances (detection delay, possible false alarms, etc.), control specifications, and reconfiguration mechanism [CEH15].

Many control techniques have been applied for the design of fault tolerant controllers. Consider for instance H_∞, Linear Parameter Varying (LPV), CA, dynamic inversion, adaptive methods,

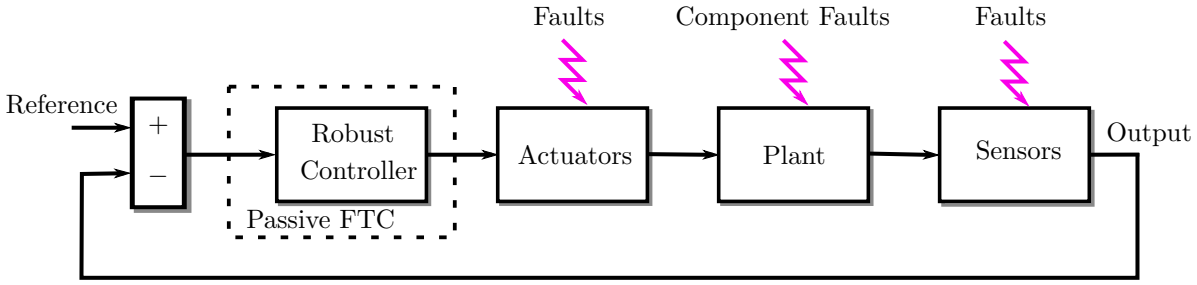

Figure 2.7: Architecture of passive FTC

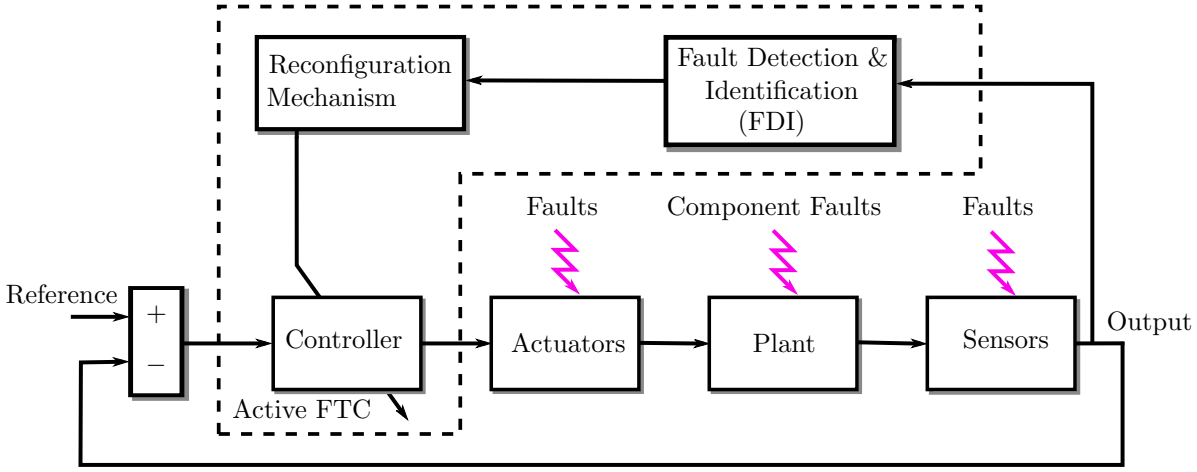

Figure 2.8: Architecture of active FTC

neural networks, Model Predictive Control (MPC) and SMC, to mention some. Table 2.1 shows a summary of references with these control techniques. Due to its robustness properties, SMC was considered as a potential alternative for reconfigurable control in [HW03]. In literature, active and passive FTC schemes, based on SMC can be found. Most active FTC approaches with SMC are focused on the development of either FDI or reconfiguration. On the other hand, passive FTC approaches found in literature are more conservative, i.e. the considered faults are mainly loss of effectiveness. Furthermore, SMO are used for FTC, specifically for fault reconstruction or for fault detection. Fault reconstruction with SMO's is achieved by employing the equivalent output error injection approach, which is the average value required to maintain the sliding motion [ESP00]. In addition, SMO are also employed to generate residuals by escalating the output estimation error. This residual then acts as a fault alarm, which is activated when its value is different from zero.

CA method is commonly used with SMC for active FTC purposes. This is mainly because, it allows the independent design of the control law. In addition, a reconfiguration of the controller is not needed when a fault occurs. Furthermore, the actuator limitations can be considered by the CA unit. In order to produce the desired control effort, the CA redistributes the control signal into the healthy actuators. In Fig. 2.9, the control allocation scheme is shown. It can be seen that CA depends on an FDI unit, so that the CA knows the availability of the actuators.

2.10 Conclusion

In this chapter, the history of the development of SMC was shortly reviewed. It starts with the description of the operating principle and the basic concepts that were derived from it. Then, the evolution of the SMC techniques and their design process is examined. At the same time, their specific limitations and advantages are reviewed.

Design Approaches	**References**
H_∞	[GS19, LSD12, LJZ18, WPC06]
LQR	[OH16, YZMQ13]
Liner Parameter Varying (LPV)	[RTAS07, RNP14, CAE19b]
Control allocation (CA)	[AE08, RKFZ15, MV11, CJ14, CEAS20]
Dynamic Inversion	[JKR08, WHD+19]
Adaptive methods	[CG10, MJTC15]
Neural Networks	[DP01, LY16, SJSL14, LLT18]
Model Predictive Control (MPC)	[IZG11, MJ03]
Sliding Modes • Active technique • Passive technique • Fault Estimation/Fault Detection	 [HEA11, XCW15, CEAS20, CAE19a, CEA19] [SWZP15, MNB15, LJPZ19, LP17, LP16, DCH+16] [ES98, ESP00, CAE19b, LP18, YYK17, CMZL20] [XYG17, FIS20, HBHS20, FdLCH+15, RKFZ15] [DCH19, CCD+17b, CCD+17a, DLCH+15]

Table 2.1: Different design approaches for FTC

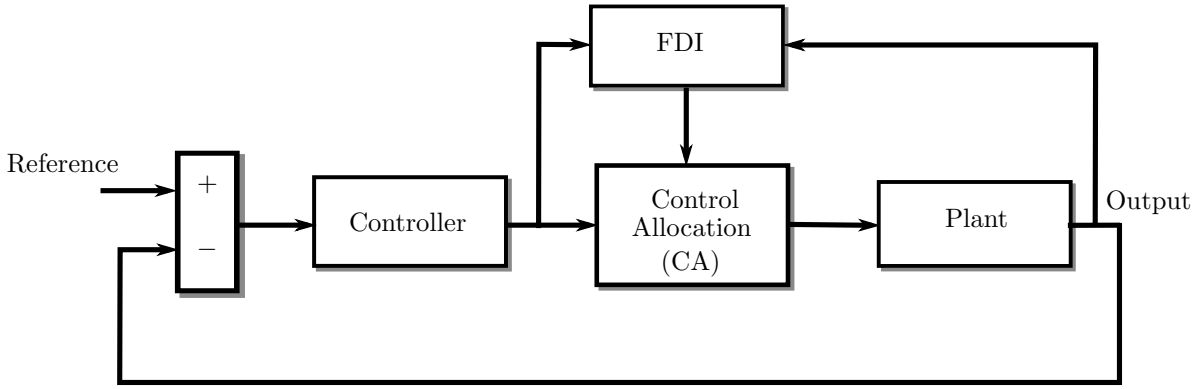

Figure 2.9: Control allocation scheme

The concept of FTC and its classification is introduced. The characteristics that differentiate active from passive approaches were also described. Furthermore, it is mentioned that SMC techniques have attracted the attention of the FTC community, due to its insensitivity properties. This idea, will be explored in the following of the manuscript.

In the next chapter, the study of the rendezvous mission and its dynamics will be studied. The attitude and position control are designed based on sliding mode techniques. Perturbations coming from the environment and some model uncertainty are considered during the design process of the controller. The work that follows will be focused on the FOSMC, STA and GSTA. This is due to the attenuation on the chattering effect, and the robustness that the STA and the GSTA offer without the need of higher order derivatives. The FOSMC will be applied for comparison purposes.

3 Design of a Sliding Mode Control Scheme

3.1 Introduction

This chapter introduces the design of SMC schemes applied to a rendezvous mission. The first part of this chapter is devoted to the description of the rendezvous mission, e.g. the phases by which it is constituted, the vehicles involved (i.e. chaser and target) and their structure. The development of the nonlinear coupled model for both dynamics, translational and rotational, is developed based on the HCW formalism. In this model, the effects of the solar arrays and the propellant sloshing are considered. A linear controllable canonical form of the model is obtained for each dynamics, i.e. two linear 3DoF models are obtained. These models, serve as the basis for the controller design. Based on the Sliding-Mode Techniques described in the previous chapter, two SMC are developed in a backstepping setup. First, the development of a FOSMC is analyzed followed by the study of the STA. The computed control signals are distributed to the actuators by the CA unit, in the chaser vehicle. The operating principle of the CA and the description of the thruster model unit are also addressed. Finally, the proposed solutions are tested in a high-fidelity benchmark that accurately simulates a rendezvous mission between a chaser spacecraft and a passive target onto a circular orbit around Earth, taking into account the coupling between attitude and translational motions, propellant sloshing, modes of the flexible appendages and the most dimensioning space disturbances (e.g. second zonal harmonic J_2, atmospheric drag, magnetic disturbance).

System description and problem formulation

The reference scenario consists of two vehicles inserted into the same circular orbit around Earth. One vehicle (the target) is a passive spacecraft (there are no available sensor and actuator) while the second one (the chaser), is equipped by a set of rendezvous sensors and actuators and a complete GNC unit. The characteristics of the orbit's rendezvous are a semi-major axis $a = 7068\,\text{km}$, an eccentricity $e = 0$ and an inclination $i = 0\,\text{deg}$. The trajectories of the spacecraft on this orbit are characterized by constant longitude of the ascending node and argument of periapsis (fixed to $\Omega = 0\,\text{rad}$ and $\omega = 0\,\text{rad}$ respectively) with initial values of the true anomaly fixed to $\nu(0) = 1.5 \times 10^{-5}\,\text{rad}$ for the target and $\nu(0) = 0\,\text{rad}$ for the chaser. With these orbital parameters, the initial distance between the two spacecraft is 100 m approximately in the y-axis direction in the so called Local Vertical Local Horizontal (LVLH) frame $\mathcal{F}_l = \{O_t; \overrightarrow{\mathbf{X_l}}, \overrightarrow{\mathbf{Y_l}}, \overrightarrow{\mathbf{Z_l}}\}$[1]. The spacecraft trajectories in the inertial frame $\mathcal{F}_i = \{O_E; \overrightarrow{\mathbf{X_i}}, \overrightarrow{\mathbf{Y_i}}, \overrightarrow{\mathbf{Z_i}}\}$[2] and in $\mathcal{F}_l$ are illustrated on Fig. 3.1 for a better understanding. The considered rendezvous trajectory corresponds to i) target acquisition

[1] The origin of the LVLH frame is at the target center of mass, the axis $\overrightarrow{\mathbf{Z_l}}$ is pointing to the opposite of O_E, the axis $\overrightarrow{\mathbf{Y_l}}$ is aligned with the negative orbital momentum vector and $\overrightarrow{\mathbf{X_l}}$ completes the frame.

[2] The inertial frame $\mathcal{F}_i$ is defined as on Fig. 2

where the chaser keeps its position at its initial position and rotates to acquire the target and *ii*) rendezvous where the chaser's attitude is controlled to keep the capture mechanism aligned with the target and while, at the same time, it performs a forced translation.

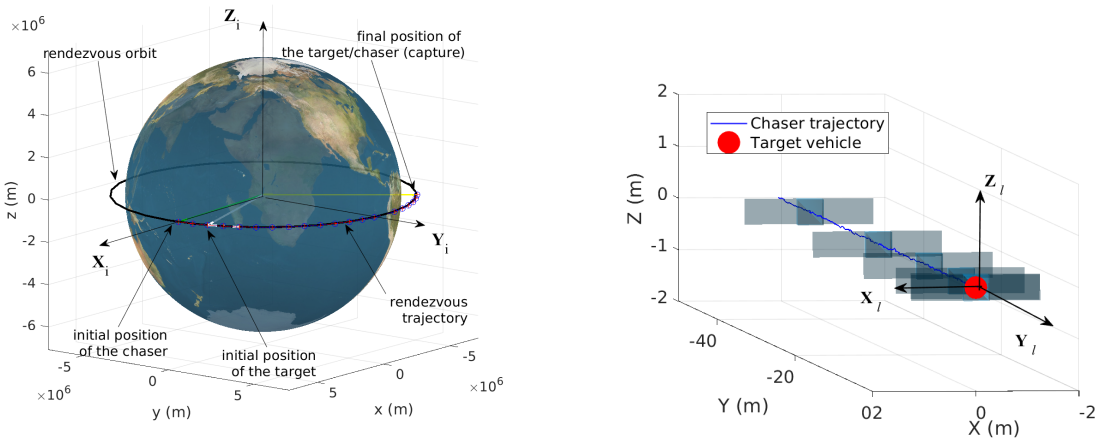

Figure 3.1: The orbit and rendezvous trajectory in $\mathcal{F}_i$ (left) and in the LVLH frame $\mathcal{F}_l$ (right). The trajectory corresponds to the results in section 3.6

The avionics architecture retained for the mission, is composed of a LIDAR which provides relative positions and velocities, an IMU and a Star Tracker. It is worth noting that, in this work, it is assumed a perfect navigation unit, i.e. all measurements are assumed to be noise free. The actuation consists of 12 thrusters of $4N$ for both attitude and position control.

The complete mission is modelled into a so-called Functional Engineering Simulator (FES) developed in Matlab/Simulink. Both chaser and target have each one an associated environment module as some characteristics depend on specific spacecraft properties. Typically, the chaser has two half-filled tanks that cause propellant sloshing and a solar array with two flexible modes, whereas the target is assumed to be a spherical object. For the chaser, the considered disturbances are the second-order zonal harmonic J_2, the atmospheric drag and effect of the Earth magnetic filed. With regard to the target, it is assumed to be affected by the J_2 disturbance and the atmospheric drag.

The derivation of the dynamic models is based on expressing linear accelerations and angular accelerations in adequate frames. Three frames are used for that purpose:

i) Earth centered inertial frame $\mathcal{F}_i$: this frame is a non-accelerating reference frame, with its origin at the center of the Earth, and the axes $\vec{\mathbf{x}}_i, \vec{\mathbf{y}}_i, \vec{\mathbf{z}}_i$ are oriented as shown in Fig. 3.1.

ii) the so-called LVLH frame $\mathcal{F}_l = \{O_t; \overrightarrow{\mathbf{X_l}}, \overrightarrow{\mathbf{Y_l}}, \overrightarrow{\mathbf{Z_l}}\}$: the center of this frame coincides with the target's CoM (center of mass), the axis $\overrightarrow{\mathbf{X_l}}$ is in the direction $\overrightarrow{O_E O_t}$, the axis $\overrightarrow{\mathbf{Y_l}}$ is tangent to the orbit, orthogonal to $\overrightarrow{\mathbf{X_l}}$ and points in the same direction than the trajectory of the capture and the axis $\overrightarrow{\mathbf{Z_l}}$ completes.

iii) chaser's body frame $\mathcal{F}_b$: the center of this frame coincides with the chaser's CoM and it's axes are oriented in such a way that an attitude angle equal to $[0, 0, 0]^\intercal$ means that the chaser is aligned with the target along its velocity axis.

We use the notation $\boldsymbol{v}^{(i)}, \boldsymbol{v}^{(l)}, \boldsymbol{v}^{(b)}$ for a vector v given in the frame $\mathcal{F}_i, \mathcal{F}_l, \mathcal{F}_b$, respectively. However, the superscript $(i), (l), (b)$ is omitted when judged not necessary.

3.2 Modelling issues

Modelling the relative translational motion between the two spacecraft

Let (x_c, y_c, z_c) be the coordinates of the chaser's CoM, in $\mathcal{F}_i$. Then, the dynamics of the chaser's translational motion is described according to [Wie98, MG12]:

$$\dot{\mathbf{x}}_c^{(i)} = f\left(\mathbf{x}_c^{(i)}\right) + \begin{bmatrix} 0_3 \\ \mathbb{I}_3 \end{bmatrix} \left(\boldsymbol{\gamma}_u^{(i)} + \boldsymbol{\gamma}_{sl}^{(i)} + \boldsymbol{\gamma}_{sa}^{(i)} + \boldsymbol{\gamma}_{dc}^{(i)}\right) \tag{3.1}$$

In this equation $\mathbf{x}_c^{(i)} = [x_c\, y_c\, z_c\, \dot{x}_c\, \dot{y}_c\, \dot{z}_c]^\intercal$ is the state vector composed by the position and velocities of the chaser along each axis of $\mathcal{F}_i$ and $\boldsymbol{\gamma}_u^{(i)}, \boldsymbol{\gamma}_{sl}^{(i)}, \boldsymbol{\gamma}_{sa}^{(i)}, \boldsymbol{\gamma}_{dc}^{(i)}$ refer to the 3-dimensional accelerations due to the propulsion unit, propellant sloshing, flexible appendages and disturbances respectively.

Similarly, let (x_t, y_t, z_t) be the coordinates of the target's CoM in $\mathcal{F}_i$. Then, the dynamics of the target's translational motion can be described according to

$$\dot{\mathbf{x}}_t^{(i)} = f\left(\mathbf{x}_t^{(i)}\right) + \begin{bmatrix} 0_3 \\ \mathbb{I}_3 \end{bmatrix} \boldsymbol{\gamma}_{dt}^{(i)} \tag{3.2}$$

where $\mathbb{I}_3$ is the identity matrix in $\mathbb{R}^3$, $\mathbf{x}_t^{(i)} = [x_t\, y_t\, z_t\, \dot{x}_t\, \dot{y}_t\, \dot{z}_t]^\intercal$ is the state vector composed by the positions and velocities of the target. $\boldsymbol{\gamma}_{dt}^{(i)}$ refers to the disturbances (accelerations) about the target's CoM.

In Eq. (3.1) and (3.2), the nonlinear state dependent function $f\left(\mathbf{x}_j^{(i)}\right), j \in \{c, t\}$ is given by

$$f\left(\mathbf{x}_j^{(i)}\right) = \begin{bmatrix} \dot{x}_j \\ \dot{y}_j \\ \dot{z}_j \\ \frac{-\mu x_j}{\left(x_j^2+y_j^2+z_j^2\right)^{3/2}} \\ \frac{-\mu y_j}{\left(x_j^2+y_j^2+z_j^2\right)^{3/2}} \\ \frac{-\mu z_j}{\left(x_j^2+y_j^2+z_j^2\right)^{3/2}} \end{bmatrix} \quad j \in \{c, t\} \tag{3.3}$$

$\mu = Gm_E$ is the Earth gravitational constant where G and m_E are the universal gravitational constant and the mass of the Earth planet, respectively.

Subscribing Eq.(3.2) to Eq.(3.1) leads to the relative translational motion between the two spacecraft, given in $\mathcal{F}_i$. The result is a state space model that involves the relative position $\Delta\boldsymbol{x}^{(i)} = \boldsymbol{x}_c^{(i)} - \boldsymbol{x}_t^{(i)}$ and the relative velocities $\Delta\dot{\boldsymbol{x}}^{(i)} = \dot{\boldsymbol{x}}_c^{(i)} - \dot{\boldsymbol{x}}_t^{(i)}$.

Now, consider the rotation matrix $\mathcal{R}_i^{(l)}(a, e, i, \Omega, \omega, \nu)$ that performs the projection of a vector $\boldsymbol{v} \in \mathbb{R}^3$ from $\mathcal{F}_i$ to $\mathcal{F}_l$, see [MG12]. With the retained target orbital parameters (see section 3.1), it can be verified that $\mathcal{R}_i^{(l)}(a, e, i, \Omega, \omega, \nu)$ depends only on the semi-major axis a and the true anomaly ν, that is $\mathcal{R}_i^{(l)}(a, \nu)$. Applying the change of coordinates $\boldsymbol{\rho} = \mathcal{R}_i^{(l)}(a, \nu)\Delta\boldsymbol{x}^{(i)}$ (and therefore $\dot{\boldsymbol{\rho}} = \mathcal{R}_i^{(l)}(a, \nu)\Delta\dot{\boldsymbol{x}}^{(i)}$, it follows that the state space model that describes the dynamics of the relative translational motion between the two spacecrafts in $\mathcal{F}_l$, takes the form of (3.4) where $j = \{c, t\}$ and $g(.)$ is a function that depend nonlinearly on $\boldsymbol{\rho}, \dot{\boldsymbol{\rho}}, a, \nu, \boldsymbol{\gamma}_{dj}^{(i)}$.

$$\begin{bmatrix} \dot{\boldsymbol{\rho}} \\ \ddot{\boldsymbol{\rho}} \end{bmatrix} = g\left(\boldsymbol{\rho}, \dot{\boldsymbol{\rho}}, a, \nu, \boldsymbol{\gamma}_{dj}^{(i)}\right) + \begin{bmatrix} 0_3 \\ \mathbb{I}_3 \end{bmatrix} \left(\frac{1}{m}\boldsymbol{F}_u^{(l)} + \boldsymbol{\gamma}_{sl}^{(l)} + \boldsymbol{\gamma}_{sa}^{(l)}\right) \tag{3.4}$$

In Eq.(3.4), m is the total mass of the chaser's spacecraft, $\boldsymbol{F}_u^{(l)} = m\mathcal{R}_i^{(l)}(a,\nu)\boldsymbol{\gamma}_u^{(i)}$ is the three-dimensional forces due to the thruster-based propulsion unit, $\boldsymbol{\gamma}_{sl}^{(l)} = m\mathcal{R}_i^{(l)}(a,\nu)\boldsymbol{\gamma}_{sl}^{(i)}$ and $\boldsymbol{\gamma}_{sa}^{(l)} = m\mathcal{R}_i^{(l)}(a,\nu)\boldsymbol{\gamma}_{sa}^{(i)}$ are forces due to propellant sloshing and the flexible appendages respectively, given in $\mathcal{F}_l$.

Since the target follows a circular Keplerian orbit, the velocity of the true anomaly satisfies the third Kepler law, i.e.

$$\dot{\nu}^2 a^3 = \text{constant} = \mu = Gm_E \Rightarrow \dot{\nu} = \sqrt{\frac{\mu}{a^3}} = n \tag{3.5}$$

where $\mu = 3.9860 \times 10^{14}\,\mathrm{m}^3/\mathrm{s}^2$. Then, because the distance between the target and the chaser during the rendezvous is much smaller than the orbit, i.e., $||\rho||_2 \ll a$, it is possible to perform a first order Taylor approximation of (3.4). This leads to the so called Clohessy-Wiltshire equations, also named the Hill equations [Wie98, MG12]:

$$\begin{bmatrix}\dot{\rho}\\ \ddot{\rho}\end{bmatrix} = \begin{bmatrix} 0 & 0 & 0 & 1 & 0 & 0\\ 0 & 0 & 0 & 0 & 1 & 0\\ 0 & 0 & 0 & 0 & 0 & 1\\ 3n^2 & 0 & 0 & 0 & 2n & 0\\ 0 & 0 & 0 & -2n & 0 & 0\\ 0 & 0 & -n^2 & 0 & 0 & 0\end{bmatrix}\begin{bmatrix}\rho\\ \dot{\rho}\end{bmatrix} + \begin{bmatrix}0_3\\ \mathbb{I}_3\end{bmatrix}\left(\frac{1}{m}F_u^{(l)} + \boldsymbol{\gamma}_v^{(l)}\right) \tag{3.6}$$

In this equation, $\boldsymbol{\gamma}_v^{(l)}$ is a generalized disturbance acceleration which is an additive approximation of the effects that $\boldsymbol{\gamma}_{sl}^{(l)}, \boldsymbol{\gamma}_{sa}^{(l)}$ and $\boldsymbol{\gamma}_{dj}^{(l)} = \mathcal{R}_i^{(l)}(a,\nu)\boldsymbol{\gamma}_{dj}^{(i)}, j = \{c,t\}$ have on the dynamics of the relative position and relative velocity.

Remark 3. *It should be outlined that $\boldsymbol{\gamma}_{sl}^{(l)}, \boldsymbol{\gamma}_{sa}^{(l)}$ and $\boldsymbol{\gamma}_{dj}^{(i)}, j = \{c,t\}$ enter endogenously the state space model (3.4). So, approximating them into a form of a generalized exogenous signal $\boldsymbol{\gamma}_v^{(l)}$ must be valid. Especially such an approximation is valid if $\boldsymbol{\gamma}_{sl}^{(l)}, \boldsymbol{\gamma}_{sa}^{(l)}$ and $\gamma_{dj}^{(i)}, j = \{c,t\}$ do not destabilize the control loop that is developed later. Fortunately, this has been revealed to be the case, see the simulation results presented in Section 4.6, which are obtained from the functional engineering simulator that does not consider any kind of approximation.*

Modelling the attitude of the chaser's spacecraft

The rotational motion of the chaser caused by an applied moment (sum of all torques acting on it) can be derived from the Euler's second law in the body frame $\mathcal{F}_b$ according to:

$$\dot{\boldsymbol{\omega}} = \boldsymbol{J}^{-1}\sum_k \boldsymbol{T}_k - \boldsymbol{J}^{-1}\boldsymbol{\omega} \times \boldsymbol{J}\boldsymbol{\omega} \tag{3.7}$$

Here, $\boldsymbol{\omega}$ is the angular velocity vector and $\boldsymbol{J} \in \mathbb{R}^{3\times 3}$ is the inertia matrix of the chaser's spacecraft without considering the solar array. In (3.7), $\sum_k \boldsymbol{T}_k = \boldsymbol{T}_u + \boldsymbol{T}_{sl} + \boldsymbol{T}_{sa} + \boldsymbol{T}_d$ describes the sum of torques about the chaser's CoM, in $\mathcal{F}_b$. $\boldsymbol{T}_u$ refers to the moment caused by the thruster-based propulsion unit and $\boldsymbol{T}_{sl}, \boldsymbol{T}_{sa}, \boldsymbol{T}_d$ refer to the moment caused by propellant sloshing, the solar array and the exogenous disturbances.

Using the individual rotation matrices from Euler (3,2,1) rotation [Fon14], the relationship between the rotational velocities $\boldsymbol{\omega}$ and the rate of the Euler angles $\boldsymbol{\Theta} = \begin{bmatrix}\phi & \theta & \psi\end{bmatrix}^\intercal$ is given after by

$$\dot{\boldsymbol{\Theta}} = \frac{1}{\cos(\theta)}\begin{bmatrix}\cos(\theta) & \sin(\phi)\sin(\theta) & \cos(\phi)\sin(\theta)\\ 0 & \cos(\phi)\cos(\theta) & -\sin(\phi)\cos(\theta)\\ 0 & \sin(\phi) & \cos(\phi)\end{bmatrix}\boldsymbol{\omega} \tag{3.8}$$

Performing a first order Taylor approximation of Eqs. (3.7) and (3.8) around $\boldsymbol{\omega} = 0$ and $\boldsymbol{\Theta} = 0$, leads to the following linear state space model of the attitude of the chaser:

$$\begin{bmatrix} \dot{\boldsymbol{\Theta}} \\ \dot{\boldsymbol{\omega}} \end{bmatrix} = \begin{bmatrix} \mathbf{0}_3 & \mathbb{I}_3 \\ \mathbf{0}_3 & \mathbf{0}_3 \end{bmatrix} \begin{bmatrix} \boldsymbol{\Theta} \\ \boldsymbol{\omega} \end{bmatrix} + \begin{bmatrix} \mathbf{0}_3 \\ \boldsymbol{J}^{-1} \end{bmatrix} (\boldsymbol{T}_u^{(b)} + \boldsymbol{T}_v^{(b)}) \tag{3.9}$$

Here, $\boldsymbol{T}_v^{(b)}$ is a generalized disturbance moment (given in $\mathcal{F}_b$) which is an additive approximation of the effects that $\boldsymbol{T}_{sl}, \boldsymbol{T}_{sa}, \boldsymbol{T}_d$ have on the dynamics of the attitude and angular velocity.

Modelling the solar array

The dynamics of the solar array is modelled using the 2nd order vector-based equation:

$$\ddot{\overline{\boldsymbol{q}}} + 2\boldsymbol{\xi}\boldsymbol{\omega}_0\dot{\overline{\boldsymbol{q}}} + \boldsymbol{\omega}_0^2\overline{\boldsymbol{q}} = -\boldsymbol{L}^\intercal \begin{bmatrix} \boldsymbol{\gamma}_{tot}^{(b)} \\ \dot{\boldsymbol{\omega}} \end{bmatrix}, \quad \overline{\boldsymbol{q}} \in \mathbb{R}^{n_s.n_p} \tag{3.10}$$

$$\boldsymbol{L} = \begin{bmatrix} \overline{\boldsymbol{L}} \\ \underline{\boldsymbol{L}} \end{bmatrix}, \quad \overline{\boldsymbol{L}}, \underline{\boldsymbol{L}} \in \mathbb{R}^{3\times(n_s.n_p)} \tag{3.11}$$

In this equation, $\boldsymbol{\gamma}_{tot}^{(b)}$ is the total acceleration given in $\mathcal{F}_b$ (i.e. $\boldsymbol{\gamma}_{tot}^{(b)} = \boldsymbol{\gamma}_c^{(b)} + \boldsymbol{\gamma}_{sa}^{(b)} + \boldsymbol{\gamma}_u^{(b)}$), $n_s = 2$ is the number of flexible modes and $n_p = 1$ is the number of solar arrays, respectively. $\boldsymbol{\xi}$ and $\boldsymbol{\omega}_0$ are also matrices of adequate dimensions that correspond to the damping ratios and the frequencies of each flexible mode. The constant matrices $\overline{\boldsymbol{L}}, \underline{\boldsymbol{L}}$ are given by:

$$\overline{\boldsymbol{L}} = \mathcal{R}_{ap}^{(b)}(\alpha)\boldsymbol{B}_T, \quad \underline{\boldsymbol{L}} = \mathcal{R}_{ap}^{(b)}(\alpha)\boldsymbol{B}_R + \mathcal{S}(d)\mathcal{R}_{ap}^{(b)}(\alpha)\boldsymbol{B}_T \tag{3.12}$$

The matrices $\boldsymbol{B}_R$ and $\boldsymbol{B}_T$ are the flexible appendage participation factor matrices. The role of the rotation matrix $\mathcal{R}_{ap}^{(b)}(\alpha)$ where α is the appendage angle, is to transform $\boldsymbol{B}_R, \boldsymbol{B}_T$, given in the appendage frame, into the body frame. $\mathcal{S}(\boldsymbol{d})$ also denotes the skew-symmetric matrix of the vector $\boldsymbol{d} \in \mathbb{R}^3$, $\boldsymbol{d}$ being the distance vector between the chaser's CoM and the center of mass of the solar array.

In this work, since the focus is on the rendezvous, it is assumed that α is constant so that $\mathcal{R}(\alpha)$ is a constant matrix.

Then

$$\begin{bmatrix} \boldsymbol{F}_{sa}^{(b)} \\ \boldsymbol{T}_{sa}^{(b)} \end{bmatrix} = -\boldsymbol{L}\ddot{\overline{\boldsymbol{q}}} - \begin{bmatrix} m_{sa}\boldsymbol{\gamma}_{tot}^{(b)} \\ \boldsymbol{J}_{sa}\dot{\boldsymbol{\omega}} \end{bmatrix} \tag{3.13}$$

In this equation, m_{sa} denotes the mass of the solar array and the matrix $\boldsymbol{J}_{sa} \in \mathbb{R}^{3\times3}$ is the total inertia of the solar array. It corresponds to the sum of the nominal inertia $\boldsymbol{J}_0$ and the so-called transport inertia.

Let us consider the chaser's attitude dependent rotation matrix $\mathcal{R}_l^{(b)}(\boldsymbol{\Theta})$ that performs the projection from the LVLH frame $\mathcal{F}_l$ onto the chaser's body frame $\mathcal{F}_b$. Noting that

$$\boldsymbol{\gamma}_u^{(b)} = \frac{1}{m}\mathcal{R}_l^{(b)}(\boldsymbol{\Theta})\boldsymbol{F}_u^{(l)}, \quad \boldsymbol{\gamma}_c^{(b)} = \mathcal{R}_l^{(b)}(\boldsymbol{\Theta})\mathcal{R}_i^{(l)}(a,\nu)\boldsymbol{\gamma}_c^{(i)} \tag{3.14}$$

$$\boldsymbol{F}_{sa}^{(b)} = m\boldsymbol{\gamma}_{sa}^{(b)} \tag{3.15}$$

it follows:

$$\boldsymbol{F}_{sa}^{(b)} = -\frac{1}{1+\frac{m_{sa}}{m}}\left[\overline{\boldsymbol{L}}\ddot{\overline{\boldsymbol{q}}} + m_{sa}\left(\frac{1}{m}\mathcal{R}_l^{(b)}(\boldsymbol{\Theta})\boldsymbol{F}_u^{(l)} + \ \mathcal{R}_l^{(b)}(\boldsymbol{\Theta})\mathcal{R}_i^{(l)}(a,\nu)\boldsymbol{\gamma}_c^{(i)}\right)\right]$$

Finally, considering the rotation matrix $\mathcal{R}_b^{(l)}(\boldsymbol{\Theta})$ that performs the projection from the chaser's body frame $\mathcal{F}_b$ onto the LVLH frame $\mathcal{F}_l$, it follows:

$$\boldsymbol{F}_{sa}^{(l)} = \mathcal{R}_b^{(l)}(\boldsymbol{\Theta})\boldsymbol{F}_{sa}^{(b)} \tag{3.16}$$

Modelling the sloshing phenomena

Propellant sloshing in the tank is modelled in this work as a 3D spring-mass model. It is considered that the chaser has two half-full tanks. Thus, the moment $\boldsymbol{T}_{sl}^{(b)} = \sum_{i=1}^{2} \boldsymbol{T}_{sl_i}^{(b)}$ is deduced from the following mass-spring damper vector-based equation

$$\begin{aligned} &\ddot{\boldsymbol{x}}_s + \tfrac{\boldsymbol{l}_s}{m_s}\dot{\boldsymbol{x}}_s + \tfrac{\boldsymbol{k}_s}{m_s}\boldsymbol{x}_s = \overline{\boldsymbol{\gamma}}_t^{(b)}, \quad \boldsymbol{x}_s \in \mathbb{R}^3 \\ &\boldsymbol{T}_{sl}^{(b)} = \boldsymbol{r} \times (\boldsymbol{k}_s\boldsymbol{x}_s + \boldsymbol{l}_s\dot{\boldsymbol{x}}_s) \end{aligned} \tag{3.17}$$

In this equation, $\boldsymbol{l}_s$ and $\boldsymbol{k}_s$ are matrices of adequate dimension, defining the damping and stiffness coefficients. m_s is the sloshing mass and $\boldsymbol{r} \in \mathbb{R}^3$ is the distance vector between the chaser's CoM and the center of mass of the tank. $\overline{\boldsymbol{\gamma}}_t^{(b)}$ is the acceleration on the considered fuel tank which is defined according to $\overline{\boldsymbol{\gamma}}_t^{(b)} = \boldsymbol{\gamma}^{(b)} - \sum_k \boldsymbol{\gamma}_k^{(b)}$ where $\sum_k \boldsymbol{\gamma}_k^{(b)}$ describes the sum of the following accelerations:

- the Coriolis acceleration: $\boldsymbol{\gamma}_1^{(b)} = 2\boldsymbol{\omega} \times \dot{\boldsymbol{x}}_s$
- the centrifugal acceleration: $\boldsymbol{\gamma}_2^{(b)} = \boldsymbol{\omega} \times (\boldsymbol{\omega} \times (\boldsymbol{r} + \boldsymbol{x}_s))$
- the Euler acceleration: $\boldsymbol{\gamma}_3^{(b)} = \dot{\boldsymbol{\omega}} \times (\boldsymbol{r} + \boldsymbol{x}_s)$
- $\boldsymbol{\gamma}^{(b)}$ is the acceleration about the CoM of the chaser

Modelling the propulsion unit.

Let $\boldsymbol{u}_T$ be the command vector of the 12 thrusters. Then, the force $\boldsymbol{F}_u^{(l)}$ and moment $\boldsymbol{T}_u^{(b)}$ due to the thrusters are given by:

$$\begin{aligned} \boldsymbol{F}_u^{(l)} &= \mathcal{R}_b^{(l)}(\boldsymbol{\Theta})\boldsymbol{F}_u^{(b)} = \mathcal{R}_b^{(l)}(\boldsymbol{\Theta})[R_{f_1} \dots R_{f_{12}}]\boldsymbol{u}_T \\ &= \mathcal{R}_b^{(l)}(\boldsymbol{\Theta})\mathbf{R}_f\boldsymbol{u}_T \end{aligned} \tag{3.18}$$

$$\boldsymbol{T}_u^{(b)} = [R_{\tau_1} \dots R_{\tau_{12}}]\boldsymbol{u}_T = \mathbf{R}_\tau \boldsymbol{u}_T,\ \mathbf{R} = \begin{bmatrix} \mathbf{R}_\tau^\intercal\ \mathbf{R}_f^\intercal \end{bmatrix}^\intercal \tag{3.19}$$

The columns of $\mathbf{R}$ are the influence coefficients defining how each thruster affects each component of $\boldsymbol{F}_u^{(b)}$ and $\boldsymbol{T}_u^{(b)}$, respectively ($\mathbf{R}$ is the thruster configuration matrix).

3.3 Control Allocation

In (3.6) and (3.9), the control commands $\boldsymbol{F}_u^{(l)}, \boldsymbol{T}_u^{(b)}$ are given in terms of forces and torques. Let $\mathcal{S}_{all} = \{1, 2, \dots, 12\}$ denotes the set of all the thruster indices, and let $u_{ck}^{(b)}(t), \forall k \in \mathcal{S}_{all}$ be the commanded opening duration of the k-th thruster. Then, the control commands $\boldsymbol{F}_u^{(b)}, \boldsymbol{T}_u^{(b)}$ generated by thrusters are given by (fault free cases)

$$\begin{bmatrix} \boldsymbol{T}_u^{(b)}(t) \\ \boldsymbol{F}_u^{(b)}(t) \end{bmatrix} = \begin{bmatrix} \mathbf{R}_\tau \\ \mathbf{R}_f \end{bmatrix} \mathbf{u}_c^{(b)}(t) = \mathbf{R}\mathbf{u}_c^{(b)}(t), \quad \mathbf{R} \in \mathbb{R}^{6\times 12} \tag{3.20}$$

The columns of $\mathbf{R}$ (called the thruster configuration matrix) are the influence coefficients defining how each thruster commands $u_{ck}^{(b)}, \forall k \in \mathcal{S}_{all}$ affects each component of $\boldsymbol{T}_u^{(b)}$ and $\boldsymbol{F}_u^{(l)}$. Thus, from (3.20), it is clear that one can independently address the model either using the torque/force control inputs (in this case, equations (3.6) and (3.9) are directly used), or using the thruster commands (in this case, it is needed to consider (3.20)). Note that reversing (3.20) is known as a CA problem which consists in solving the following optimisation problem

$$\mathbf{u}_c^{(b)}(t) = \underset{\mathbf{u}_c^{(b)} \in \mathcal{U} = \{u_{ck}^{(b)} : 0 \le u_{ck}^{(b)} \le u_{kmax}\}, \forall k \in \mathcal{S}_{all}}{argmin} \left\| \mathbf{W}_v(\mathbf{R}\mathbf{u}_c^{(b)}(t) - \mathbf{v}_r) \right\|_p \tag{3.21}$$

where $\mathbf{v}_r$ is the vector of the desired force and torque commands and u_{kmax} is the maximum opening value of the kth thruster. Here it is equal to $u_{kmax} = 4N\,\forall k \in \mathcal{S}_{all}$. The nonsingular weighting matrix $\mathbf{W}_v$ affects the prioritization among force/torque components. The different choice of the vector p-norm results in i) minimum flow rate allocation for $p = 1$, minimum power allocation for $p = 2$ and iii) minimum peak torque/force allocation for $p = \infty$. Any algorithm that solves the optimisation problem stated by Eq. (3.21) is called a CA unit (known also as a thruster management unit), see Fig. 3.2 that illustrates the placement of the CA unit in a control loop.

Algorithm 1, whose foundations come from the nonlinear pseudo-inverse controller technique initially formulated by [JWD95], states the algorithm that solves (3.21). The algorithm terminates if the precision ϵ of the allocated torques/forces, weighted by W_v, is achieved (here $\epsilon = 10^{-10}$) or if the maximum number of iterations $N_{iter}^{max} = 350$ is reached. MIB stands for the Minimum Impulse Bit (minimum shooting time that a thruster can execute), $\lambda = 1.7$ allows to manage the convergence time and $M_k^{\ddagger}, k = 1, ..., 12$ stands for the generalized inverse of $M_k, k = 1, ..., 12$, optimal in the sense of the considered p-norm. The indices $k = 1, ..., 12$ coincide with the indices of (3.19).

Algorithm 1 Solution of (3.21)

Set $N_{iter} = 0$, $\mathbf{v} = \mathbf{v}_r$ and $\bar{M}_k = M$;
while $\|\mathbf{W}_v * error\|_1 > \epsilon$ AND $N_{iter} < N_{iter}^{max}$ **do**
  $\mathbf{v} = \mathbf{v} + \lambda * error$;
  $\mathbf{u}^{pc} = M_k^{\ddagger}\mathbf{v}$;
  $\mathbf{u}^{c} = (\mathbf{u}^{pc} + |\mathbf{u}^{pc}|)/2$;
  for $k = 1$ to 12 **do**
    if $u_k^c > \bar{u}_k$ **then** $u_k^c = \bar{u}_k$; **end if**
    if $u_k^c < MIB$ **then** $u_k^c = 0$; **end if**
  end for
  $error = \bar{\boldsymbol{M}}_i \boldsymbol{u}^c - \boldsymbol{v}_r$; $N_{iter} = N_{iter} + 1$;
end while
Set $\boldsymbol{u} = \boldsymbol{u}^c$;

3.4 Sliding Mode Control in a Backstepping Setup

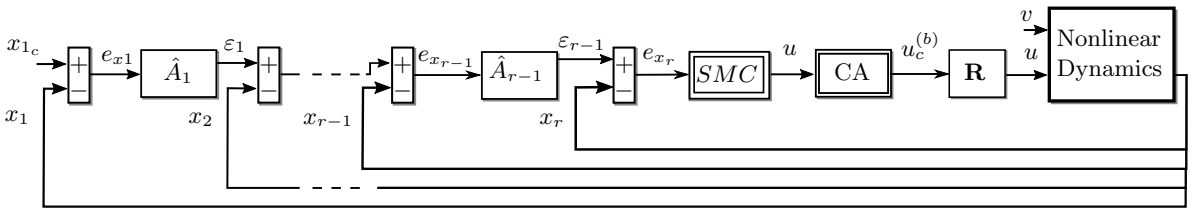

Figure 3.2: Backstepping and Sliding Mode Control Setup

Consider the following block-controllable form of a system's model, composed into r connected sub-systems [DILU90]:

$$\dot{x}_1 = A_1 x_1 + B_1 x_2 \tag{3.22}$$
$$\dot{x}_i = A_i \overline{x}_i + B_i x_{i+1} \tag{3.23}$$
$$\dot{x}_r = A_r \overline{x}_r + B_r (u + v) \tag{3.24}$$

for $i = \overline{2, r-1}$. Here $x = [x_1^\intercal, x_2^\intercal, \ldots, x_r^\intercal]^\intercal \in \mathbb{R}^n$, $u \in \mathbb{R}^m$ and $v \in \mathbb{R}^m$ refer to the system's state, control input and (matched) disturbance vectors respectively. $\overline{x}_i$ is defined by $\overline{x}_i = [x_1^\intercal, x_2^\intercal, \ldots, x_i^\intercal]^\intercal, x_i \in \mathbb{R}^{n_i}$ so that $n_i = \text{rank}(B_i)$, $\sum_{i=1}^{r} n_i = n$. The sub-system (3.22)-(3.23) for

$i = \overline{2, r-1}$ represents the sub-actuated dynamics and (3.24) corresponds to the actuated dynamics. Thus, $x_r \in \mathbb{R}^m$. The matrices A_i, B_i are of adequate dimension.

The goal is to design the state feedback sliding mode control law that obeys to a backstepping paradigm so that $x_1(t)$ follows an *a priori* given trajectory $x_{1c}(t)$, $\forall t \geq 0$.

Assumption 1. *Let $v \in \mathbb{R}^m$. The component v_j are bounded, i.e. $|v_j| \leq v_{0j}^+$ and the component of $\dot{v}_j$ are bounded, i.e. $|\dot{v}_j| \leq v_{1j}^+, j = \overline{1, m}$.*

Assumption 2. *The time derivatives of x_{1c} up to order $r-1$ are assumed to be bounded and available.*

Assumption 1 is required for the existence of the super-twisting control technique, see Eq. (3.35). For small values of r, assumption 2 is reasonable from a practical point of view since the successive time derivatives of $x_{1c}(t)$ are generally endogenous signals in a trajectory planing algorithm. Furthermore, sliding mode-based differentiation techniques can be used for estimating the derivatives up to $r-1$, see Section 2.5.5.

The backstepping philosophy consists in computing the internal signals $\varepsilon_i, i = \overline{1, r-1}$ in $r-1$ steps and used $x_{i+1}, i = \overline{1, r-1}$ as virtual controls. Then, at the r^{th} step, the control law is conceived such that the state trajectories reach the sliding surface and remain there. A FOSMC and a STA are used for that purpose. The main goal of employing two sliding mode control techniques is to illustrate the differences in performance between each method. In the following, the case for the FOSMC is firstly explained followed by the STA case.

3.4.1 First Order Sliding Mode Controller in a Backstepping setup

The overall controller design procedure can be described in a general form with the following steps:

Step 1. Define the tracking error according to $e_{x_1} = x_{1c} - x_1$. Then, as it is suggested by Eq. (3.22), x_2 is used as a virtual control so that $x_2 := \varepsilon_1$ where

$$\varepsilon_1 = B_1^{\dagger}(\dot{x}_{1c} - A_1 x_1 - \hat{A}_1 e_{x_1}) \tag{3.25}$$

where $\hat{A}_1 < 0$ contains the desired convergence performance of x_1 towards x_{1c}. Notice that since $rank(B_i) = n_i$, then $B_i B_i^{\intercal}$ is invertible, thus $B_i^{\dagger} = B_i^{\intercal}(B_i B_i^{\intercal})^{-1}$ is the right inverse matrix of B_i.

Step i, $\mathbf{i = \overline{2, r-1}}$. Define the error as $e_{x_i} = \varepsilon_{i-1} - x_i$ and the virtual control according to:

$$\varepsilon_i = B_i^{\dagger}(\dot{\varepsilon}_{i-1} - A_i \bar{x}_i - \hat{A}_i e_{x_i} + B_{i-1}^{\intercal} e_{x_{i-1}}) \tag{3.26}$$

where $\hat{A}_i < 0$, $i = \overline{2, r-1}$.

Step r. With the sliding surface defined by $e_{x_r} = \varepsilon_{r-1} - x_r$, the control law is given by:

$$u = \underbrace{B_r^{\dagger}(\dot{\varepsilon}_{r-1} - A_r \bar{x}_r + B_{r-1}^{\intercal} e_{x_{r-1}})}_{u_l} - u_n \tag{3.27}$$

$u_n \in \mathbb{R}^m$ is the sliding mode controller. For the FOSMC, it is defined as follows:

$$u_n = \alpha \, \text{sign}(e_{x_r}) \tag{3.28}$$

where the constraints for the selection of α are further analyzed, see Eq.(3.29). The process to obtain the generalized equations (3.25)-(3.27) is exemplified for a system with $r = 3$, in the Appendix section A.2

Assumption 3. *The components of* $B_{r-1}^{\intercal}\dot{e}_{x_{r-1}}$ *are bounded*

The following theorem solves the control design problem:

Theorem 1. *Consider the system* (3.22)-(3.24)*, whose control signal is designed following the procedure shown in* (3.25)-(3.28)*. The closed loop system is stable and the controller* (3.27) *tracks the reference signal* x_{1c} *while annihilating* v *in finite-time.*

Proof. The proof is conducted in two stages: First, the convergence of the trajectories to the sliding surface $e_{x_r} = 0$ is shown. Then, a Lyapunov function is designed to demonstrate the convergence of the sub-actuated dynamics.

To proceed, the convergence of the individual components of the sliding surface e_{x_r} to zero is demonstrated. Based on the definition of $e_{x_r} = \varepsilon_{r-1} - x_r$, and by applying the control law (3.28), its derivative is defined as follows:

$$\begin{aligned}
\dot{e}_{x_r} &= \dot{\varepsilon}_{r-1} - \dot{x}_r = \dot{\varepsilon}_{r-1} - A_r\bar{x}_r - B_r(u+v) \\
&= \dot{\varepsilon}_{r-1} - A_r\bar{x}_r - B_r\left[B_r^{\dagger}\left(\dot{\varepsilon}_{r-1} - A_r\bar{x}_r + B_{r-1}^{\intercal}e_{x_{r-1}}\right) - u_n + v\right] \\
&= \dot{\varepsilon}_{r-1} - A_r\bar{x}_r - \dot{\varepsilon}_{r-1} + A_r\bar{x}_r - B_{r-1}^{\intercal}e_{x_{r-1}} + B_r(u_n - v) \\
&= -B_{r-1}^{\intercal}e_{x_{r-1}} + B_r(u_n - v) = -B_{r-1}^{\intercal}e_{x_{r-1}} + B_r(\alpha\,\mathrm{sign}(e_{x_r}) - v) \\
&= B_r\alpha\,\mathrm{sign}(e_{x_r}) + \delta_j
\end{aligned} \tag{3.29}$$

with $j = \overline{1,m}$, which represents the components of the vector $\delta_j = -B_{r-1}^{\intercal}e_{x_{r-1}} - B_r v$. From Assumptions 1 and 3, the term $\dot{\delta} = -B_{r-1}^{\intercal}\dot{e}_{x_{r-1}} - B_r\dot{v}$ is bounded. This means that there is a constant $\tilde{\delta}_j$ that $|\dot{\delta}_j| \leq |(B_{r-1}^{\intercal}\dot{e}_{x_{r-1}})_j| + |B_r|v_{1_j}^{+} \leq \tilde{\delta}_j, j = \overline{1,m}$. Then, the system can be stabilized if the gain $\alpha > \tilde{\delta}$, achieving $e_{x_r} = 0$ in finite-time and thus $x_r = \varepsilon_{r-1}$ in finite time.

To proof the convergence of the sub-actuated dynamics, the following Lyapunov function is employed:

$$V = \frac{1}{2}e_{x_1}^{\intercal}e_{x_1} + \ldots + \frac{1}{2}e_{x_r}^{\intercal}e_{x_r} \tag{3.30}$$

Its derivative is defined as

$$\dot{V} = e_{x_1}^{\intercal}\dot{e}_{x_1} + \ldots + e_{x_r}^{\intercal}\dot{e}_{x_r} \tag{3.31}$$

with the expression of $\dot{e}_{x_i}, i = \overline{1,r}$ stated in the above developments, equations (3.22)-(3.24) and the control law u given by (3.27), it can be verified that

$$\dot{V} = \sum_{k=1}^{r-1} e_{x_k}^{\intercal}\hat{A}_k e_{x_k} + e_{x_r}^{\intercal}B_r(u_n - v) \tag{3.32}$$

Due to $e_{x_r} = 0$, the time derivative of V yields to $\dot{V} = \sum_{k=1}^{r-1} e_{x_k}^{\intercal}\hat{A}_k e_{x_k}$. Since $\hat{A}_k < 0, k = \overline{1,r-1}$, it follows that $\dot{V} < 0$ (sufficient condition) and thus that the proposed control law is asymptotically stable. Consequently, $x_i \to \varepsilon_{i-1}, i = \overline{2,r-1}$. Therefore $x_1 \to x_{1c}$, achieving tracking of the trajectory $x_{1c}(t)$ asymptotically.

□

Remark 4. *Tuning* $\hat{A}_k, k = \overline{1,r-1}$ *enables to manage the convergence time of* $x_i(t)$ *to* $\varepsilon_{i-1}(t), i = \overline{2,r-1}$ *and* $x_1(t)$ *to* $x_{1c}(t)$*. Therefore, the convergence time of* $e_{x_{r-1}}$ *(and thus* $\dot{e}_{x_{r-1}}$*) to zero can be reduced if* $\hat{A}_{r-1}$ *has small eigenvalues (fast dynamics). This may lead the terms* $\left|(B_{r-1}^{\intercal}\dot{e}_{x_{r-1}})_j\right|$ *negligible in front of* v_{1j}^{+}*,* $j = \overline{1,m}$*. A consequence is that, practically, the constants* $\tilde{\delta}_j$ *can be chosen as over approximated upper bounds of* v_{1j}^{+}*,* $j = \overline{1,m}$*. In other words, the knowledge of*

$\left|(B_{r-1}^{\intercal}\dot{e}_{x_{r-1}})_j\right|$, $j=\overline{1,m}$ *is not required.*

Furthermore, since the finite-time convergence of the last step, i.e. $e_{x_r}=0$*, is first proved and then used to prove asymptotic convergence of the controller, it is natural to ask about the transient behaviour of other* $e_{x_k}, k=\overline{1,r-1}$*, especially to guarantee the boundedness of the tracking error. This can be managed adequately through the adequate choice of* $\hat{A}_k, k=\overline{1,r-1}$*.*

3.4.2 Super-Twisting Control in a Backstepping setup

In this section, a STA is designed to be the part of the controller in charge of compensating the disturbances. It is defined as u_n, and it is expressed as:

$$u_n = K_1\Psi_1 + K_2\int_{t_0}^{t}\Psi_2 dt \tag{3.33}$$

with the matrices $K_1=\text{diag}(k_{11},\dots k_{1m})$, $K_2=\text{diag}(k_{21},\dots k_{2m})$, $\Psi_1=\text{diag}(\Psi_{11},\dots,\Psi_{1m})$ and $\Psi_2=\text{diag}(\Psi_{21},\dots,\Psi_{2m})$, where

$$\Psi_{1j}=|e_{x_{r_j}}|^{\frac{1}{2}}\,\text{sign}(e_{x_{r_j}}),\ \Psi_{2j}=\text{sign}(e_{x_{r_j}}), j=\overline{1,m} \tag{3.34}$$

and where the components of the matrices gains K_1 and K_2 satisfy

$$k_{2j}>\tilde{\delta}_j,\quad k_{1j}>\sqrt{k_{2j}+\tilde{\delta}_j},\quad j=\overline{1,m} \tag{3.35}$$

where the constants $\tilde{\delta}_j, j=\overline{1,m}$ are defined later.

Theorem 2. *Consider the system in Eqs.(3.22)-(3.24) whose control signal is designed according to Eq.(3.27) with the expression in Eq.(3.33). The closed loop system is stable and the controller (3.27) tracks the reference signal* x_{1c} *while annihilating* v *in finite-time.*

Proof. Following the procedure of the proof of Theorem 1, one can start by differentiating e_{x_r} and applying the control law (3.27), then the derivative of the error is defined as:

$$\dot{e}_{x_{r_j}}=B_r\left(-k_{1j}\Psi_{1j}-k_{2j}\int_{t_0}^{t}\Psi_{2j}dt\right)+\delta_j \tag{3.36}$$

with $j=\overline{1,m}$. δ_j represents the components of the vector $\delta=-B_{r-1}^{\intercal}e_{x_{r-1}}-B_r v$. Defining $\mu_j=B_r\left(-k_{2j}\int_{t_0}^{t}\Psi_{2j}dt\right)+\delta_j$ yields to

$$\dot{e}_{x_{r_j}}=B_r\left(-k_{1j}\Psi_{1j}\right)+\mu_j,\quad \dot{\mu}_j=B_r\left(-k_{2j}\Psi_{2j}\right)+\dot{\delta}_j \tag{3.37}$$

with $\dot{\delta}=-B_{r-1}^{\intercal}\dot{e}_{x_{r-1}}-B_r\dot{v}$ which under Assumptions 1 and 3 is bounded, i.e. there exist constants $\tilde{\delta}_j$ such that $|\dot{\delta}_j|\leq\left|(B_{r-1}^{\intercal}\dot{e}_{x_{r-1}})_j\right|+|B_r|v_{1j}^{+}\leq\tilde{\delta}_j$, $j=\overline{1,m}$. Then, it was shown in [SH17] that the auxiliary system (3.37) can be stabilized by selecting the gains k_{1j} and k_{2j} as in (3.35), achieving $e_{x_r}=0$ in finite time, therefore $x_r\equiv\varepsilon_{r-1}$ in finite time. □

The second part of the proof consists of demonstrating the convergence of the sub-actuated dynamics. As shown in the previous section, this is accomplished by using the Lyapunov function defined in Eq.(3.30). The difference from the previous procedure is that u_n is defined as in Eq.(3.33).

3.5 Derivation of the control law parameters

Two separate control laws, for attitude tracking and relative position tracking, are derived. Their design is based on the procedure explained in Sections 3.4.1 and 3.4.2. It is applied to the linearized model expressed in (3.6) and (3.9). The control inputs and matched disturbances are defined according to:

- $u = \frac{1}{m}F_u^{(l)}, B_r = \mathbb{I}_3$ and $v = \gamma_v^{(l)}$ in the case of (3.6),
- $u = T_u^{(b)}, B_r = J^{-1}$ and $v = T_v^{(b)}$ in the case of (3.9),

then, (3.6) and (3.9) are of the form (3.22)-(3.24) with $r = 2$, where:

- $x_1 = \rho, x_r = x_2 = \dot{\rho}$ in the case of the model (3.6),
- $x_1 = \Theta, x_r = x_2 = \omega$ in the case of the model (3.9).

Furthermore, since the LIDAR provides the measurement of the states $x_1 = \rho$ and $x_2 = \dot{\rho}$ in the case of the model (3.6), the Star Tracker provides the measurement of the state $x_1 = \Theta$ and the IMU provides the measurement of the state $x_2 = \omega$ in the case of the model (3.9), then the problem's formulation obeys to the one stated in Section 3.4. By using the functional engineering simulator, numerical values for bounds $v_{1j}^+, j = \overline{1,3}$ (see Assumption 1) are estimated: *relative position loop:* $v_1^+ = (0.0565,\ 0.0198,\ 0.0302)$, *attitude loop:* $v_1^+ = (0.0240,\ 0.0023,\ 0.0368)$.

3.5.1 First Order Sliding Mode Controller

In the following, the controller for position tracking is developed with the objective of serving as an example of the design process. It is based on the linearized model (3.6), which is first rewritten in the following form:

$$\begin{bmatrix}\dot{x}_1\\ \dot{x}_2\end{bmatrix} = \left[\begin{array}{ccc:ccc} 0 & 0 & 0 & 1 & 0 & 0\\ 0 & 0 & 0 & 0 & 1 & 0\\ 0 & 0 & 0 & 0 & 0 & 1\\ \hdashline 3n^2 & 0 & 0 & 0 & 2n & 0\\ 0 & 0 & 0 & -2n & 0 & 0\\ 0 & 0 & -n^2 & 0 & 0 & 0 \end{array}\right] \begin{bmatrix}x_1\\ x_2\end{bmatrix} + \begin{bmatrix}0_3\\ \mathbb{I}_3\end{bmatrix}(u+v) = \left[\begin{array}{c:c} A_{11} & A_{12}\\ \hdashline A_{21} & A_{22}\end{array}\right] \begin{bmatrix}x_1\\ x_2\end{bmatrix} + \begin{bmatrix}0_3\\ \mathbb{I}_3\end{bmatrix}(u+v) \tag{3.38}$$

According to the procedure explained in Section 3.4.1, one begins with the definition of the error $e_{x_1} = x_{1_c} - x_1$. Its derivative is expressed as:

$$\dot{e}_{x_1} = \dot{x}_{1_c} - \dot{x}_1 = \dot{x}_{1_c} - A_{11}x_1 - A_{12}x_2 \tag{3.39}$$

Then, given that x_2 is used as a virtual controller, $x_2 := \varepsilon_1$:

$$\varepsilon_1 = (A_{12})^+ \left(\dot{x}_{1_c} - A_{11}x_1 - \hat{A}_1 e_{x_1}\right) \tag{3.40}$$

Finally, the control law is defined as:

$$u = \dot{\varepsilon}_1 - A_{21}x_1 - A_{22}x_2 + (A_{12})^\intercal e_{x_1} - u_n \tag{3.41}$$

where u_n is defined in (3.28) with the sliding surface $e_{x_2} = \varepsilon_1 - x_2$. The convergence of the sliding surface is demonstrated as follows:

$$\begin{aligned}\dot{e}_{x_2} &= \dot{\varepsilon}_1 - \dot{x}_2 = \dot{\varepsilon}_1 - A_{21}x_1 - A_{22}x_2 - u - v\\ &= \dot{\varepsilon}_1 - A_{21}x_1 - A_{22}x_2 + \dot{\varepsilon}_1 + A_{21}x_1 + A_{22}x_2 - (A_{12})^\intercal e_{x_1} + u_n - v\\ &= -(A_{12})^\intercal e_{x_1} + u_n - v = -(A_{12})^\intercal e_{x_1} + \alpha\,\mathrm{sign}(e_{x_2}) - v\\ &= \alpha\,\mathrm{sign}(e_{x_2}) + \delta\end{aligned} \tag{3.42}$$

with $\delta = -(A_{12})^\intercal e_{x_1} - v$. To guarantee a sliding motion, α is selected according to (3.29). The proof of the convergence of the sub-actuated dynamics is analyzed by employing a Lyapunov function as described in (3.30):

$$V = V_1 + V_2 = \frac{1}{2} e_{x_1}^\intercal e_{x_1} + \frac{1}{2} e_{x_2}^\intercal e_{x_2} \tag{3.43}$$

First, the derivative of V_1 is obtained by considering $x_2 = \varepsilon_1 - e_{x_2}$, which is obtained from the definition of e_{x_2}. It follows:

$$\begin{aligned} \dot{V}_1 &= e_{x_1}^\intercal \dot{e}_{x_1} = e_{x_1}^\intercal \left(\dot{x}_{1_c} - A_{11}x_1 - A_{12}x_2\right) = e_{x_1}^\intercal \left(\dot{x}_{1_c} - A_{11}x_1 - A_{12}\left[\varepsilon_1 - e_{x_2}\right]\right) \\ &= e_{x_1}^\intercal \left(\dot{x}_{1_c} - A_{11}x_1 - A_{12}\left[(A_{12})^+ \left(\dot{x}_{1_c} - A_{11}x_1 - \hat{A}_1 e_{x_1}\right) - e_{x_2}\right]\right) \\ &= e_{x_1}^\intercal \hat{A}_1 e_{x_1} + e_{x_1}^\intercal A_{12} e_{x_2} \end{aligned} \tag{3.44}$$

where the definition of $\dot{e}_{x_1}$ is obtained from (3.39). The derivative of V_2 is then obtained as:

$$\dot{V}_2 = e_{x_2}^\intercal \dot{e}_{x_2} = e_{x_2}^\intercal \left[\alpha \operatorname{sign}(e_{x_2}) + \delta\right] = e_{x_2}^\intercal \left[\alpha \operatorname{sign}(e_{x_2}) - (A_{12})^\intercal e_{x_1} - v\right] \tag{3.45}$$

where the definition of $\dot{e}_{x_2}$ is obtained from (3.42). Then, by employing the results obtained in (3.44) and (3.45), the total derivative of V is expressed as:

$$\dot{V} = \dot{V}_1 + \dot{V}_2 = e_{x_1}^\intercal \hat{A}_1 e_{x_1} + e_{x_1}^\intercal A_{12} e_{x_2} + e_{x_2}^\intercal \left[\alpha \operatorname{sign}(e_{x_2}) - (A_{12})^\intercal e_{x_1} - v\right] \tag{3.46}$$

by using the following property $e_{x_2}^\intercal A_{12}^\intercal e_{x_1} = e_{x_1}^\intercal A_{12} e_{x_2}$, it follows:

$$\begin{aligned} \dot{V} &= e_{x_1}^\intercal \hat{A}_1 e_{x_1} + e_{x_1}^\intercal A_{12} e_{x_2} - e_{x_1}^\intercal A_{12} e_{x_2} + e_{x_2}^\intercal \left[\alpha \operatorname{sign}(e_{x_2}) - v\right] \\ &= e_{x_1}^\intercal \hat{A}_1 e_{x_1} + e_{x_2}^\intercal \left[\alpha \operatorname{sign}(e_{x_2}) - v\right] \end{aligned} \tag{3.47}$$

The convergence of e_{x_1} is guaranteed according to Remark 4. Same procedure is applied for the design of the control for attitude tracking by using the model described in (3.9). The interested reader can find the exemplified design process for the case $r = 3$ in the Appendix, Section A.2.

For the simulation, the gains were selected based on Remark 4. The backstepping gain is chosen as $\hat{A}_1 = -\mathbb{I}_3$ for both, the attitude and relative position loop. With respect to the sliding gain α, it must be chosen so that its value is chosen high enough to enforce the sliding motion. This leads to $\alpha = 0.25\mathbb{I}_3$ for the attitude loop and $\alpha = 0.08\mathbb{I}_3$ for the relative position loop.

3.5.2 Super-Twisting Sliding Mode Controller

The design procedure for both control laws, attitude and translation, is similar to the one employed for the FOSMC case. Take for instance the fact that equations (3.39)-(3.41) are equally defined for the STA. The main difference relies on the definition employed for u_n, which is based on (3.33). Consequently, the convergence proofs are different as shown in the following.

The sliding surface employed is the same as for the FOSMC case, i.e. $e_{x_2} = \varepsilon_1 - x_2$. Its convergence is demonstrated based on its derivative as

$$\begin{aligned} \dot{e}_{x_2} &= \dot{\varepsilon}_1 - \dot{x}_2 = \dot{\varepsilon}_1 - A_{21}x_1 - A_{22}x_2 - u - v \\ &= \dot{\varepsilon}_1 - A_{21}x_1 - A_{22}x_2 + \dot{\varepsilon}_1 + A_{21}x_1 + A_{22}x_2 - (A_{12})^\intercal e_{x_1} + u_n - v \\ &= -(A_{12})^\intercal e_{x_1} + u_n - v = -(A_{12})^\intercal e_{x_1} + K_1\Psi_1 + K_2 \int_{t_0}^{t} \Psi_2 dt - v \\ &= K_1\Psi_1 + K_2 \int_{t_0}^{t} \Psi_2 dt + \delta \end{aligned} \tag{3.48}$$

with $\delta = -(A_{12})^{\intercal} e_{x_1} - v$. The gains are selected according to (3.35) and Remark 4. The convergence of the sub-actuated dynamics, employs the Lyapunov function expressed in (3.43). The derivative of V_1 is defined as in (3.44), while the derivative of V_2 is defined as

$$\dot{V}_2 = e_{x_2}^{\intercal} \dot{e}_{x_2} = e_{x_2}^{\intercal} \left[K_1 \Psi_1 + K_2 \int_{t_0}^{t} \Psi_2 dt + \delta \right] = e_{x_2}^{\intercal} \left[-(A_{12})^{\intercal} e_{x_1} + K_1 \Psi_1 + K_2 \int_{t_0}^{t} \Psi_2 dt - v \right] \quad (3.49)$$

Then, by employing (3.44) and (3.49), the derivative of V is expressed as:

$$\begin{aligned} \dot{V} &= e_{x_1}^{\intercal} \hat{A}_1 e_{x_1} + x_1{}^{\intercal} A_{12} e_{x_2} + e_{x_2}^{\intercal} \left[-(A_{12})^{\intercal} e_{x_1} + K_1 \Psi_1 + K_2 \int_{t_0}^{t} \Psi_2 dt - v \right] \\ &= e_{x_1}^{\intercal} \hat{A}_1 e_{x_1} + e_{x_1}^{\intercal} A_{12} e_{x_2} - e_{x_1}^{\intercal} A_{12} e_{x_2} + e_{x_2}^{\intercal} \left[-(A_{12})^{\intercal} e_{x_1} + K_1 \Psi_1 + K_2 \int_{t_0}^{t} \Psi_2 dt - v \right] \\ &= e_{x_1}^{\intercal} \hat{A}_1 e_{x_1} + e_{x_1}^{\intercal} A_{12} e_{x_2} + e_{x_2}^{\intercal} \left[-(A_{12})^{\intercal} e_{x_1} + K_1 \Psi_1 + K_2 \int_{t_0}^{t} \Psi_2 dt - v \right] \\ &= e_{x_1}^{\intercal} \hat{A}_1 e_{x_1} + e_{x_2}^{\intercal} \left[+K_1 \Psi_1 + K_2 \int_{t_0}^{t} \Psi_2 dt - v \right] \end{aligned} \quad (3.50)$$

Similar to the FOSMC, the convergence of e_{x_1} is guaranteed by Remark 4. For the simulation, three parameters have to be chosen for each control law, namely $\hat{A}_1$ (which enforces the tracking dynamics) and K_1, K_2 according to (3.35) (to ensure stability of the super-twisting algorithm). The following values have been chosen for $\hat{A}_1$: *relative position loop:* $\hat{A}_1 = -\mathbb{I}_3$, *attitude loop:* $\hat{A}_1 = -100\mathbb{I}_3$. K_1 and K_2 are then designed following remark 2: *relative position loop:* $K_1 = diag(0.34, 0.2, 0.25)$; $K_2 = diag(0.057, 0.02, 0.031)$, *attitude loop:* $K_1 = diag(0.22, 0.068, 0.28)$; $K_2 = diag(0.025,\ 0.0024, 0.037)$.

3.6 Simulation results

The performance of the designed SMC control laws is finally assessed using the functional engineering simulator. It has a CA unit which is in charge of distributing the control signal into the thrusters. Its operating principle follows the description in (3.21). In addition, it has a path planning (guidance) algorithm implemented which is in charge of generating the position/velocity and attitude/angular velocity profiles for the target acquisition, rendezvous and capture phases. Here, it is based on a spline-based approach to generate smooth profiles in order to approach the target along its velocity axis smoothly. It is worth noting that the simulator considers the nonlinear models and their coupling effects, the second-order zonal harmonic J_2, atmospheric drag, gravity gradient, magnetic disturbances, propellant sloshing and the flexible modes of the solar array. In addition, the navigation unit is assumed to be perfect, i.e. no measurement noise is considered.

The investigated scenario used the following parameters:

- Chaser's mass $m = 300\,\text{kg}$
- Chaser's inertia $J = [30, 1, 1; 1, 40, 1; 1, 1, 25]$
- Thruster's saturation= 4 N, Minimum Impulse Bit = 0.1
- Thruster configuration and geometry of the chaser (including the location of its CoM) as shown in figure 3.3.
- Sampling time= 0.25 s

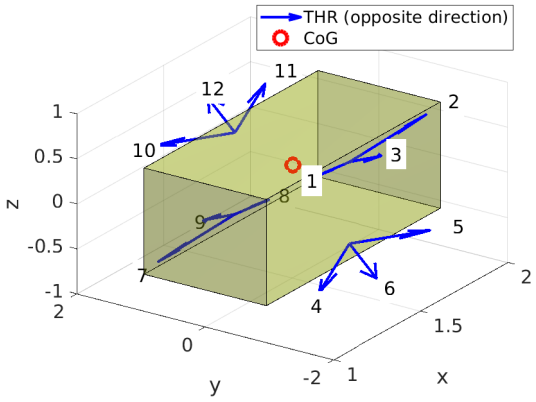

Figure 3.3: Thruster configuration and geometry of the chaser (including the location of its CoM)

3.6.1 First Order Sliding Mode Control

In this section, the response of the system, when employing FOSMC, is analyzed. In Fig. 3.4 (left column), the attitude tracking and the reference signal are shown. The position tracking and the reference signal are illustrated in the right column. It can be seen that the states follows the reference trajectories. Figure 3.5 presents the behaviour of the angular (left column) and translational velocities (right column). Angular velocities present a more visible "chattering" effect than the translational velocities. However, this oscillation stays close to zero. The control signals computed by the FOSMC are shown on the upper part of Figure 3.6, where the chattering effect is visible. In the lower part of Figure 3.6, the tracking errors of attitude and position are shown. It can be seen that the attitude error oscillates around zero. In the position error graphic, a small drift on the error as well as its recovery, are visible. As mentioned before, the control signals are distributed to the thrusters by the CA unit. These distributed signals, are shown on Figure 3.7 for each thruster. As seen in this figure, the thrusters are not saturated.

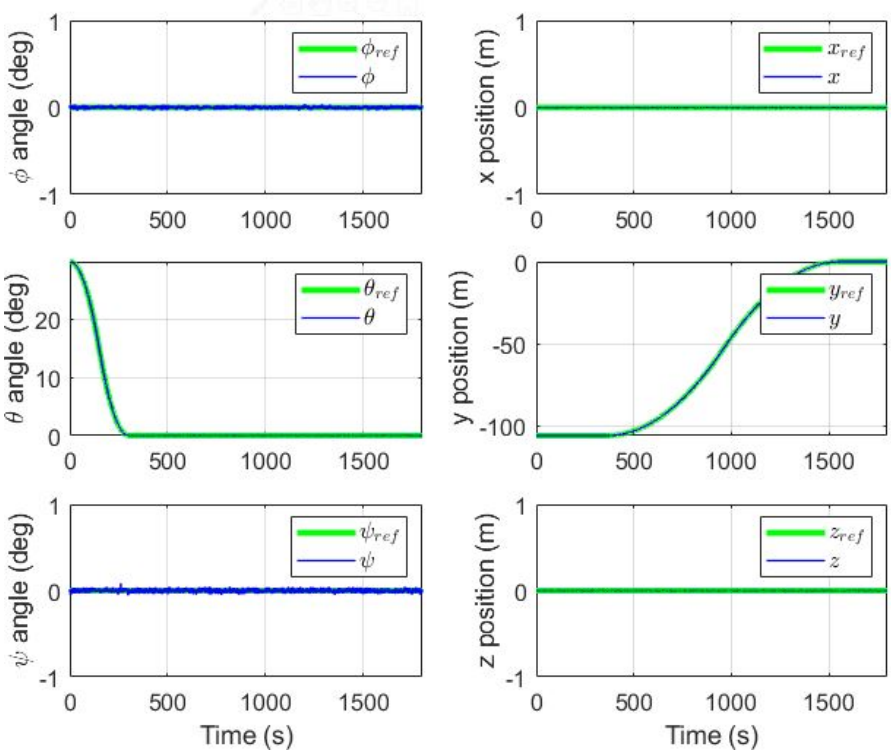

Figure 3.4: Positions and Angles with FOSMC

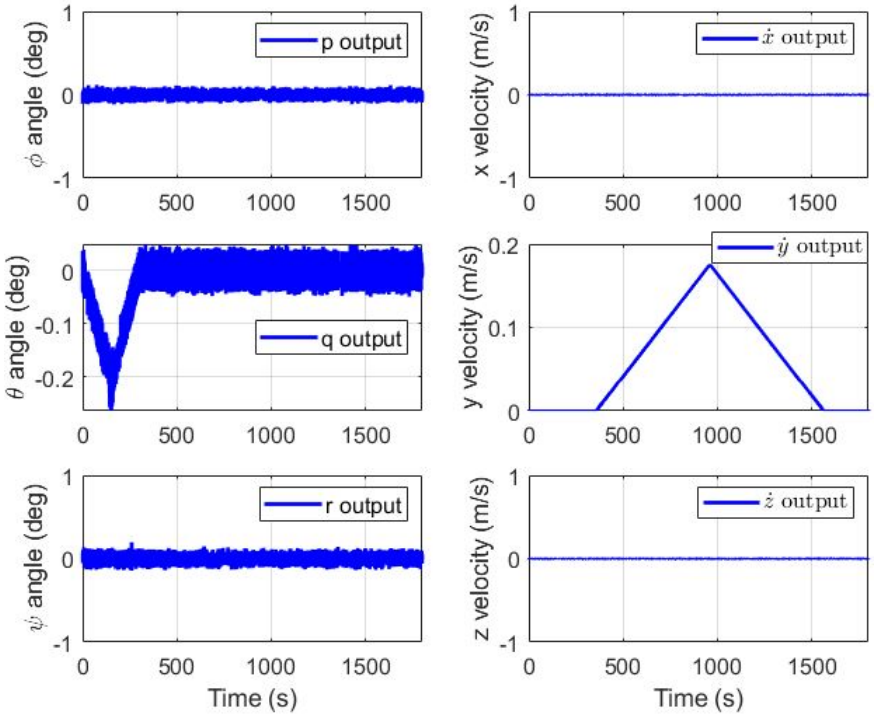

Figure 3.5: Angular and Transitional velocities with FOSMC

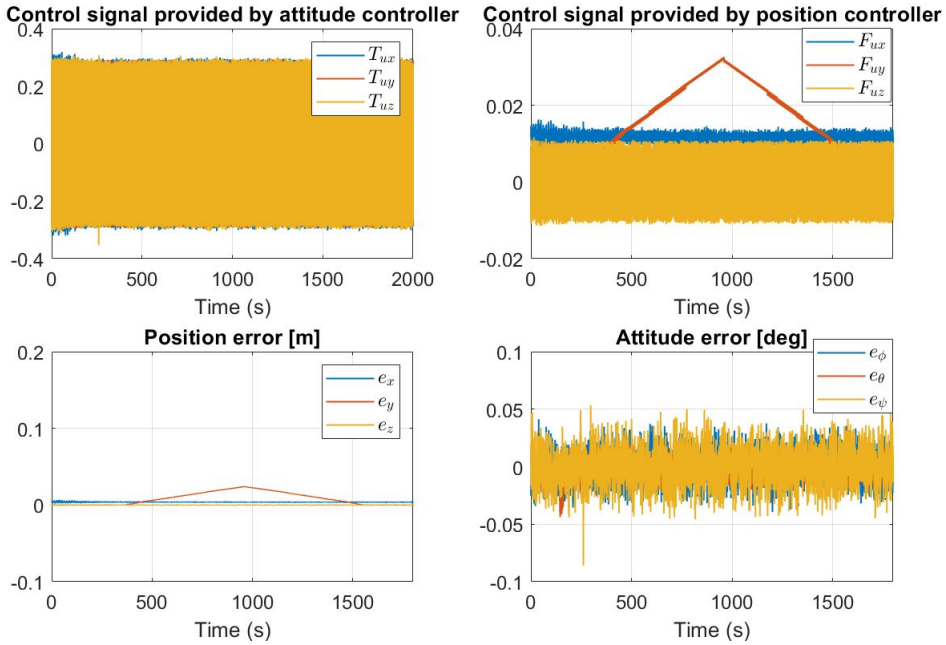

Figure 3.6: Tracking errors and control signals with FOSMC

3.6.2 Super-Twisting Sliding Mode Control

Fig. 3.8 shows the attitude (left column) and the relative position (right column), with their respective reference signals. It can be seen that there is a satisfactory tracking. Furthermore, when compared to Fig. 3.4, a reduction on the "chattering"effect can be appreciated. Fig. 3.9 illustrates the behaviour of the velocities with the STA. When compared to Fig. 3.5, the main difference can be observed in the magnitude of the "chattering", specifically in the angular velocities. The

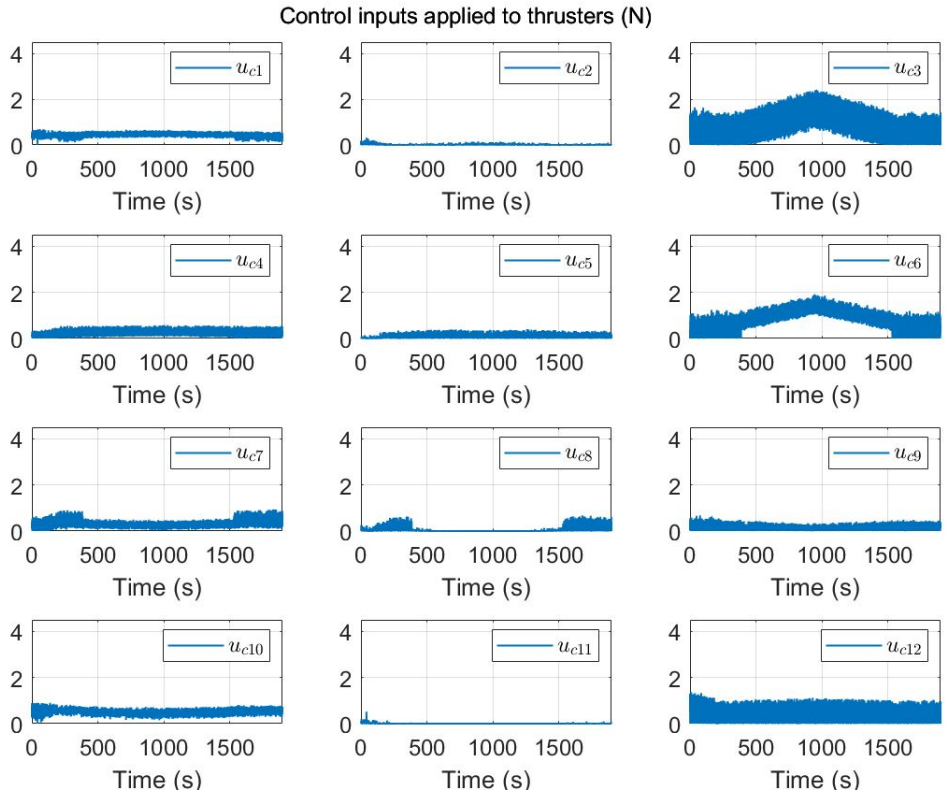

Figure 3.7: Signals applied to thrusters with FOSMC

control signals obtained by the STA are shown in the upper part of Fig. 3.10. The attitude and relative position tracking errors are presented in the lower part of Fig. 3.10. It can be seen that the magnitude of the error reduced when compared to Fig. 3.6. In Fig. 3.11, the control signals applied to each thruster are illustrated.

The capture process of the target by the chaser is illustrated in Fig. 3.12. Both phases, the acquisition phase and the rendezvous phase, are observed. The target is represented by the red square. By zooming in on Fig. 3.12, at the beginning of the trajectory, a closer look to the acquisition phase is obtained. See for instance in Fig. 3.13, where the chaser keeps its position and only performs a rotation. This, with the objective of aligning with the target. After this step, the chaser goes into the second phase, which involves a translation towards the target.

3.7 Conclusion

This chapter described the rendezvous mission and the characteristics of the scenario considered. The developments of the model and its linearization was described. Then, the design procedure for the development of controllers for attitude and position tracking was done. The design is based on two sliding mode techniques in a backstepping setup. For the design of the controller, the coupling effect between the dynamics was neglected and the disturbances are approximated as an exogenous signal, see Remark 3. The proposed solutions were tested in a nonlinear simulator. The results obtained showed that both controllers are stable, robust against perturbations and would not saturate the thrusters. The main difference between both solutions is the already known "chattering" effect. A reduction on the magnitude of the chattering is observed when comparing Figs. 3.8-3.11 against the results obtained when applying the FOSMC, i.e Figs. 3.4-3.7. In addition, the STA controller showed higher robustness against perturbations, see for example Fig. 3.6 against Fig. 3.10.

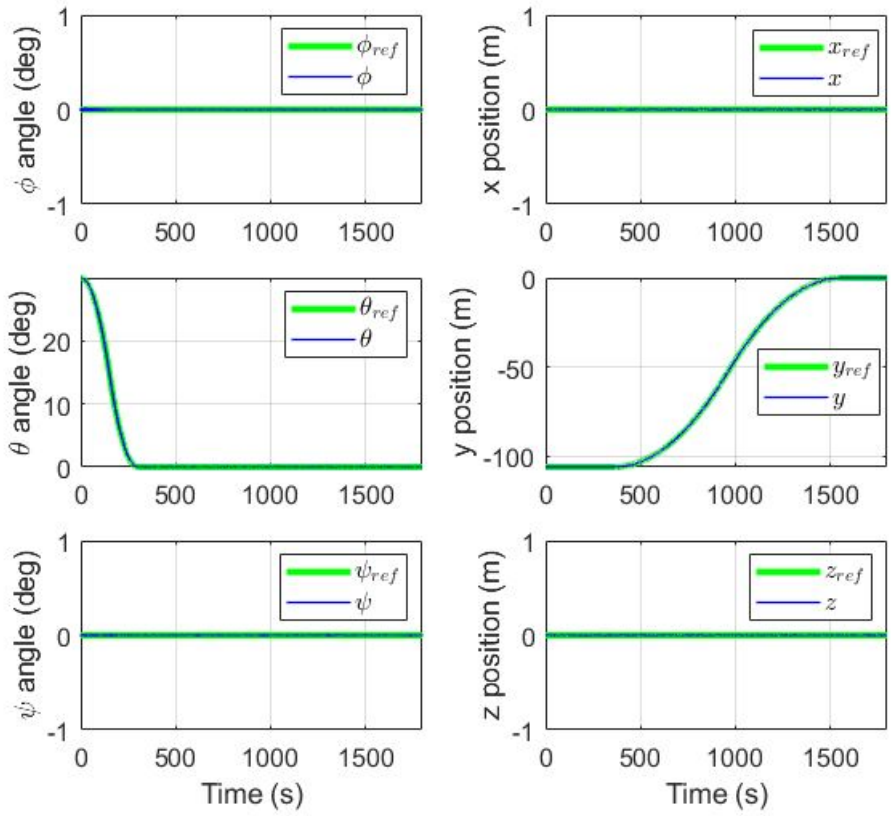

Figure 3.8: Positions and Angles with STA

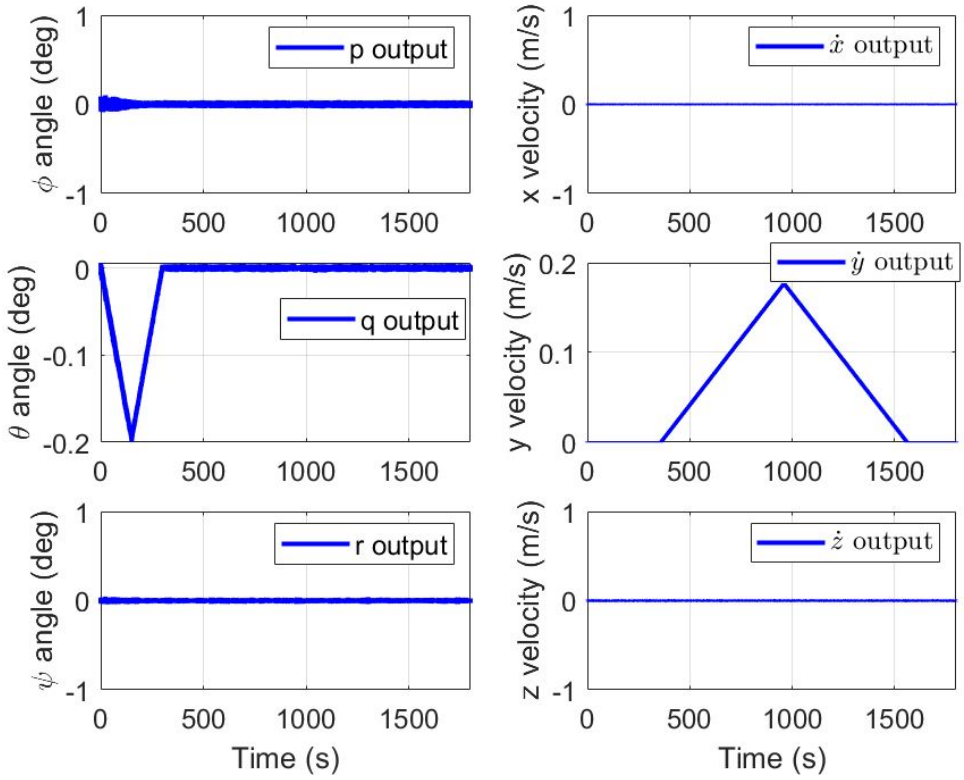

Figure 3.9: Angular and Transitional velocities with STA

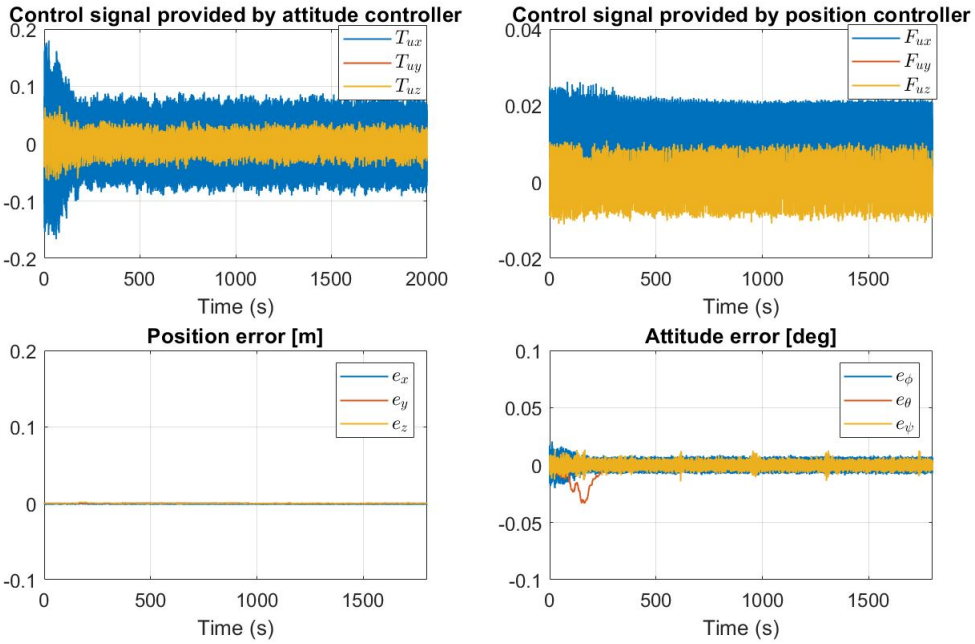

Figure 3.10: Tracking errors and control signals with STA

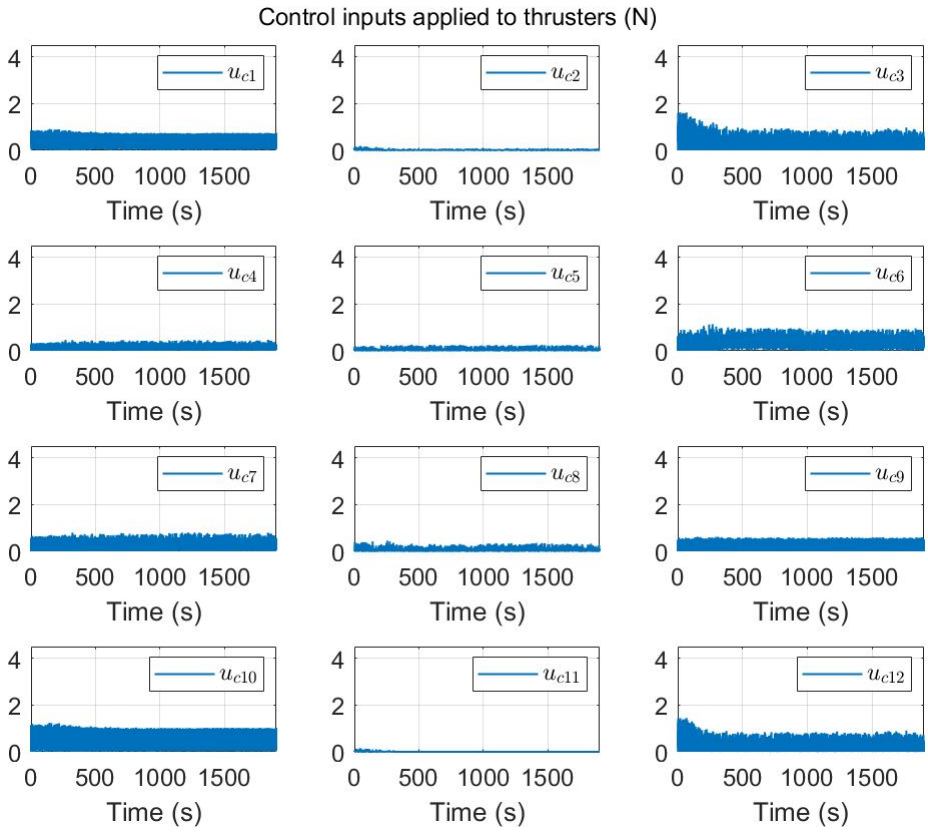

Figure 3.11: Signals applied to thrusters with STA

It is known that in reality the system is more complex than the one considered in this chapter. Starting by the fact that the disturbances are state dependent and approximating them decreases the accuracy of the solution. In addition, it should be considered that the success of the mission can be threatened by sudden faults. The insensitivity property of the SMC will be exploited in

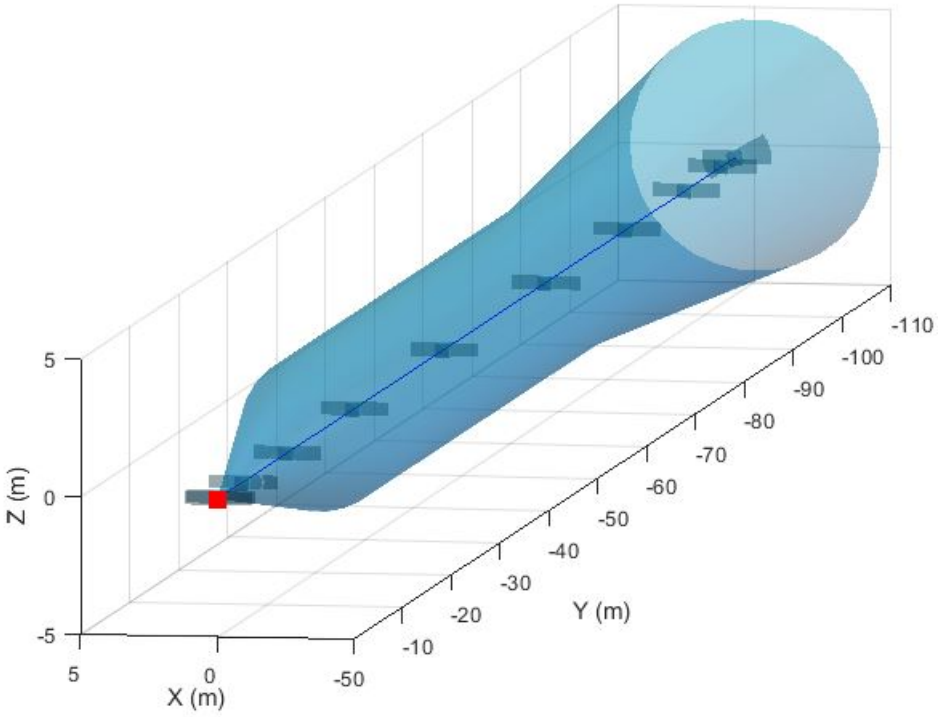

Figure 3.12: Mission Transition Trajectory

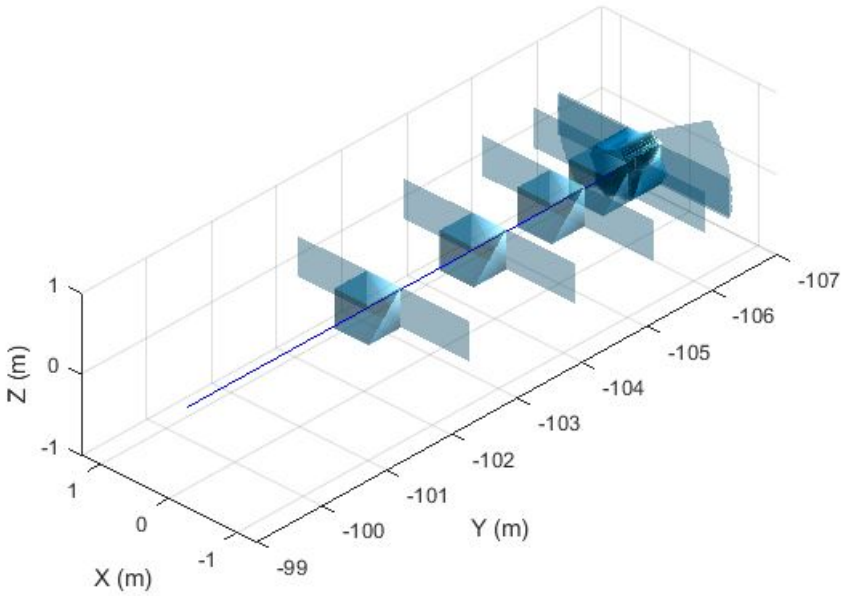

Figure 3.13: Zoom at the beginning of the trajectory

this direction in the following chapter. In addition, the idea of a nonlinear controller, i.e. one that takes into account the coupling effect between dynamics, will also be explored in following chapter.

4 Design of a Fault Tolerant Control Scheme in Dual Quaternion Formalism

4.1 Introduction

Based on the results obtained on the previous chapter, the development of a control strategy with fault tolerance capabilities is explored in this chapter. The state dependent perturbations (sloshing phenomena and flexible modes) are no longer treated as an exogenous approximated signal. Thus, the development of a coupled model (6DoF) is necessary in order to take into account the coupling effects. This is achieved by employing the Dual Quaternion formalism, which is a combination of complex numbers and quaternions. Furthermore, the occurrence of sudden faults is considered, specifically, a stuck open and a stuck closed thruster fault. The proposed FTC solution is based on the GSTA theory, nested with a nonlinear fault estimator and an anti-windup strategy. Stability of the proposed FTC solution is investigated and it is proved that the overall FTC scheme is asymptotically stable. It is then tested in a functional engineering simulator that accurately simulates the capture of a passive target by a chaser spacecraft, onto a circular orbit around the Earth, considering a realistic navigation unit, the flexible modes of the solar arrays of the chaser and the most significant environmental perturbations, i.e., Earth gravity, the second zonal harmonic J_2, atmospheric drag and magnetic disturbances. Mission-oriented criteria are proposed to analyse the results, and it is shown that the proposed FTC solution exhibit satisfactory performance, since the capture performance are met, despite the loss of controllability of the faulty actuator.

4.2 Fault recoverability/compensability

As mentioned in Section 2.9, FTC capabilities rely on the structure of the system. For instance, if a system does not have an adequate redundancy, the system cannot effectively compensate the faults despite of the control strategy selected. Redundancy can be provided by software/hardware or analytically (relationship between variables in the system). Control reconfigurability was proposed in [WZS00], as a redundancy measure in the context of feedback control. It reveals the feasibility and limitations of the model used for FTC. Furthermore, it analyzes the remaining controllability and observability properties of a system in adverse conditions. As a consequence, modifications can be applied to enhance the reliability of the system. This concept is also employed to evaluate the size of the set of fault tolerant situations, i.e. the number of recoverable and non-recoverable situations after the occurrence of a fault. This is known as fault recoverability, and has been addressed with different approaches, see for instance [FKB99, Sta05, YJS12, GCTS09, BKL+06, SB10, YJSZ15, QTHH16, CJT15, ZTCHD17].

Having in mind this necessary condition, it is proposed in this chapter to improve the hardware redundancy to observe a recoverable situation after fault occurrence. A new configuration of thrusters was designed to specifically address FTC strategies. The set of 24 thrusters was placed on the chaser such that the nominal attainable set of propulsion torques $\boldsymbol{\tau}$ and forces $\boldsymbol{f}$ is likewise attainable by combining the thrusts of any $N-1=23$ thrusters, see Fig. 4.1. This means that stability and an acceptable performance can be maintained with 23 thrusters. This is verified with the fault recoverability analysis, as shown in the following.

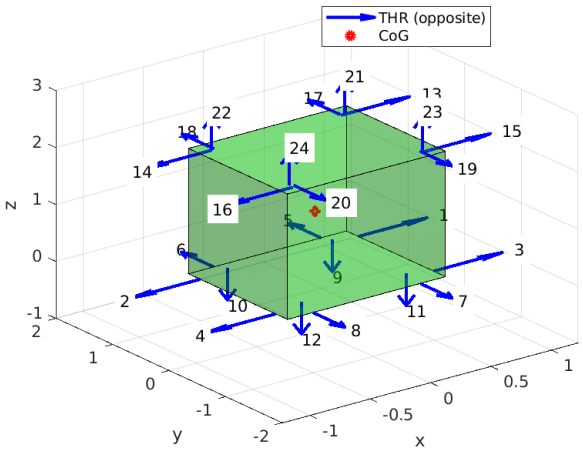

Figure 4.1: Thruster configuration, geometry of the chaser and CoM

To derive the fault recoverability criterion, one begins by defining the set of Ω_a which contains the forces/moments related to the studied thruster configuration as:

$$\Omega_a(\boldsymbol{A},\boldsymbol{b}) = \left\{ \begin{bmatrix} \boldsymbol{\tau}_{c_u}^{(c)}(t) \\ \boldsymbol{f}_{c_u}^{(c)}(t) \end{bmatrix} = \boldsymbol{R}\boldsymbol{u}_c^{(c)} \in \mathbb{R}^6 \;\middle|\; \boldsymbol{A} \begin{bmatrix} \boldsymbol{\tau}_{c_u}^{(c)}(t) \\ \boldsymbol{f}_{c_u}^{(c)}(t) \end{bmatrix} \leq \boldsymbol{b} \right\} \tag{4.1}$$

where $\boldsymbol{A} \in \mathbb{R}^{m\times k}$ is a real matrix with rows $\boldsymbol{a}_i^\intercal$, $\boldsymbol{b} \in \mathbb{R}^k$ is a real vector with entries $\boldsymbol{b}_i$ (see Appendix A.3), $\boldsymbol{R}$ is called the thruster configuration matrix and $\boldsymbol{u}_c^{(c)}$ is the commanded opening of the thrusters, which describes the following set:

$$\mathbb{U} = \left\{ \boldsymbol{u}_c^{(c)} = [u_{c_1}^{(c)},\ldots,u_{c_k}^{(c)}]^\intercal \in \mathbb{R}^{24} \;\middle|\; u_{cmin_k}^{(c)} \leq u_{c_k}^{(c)} \leq u_{cmax_k}^{(c)} \text{ for } k=1,\ldots,24 \right\} \tag{4.2}$$

and let $\tilde{\mathbb{U}}$ be the set of the commanded opening of the thrusters considering a fault in the k-th thruster:

$$\tilde{\mathbb{U}} = \left\{ \tilde{\boldsymbol{u}}_c^{(c)} = (\boldsymbol{I}_{24} - \Psi(t))\boldsymbol{u}_c^{(c)} \in \mathbb{R}^{24} \;\middle|\; \Psi(t) = \operatorname{diag}\left(\psi_1(t),\ldots,\psi_{24}(t)\right), \text{where } 0 \leq \psi_k(t) \leq 1 \right\} \tag{4.3}$$

where $\boldsymbol{\Psi}_k$ is used to represent the status of the k-th thruster, as it is further explained in (4.66). Let Ω_a^k be the restricted set of attainable forces/moments using all the thrusters but the k-th one due to a fault, then $\Omega_a^k \subseteq \Omega_a$.

$$\Omega_a^k(\boldsymbol{A}_f,\boldsymbol{b}_f) := \left\{ \begin{bmatrix} \boldsymbol{\tau}_{c_f}^{(c)}(t) \\ \boldsymbol{f}_{c_f}^{(c)}(t) \end{bmatrix} = \boldsymbol{R}\tilde{\boldsymbol{u}}_c^{(c)} \in \mathbb{R}^6 \;\middle|\; A_f \begin{bmatrix} \boldsymbol{\tau}_{c_f}^{(c)}(t) \\ \boldsymbol{f}_{c_f}^{(c)}(t) \end{bmatrix} \leq \boldsymbol{b}_f \right\} \tag{4.4}$$

where $\boldsymbol{A}_f \in \mathbb{R}^{m\times k}$ is a real matrix with rows $\boldsymbol{a}_{i_f}^\intercal$, $\boldsymbol{b}_f \in \mathbb{R}^k$ is a real vector with entries $\boldsymbol{b}_{i_f}$. Consider for example, a thruster that remains stuck open at its maximum actuation value, the set of attainable forces/moments will be a subset of the original set, i.e. when

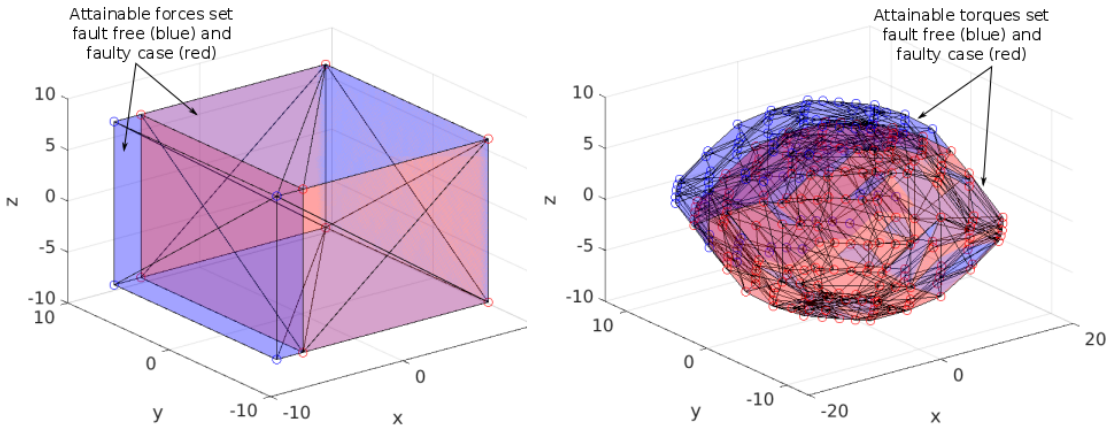

Figure 4.2: Set of attainable forces/torques with stuck open thruster fault

all thrusters were completely functional. This is shown in Fig. 4.2, where the behaviour of the set of attainable forces and moments is illustrated, considering that thruster 2 remained stuck open at its maximum actuation value. In this figure, Ω_a is colored in blue, whilst Ω_a^2 is in red.

Furthermore, the set of attainable forces/moments is also studied for the case when one thruster remains stuck closed. This means that no more actuation is received from that specific thruster. Fig. 4.3 illustrates this behaviour. Once again, Ω_a is colored in blue, whilst Ω_a^2 is in red. The investigated faulty situations (one thruster is fully open or closed) are recoverable given that the faulty set shows a small reduction when compared to the fault free set.

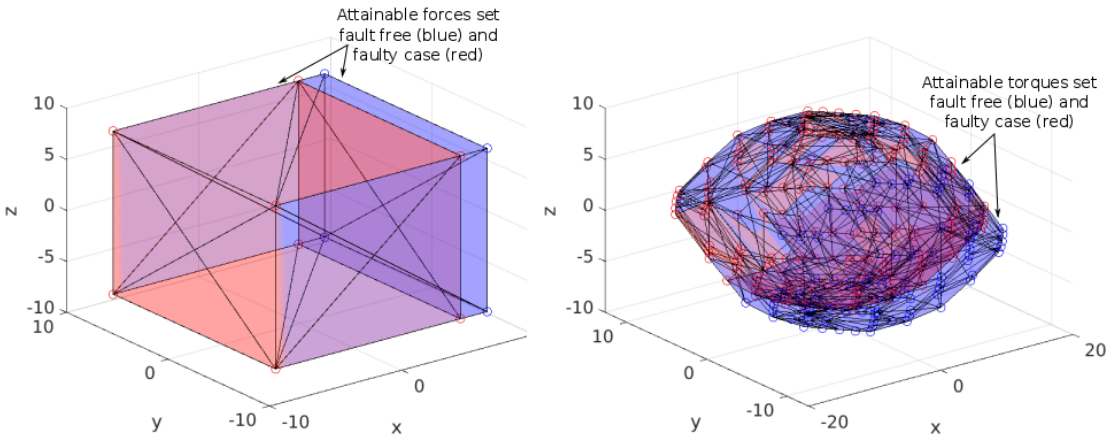

Figure 4.3: Set of attainable forces/torques with stuck close thruster fault

4.3 Mathematical background

4.3.1 Quaternions

Quaternions are the extension of complex numbers to hypercomplex numbers [Cli82, Ham48, Stu91]. A quaternion is defined as:

$$\mathbf{q} = q_0 + q_1 i + q_2 j + q_3 k \tag{4.5}$$

where $q_0 \in \mathbb{R}$ is the scalar part and $q_1 i + q_2 j + q_3 k \in \mathbb{R}^3$ corresponds to a complex part [Ham48]. The multiplication of the imaginary components has the following properties:

$$i^2 = j^2 = k^2 = -1 \tag{4.6}$$

$$\begin{aligned} ij &= -ji = k \\ jk &= -jk = i \\ ki &= -ki = j \end{aligned}$$

Quaternions can also be represented as a combination of a scalar (q_s) and complex vector part as ($\mathbf{q}_v$) $\mathbf{q} = [q_s, \mathbf{q}_v^\intercal]^\intercal$. Let $\mathbf{q}$, $\mathbf{q}_a$ and $\mathbf{q}_b$ represent arbitrary quaternions. The basic operations of the quaternions are defined as:

- Conjugate

$$\mathbf{q}^* = \begin{bmatrix} q_s & -\mathbf{q}_v^\intercal \end{bmatrix}^\intercal \tag{4.7}$$

- Multiplication

$$\mathbf{q}_a \circ \mathbf{q}_b = \begin{bmatrix} q_{s1}q_{s2} - \mathbf{q}_{v1} \cdot \mathbf{q}_{v2} \\ q_{s1}\mathbf{q}_{v2} + q_{s2}\mathbf{q}_{v1} + \mathbf{q}_{v1} \times \mathbf{q}_{v2} \end{bmatrix} \tag{4.8}$$

- Dot product

$$\mathbf{q}_a \cdot \mathbf{q}_b = \frac{1}{2}(\mathbf{q}_a \circ \mathbf{q}_b^* + \mathbf{q}_b \circ \mathbf{q}_a^*) \tag{4.9}$$

- Cross product

$$\mathbf{q}_a \times \mathbf{q}_b = \frac{1}{2}(\mathbf{q}_a \circ \mathbf{q}_b - \mathbf{q}_b^* \circ \mathbf{q}_a^*) = \begin{bmatrix} 0 \\ q_{s1}\mathbf{q}_{v2} + q_{s2}\mathbf{q}_{v1} + \mathbf{q}_{v1} \times \mathbf{q}_{v2} \end{bmatrix} \tag{4.10}$$

Quaternion multiplication can also be expressed in matrix form as:

$$\mathbf{p} \circ \mathbf{q} = \begin{bmatrix} p_0 \\ p_1 \\ p_2 \\ p_3 \end{bmatrix} \circ \begin{bmatrix} q_0 \\ q_1 \\ q_2 \\ q_3 \end{bmatrix} = \begin{bmatrix} p_s \\ \mathbf{p}_v \end{bmatrix} \circ \begin{bmatrix} q_s \\ \mathbf{q}_v \end{bmatrix} = (\mathbf{p})^+ \mathbf{q} = (\mathbf{q})^- \mathbf{p} \tag{4.11}$$

where

$$\mathbf{p}^+ = \begin{bmatrix} p_s & -\mathbf{p}_v^\intercal \\ \mathbf{p}_v & p_s\mathbf{I} + C(\mathbf{p}_v) \end{bmatrix} \tag{4.12}$$

$$\mathbf{q}^- = \begin{bmatrix} q_s & -\mathbf{q}_v^\intercal \\ \mathbf{q}_v & q_s\mathbf{I} - C(\mathbf{q}_v) \end{bmatrix} \tag{4.13}$$

$C(\mathbf{q}_v)$ denotes the vector cross product matrix defined as:

$$C(\mathbf{q}_v) = \begin{bmatrix} 0 & -q_3 & q_2 \\ q_3 & 0 & -q_1 \\ -q_2 & q_1 & 0 \end{bmatrix} \tag{4.14}$$

The computation of (4.12), (4.13) and (4.14) can be found in the Appendix A.4. The norm of a quaternion is defined as:

$$\begin{aligned} |\mathbf{q}|^2 &= \mathbf{q} \circ \mathbf{q}^* \\ &= \begin{bmatrix} q_s q_s + \mathbf{q}_v \cdot \mathbf{q}_v \\ q_s\mathbf{q}_v - q_s\mathbf{q}_v - \mathbf{q}_v \times \mathbf{q}_v \end{bmatrix} \\ &= \begin{bmatrix} q_s^2 + \mathbf{q}_v \cdot \mathbf{q}_v \\ 0 \end{bmatrix} = \begin{bmatrix} q_s^2 + |\mathbf{q}_v|^2 \\ 0 \end{bmatrix} \end{aligned} \tag{4.15}$$

If the norm of the quaternion is $|\mathbf{q}| = 1$ the quaternion is called unit quaternion. Unit quaternions are used to represent a rotation of an angle θ around a unit axis $\mathbf{n}$, and they are defined as:

$$\mathbf{q} = \left[cos\left(\frac{\theta}{2}\right) \quad \mathbf{n}sin\left(\frac{\theta}{2}\right)^{\intercal}\right]^{\intercal} \tag{4.16}$$

Unit quaternions can be employed for describing rotations. Consider for example a vector $\boldsymbol{r}^I \in \mathbb{R}^3$ in the frame $\mathcal{I}$. This vector can be expressed in the a new frame $\mathcal{N}$ as follows:

$$\boldsymbol{r}^{\underline{N}} = \mathbf{q}^* \circ \boldsymbol{r}^{\underline{I}} \circ \mathbf{q} \tag{4.17}$$

where $\boldsymbol{r}^{\underline{N}}$ and $\boldsymbol{r}^{\underline{I}}$ are two quaternions with vanishing scalar part, i.e. $\boldsymbol{r}^{\underline{N}} = \left[0, \boldsymbol{r}^N\right]$ and $\boldsymbol{r}^{\underline{I}} = \left[0, \boldsymbol{r}^I\right]$.

4.3.2 Dual numbers

A dual number is defined as:

$$\bar{a} = a_r + \varepsilon a_d \quad \varepsilon \neq 0 \quad \varepsilon^2 = 0 \tag{4.18}$$

where $a_r \in \mathbb{R}$ is the real part, $a_d \in \mathbb{R}$ is the dual part and ε is the dual unit [Cli82][Stu91]. Let $\bar{a}$ and $\bar{b}$ represent dual numbers, then the basic operations for dual numbers are defined as:

$$\bar{a} + \bar{b} = a_r + b_r + \varepsilon(a_d + b_d) \tag{4.19}$$

$$\lambda\bar{a} = \lambda a_r + \varepsilon\lambda a_d \tag{4.20}$$

$$\bar{a}\bar{b} = a_r b_r + \varepsilon(a_r b_d + b_r a_d) \tag{4.21}$$

for any scalar λ[WHWH06].

4.3.3 Dual vectors and matrices

Dual vectors and matrices are vectors and matrices that have as elements dual numbers. They are defined as follows:

$$\bar{\mathbf{a}} = \mathbf{a}_r + \varepsilon\mathbf{a}_d \tag{4.22}$$

$$\bar{\mathbf{A}} = \mathbf{A}_r + \varepsilon\mathbf{A}_d \tag{4.23}$$

where $\mathbf{a}_r, \mathbf{a}_d \in \mathbb{R}^n$ are real vectors and $\mathbf{A}_r, \mathbf{A}_d \in \mathbb{R}^{n\times n}$ are real matrices. Their operations are defined as:

$$\bar{\mathbf{a}} \pm \bar{\mathbf{b}} = (\mathbf{a}_r + \varepsilon\mathbf{a}_d) \pm (\mathbf{b}_r + \varepsilon\mathbf{b}_d) = (\mathbf{a}_r \pm \mathbf{b}_r) + \varepsilon(\mathbf{a}_d \pm \mathbf{b}_d) \tag{4.24}$$

$$\bar{\mathbf{a}}^{\intercal} = \mathbf{a}_r^{\intercal} + \varepsilon\mathbf{a}_d^{\intercal} \tag{4.25}$$

$$h\bar{\mathbf{a}} = h(\mathbf{a}_r + \varepsilon\mathbf{a}_d) = h\mathbf{a}_r + \varepsilon h\mathbf{a}_d \tag{4.26}$$

$$\bar{\mathbf{a}} \cdot \bar{\mathbf{b}} = \mathbf{a}_r^{\intercal} \cdot \mathbf{b}_r + \varepsilon(\mathbf{a}_r^{\intercal} \cdot \mathbf{b}_d + \mathbf{a}_d^{\intercal} \cdot \mathbf{b}_r) \tag{4.27}$$

$$\bar{\mathbf{a}} \times \bar{\mathbf{b}} = \mathbf{a}_r \times \mathbf{b}_r + \varepsilon(\mathbf{a}_r \times \mathbf{b}_d + \mathbf{a}_d \times \mathbf{b}_r) \tag{4.28}$$

$$|\bar{\mathbf{a}}| = |\mathbf{a}_r| + \varepsilon|\mathbf{a}_d| \tag{4.29}$$

$$\text{sign}\,(\bar{\mathbf{a}}) = \text{sign}\,(\mathbf{a}_r) + \varepsilon\,\text{sign}\,(\mathbf{a}_d) \tag{4.30}$$

$$\lambda(\bar{\mathbf{A}}) = \lambda(\mathbf{A}_r) + \varepsilon\lambda(\mathbf{A}_d) \tag{4.31}$$

$$\bar{\mathbf{a}} \circ \bar{\mathbf{b}} + \bar{\mathbf{b}}^* \circ \bar{\mathbf{a}} = \bar{\mathbf{a}} \circ \bar{\mathbf{b}} - \bar{\mathbf{b}} \circ \bar{\mathbf{a}} = 2\bar{\mathbf{a}} \times \bar{\mathbf{b}} \tag{4.32}$$

$$\langle\bar{\mathbf{a}}|\bar{\mathbf{b}}\rangle = \mathbf{a}_r^{\intercal} \cdot \mathbf{a}_d + \mathbf{b}_r^{\intercal} \cdot \mathbf{b}_d \tag{4.33}$$

where $\bar{\mathbf{a}}$, $\bar{\mathbf{b}}$ are dual vectors, $\bar{\mathbf{A}}$ is a dual matrix, h is a real number, and $\lambda(\cdot)$ denotes the eigenvalue of the corresponding matrix.

The set of dual vectors are denoted in the following $\mathbb{V}$, which is defined according to $\mathbb{V} = \{\bar{\mathbf{v}} : \bar{\mathbf{v}} = \mathbf{v}_r + \varepsilon\mathbf{v}_d,\ \mathbf{v}_r, \mathbf{v}_d \in \mathbb{R}\}$. The notation $\mathbb{V}^n$ is used to refer to the set of dual vectors of dimension n. Following this notation, the complement operator of the dual unit ε, is defined as:

$$\frac{d}{d\varepsilon}\hat{\mathbf{v}} = \frac{d}{d\varepsilon}(\mathbf{v}_r + \varepsilon\mathbf{v}_d) = \mathbf{v}_d \tag{4.34}$$

4.3.4 Dual quaternions

A dual quaternion $\bar{\mathbf{q}}$ is a quaternion which has as elements two quaternions $\mathbf{q}_r$ and $\mathbf{q}_d$ that represent its real and dual parts as $\bar{\mathbf{q}} = \mathbf{q}_r + \varepsilon\mathbf{q}_d = [\mathbf{q}_r, \mathbf{q}_d]^\intercal$. The operations related to dual quaternions are similar to the ones applied to quaternions, dual numbers and vectors. Additional operations are defined as:

$$\bar{\mathbf{q}}^* = \mathbf{q}_r^* + \varepsilon\mathbf{q}_d^* \tag{4.35}$$

$$\bar{\mathbf{q}}_a \circ \bar{\mathbf{q}}_b = \mathbf{q}_{ar} \circ \mathbf{q}_{br} + \varepsilon(\mathbf{q}_{ar} \circ \mathbf{q}_{bd} + \mathbf{q}_{ad} \circ \mathbf{q}_{br}) \tag{4.36}$$

Along this manuscript, $\bar{\mathbf{1}} = \mathbf{1} + \varepsilon\mathbf{0}$ and $\bar{\mathbf{0}} = \mathbf{0} + \varepsilon\mathbf{0}$ represent the identity and zero in the dual space with $\mathbf{1} = [1, 0, 0, 0]^\intercal$ and $\mathbf{0} = [0, 0, 0, 0]^\intercal$.

The product of a dual number $\bar{c}$ with a dual quaternion $\bar{\mathbf{d}}$ is defined as [GV16]:

$$\bar{c} * \bar{\mathbf{d}} = (c_r + \varepsilon c_d) * (\mathbf{d}_r + \varepsilon\mathbf{d}_d) = c_r\mathbf{d}_r + \varepsilon c_d\mathbf{d}_d \tag{4.37}$$

4.4 Problem statement

4.4.1 The reference mission

The reference mission considered for the FTC strategy is similar to the one described previously in Chapter 3. This means that the rendezvous studied is between an active spacecraft and a passive spacecraft, called the chaser and target, respectively. The characteristics of the orbit remain as described in Section 3.1. The main difference is the thruster structure considered for the chaser, which consists of 24 thrusters of 2 N as shown in Fig. 4.1. This structure has been designed especially to study fault-tolerant strategies, as explained in Section 4.2.

At sensor level, more precisely in terms of outputs available from the navigation unit, it is assumed that the relative position, velocity and acceleration between the two spacecraft are available, as well as the attitude, angular rate and angular acceleration of the chaser. The retained characteristics of the navigation outputs are:

- a precision of 2 mm, 0.2 mm/s and 0.2 mm/s^2 for relative position, velocity and acceleration, over the three axes;
- a precision of 0.1 deg, 0.01 deg/s and 0.01 deg/s^2 for chaser attitude, angular rate and angular acceleration, over the three axes.

Furthermore, it is assumed that the chaser is equipped by a solar array with flexible modes located at 0.1 rad/s and 0.5 rad/s, each mode having a damping factor fixed to 0.003. Moreover, it is assumed that the chaser is equipped with two propellant tanks that are considered to be partially filled, so that the motion of the spacecraft causes propellant sloshing over three modes. The sloshing modes are assumed to be located at 0.4 rad/s, 0.8 rad/s and 1 rad/s, each of them having a damping factor fixed to 0.1. The chaser's characteristics are listed in table 4.1. With regards to the target, it is supposed to be a spheric object. For the capture mechanism, it is supposed to be a basket. The mission consists of the capture of the target by the chaser spacecraft, i.e. the target is captured in the basket.

Finally, as expressed in Chapter 3, the complete mission is modelled into the FES developed in Matlab/Simulink. Within the FES, the chaser and the target have each one an associated environment module as some characteristics depend on specific spacecraft properties. Typically, the dynamic equations associated to the chaser, consider the flexible modes due to propellant sloshing and the solar array, whereas the dynamic equations are those of a punctual mass.

Assumption 4. *The focus of this work is to develop a FTC solution at control level and not at guidance level. This means, that the trajectory path computed by the guidance algorithm cannot be modified after the occurrence of a fault.*

4.4.2 Coordinate frames and notations

To establish the model of relative motion between the chaser and the target, the following coordinate frames are defined:

i) Earth centered inertial frame $\mathcal{F}_i$: this frame is a non-accelerating reference frame, with its origin at the center of the Earth, and the axes $\vec{\mathbf{x}}_i, \vec{\mathbf{y}}_i, \vec{\mathbf{z}}_i$ are oriented as shown in Fig. 4.4, i.e. the $\vec{x}_i$ axis is pointing to the vernal equinox, the $\vec{z}_i$ axis is pointing to the north and parallel to the rotation axis of the Earth and the $\vec{y}_i$ axis completes the frame.

ii) target frame $\mathcal{F}_t$: the center of this frame coincides with the target's CoM, and it's axes are oriented in such a way that an attitude angle equal to $[0, 0, 0]^\intercal$ means that $\mathcal{F}_t$ coincides with $\mathcal{F}_l$.

iii) chaser frame $\mathcal{F}_c$: the center of this frame coincides with the chaser's CoM and it's axes are oriented in such a way that an attitude angle equal to $[0, 0, 0]^\intercal$ means that the chaser is aligned with the target along its velocity axis.

iv) LVLH frame $\mathcal{F}_l$: the origin of the LVLH frame is at the target CoM, the axis $\vec{z}_l$ is in the orbital plane, from the target's CoM towards the Earth center. The axis $\vec{y}_l$ is normal to the orbital plane and in the opposite direction and parallel to the orbital angular momentum vector. The $\vec{x}_l$ is in the direction of the velocity vector of the target. The LVLH frame is mainly used to plot the figures and analyse the results, since it offers a good understanding of the pose of the two spacecraft on the orbit. Note this frame convention is different from the one employed in Chapter 3.

The notation $\boldsymbol{r}^{(i)}, \boldsymbol{r}^{(t)}, \boldsymbol{r}^{(c)}$ is used for a vector $\boldsymbol{r}$ given in the frame $\mathcal{F}_i, \mathcal{F}_t, \mathcal{F}_c$, respectively. When dealing with the LVLH frame, the index "LVLH" is used. The notation $\boldsymbol{r}_e^{(c)}$ should be interpreted as a relative vector error between the chaser and the target, given in $\mathcal{F}_c$. Finally, the notation $\boldsymbol{\omega}_c^{(c)}/\boldsymbol{\omega}_t^{(t)}$ denotes the angular velocity of $\mathcal{F}_c/\mathcal{F}_t$ relative to $\mathcal{F}_i$, expressed in $\mathcal{F}_c/\mathcal{F}_t$.

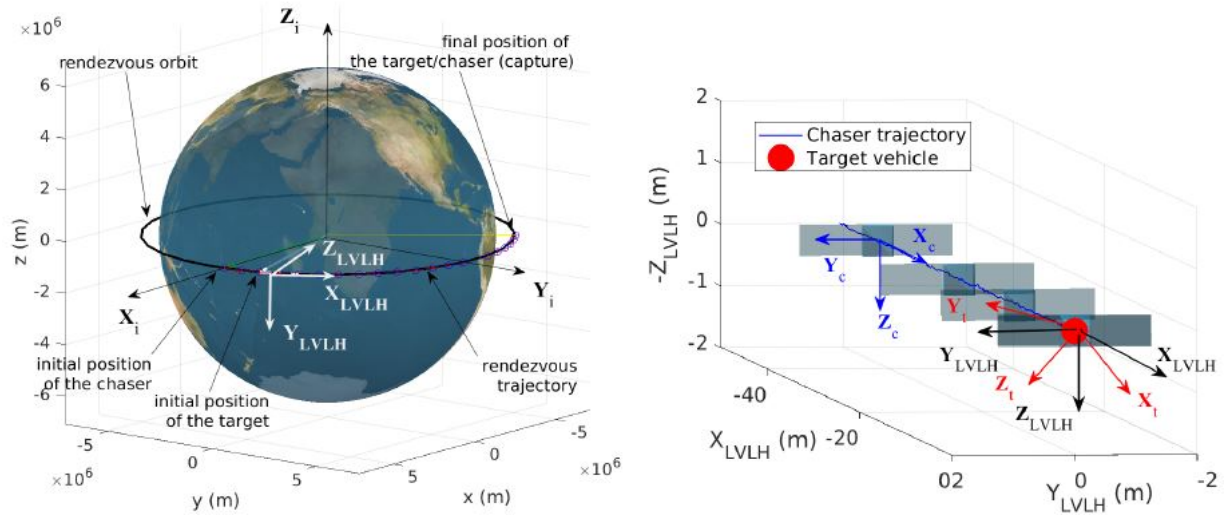

Figure 4.4: The orbit and rendezvous trajectory in $\mathcal{F}_i$ (left) and in the last 40 m in the LVLH frame $\mathcal{F}_l$ (right). The trajectory corresponds to the results in section 4.6

4.4.3 Dual quaternion kinematics and dynamic models

The chaser case

Let $\bar{\mathbf{q}}_c \in \mathbb{H}_d$ be the dual quaternion describing the rotation $\mathbf{q}_c \in \mathbb{H}$ of the chaser followed by a translation $\boldsymbol{r}_c \in \mathbb{R}^3$. The kinematics equation of the chaser is given by [BS99, WS12]

$$\dot{\bar{\mathbf{q}}}_c = \frac{1}{2}\bar{\mathbf{q}}_c \circ \bar{\boldsymbol{\omega}}_c^{(c)} \tag{4.38}$$

where $\bar{\boldsymbol{\omega}}_c^{(c)} \in \mathbb{V}^3$ is a dual vector, called the dual velocity of the chaser, given in the chaser frame $\mathcal{F}_c$, and defined according to:

$$\bar{\boldsymbol{\omega}}_c^{(c)} = \boldsymbol{\omega}_c^{(c)} + \varepsilon\left(\dot{\boldsymbol{r}}_c^{(c)} + \boldsymbol{\omega}_c^{(c)} \times \boldsymbol{r}_c^{(c)}\right) \tag{4.39}$$

The expression in (4.39) employs the property shown in (4.17). This applies for further multiplication operations between a vector in $\mathbb{R}^3$ and a quaternion. Let the dual inertia matrix be now introduced to fully describe the rigid body dynamics with dual quaternions. From [WLS+12], it is defined according to

$$\begin{aligned}\bar{\mathbf{M}} &= m\frac{d}{d\varepsilon}\mathbf{I}_3 + \varepsilon\boldsymbol{J} \\ &= \begin{bmatrix} m\frac{d}{d\varepsilon} + \varepsilon J_{xx} & \varepsilon J_{xy} & \varepsilon J_{xz} \\ \varepsilon J_{xy} & m\frac{d}{d\varepsilon} + \varepsilon J_{yy} & \varepsilon J_{yz} \\ \varepsilon J_{xz} & \varepsilon J_{yz} & m\frac{d}{d\varepsilon} + \varepsilon J_{zz} \end{bmatrix}\end{aligned} \tag{4.40}$$

where m is the chaser mass, $\boldsymbol{J}$ is its inertia matrix, $\mathbf{I}_3 \in \mathbb{R}^{3\times3}$ is the real identity matrix. The inverse of $\bar{\mathbf{M}}$ is defined as $\bar{\mathbf{M}}^{-1} = \boldsymbol{J}^{-1}\frac{d}{d\varepsilon} + \varepsilon\frac{1}{m}\mathbf{I}_3$. The dual momentum of the chaser is expressed as [WS12]:

$$\bar{\boldsymbol{M}}\bar{\boldsymbol{\omega}}_c^{(c)} = m\left(\dot{\boldsymbol{r}}_c^{(c)} + \boldsymbol{\omega}_c^{(c)} \times \boldsymbol{r}_c^{(c)}\right) + \varepsilon\boldsymbol{J}\boldsymbol{\omega}_c^{(c)} \tag{4.41}$$

Then, the dynamics equation of the chaser is given by [BS99, WS12]

$$\dot{\bar{\boldsymbol{\omega}}}_c^{(c)} = -\bar{\boldsymbol{M}}^{-1}\left(\bar{\boldsymbol{\omega}}_c^{(c)} \times \bar{\boldsymbol{M}}\bar{\boldsymbol{\omega}}_c^{(c)}\right) + \bar{\boldsymbol{M}}^{-1}\bar{\boldsymbol{f}}_c^{(c)} \tag{4.42}$$

where $\bar{\boldsymbol{f}}_c^{(c)} = \boldsymbol{f}_c^{(c)} + \varepsilon\boldsymbol{\tau}_c^{(c)}$ is a dual vector in $\mathbb{V}^3$, called the total dual force applied to the center of mass, $\boldsymbol{f}_c^{(c)} \in \mathbb{R}^3$ and $\boldsymbol{\tau}_c^{(c)} \in \mathbb{R}^3$ referring to the total force and total torque, respectively.

In this work, the considered forces and torques are:

- the force and the torque due to the propulsion unit, denoted $\boldsymbol{f}_{c_u}^{(c)} \in \mathbb{R}^3$ and $\boldsymbol{\tau}_{c_u}^{(c)} \in \mathbb{R}^3$ in the following;
- the force $\boldsymbol{f}_{SA}^{(c)} \in \mathbb{R}^3$ and the torque $\boldsymbol{\tau}_{SA}^{(c)} \in \mathbb{R}^3$ due to the flexible modes of the solar array;
- the force $\boldsymbol{f}_P^{(c)} \in \mathbb{R}^3$ and the torque $\boldsymbol{\tau}_P^{(c)} \in \mathbb{R}^3$ due to propellant sloshing;
- the Earth gravity $\boldsymbol{f}_\nabla^{(c)} \in \mathbb{R}^3$;
- the force $\boldsymbol{f}_{J2}^{(c)} \in \mathbb{R}^3$ due to the J_2 effect (Earth's oblateness);
- the force $\boldsymbol{f}_{atm}^{(c)} \in \mathbb{R}^3$ due to atmospheric drag;
- a generalized torque disturbance $\boldsymbol{\tau}_g^{(c)} \in \mathbb{R}^3$ that covers the gravity gradient, the Earth magnetic filed and the atmospheric drag;

- the force $\boldsymbol{f}_{c_f}^{(c)} \in \mathbb{R}^3$ and the torque $\boldsymbol{\tau}_{c_f}^{(c)} \in \mathbb{R}^3$ due to the occurrence of faults in the propulsion unit.

The generalized torque disturbance $\boldsymbol{\tau}_g^{(c)}$, is considered to be a three-dimensional decorelated white noise filtered by a discrete time former filter F, that has been determined by the French Space Agency in the work reported in [PFH16], i.e.

$$F(z) \approx \frac{5.137e-05z^2 + 0.0001027z + 5.137e-05}{z^2 - 1.233z + 0.2329}\boldsymbol{I}_3 \tag{4.43}$$

With regards to the Earth gravity, the atmospheric drag and the J_2 effect, they are given by [AVG+09, Jew17, Sid97] (the following equations are given in the inertial frame $\mathcal{F}_i$):

$$\boldsymbol{f}_{\nabla}^{(i)} = -\frac{m\mu \boldsymbol{r}_c^{(i)}}{\|\boldsymbol{r}_c^{(i)}\|^3} \tag{4.44}$$

$$\boldsymbol{f}_{atm}^{(i)} = -\frac{1}{2}\rho(h)SC_d\left(\dot{\boldsymbol{r}}_c^{(i)}\right)^2 \tag{4.45}$$

$$\boldsymbol{f}_{J2}^{(i)} = -\frac{3}{2}\frac{m\mu J_2 Re^2}{\|\boldsymbol{r}_c^{(i)}\|^5}\left(\boldsymbol{D} - 5\left(\frac{z_c^{(i)}}{\|\boldsymbol{r}_c^{(i)}\|}\right)^2\boldsymbol{I}_3\right)\boldsymbol{r}_c^{(i)} \tag{4.46}$$

In these equations, $S = 2\,\mathrm{m}^2$ is the dimensional cross-sectional area of the spacecraft and $C_d = 2$ is the drag coefficient. $\rho(h)$ is the atmospheric density at the altitude h. $J_2 = 0.0010826267$ and $\boldsymbol{D} = \mathrm{diag}(1,1,3)$. $Re = 6378.137\,\mathrm{km}$ is the Earth's mean equatorial radius, and $\boldsymbol{r}_c^{(i)} = \left[x_c^{(i)}, y_c^{(i)}, z_c^{(i)}\right]^\intercal$ is the position vector of the chaser expressed in $\mathcal{F}_i$. $\mu = 3.986\,004\,4 \times 10^{14}\,\mathrm{m}^3/\mathrm{s}^2$ is the Earth's gravitational parameter.

The flexible modes of the solar array are modelled according to [HCT+19, HLPSA15]

$$\begin{aligned}\boldsymbol{f}_{SA}^{(c)} &= -\boldsymbol{L}_f\ddot{\boldsymbol{x}}_a - m_{SA}\boldsymbol{\gamma}_c^{(c)},\ \boldsymbol{f}_c^{(c)} = m\boldsymbol{\gamma}_c^{(c)}\\ \boldsymbol{\tau}_{SA}^{(c)} &= -\boldsymbol{L}_\tau\ddot{\boldsymbol{x}}_a - \boldsymbol{J}_{SA}\dot{\boldsymbol{\omega}}_c^{(c)}\end{aligned} \tag{4.47}$$

where $\boldsymbol{\gamma}_c^{(c)}$ and $\dot{\boldsymbol{\omega}}_c^{(c)}$ are derived from (4.42) and from the following second order vector-based equation

$$\ddot{\boldsymbol{x}}_a + 2\xi\omega_0\dot{\boldsymbol{x}}_a + \omega_0^2\boldsymbol{x}_a = -\boldsymbol{L}^\intercal\begin{bmatrix}\boldsymbol{\gamma}_c^{(c)}\\ \dot{\boldsymbol{\omega}}_c^{(c)}\end{bmatrix} \tag{4.48}$$

with $\boldsymbol{x}_a \in \mathbb{R}^{n_s\cdot n_p}$, $\boldsymbol{L} = [\boldsymbol{L}_f^\intercal\ \boldsymbol{L}_\tau^\intercal]^\intercal, \boldsymbol{L}_f, \boldsymbol{L}_\tau \in \mathbb{R}^{3\times(n_s\cdot n_p)}$, $\boldsymbol{L}_f = \mathcal{R}(\beta)\boldsymbol{B}_T$ and $\boldsymbol{L}_\tau = \mathcal{R}(\beta)\boldsymbol{B}_R + \mathcal{S}(d)\mathcal{R}(\beta)\boldsymbol{B}_T$. n_p is the number of solar arrays and n_s is the number of flexible modes per solar array. In our application case, $n_p = 1$ and $n_s = 2$ (see section 4.4.1), ξ and ω_0 are matrices of adequate dimensions that correspond to damping ratios and the frequencies for each flexible mode. m_{SA} and $\boldsymbol{J}_{SA}$ refer to the mass and the inertia matrix of the solar array, respectively. The matrices $\boldsymbol{B}_T$ and $\boldsymbol{B}_R$ are the flexible appendage participation factor matrices. The role of the rotation matrix $\mathcal{R}(\beta)$, where β is the appendage angle, is to transform $\boldsymbol{B}_T$ and $\boldsymbol{B}_R$, given in the appendage frame, into the body frame. $\mathcal{S}$ denotes the skew-symmetric matrix of the vector $d \in \mathbb{R}^3$, where d is the distance vector between the chaser's CoM and the CoM of the solar array. In this work, β is considered constant which means that $\mathcal{R}(\beta)$ is constant, i.e. the solar array is considered to be immobile.

Propellant sloshing is modelled as a 3D-mass spring model as proposed in [HCT+19, HLPSA15],

i.e.

$$\begin{aligned}
&\ddot{\boldsymbol{x}}_{s_i} + \frac{\boldsymbol{l}_{s_i}}{m_{s_i}}\dot{\boldsymbol{x}}_{s_i} + \frac{\boldsymbol{k}_{s_i}}{m_{s_i}}\boldsymbol{x}_{s_i} = \boldsymbol{\gamma}_c^{(c)}, \quad \boldsymbol{x}_{s_i} \in \mathbb{R}^3, i = 1,2 \\
&\boldsymbol{f}_P^{(c)} = (m_{s_1} + m_{s_2})\boldsymbol{\gamma}_c^{(c)} \\
&\boldsymbol{\tau}_P^{(c)} = \sum_{i=1}^{2} \boldsymbol{r}_i \times (\boldsymbol{k}_{s_i}\boldsymbol{x}_{s_i} + \boldsymbol{l}_{s_i}\dot{\boldsymbol{x}}_{s_i})
\end{aligned} \tag{4.49}$$

The matrices $\boldsymbol{l}_{s_i}$ and $\boldsymbol{k}_{s_i}$, $i = 1,2$ define the damping and stiffness coefficients associated to the two tanks, m_{s_i} is the propellant mass in the i-th tank and $\boldsymbol{r}_1 = \boldsymbol{r}_2$ is the distance vector between the CoM of the chaser and the CoM of the fuel in a tank.

The numerical value of the main characteristics considered in this thesis, are listed in table 4.1. Modelling the propulsion unit and the faults are considered later, see section 4.4.5.

Then, using the dual vector algebra, it follows

$$\bar{\boldsymbol{f}}_c^{(c)} = \bar{\boldsymbol{f}}_{c_u}^{(c)} + \bar{\boldsymbol{f}}_{c_d}^{(c)} + \bar{\boldsymbol{f}}_{c_f}^{(c)} \tag{4.50}$$

where $\bar{\boldsymbol{f}}_{c_d}^{(c)} = \bar{\boldsymbol{f}}_{SA}^{(c)} + \bar{\boldsymbol{f}}_P^{(c)} + \bar{\boldsymbol{f}}_\nabla^{(c)} + \bar{\boldsymbol{f}}_{J2}^{(c)} + \bar{\boldsymbol{f}}_{atm}^{(c)} + \bar{\boldsymbol{f}}_g^{(c)}$ is the dual force about the disturbances, all terms being a dual vector defined in $\mathbb{V}^3$.

MCI	mass: $m = 300\,\text{kg}$	inertia: $\boldsymbol{J} = \begin{bmatrix} 30 & 1 & 1 \\ 1 & 40 & 1 \\ 1 & 1 & 15 \end{bmatrix}\,\text{kg m}^2$		CoM (center of mass): [1.5 0.2 0.15]m	
slosh models	damping coeff.	frequency of mode 1	frequency of mode 2	frequency of mode 3	propellant mass
Tank 1	0.1	0.4 rad/s	0.8 rad/s	1 rad/s	10 kg
Tank 2	0.1	0.4 rad/s	0.8 rad/s	1 rad/s	20 kg
solar array	damping coeff.	frequency of mode 1	frequency of mode 2	inertia	mass
	$3e^{-3}$	0.1 rad/s	0.5 rad/s	$\boldsymbol{J}_{SA}$ =diag(10, 1, 10)kg m^2	m_{SA} = 40 kg
	ΔCoM chaser - SA $d = [0\ \ 2\ \ 0]$m	appendage angle $\beta = 0°$	participation factor matrix $\boldsymbol{B}_R$: $\begin{bmatrix} 36.64 & 0 \\ 0 & 0.06 \\ 0 & -37 \end{bmatrix}$		
			participation factor matrix $\boldsymbol{B}_T$: $\begin{bmatrix} 0 & 6.8 \\ -0.01 & 0 \\ 6.54 & 0 \end{bmatrix}$		

Table 4.1: Numerical value of the main characteristics of the chaser spacecraft

The target case

Similar to the above developments, the kinematics and dynamic models of the target corresponds to (4.38),(4.39) and (4.42), where the notations "$\bullet_c$" and "$\bullet^{(c)}$" are replaced by "$\bullet_t$" and "$\bullet^{(t)}$", respectively. For instance, $\dot{\bar{\mathbf{q}}}_t = \frac{1}{2}\bar{\mathbf{q}}_t \circ \bar{\boldsymbol{\omega}}_t^{(t)}$ refers to the kinematics equation of the target. Of course, dealing with the target, the dual forces due to the actuation unit, the solar array flexible modes and propellant sloshing, do not exist, so that the total dual force that is applied to the target is concerned by the disturbances, i.e. $\bar{\boldsymbol{f}}_{t_d}^{(t)} = \bar{\boldsymbol{f}}_\nabla^{(t)} + \bar{\boldsymbol{f}}_{J_2}^{(t)} + \bar{\boldsymbol{f}}_{atm}^{(t)} + \bar{\boldsymbol{f}}_g^{(t)}$.

4.4.4 Dual quaternion based relative coupled dynamics

By virtue of the dual quaternion algebra, the motion between the target and the chaser can be expressed in the chaser frame as the relative quaternion described by

$$\bar{\mathbf{q}}_e = \bar{\mathbf{q}}_t^* \circ \bar{\mathbf{q}}_c = \mathbf{q}_e + \varepsilon \frac{1}{2} \mathbf{q}_e \circ \boldsymbol{r}_e^{(c)} \tag{4.51}$$

where $\boldsymbol{r}_e^{(c)} = \boldsymbol{r}_c^{(c)} - \mathbf{q}_t^* \circ \mathbf{q}_c \circ \boldsymbol{r}_t^{(t)} \circ \mathbf{q}_c^* \circ \mathbf{q}_t$ is the relative position between the chaser and the target expressed in the chaser frame $\mathcal{F}_c$. The time derivative of this relative error takes the following form:

$$\dot{\bar{\mathbf{q}}}_e = \dot{\bar{\mathbf{q}}}_t^* \circ \bar{\mathbf{q}}_c + \bar{\mathbf{q}}_t^* \circ \dot{\bar{\mathbf{q}}}_c \tag{4.52}$$

Based on (4.38), the definition of $\dot{\bar{\mathbf{q}}}_t = \frac{1}{2} \bar{\mathbf{q}}_t \circ \bar{\boldsymbol{\omega}}_t^{(t)}$ is obtained. Substituting this definition and (4.38) in (4.52), it follows:

$$\begin{aligned} \dot{\bar{\mathbf{q}}}_e &= -\frac{1}{2} \bar{\boldsymbol{\omega}}_t^{(t)} \circ \bar{\mathbf{q}}_t^* \circ \bar{\mathbf{q}}_c + \frac{1}{2} \bar{\mathbf{q}}_t^* \circ \bar{\mathbf{q}}_c \circ \bar{\boldsymbol{\omega}}_c^{(c)} \\ &= \frac{1}{2} \bar{\mathbf{q}}_t^* \circ \bar{\mathbf{q}}_c \circ \left(\bar{\boldsymbol{\omega}}_c^{(c)} - \bar{\mathbf{q}}_t^* \circ \bar{\mathbf{q}}_c \circ \bar{\boldsymbol{\omega}}_t^{(t)} \circ \bar{\mathbf{q}}_c^* \circ \bar{\mathbf{q}}_t \right) \end{aligned} \tag{4.53}$$

Let $\bar{\boldsymbol{\omega}}_e^{(c)} = \bar{\boldsymbol{\omega}}_c^{(c)} - \bar{\mathbf{q}}_t^* \circ \bar{\mathbf{q}}_c \circ \bar{\boldsymbol{\omega}}_t^{(t)} \circ \bar{\mathbf{q}}_c^* \circ \bar{\mathbf{q}}_t$ be now considered. Following (4.51), the relative kinematic error equation can thus be expressed as:

$$\dot{\bar{\mathbf{q}}}_e = \frac{1}{2} \bar{\mathbf{q}}_e \circ \bar{\boldsymbol{\omega}}_e^{(c)} \tag{4.54}$$

According to [DHFM17], the relative dual angular velocity described as $\bar{\boldsymbol{\omega}}_e^{(c)} = \boldsymbol{\omega}_e^{(c)} + \varepsilon \left(\dot{\boldsymbol{r}}_e^{(c)} + \boldsymbol{\omega}_e^{(c)} \times \boldsymbol{r}_e^{(c)} \right)$ can also be expressed as:

$$\bar{\boldsymbol{\omega}}_e^{(c)} = \bar{\boldsymbol{\omega}}_c^{(c)} - \bar{\mathbf{q}}_e^* \circ \bar{\boldsymbol{\omega}}_t^{(t)} \circ \bar{\mathbf{q}}_e \tag{4.55}$$

Computing the time derivative of (4.55) gives:

$$\dot{\bar{\boldsymbol{\omega}}}_e^{(c)} = \dot{\bar{\boldsymbol{\omega}}}_c^{(c)} - \left(\dot{\bar{\mathbf{q}}}_e^* \circ \bar{\boldsymbol{\omega}}_t^{(t)} \circ \bar{\mathbf{q}}_e + \bar{\mathbf{q}}_e^* \circ \dot{\bar{\boldsymbol{\omega}}}_t^{(t)} \circ \bar{\mathbf{q}}_e + \bar{\mathbf{q}}_e^* \circ \bar{\boldsymbol{\omega}}_t^{(t)} \circ \dot{\bar{\mathbf{q}}}_e \right) \tag{4.56}$$

Substituting $\dot{\bar{\mathbf{q}}}_e$ by its definition in (4.54), the expression (4.56) becomes:

$$\dot{\bar{\boldsymbol{\omega}}}_e^{(c)} = \dot{\bar{\boldsymbol{\omega}}}_c^{(c)} + \frac{1}{2} \bar{\mathbf{q}}_e^* \circ \bar{\boldsymbol{\omega}}_e^{(c)} \circ \bar{\boldsymbol{\omega}}_t^{(t)} \circ \bar{\mathbf{q}}_e - \bar{\mathbf{q}}_e^* \circ \dot{\bar{\boldsymbol{\omega}}}_t^{(t)} \circ \bar{\mathbf{q}}_e - \bar{\mathbf{q}}_e^* \circ \bar{\boldsymbol{\omega}}_t^{(t)} \circ \frac{1}{2} \bar{\mathbf{q}}_e \circ \bar{\boldsymbol{\omega}}_e^{(c)} \tag{4.57}$$

Using the identity (4.32) and applying it to the terms $\frac{1}{2} \bar{\mathbf{q}}_e^* \circ \bar{\boldsymbol{\omega}}_e^{(c)} \circ \bar{\boldsymbol{\omega}}_t^{(t)} \circ \bar{\mathbf{q}}_e - \bar{\mathbf{q}}_e^* \circ \bar{\boldsymbol{\omega}}_t^{(t)} \circ \frac{1}{2} \bar{\mathbf{q}}_e \circ \bar{\boldsymbol{\omega}}_e^{(c)}$, the equation (4.57) can be reformulated as:

$$\dot{\bar{\boldsymbol{\omega}}}_e^{(c)} = \dot{\bar{\boldsymbol{\omega}}}_c^{(c)} - \bar{\mathbf{q}}_e^* \circ \dot{\bar{\boldsymbol{\omega}}}_t^{(t)} \circ \bar{\mathbf{q}}_e + \bar{\boldsymbol{\omega}}_e^{(c)} \times \left(\bar{\mathbf{q}}_e^* \circ \bar{\boldsymbol{\omega}}_t^{(t)} \circ \bar{\mathbf{q}}_e \right) \tag{4.58}$$

Let $\bar{\boldsymbol{f}}_{ct}^{(c)} = \bar{\boldsymbol{f}}_c^{(c)} - \bar{\boldsymbol{f}}_t^{(c)}$ where $\bar{\boldsymbol{f}}_t^{(c)} \in \mathbb{V}^3$ refers to the total dual force affecting the target (see section 4.4.3), given in the chaser frame, i.e. $\bar{\boldsymbol{f}}_t^{(c)}$ is deduced from $\bar{\boldsymbol{f}}_{t_d}^{(t)}$ by means of the following change of coordinates:

$$\bar{\boldsymbol{f}}_t^{(c)} = \bar{\mathbf{q}}_e^* \circ \bar{\boldsymbol{f}}_{t_d}^{(t)} \circ \bar{\mathbf{q}}_e \tag{4.59}$$

Then, substituting (4.42) into (4.58) leads to

$$\dot{\bar{\boldsymbol{\omega}}}_e^{(c)} = -\bar{\boldsymbol{M}}^{-1} \circ \left(\bar{\boldsymbol{\omega}}_c^{(c)} \times \bar{\boldsymbol{M}} \circ \bar{\boldsymbol{\omega}}_c^{(c)} \right) + \bar{\boldsymbol{M}}^{-1} \circ \bar{\boldsymbol{f}}_{ct}^{(c)} - \bar{\mathbf{q}}_e^* \circ \dot{\bar{\boldsymbol{\omega}}}_t^{(t)} \circ \bar{\mathbf{q}}_e + \bar{\boldsymbol{\omega}}_e^{(c)} \times \left(\bar{\mathbf{q}}_e^* \circ \bar{\boldsymbol{\omega}}_t^{(t)} \circ \bar{\mathbf{q}}_e \right) \tag{4.60}$$

The relative kinematic (4.54) and dynamic (4.60) equations are defined similarly to the developments presented in [BS99, WS12].

4.4.5 Thruster-based propulsion unit with fault model considerations

In (4.60), the control command is given in terms of the dual force $\bar{\boldsymbol{f}}_{c_u}^{(c)} = \boldsymbol{f}_{c_u}^{(c)} + \varepsilon\boldsymbol{\tau}_{c_u}^{(c)}$. To execute a control law practically, one needs to solve the force $\boldsymbol{f}_{c_u}^{(c)}$ and torque $\boldsymbol{\tau}_{c_u}^{(c)}$ from $\bar{\boldsymbol{f}}_{c_u}^{(c)}$, and then, to allocate them on the spacecraft, by means of an actuation system. As mentioned before, it is considered that the chaser has a set of 24 thrusters of 2 N, in the configuration shown in Fig. 4.1.

For that purpose, the formula (4.60) is divided into its real part and dual part. Noticing the particular geometry of the target and the capture mechanism, one can simplify the relative attitude model to the attitude model of the chaser. This simply illustrates the fact that, since the target is a spheric spacecraft and the capture mechanism is a basket, the only attitude control requirement to satisfy, is the attitude of the chaser, and not the relative attitude between the two spacecraft. Mathematically, this leads to the consideration of the following equations:

$$\dot{\boldsymbol{\omega}}_e^{(c)} = -\boldsymbol{J}^{-1}\left(\boldsymbol{\omega}_e^{(c)} \times \boldsymbol{J}\boldsymbol{\omega}_e^{(c)}\right) + \boldsymbol{J}^{-1}\left(\boldsymbol{\tau}_{c_u}^{(c)} + \boldsymbol{\tau}_{ct_d}^{(c)} + \boldsymbol{\tau}_{c_f}^{(c)}\right) \tag{4.61}$$

for the rotational dynamics, and

$$\ddot{\boldsymbol{r}}_e^{(c)} = -\boldsymbol{\omega}_e^{(c)} \times \dot{\boldsymbol{r}}_e^{(c)} - \boldsymbol{\omega}_e^{(c)} \times \boldsymbol{\omega}_e^{(c)} \times \boldsymbol{r}_e^{(c)} + \frac{\boldsymbol{f}_{c_u}^{(c)}}{m} + \frac{\boldsymbol{f}_{ct_d}^{(c)}}{m} + \frac{\boldsymbol{f}_{c_f}^{(c)}}{m} \tag{4.62}$$

for the translational dynamics, with $\boldsymbol{\omega}_e^{(c)} = \boldsymbol{\omega}_c^{(c)}$, $\bar{\boldsymbol{f}}_{ct_d}^{(c)} \in \mathbb{V}^3 : \bar{\boldsymbol{f}}_{ct_d}^{(c)} = \bar{\boldsymbol{f}}_{c_d}^{(c)} - \bar{\boldsymbol{f}}_t^{(c)} = \boldsymbol{f}_{ct_d}^{(c)} + \varepsilon\boldsymbol{\tau}_{ct_d}^{(c)}$, $\boldsymbol{f}_{ct_d}^{(c)} \in \mathbb{R}^3$ and $\boldsymbol{\tau}_{ct_d}^{(c)} \in \mathbb{R}^3$ referring to the induced force and torque due to disturbances affecting both the chaser and target spacecraft, given in the chaser frame $\mathcal{F}_c$. The detailed mathematical development for obtaining (4.61) and (4.62) can be found in the Appendix A.5.

Let $u_{c_k}^{(c)}(t)$, $k = \overline{1,24}$ be the commanded opening of the k-th thruster valve. Then, the control commands $\boldsymbol{\tau}_{c_u}^{(c)}$, $\boldsymbol{f}_{c_u}^{(c)}$ generated by the 24 thrusters are given by (for fault free cases)

$$\begin{bmatrix} \boldsymbol{\tau}_{c_u}^{(c)}(t) \\ \boldsymbol{f}_{c_u}^{(c)}(t) \end{bmatrix} = \begin{bmatrix} \boldsymbol{R}_\tau \\ \boldsymbol{R}_f \end{bmatrix} \boldsymbol{u}_c^{(c)}(t) = \boldsymbol{R}\boldsymbol{u}_c^{(c)}(t), \quad \boldsymbol{R} \in \mathbb{R}^{6\times 24} \tag{4.63}$$

The columns of $\boldsymbol{R}$ (called the thruster configuration matrix) are the influence coefficients defining how each thruster commands $u_{c_k}^{(c)}$, $k = \overline{1,24}$ affects each component of $\boldsymbol{\tau}_{c_u}^{(c)}$ and $\boldsymbol{f}_{c_u}^{(c)}$.

From (4.63), it is clear that one can independently address the model either using the torque/force control inputs (in this case, equations (4.61) and (4.62) are directly used), or using the thruster commands (in this case, (4.63) is considered).

The CA unit is described in a similar manner as in Section 3.3, but considering that the maximum opening valve value is $u_{max_k} = 2\,\text{N}$ and that $k = \overline{1,24}$. The placement of the CA unit in the control loop is illustrated in Fig. 4.5.

With regards to the faults considered in this work, the focus is on the stuck open (fully open) and stuck closed (closed thruster) faults, i.e. a thruster valve opens/closes during operating, until its maximum/minimum position. The following mathematical model can be used to describe these faults [Hen08, HCT+19]

$$\phi_k(t) = \begin{cases} \max\{u_k(t), 1\} & \text{if stuck open} \\ 0 & \text{if stuck closed} \end{cases} \tag{4.64}$$

where the index k refers to the k^{th} thruster. Assuming no simultaneous faults, the considered thruster faults can be modeled in a multiplicative way according to (2.89), as (the notation "$\tilde{\bullet}$"

outlines the faulty case)

$$\tilde{u}_{c_k}^{(c)}(t) = (\mathbb{I}_{24} - \Psi(t))\, u(t) \tag{4.65}$$

with $\Psi(t) = diag\,(\psi_1(t), ..., \psi_{24}(t))$, where $0 \leq \psi_k(t) \leq 1, k = \overline{1,24}$ are unknown. The status of the kth thruster is modeled by ψ_k as follows:

$$\psi_k(t) = \begin{cases} 0 & \text{if healthy} \\ 1 - \phi_k(t)/u_{c_k}^{(c)}(t) & \text{if faulty} \end{cases} \tag{4.66}$$

where ϕ_k enables to consider the two different fault scenarios.

Thus, $\tilde{u}_{c_k}^{(c)}(t)$ is nothing else that the real opening of the k^{th} thruster valve at the time t, which is of course not known. It follows from (4.65) and (4.63) that the force $\boldsymbol{f}_{c_f}^{(c)}$ and the torque $\boldsymbol{\tau}_{c_f}^{(c)}$ due to the occurrence of the faults, are given by

$$\begin{bmatrix} \boldsymbol{\tau}_{c_f}^{(c)}(t) \\ \boldsymbol{f}_{c_f}^{(c)}(t) \end{bmatrix} = \sum_{k=1}^{24} \boldsymbol{K}_k f_k(t) \tag{4.67}$$

where the k^{th} column of the matrix $\boldsymbol{K}$ is the k^{th} fault signature associated to the k^{th} fault mode f_k. The indices $k = \overline{1,24}$ also coincide with the numbering of thrusters as given in Fig. 4.1, and thus with the columns of the matrix $\boldsymbol{R}$.

4.4.6 Fault tolerant control problem formulation

Thanks to the developments stated in the previous section, the fault tolerant control problem can be addressed either using equations (4.61) and (4.62), i.e. using a force/torque formulation, or with (4.61)-(4.65), i.e. based on a thruster command formulation. The proposed solution is based on the force/torque formulation. Fig. 4.5 gives an illustration of the FTC solution. As it can be seen, the proposed solution consists of a control signal defined by

$$\bar{\boldsymbol{f}}_{FTC}^{(c)} = \bar{\boldsymbol{f}}_{sm}^{(c)} - \bar{\hat{\boldsymbol{f}}}^{(c)} = \boldsymbol{f}_{sm}^{(c)} - \hat{\boldsymbol{f}}^{(c)} + \varepsilon \left(\boldsymbol{\tau}_{sm}^{(c)} - \hat{\boldsymbol{\tau}}^{(c)} \right) \tag{4.68}$$

where the control signals $\boldsymbol{f}_{sm}^{(c)}$ and $\boldsymbol{\tau}_{sm}^{(c)}$ are achieved by means of a SMC law, and more precisely, using the GSTA, see Section 2.5.4. The control signals $\hat{\boldsymbol{f}}^{(c)}$ and $\hat{\boldsymbol{\tau}}^{(c)}$ are achieved using a nonlinear estimator that provides the estimates of the real and the dual parts of the disturbances $\bar{\boldsymbol{f}}_{ct_d}^{(c)}$ and faults $\bar{\boldsymbol{f}}_{f}^{(c)}$. Finally, because it is of prime importance to consider physical limitations of actuators, especially within the context of FTC, an anti-windup system is joint to the GSTA-based controller. The external anti-windup principle [HMT+10] is used for that purpose.

Then, the problem turns out to be the design of the disturbance/fault estimator and the GSTA control law, so that the chaser tracks an attitude and a relative position reference trajectory $(\mathbf{q}_{ref}(t), \boldsymbol{r}_{ref}^{(c)}(t))$ that define the rendezvous and capture profiles, despite the presence of the disturbances $\bar{\boldsymbol{f}}_{ct_d}^{(c)}$ and the occurrence of faults $\bar{\boldsymbol{f}}_{c_f}^{(c)}$, while keeping stability in case of thruster saturations.

4.5 Design of the FTC system

4.5.1 The nonlinear fault/disturbance estimator

Following equations (4.61) and (4.62), it is required to design two estimators. The first one operates at the torque level and is in charge to estimate the disturbance and fault terms $\boldsymbol{\tau}_{ct_d}^{(c)}$ and

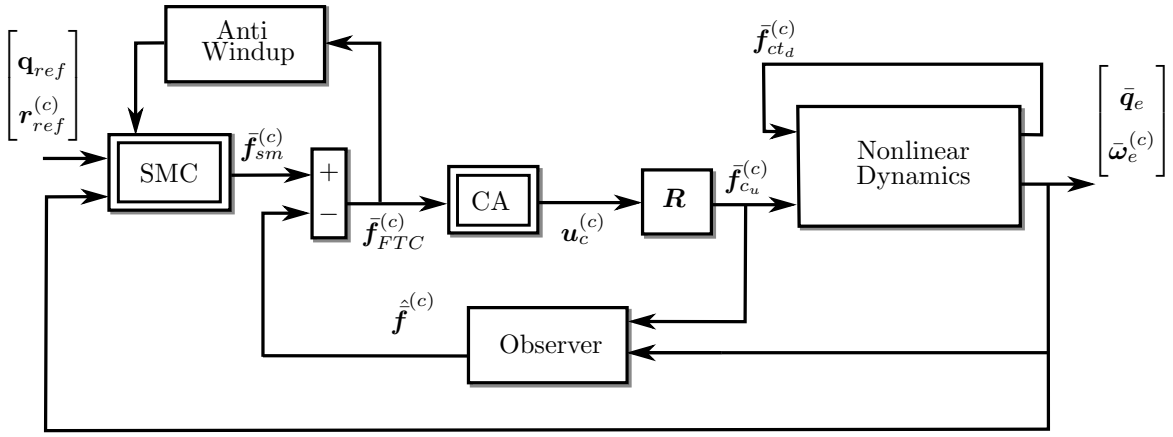

Figure 4.5: Control setup

$\boldsymbol{\tau}_{c_f}^{(c)}$. The second one operates at the force level and is in charge to estimate the disturbance and fault terms $\boldsymbol{f}_{ct_d}^{(c)}$ and $\boldsymbol{f}_{c_f}^{(c)}$.

From (4.61), the following estimate is proposed:

$$\begin{aligned} \hat{\dot{\boldsymbol{\omega}}}_c^{(c)} &= \boldsymbol{F}_\tau + \boldsymbol{J}^{-1}\boldsymbol{\tau}_{c_u}^{(c)} \\ \boldsymbol{F}_\tau &= -\boldsymbol{J}^{-1}\left(\boldsymbol{\omega}_c^{(c)} \times \boldsymbol{J}\boldsymbol{\omega}_c^{(c)}\right) \end{aligned} \tag{4.69}$$

Then, it is immediate to see that

$$\dot{\boldsymbol{\omega}}_c^{(c)} - \hat{\dot{\boldsymbol{\omega}}}_c^{(c)} = \boldsymbol{J}^{-1}\left(\boldsymbol{\tau}_{ct_d}^{(c)} + \boldsymbol{\tau}_{c_f}^{(c)}\right) \tag{4.70}$$

and thus, that an estimate of the disturbances and fault torques (sum of the two terms $\boldsymbol{\tau}_{ct_d}^{(c)}$ and $\boldsymbol{\tau}_{c_f}^{(c)}$) can be derived by reversing (4.70).

Similarly, the following estimate can be derived from (4.62)

$$\begin{aligned} \hat{\ddot{\boldsymbol{r}}}_e^{(c)} &= \boldsymbol{F}_f + \frac{\boldsymbol{f}_{c_u}^{(c)}}{m} \\ \boldsymbol{F}_f &= -\boldsymbol{\omega}_c^{(c)} \times \dot{\boldsymbol{r}}_e^{(c)} - \boldsymbol{\omega}_c^{(c)} \times \boldsymbol{\omega}_c^{(c)} \times \boldsymbol{r}_e^{(c)} \end{aligned} \tag{4.71}$$

and then, an estimate of the disturbances and fault forces (sum of the two terms $\boldsymbol{f}_{ct_d}^{(c)}$ and $\boldsymbol{f}_{c_f}^{(c)}$) can be derived by reversing the following equation:

$$\ddot{\boldsymbol{r}}_e^{(c)} - \hat{\ddot{\boldsymbol{r}}}_e^{(c)} = \frac{\boldsymbol{f}_{ct_d}^{(c)}}{m} + \frac{\boldsymbol{f}_{c_f}^{(c)}}{m} \tag{4.72}$$

Remember that the navigation unit is assumed to provide $\dot{\boldsymbol{\omega}}_c^{(c)}, \ddot{\boldsymbol{r}}_e^{(c)}$ and all variables that enter in $\boldsymbol{F}_\tau$ and $\boldsymbol{F}_f$, leading the aforementioned approach, computationally viable.

4.5.2 The general super twisting algorithm-based controller

Practically, it is reasonable to consider that (4.70) and (4.72) provide corrupted estimates for $\boldsymbol{\tau}_{ct_d}^{(c)} + \boldsymbol{\tau}_{c_f}^{(c)}$ and $\boldsymbol{f}_{ct_d}^{(c)} + \boldsymbol{f}_{c_f}^{(c)}$. Let us denote $\boldsymbol{\tau}_\Delta$ and $\boldsymbol{f}_\Delta$ these corruption terms, introduced such that:

$$\hat{\boldsymbol{\tau}}^{(c)} = \boldsymbol{J}\left(\dot{\boldsymbol{\omega}}_c^{(c)} - \hat{\dot{\boldsymbol{\omega}}}_c^{(c)}\right) = \boldsymbol{\tau}_{ct_d}^{(c)} + \boldsymbol{\tau}_{c_f}^{(c)} - \boldsymbol{\tau}_\Delta \tag{4.73}$$

$$\hat{\boldsymbol{f}}^{(c)} = m\left(\ddot{\boldsymbol{r}}_e^{(c)} - \hat{\ddot{\boldsymbol{r}}}_e^{(c)}\right) = \boldsymbol{f}_{ct_d}^{(c)} + \boldsymbol{f}_{c_f}^{(c)} - \boldsymbol{f}_\Delta \tag{4.74}$$

It is recalled that $\boldsymbol{\tau}_{ct_d}^{(c)}$ and $\boldsymbol{f}_{ct_d}^{(c)}$ include the dynamics of the flexible appendage and propellant sloshing, and then that they are functions of the system's state, see section 3.1 if necessary. Towards this end, it is assumed that $\boldsymbol{\tau}_\Delta$ and $\boldsymbol{f}_\Delta$ also depend on the system's state.

The following assumption, which guarantees that the forces and torques computed by the FTC law can be allocated by the CA algorithm on the thrusters, is now considered without loss of generality.

Assumption 5. *$\|\boldsymbol{f}_{FTC}^{(c)} - \boldsymbol{f}_{cu}^{(c)}\| \leq \epsilon$ and $\|\boldsymbol{\tau}_{FTC}^{(c)} - \boldsymbol{\tau}_{cu}^{(c)}\| \leq \epsilon$ with $\epsilon \to 0$. Here, the notation $\|\bullet\|$ is defined as the element-wise absolute value.*

Then, with (4.68), (4.73), (4.74) and under assumption 5, it can be verified that (4.61) and (4.62) can be rewritten:

$$\dot{\boldsymbol{\omega}}_c^{(c)} = \boldsymbol{F}_\tau + \boldsymbol{J}^{-1}\left(\boldsymbol{\tau}_{sm}^{(c)} + \boldsymbol{\tau}_\Delta\right) \tag{4.75}$$

$$\ddot{\boldsymbol{r}}_e^{(c)} = \boldsymbol{F}_f + \frac{1}{m}\left(\boldsymbol{f}_{sm}^{(c)} + \boldsymbol{f}_\Delta\right) \tag{4.76}$$

These equations are nothing else than the dynamics to be controlled by the GSTA-based controller.

The following assumption which is required for the existence of the GSTA, is made:

Assumption 6. *Let $\boldsymbol{\varphi} = \left[\left(\boldsymbol{J}^{-1}\boldsymbol{\tau}_\Delta\right)^\intercal \quad \frac{1}{m}\boldsymbol{f}_\Delta^\intercal\right]^\intercal$ be a vector of perturbations, that depends on a vector $\boldsymbol{s}$, a function of $\boldsymbol{q}_c, \boldsymbol{\omega}_c^{(c)}, \boldsymbol{r}_e^{(c)}, \dot{\boldsymbol{r}}_e^{(c)}$ ($\boldsymbol{s}$ will be the sliding surface later). It is assumed that $|\partial\boldsymbol{\varphi}/\partial t| \leq \delta_1$ and $|\partial\boldsymbol{\varphi}/\partial\boldsymbol{s}| \leq \delta_2$, where $|\bullet|$ states for the Euclidean norm.*

The following GSTA control scheme is proposed:

$$\boldsymbol{\tau}_{sm}^{(c)} = \boldsymbol{J}\left(-\boldsymbol{F}_\tau - \boldsymbol{K}_\tau\left[\frac{1}{2}\left[(\mathbf{q}_\epsilon)_s\boldsymbol{\omega}_c^{(c)} + (\mathbf{q}_\epsilon)_v \times \boldsymbol{\omega}_c^{(c)}\right]\right] - \boldsymbol{\alpha}_{1\tau}\boldsymbol{\phi}_{1\tau}(\boldsymbol{s}_\tau) - \boldsymbol{\alpha}_{2\tau}\int_0^t \boldsymbol{\phi}_{2\tau}(\boldsymbol{s}_\tau(\chi))d\chi\right) \tag{4.77}$$

$$\boldsymbol{f}_{sm}^{(c)} = m\left(-\boldsymbol{F}_f - \boldsymbol{K}_f\dot{\boldsymbol{r}}_\epsilon^{(c)} - \boldsymbol{\alpha}_{1f}\boldsymbol{\phi}_{1f}(\boldsymbol{s}_f) - \boldsymbol{\alpha}_{2f}\int_0^t \boldsymbol{\phi}_{2f}(\boldsymbol{s}_f(\chi))d\chi\right) \tag{4.78}$$

In these equations, $\mathbf{q}_\epsilon = \mathbf{q}_{ref}^* \circ \mathbf{q}_c$ and $\boldsymbol{r}_\epsilon^{(c)} = \boldsymbol{r}_{ref}^{(c)} - \boldsymbol{r}_e^{(c)}$ denote the chaser's quaternion tracking error and the relative position tracking error, respectively. $(\mathbf{q}_\epsilon)_s$ and $(\mathbf{q}_\epsilon)_v$ denote the scalar and vector part of the quaternion $\mathbf{q}_\epsilon$, respectively. In addition, according to [DHM16, WLS13], the decomposition of $\dot{\mathbf{q}}_\epsilon$ in scalar and vector part is defined as:

$$(\dot{\mathbf{q}}_\epsilon)_s = -\frac{1}{2}(\mathbf{q}_\epsilon)_v^\intercal\,\boldsymbol{\omega}_c^{(c)} \tag{4.79}$$

$$(\dot{\mathbf{q}}_\epsilon)_v = \frac{1}{2}\left[(\mathbf{q}_\epsilon)_s\,\boldsymbol{\omega}_c^{(c)} + (\mathbf{q}_\epsilon)_v \times \boldsymbol{\omega}_c^{(c)}\right] \tag{4.80}$$

In (4.77) and (4.78), $\boldsymbol{\phi}_{1j}(\boldsymbol{s}_j) = \lfloor\boldsymbol{s}_j\rceil^{1/2} + \boldsymbol{\beta}_j\boldsymbol{s}_j$ and $\boldsymbol{\phi}_{2j}(\boldsymbol{s}_j) = \frac{1}{2}\lfloor\boldsymbol{s}_j\rceil^0 + \frac{3}{2}\boldsymbol{\beta}_j\lfloor\boldsymbol{s}_j\rceil^{1/2} + \boldsymbol{\beta}_j^2 s$ are diagonal matrix functions, where $\lfloor\boldsymbol{s}_j\rceil^q = |\boldsymbol{s}_j|^q \operatorname{sign}(\boldsymbol{s}_j)$, for $j \in \{\tau, f\}$. $\boldsymbol{K}_j, \boldsymbol{\alpha}_{ij}, \boldsymbol{\beta}_j \in \mathbb{R}^3, i = 1, 2,\ j \in \{\tau, f\}$ are diagonal gain matrices to be designed. $\boldsymbol{s}_\tau$ and $\boldsymbol{s}_f$ denote sliding surfaces that are defined according to:

$$\boldsymbol{s}_\tau = \boldsymbol{\omega}_c^{(c)} + \boldsymbol{K}_\tau(\mathbf{q}_\epsilon)_v \tag{4.81}$$

$$\boldsymbol{s}_f = \dot{\boldsymbol{r}}_\epsilon^{(c)} + \boldsymbol{K}_f\boldsymbol{r}_\epsilon^{(c)} \tag{4.82}$$

The following theorem provides the solution to the design of $\boldsymbol{K}_j, \boldsymbol{\alpha}_{ij}, \boldsymbol{\beta}_j \in \mathbb{R}^3, i = 1, 2,\ j \in \{\tau, f\}$.

Theorem 3. *Under assumption 6, the control law (4.77)-(4.82) ensures trajectory tracking, globally and in finite time, despite the presence of the state-dependent perturbations $\boldsymbol{\tau}_\Delta$ and $\boldsymbol{f}_\Delta$, if $\boldsymbol{K}_\tau > 0, \boldsymbol{K}_f > 0$ and if there exists any $\kappa > 0$, $\boldsymbol{\alpha}_{1\tau}, \boldsymbol{\alpha}_{1f}, \boldsymbol{\alpha}_{2\tau}, \boldsymbol{\alpha}_{2f}, \boldsymbol{\beta}_\tau$ and $\boldsymbol{\beta}_f$ such that:*

$$\alpha_{1i} > \frac{2(1+\kappa)\delta_2}{\beta_i}, \ \alpha_{2i} > \frac{1}{4h_i\kappa}\left(2\delta_1\frac{1+\kappa}{\alpha_{1i}} + \frac{\kappa\delta_2}{\beta_i}\right)^2 + 2\delta_1 \tag{4.83}$$

$$h_i = 1 - \frac{\delta_2(1+\kappa)}{\beta_i\alpha_{1i}} \quad i = \overline{1,6} \tag{4.84}$$

$$\boldsymbol{\alpha}_j = diag\,(\boldsymbol{\alpha}_{j\tau}, \boldsymbol{\alpha}_{jf}) = diag(\alpha_{ji}) \quad j = 1,2 \quad i = \overline{1,6} \tag{4.85}$$

$$\boldsymbol{\beta} = diag\,(\boldsymbol{\beta}_\tau, \boldsymbol{\beta}_f) = diag(\beta_i) \quad i = \overline{1,6} \tag{4.86}$$

Proof. - Conditions on $\boldsymbol{\alpha}_{1\tau}, \boldsymbol{\alpha}_{1f}, \boldsymbol{\alpha}_{2\tau}, \boldsymbol{\alpha}_{2f}, \boldsymbol{\beta}_\tau$ and $\boldsymbol{\beta}_f$: Consider the definition of the sliding surface (4.81). Then, it follows with (4.75) and (4.80):

$$\dot{\boldsymbol{s}}_\tau = \dot{\boldsymbol{\omega}}_c^{(c)} + \boldsymbol{K}_\tau(\dot{\mathbf{q}}_\epsilon)_v = \boldsymbol{F}_\tau + \boldsymbol{J}^{-1}\left(\boldsymbol{\tau}_{sm}^{(c)} + \boldsymbol{\tau}_\Delta^{(c)}\right) + \boldsymbol{K}_\tau\left[\frac{1}{2}\left[(\mathbf{q}_\epsilon)_s\boldsymbol{\omega}_c^{(c)} + (\mathbf{q}_\epsilon)_v \times \boldsymbol{\omega}_c^{(c)}\right]\right] \tag{4.87}$$

Substituting (4.77) in (4.87), it follows

$$\dot{\boldsymbol{s}}_\tau = -\boldsymbol{\alpha}_{1\tau}\boldsymbol{\phi}_{1\tau}(\boldsymbol{s}_\tau) - \boldsymbol{\alpha}_{2\tau}\int_0^t \boldsymbol{\phi}_{2\tau}(\boldsymbol{s}_\tau(\chi))d\chi + \boldsymbol{J}^{-1}\boldsymbol{\tau}_\Delta \tag{4.88}$$

Now, consider the auxiliary variable $\boldsymbol{z}_\tau = -\boldsymbol{\alpha}_{2\tau}\int_0^t \boldsymbol{\phi}_{2\tau}(\boldsymbol{s}_\tau(\chi))d\chi + \boldsymbol{J}^{-1}\boldsymbol{\tau}_\Delta$. Then, (4.88) can be rewritten according to the following pair of differential equations:

$$\dot{\boldsymbol{s}}_\tau = -\boldsymbol{\alpha}_{1\tau}\boldsymbol{\phi}_{1\tau}(\boldsymbol{s}_\tau) + \boldsymbol{z}_\tau \tag{4.89}$$

$$\dot{\boldsymbol{z}}_\tau = -\boldsymbol{\alpha}_{2\tau}\boldsymbol{\phi}_{2\tau}(\boldsymbol{s}_\tau) + \boldsymbol{J}^{-1}\dot{\boldsymbol{\tau}}_\Delta \tag{4.90}$$

Similarly, it can be verified that the following equations can be derived from (4.78) and (4.82):

$$\dot{\boldsymbol{s}}_f = -\boldsymbol{\alpha}_{1f}\boldsymbol{\phi}_{1f}(\boldsymbol{s}_f) + \boldsymbol{z}_f \tag{4.91}$$

$$\dot{\boldsymbol{z}}_f = -\boldsymbol{\alpha}_{2f}\boldsymbol{\phi}_{2f}(\boldsymbol{s}_f) + \frac{1}{m}\dot{\boldsymbol{f}}_\Delta \tag{4.92}$$

with $\boldsymbol{z}_f = -\boldsymbol{\alpha}_{2f}\int_0^t \boldsymbol{\phi}_{2f}(\boldsymbol{s}_f(\chi))d\chi + \frac{1}{m}\boldsymbol{f}_\Delta$.

It is now fundamental to remind that $\boldsymbol{\tau}_\Delta$ and $\boldsymbol{f}_\Delta$ depend on both the rotational and translational states. Then (4.89)-(4.92) are coupled through the perturbations terms $\dot{\boldsymbol{\tau}}_\Delta$ and $\dot{\boldsymbol{f}}_\Delta$. In other words, and as stated in the introduction, the control problem described by (4.89)-(4.92) is a 6DOF control problem and then, the system of equations (4.89)-(4.90) can not be treated separately from the system of equations (4.91)-(4.92).

To proceed (4.89)-(4.92) are merged together and rewritten in the compact form

$$\dot{\boldsymbol{s}} = -\boldsymbol{\alpha}_1\boldsymbol{\phi}_1(s) + \boldsymbol{z} \tag{4.93}$$

$$\dot{\boldsymbol{z}} = -\boldsymbol{\alpha}_2\boldsymbol{\phi}_2(s) + \dot{\boldsymbol{\varphi}}(\boldsymbol{s}) \tag{4.94}$$

with $\boldsymbol{s} = \begin{bmatrix}\boldsymbol{s}_\tau^\intercal & \boldsymbol{s}_f^\intercal\end{bmatrix}^\intercal$, $\boldsymbol{z} = \begin{bmatrix}\boldsymbol{z}_\tau^\intercal & \boldsymbol{z}_f^\intercal\end{bmatrix}^\intercal$, $\boldsymbol{\varphi} = \begin{bmatrix}(\boldsymbol{J}^{-1}\boldsymbol{\tau}_\Delta)^\intercal & \frac{1}{m}\boldsymbol{f}_\Delta^\intercal\end{bmatrix}^\intercal$, $\boldsymbol{\alpha}_1 = \text{diag}\,(\boldsymbol{\alpha}_{1\tau}, \boldsymbol{\alpha}_{1f})$ and $\boldsymbol{\alpha}_2 = \text{diag}\,(\boldsymbol{\alpha}_{2\tau}, \boldsymbol{\alpha}_{2f})$. Then, noticing that, each matrix and matrix functions that enter in this equation have a diagonal structure and $\dot{\boldsymbol{\varphi}}(\boldsymbol{s}) = \frac{\partial\boldsymbol{\varphi}}{\partial t} + \left(\frac{\partial\boldsymbol{\varphi}}{\partial\boldsymbol{s}}\right)\dot{\boldsymbol{s}}$, it follows under assumption 6, that direct application of corollary 1 in [CFM18] leads to the conditions (4.83)-(4.86).

- *Conditions on $\boldsymbol{K}_\tau$ and $\boldsymbol{K}_f$:* Once $\boldsymbol{s}_\tau = 0$ is reached, $\boldsymbol{\omega}_c^{(c)} = -\boldsymbol{K}_\tau(\mathbf{q}_\epsilon)_v$. Consider the following Lyapunov function:

$$V_\tau = [1 - (\mathbf{q}_\epsilon)_s]^2 + (\mathbf{q}_\epsilon)_v^\intercal(\mathbf{q}_\epsilon)_v \tag{4.95}$$

The following expression is obtained by differentiating V_τ versus time, and employing (4.79)-(4.80):

$$\begin{aligned}
\dot{V}_\tau =& -2[1 - (\mathbf{q}_\epsilon)_s](\dot{\mathbf{q}}_\epsilon)_s + 2(\mathbf{q}_\epsilon)_v^\intercal(\dot{\mathbf{q}}_\epsilon)_v \\
=& -2[1 - (\mathbf{q}_\epsilon)_s][-\frac{1}{2}(\mathbf{q}_\epsilon)_v^\intercal\boldsymbol{\omega}_c^{(c)}] + 2(\mathbf{q}_\epsilon)_v^\intercal\frac{1}{2}[(\mathbf{q}_\epsilon)_s\boldsymbol{\omega}_c^{(c)} + (\mathbf{q}_\epsilon)_v \times \boldsymbol{\omega}_c^{(c)}] \\
=& -2[-\frac{1}{2}(\mathbf{q}_\epsilon)_v^\intercal\boldsymbol{\omega}_c^{(c)} + \frac{1}{2}(\mathbf{q}_\epsilon)_s(\mathbf{q}_\epsilon)_v^\intercal\boldsymbol{\omega}_c^{(c)}] + 2(\mathbf{q}_\epsilon)_v^\intercal\frac{1}{2}[(\mathbf{q}_\epsilon)_s\boldsymbol{\omega}_c^{(c)} + (\mathbf{q}_\epsilon)_v \times \boldsymbol{\omega}_c^{(c)}] \\
=& -[(\mathbf{q}_\epsilon)_v^\intercal\boldsymbol{K}_\tau(\mathbf{q}_\epsilon)_v - (\mathbf{q}_\epsilon)_s(\mathbf{q}_\epsilon)_v^\intercal\boldsymbol{K}_\tau(\mathbf{q}_\epsilon)_v] - (\mathbf{q}_\epsilon)_v^\intercal(\mathbf{q}_\epsilon)_s\boldsymbol{K}_\tau(\mathbf{q}_\epsilon)_v \\
=& -(\mathbf{q}_\epsilon)_v^\intercal\boldsymbol{K}_\tau(\mathbf{q}_\epsilon)_v
\end{aligned} \tag{4.96}$$

which is strictly definite negative iff $\boldsymbol{K}_\tau > 0$. Similarly, once $\boldsymbol{s}_f = 0$ is reached, $\dot{\boldsymbol{r}}_\epsilon^{(c)} = -\boldsymbol{K}_f\boldsymbol{r}_\epsilon^{(c)}$. Consider the following Lyapunov function:

$$V_f = \frac{1}{2}\boldsymbol{r}_\epsilon^{(c)\intercal}\boldsymbol{r}_\epsilon^{(c)} \tag{4.97}$$

By differentiating V_f versus time, it follows:

$$\dot{V}_f = \boldsymbol{r}_\epsilon^{(c)\intercal}\dot{\boldsymbol{r}}_\epsilon^{(c)} = -\boldsymbol{r}_\epsilon^{(c)\intercal}\boldsymbol{K}_f\boldsymbol{r}_\epsilon^{(c)} \tag{4.98}$$

which is definite negative iff $\boldsymbol{K}_f > 0$. □

4.5.3 The anti-windup system

If equations (4.77) and (4.78) are directly used as the control law, saturation caused by the integral term may lead to a severe overshoot in the system, or provoke instability of the closed loops. This point becomes especially crucial when dealing with the fault tolerant control problem, since faults may cause actuator saturation. Here, anti-windup coefficients of the general form $e^{\lambda c_i}, \lambda < 0$ are introduced in (4.77) and (4.78) as follows:

$$\begin{aligned}
\boldsymbol{\tau}_{sm}^{(c)} =& \boldsymbol{J}\left(-\boldsymbol{F}_\tau - \boldsymbol{K}_\tau\left[\frac{1}{2}\left[(\mathbf{q}_\epsilon)_s\boldsymbol{\omega}_c^{(c)} + (\mathbf{q}_\epsilon)_v \times \boldsymbol{\omega}_c^{(c)}\right]\right] - \boldsymbol{\alpha}_{1\tau}\boldsymbol{\phi}_{1\tau}(\boldsymbol{s}_\tau)\right. \\
& \left. -\boldsymbol{\alpha}_{2\tau}\mathrm{diag}(e^{\lambda\Delta_{\tau i}})\int_0^t \boldsymbol{\phi}_{2\tau}(\boldsymbol{s}_\tau(\chi))d\chi\right)
\end{aligned} \tag{4.99}$$

$$\boldsymbol{f}_{sm}^{(c)} = m\left(-\boldsymbol{F}_f - \boldsymbol{K}_f\dot{\boldsymbol{r}}_\epsilon^{(c)} - \boldsymbol{\alpha}_{1f}\boldsymbol{\phi}_{1f}(\boldsymbol{s}_f) - \boldsymbol{\alpha}_{2f}\mathrm{diag}(e^{\lambda\Delta_{fi}})\int_0^t \boldsymbol{\phi}_{2f}(\boldsymbol{s}_f(\chi))d\chi\right) \quad i = \overline{1,3} \tag{4.100}$$

To explain the role of $\Delta_{\tau i}, \Delta_{fi}$, $i = \overline{1,3}$, recall that the thruster configuration consists of 24 thrusters of $2N$. Then, the control vector $\boldsymbol{u}_c^{(c)}$ ranges in a hypercube of dimension 24. The images of this hypercube through the thruster configuration matrices $\boldsymbol{R}_\tau$ and $\boldsymbol{R}_f$ (see eq. (4.63)) are polytopes $\boldsymbol{\Pi}_\tau$ and $\boldsymbol{\Pi}_f$ (computed as in (4.1)). As explained in Section 4.2, these polytopes are nothing else than the torque and force domains, that can be attained by the thruster-based actuation unit. Thus, saturation occurs if a torque and/or a force outside of $\boldsymbol{\Pi}_\tau$ and $\boldsymbol{\Pi}_f$, is asked to be allocated on the thrusters, see Fig. 4.6 that gives an illustration for the torque case.

If saturation occurs, which means that $\boldsymbol{\tau}_{FTC}^{(c)}$ and/or $\boldsymbol{f}_{FTC}^{(c)}$ are outside $\boldsymbol{\Pi}_\tau$ and $\boldsymbol{\Pi}_f$, respectively, then the nearest attainable torque and/or force that belongs to $\boldsymbol{\Pi}_\tau/\boldsymbol{\Pi}_f$, is computed, in the least

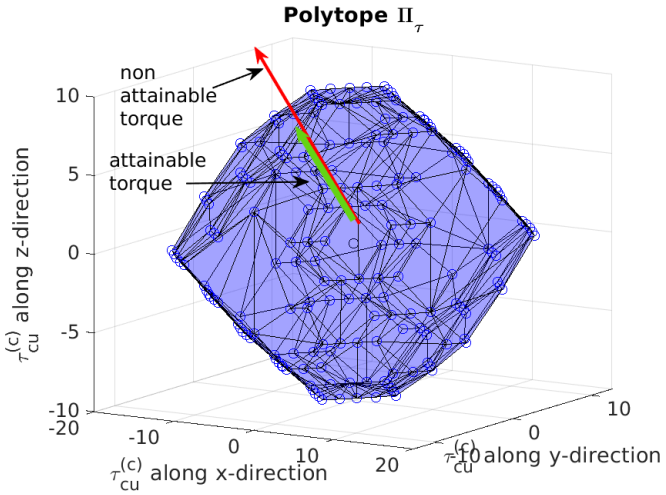

Figure 4.6: The polytope $\boldsymbol{\Pi}_\tau$ (attainable torque domain)

square optimal sense. To formulate this problem, denote $\boldsymbol{\tau}_0^{(c)}$ and $\boldsymbol{f}_0^{(c)}$ as the optimal attainable torque and force. Then the problem turns out to solve on-line, the following optimisation problems

$$\begin{aligned} &\min_{\boldsymbol{\tau}_0^{(c)}} \left\| \boldsymbol{\tau}_{FTC}^{(c)} - \boldsymbol{\tau}_0^{(c)} \right\|_2 \quad \text{s.t.} \quad \boldsymbol{\tau}_0^{(c)} \in \boldsymbol{\Pi}_\tau \\ &\min_{\boldsymbol{f}_0^{(c)}} \left\| \boldsymbol{f}_{FTC}^{(c)} - \boldsymbol{f}_0^{(c)} \right\|_2 \quad \text{s.t.} \quad \boldsymbol{f}_0^{(c)} \in \boldsymbol{\Pi}_f \end{aligned} \tag{4.101}$$

The terms $\Delta_{\tau i}, \Delta_{fi}$, $i = \overline{1,3}$ are then defined according to:

$$\begin{aligned} &\boldsymbol{\Delta}_\tau = \boldsymbol{\tau}_{FTC}^{(c)} - \boldsymbol{\tau}_0^{(c)} \quad \boldsymbol{\Delta}_f = \boldsymbol{f}_{FTC}^{(c)} - \boldsymbol{f}_0^{(c)} \\ &\boldsymbol{\Delta}_\tau = \text{vec}(\Delta_{\tau i}),\ \boldsymbol{\Delta}_f = \text{vec}(\Delta_{fi}),\ \Delta_{\tau i} \geq 0, ,\ \Delta_{fi} \geq 0 \quad i = \overline{1,3} \end{aligned} \tag{4.102}$$

Thus, with $\lambda < 0$, when $\Delta_{\tau i}, \Delta_{fi}$ is large enough for some "i", $e^{\lambda \Delta_{\tau i}}, e^{\lambda \Delta_{fi}}$ is near zero according to the property of the exponential function, vanishing the integral terms in the GSTA. *A contrario*, provided that the system is not saturated, $\boldsymbol{\tau}_0^{(c)} = \boldsymbol{\tau}_{FTC}^{(c)}$ and $\boldsymbol{f}_0^{(c)} = \boldsymbol{f}_{FTC}^{(c)}$. Then, the value of $e^{\lambda \Delta_{\tau i}}, e^{\lambda \Delta_{fi}}$, $i = \overline{1,3}$ is invariant and equal to 1, no matter how the GSTA will react to faults, the integral terms operate normally.

4.6 Simulation results

The performance of the proposed FTC architecture are next assessed using the Matlab/Simulink FES. A path planning algorithm based on a spline-based technique, has been implemented to generate smooth attitude quaternion $\mathbf{q}_{ref}(t)$ and relative position $\boldsymbol{r}_{ref}^{(c)}(t)$ references. With regards to the parameters of the GSTA (4.99) and (4.100), the following numerical values have been retained:

$$\begin{aligned} &\boldsymbol{\alpha}_{1\tau} \approx \text{diag}(0.002145, 0.001898, 0.002487) \\ &\boldsymbol{\alpha}_{2\tau} \approx \text{diag}(0.3373, 0.264, 0.4539).10^{-3} \\ &\boldsymbol{\alpha}_{1f} \approx \text{diag}(0.05056, 0.03464, 0.04609) \\ &\boldsymbol{\alpha}_{2f} \approx \text{diag}(0.01875, 0.0088, 0.01558) \\ &\boldsymbol{\beta}_\tau = \boldsymbol{\beta}_f = \text{diag}(1, 1.1, 1).10^{-4}, \quad \boldsymbol{K}_\tau = \boldsymbol{K}_f = \mathbb{I}_3 \end{aligned}$$

4.6.1 The perfect navigation case

One can begin by analyzing the behaviour of the system under nominal conditions, i.e. when noise does not affect the navigation unit and no faults are present. In Fig. 4.7, both phases of the rendezvous mission, acquisition and forced translation, are indicated. The chaser's orientation and relative position (in the LVLH frame) is illustrated in Fig. 4.7.a. In addition, in this figure the tracking errors can be appreciated. Fig. 4.7.c shows the thruster commands $\boldsymbol{u}_c^{(c)}(t)$ computed by the CA unit (3.21). The contribution of each thruster is better illustrated in Fig. 4.8. It is recalled that the proposed FTC solution $\bar{\boldsymbol{f}}_{FTC}^{(c)}$ consists of the GSTA controller $\bar{\boldsymbol{f}}_{sm}^{(c)}(t)$ and the estimation of the fault/disturbance estimator $\bar{\hat{\boldsymbol{f}}}^{(c)}$. When in nominal case, the output of the estimator represents the disturbances only. i.e. the sloshing phenomena and the flexible modes, as shown in Fig. 4.7.e. Finally, the proposed FTC solution $\bar{\boldsymbol{f}}_{FTC}^{(c)}$ is shown in Fig. 4.7.d and the GSTA controller $\bar{\boldsymbol{f}}_{sm}^{(c)}(t)$ in Fig. 4.7.f.

The simulated fault consists of a stuck open fault that occurs in the thruster 1 at time $t = 40s$, and is maintained until the end of the simulation. The fault time occurrence has been chosen, so that it covers both the acquisition phase and the forced translation phase. Fig. 4.9 show the results. Fig. 4.9.a illustrates the attitude, and Fig. 4.9.b gives the relative position (in the LVLH frame). The attitude and relative position tracking errors are also plotted, to appreciate the results. As in Fig. 4.7, the target acquisition phase and the forced translation phase are highlighted on the plots, for a better understanding of the motion performed by the chaser. The thruster commands $\boldsymbol{u}_c^{(c)}(t)$ computed by the CA, are illustrated on Fig. 4.9.c. A zoom is incorporated in the figure, to better appreciate the behaviour of $\boldsymbol{u}_c^{(c)}(t)$. The total control signal provided by the overall FTC scheme (dual force $\bar{\boldsymbol{f}}_{FTC}^{(c)}(t)$, see (4.68)) is shown on Fig. 4.9.d. The fault/disturbance dual force estimate $\bar{\hat{\boldsymbol{f}}}^{(c)}(t)$ is illustrated on 4.9.e and the dual force $\bar{\boldsymbol{f}}_{sm}^{(c)}(t)$ delivered by the GSTA controllers is shown on Fig. 4.9.f.

In addition, the contribution of each thruster is shown in Fig. 4.10. In this figure, the signals shown correspond to the computation of the control algorithm. It should be noted that the solution takes into account the faulty thruster, due to the fact that the control algorithm is unaware of the occurrence of the fault.

As it can be seen, during the acquisition phase, the attitude error does not exceed 0.4 deg and the relative position is less than 5 cm. During the forced translation phase and at the capture point, these errors are very close to zero. Furthermore, it can be seen on 4.9.c that these performance are obtained without actuator saturation, except during a short time which correspond to the transient behaviour of the FTC algorithm due to the fault occurrence. From the zoom presented in 4.9.c, it can be observed a sinus-like behaviour of $\boldsymbol{u}_c^{(c)}(t)$. The spectral density of $\boldsymbol{u}_c^{(c)}(t)$ reveals frequency components located at frequencies that correspond to the flexible modes of the solar array and propellant sloshing, which is quite reassuring.

In conclusion, the effectiveness of the proposed solution was proven under fault-free and faulty case, while considering a perfect navigation unit. This means that the tracking performance is maintained despite the occurrence of the fault. It is worth noting that the proposed FTC solution does not destabilize the system in the absence of faults.

4.6.2 Navigation unit in the loop

In this section, it is considered that the navigation unit provides noisy measurements. Recall that the navigation unit has a precision of 2 mm, 0.2 mm/s and 0.2 mm/s^2 for relative position, velocity and acceleration, over the three axes, and a precision of 0.1 deg, 0.01 deg/s and 0.01 deg/s^2 for

chaser attitude, angular rate and angular acceleration, over the three axes. In the presence of a fault, it is desired that the system maintains a performance as close as the one obtained under fault-free conditions. Thus, this performance is first illustrated in Fig. 4.11. The effects of the noise in the navigation unit can be clearly observed when comparing Fig. 4.7 against Fig. 4.11. The noise effect can be observed in a more clear way when comparing Fig. 4.8 against Fig. 4.12, where the contribution of each thruster is shown.

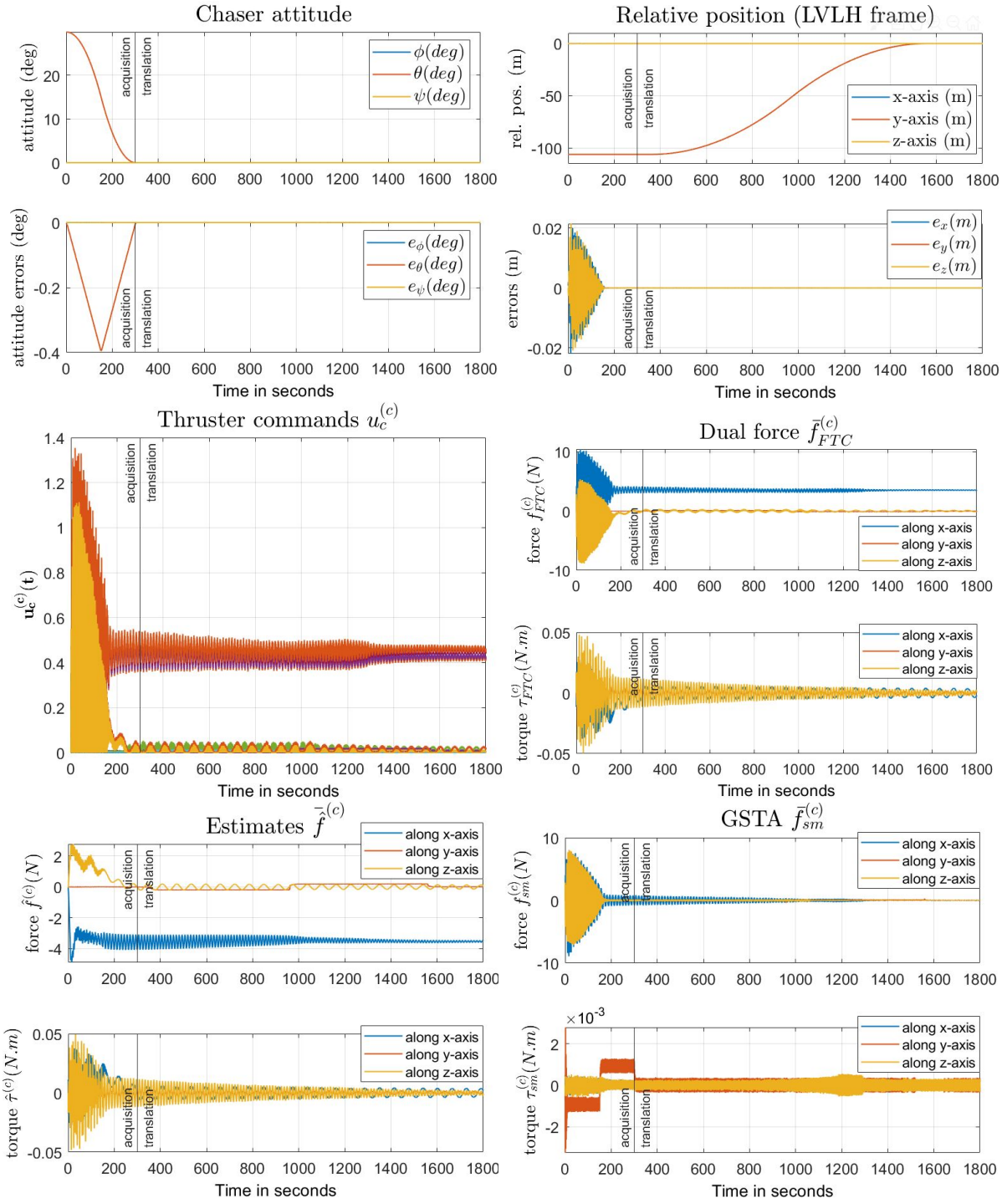

Figure 4.7: Nominal case with perfect navigation unit: a) Attitude of the chaser - b) Relative position - c) thruster commands $\boldsymbol{u}_c^{(c)}$ - d) dual force $\bar{\boldsymbol{f}}_{FTC}^{(c)}$ - e) fault/disturbance dual force estimate $\bar{\hat{\boldsymbol{f}}}^{(c)}$ - f) GSTA dual force $\bar{\boldsymbol{f}}_{sm}^{(c)}$.

The performance of the FTC scheme is now analyzed by considering the same faulty situation, but with a noisy navigation unit in the loop. The results are shown in Fig. 4.13. The effect of the navigation errors and measurement noises on the control signals can be appreciated in Fig.

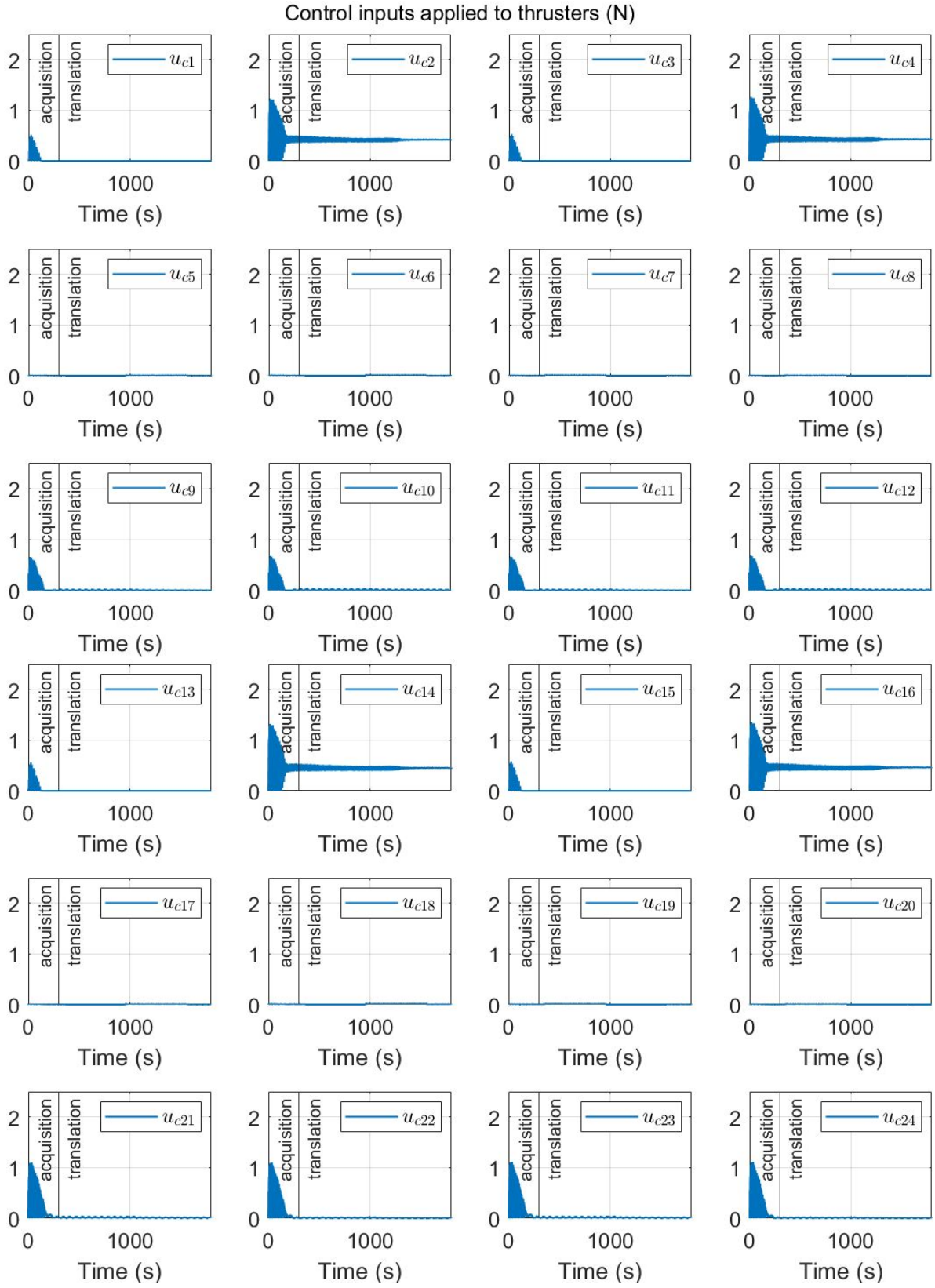

Figure 4.8: Control inputs applied to each thruster for the nominal case with perfect navigation unit

4.13.c to 4.13.e. However, despite this phenomenon, the capture performance is satisfactory, since during the last 10 meters, the attitude error does not exceed 0.05 deg and the relative position is less than 1 cm along the three axis. It can be inferred from the presented figures that the obtained results are satisfactory since the proposed FTC solution has the capability of compensating the occurrence of the fault despite the noisy measurements.

Furthermore, the control signals applied to each thruster are shown in Fig. 4.14. It is important

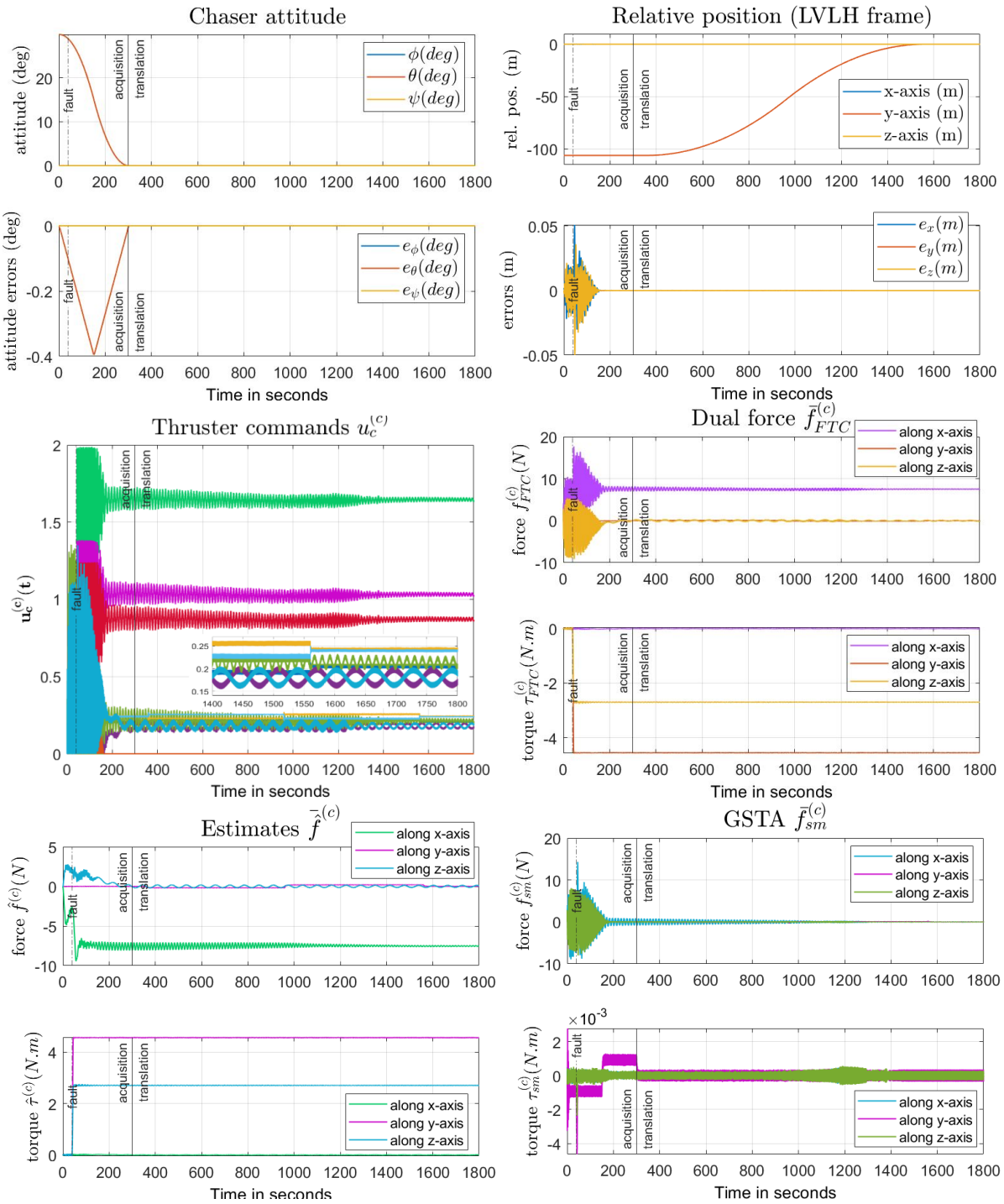

Figure 4.9: Perfect navigation and stuck-open fault in THR 1: a) Attitude of the chaser - b) Relative position - c) thruster commands $\boldsymbol{u}_c^{(c)}$ - d) dual force $\bar{\boldsymbol{f}}_{FTC}^{(c)}$ - e) fault/disturbance dual force estimate $\hat{\bar{\boldsymbol{f}}}^{(c)}$ - f) GSTA dual force $\bar{\boldsymbol{f}}_{sm}^{(c)}$.

to note that in this figure, the observed signals represent the values that the control algorithm computed and not the output of the thruster. This is why the value of the signal that corresponds to the first thruster does not represent the stuck open fault. In addition, the reader must remember that given that the control algorithm is unaware of the occurrence of the fault, the solution includes a computed signal for the faulty thruster.

4.6.3 Simulation campaign with the FES

The proposed FTC solution is finally evaluated through an intensive simulation campaign using the Matlab/Simulink FES. A total of 48 runs have been done, so that each faulty situation is

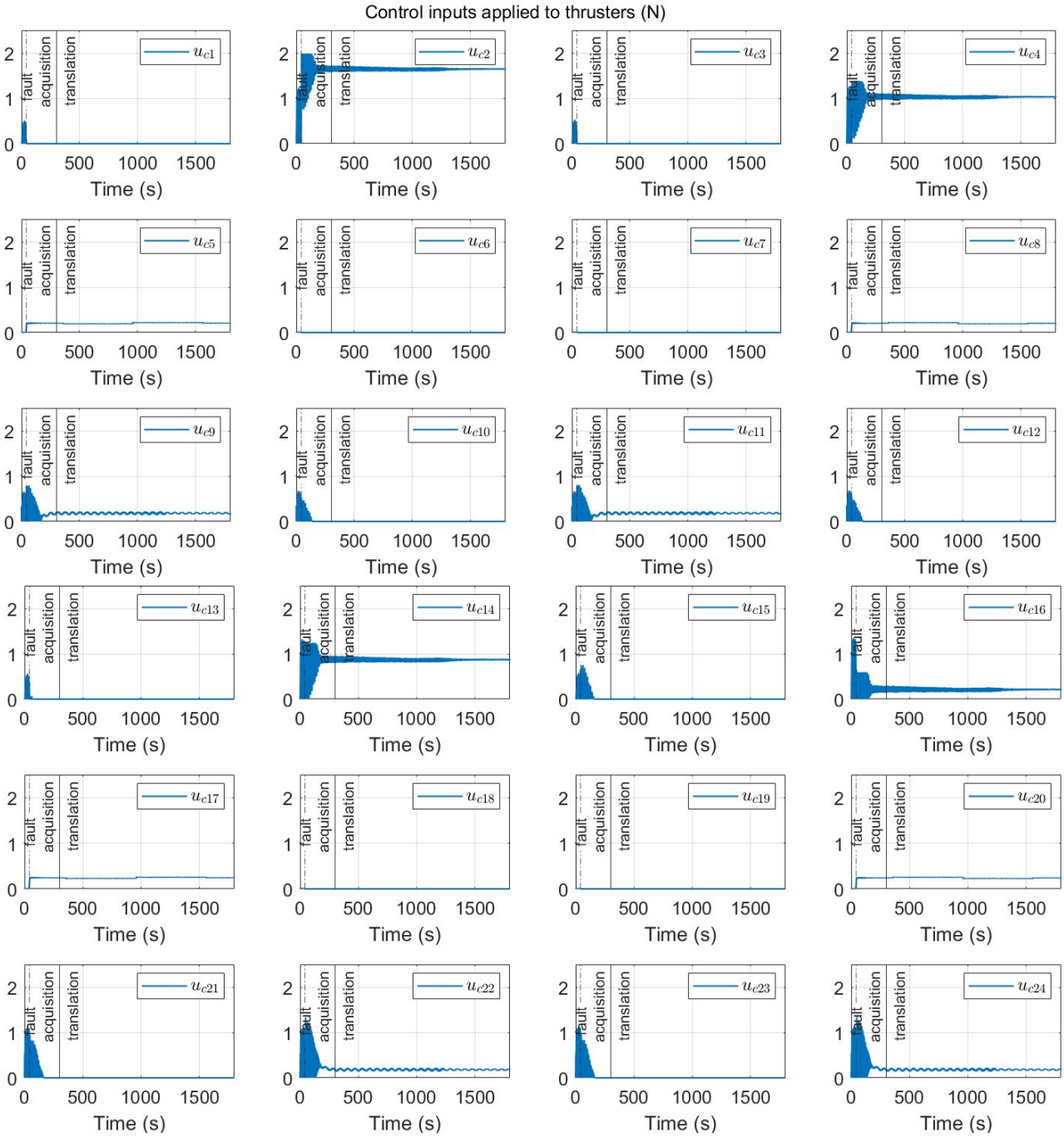

Figure 4.10: Control inputs applied to each thruster for the perfect navigation and stuck-open fault in THR 1

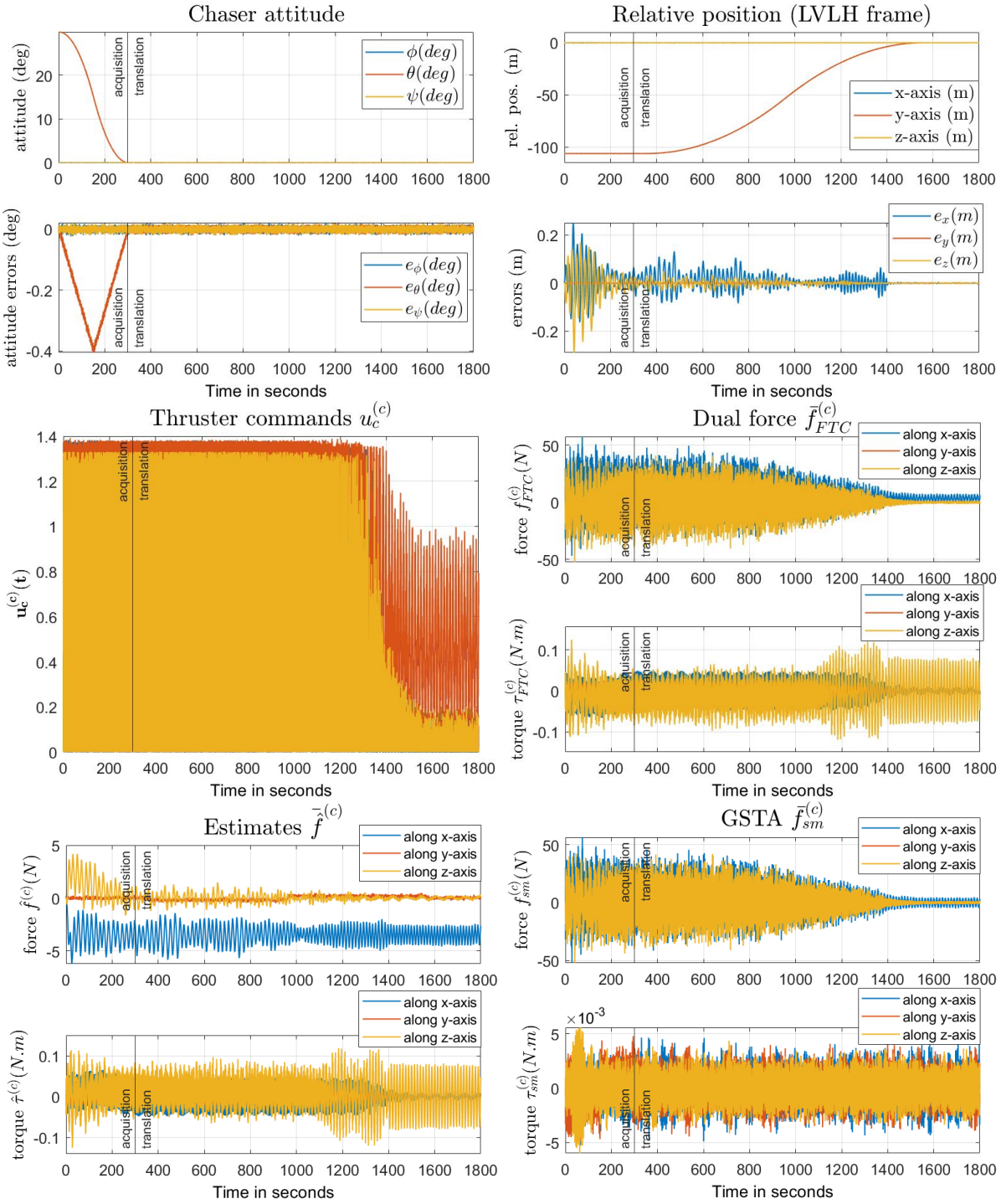

Figure 4.11: Fault free case with navigation in the loop: a) Attitude of the chaser - b) Relative position - c) dual force $\bar{\boldsymbol{f}}_{FTC}^{(c)}$ - d) thruster commands $\boldsymbol{u}_c^{(c)}$ - e) fault/disturbance dual force estimates $\hat{\bar{\boldsymbol{f}}}^{(c)}$ - f) GSTA dual force $\bar{\boldsymbol{f}}_{sm}^{(c)}$.

covered. More precisely, for each thruster, a stuck open fault and a stuck close fault are simulated at $t = 40s$ and is maintained during the end of the simulation.

As mentioned before, the importance of the anti-windup strategy relies on avoiding thruster saturation due to the control law. To highlight its effect, a simulation campaign that does not consider the anti-windup strategy and noise in the navigation unit, is done. In the following, this is called

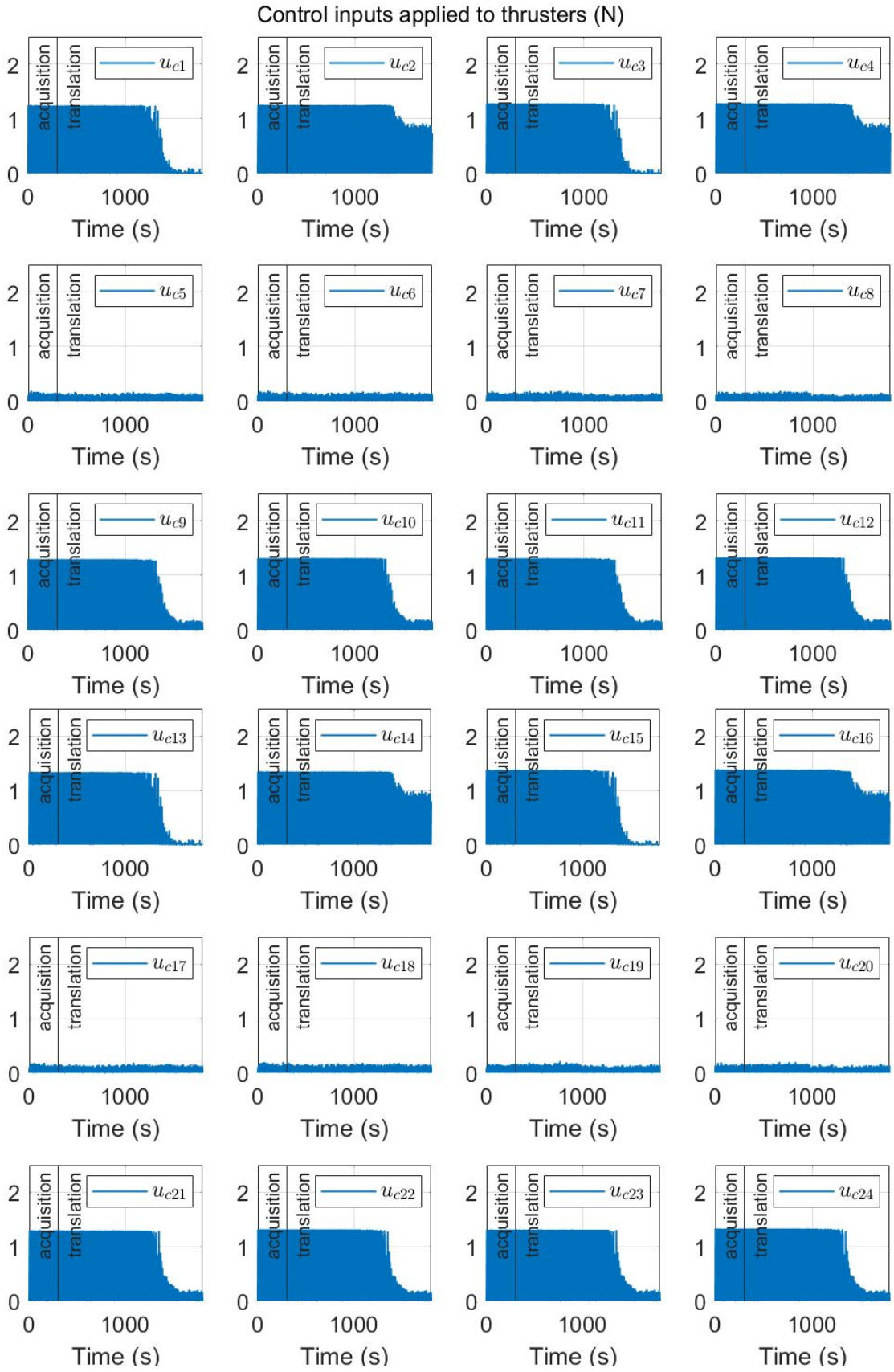

Figure 4.12: Control inputs applied to each thruster for the fault free case with navigation in the loop

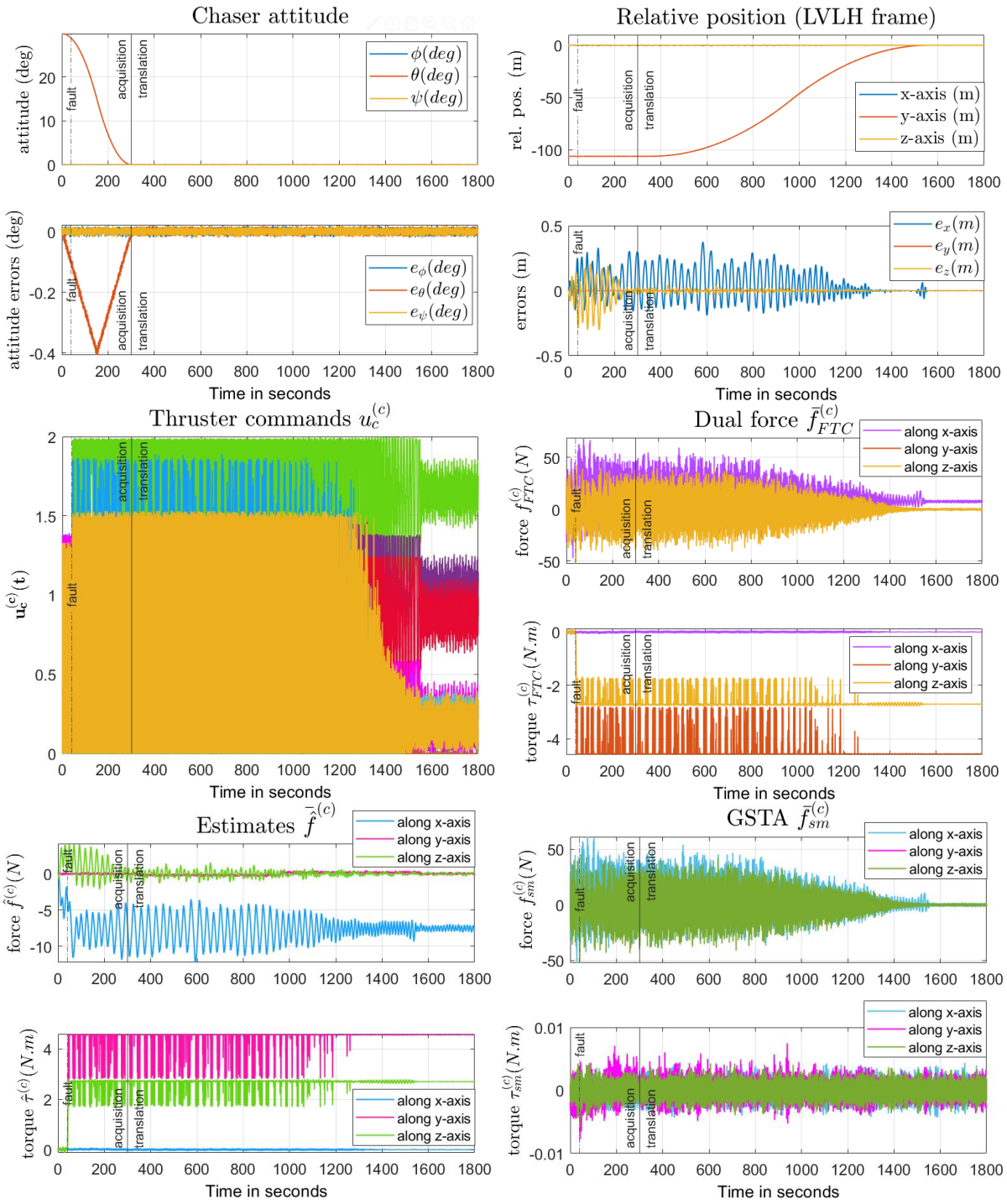

Figure 4.13: Navigation in the loop and stuck-open fault in THR 1: a) Attitude of the chaser - b) Relative position - c) dual force $\bar{\boldsymbol{f}}_{FTC}^{(c)}$ - d) thruster commands $\boldsymbol{u}_c^{(c)}$ - e) fault/disturbance dual force estimates $\bar{\hat{\boldsymbol{f}}}^{(c)}$ - f) GSTA dual force $\bar{\boldsymbol{f}}_{sm}^{(c)}$.

case 1. Furthermore, a second simulation campaign is carried out which considers the anti-windup strategy and noise in the navigation unit. In the following, this is called case 2. The performance of the FTC solution is next evaluated using the following mission-oriented criteria.

- Dealing with relative position and velocity, it is required to maintain the relative position inside the so-called rendezvous corridor, during the complete forced translation phase. This can be observed in Fig. 4.16.c. unlike what is shown in Fig.4.15.c. At the capture point, the position misalignment must be less than 20 cm along the X and Z axis, and the lateral X and Z velocities

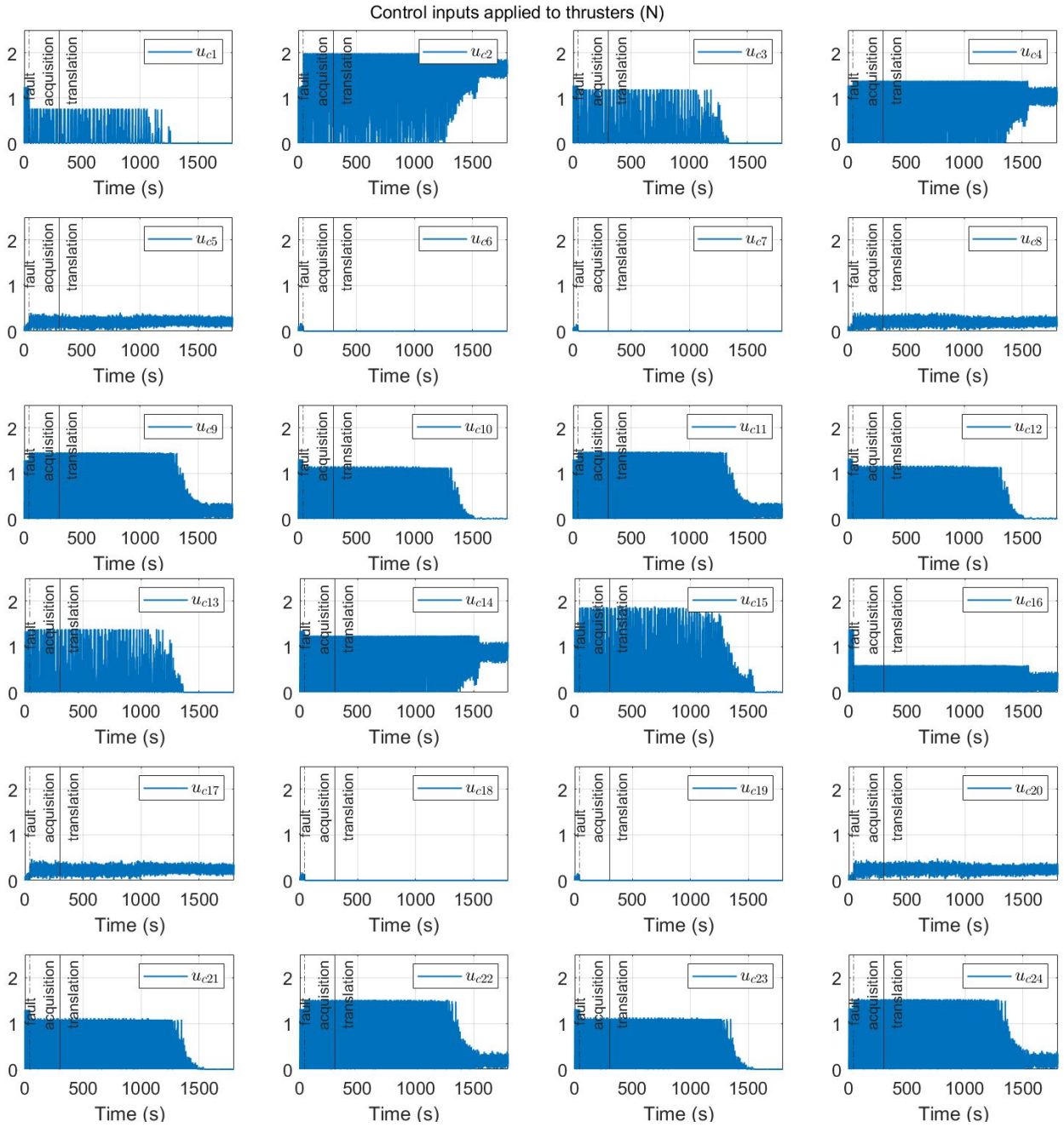

Figure 4.14: Control inputs applied to each thruster for the navigation in the loop and stuck-open fault in THR 1

must be less than 1 cm/s nominally, the worst case being fixed to 4 cm/s. In terms of longitudinal Y axis, the velocity must be less than 1 cm/s. In Fig. 4.16.a and Fig. 4.16.b it can be seen that the relative velocity and position requirements are met, whilst in Fig. 4.15.a and Fig. 4.15.b it is shown that when considered thruster 4 or 16 as faulty, the position and velocity requirements are not longer met, i.e. this represents a failed capture of the target.

- With regards to attitude performance, it is required after the acquisition phase, to maintain the attitude to less than 1 deg along the three axis (pitch $\phi(t)$, yaw $\theta(t)$, roll $\psi(t)$) during the forced translation, so that the capture mechanism is correctly aligned with the target. From Fig. 4.15.d and Fig. 4.16.d, it can be seen that this requirement is met. At the capture point, the attitude misalignment must be less than 1 deg, and the angular rate must be less than 0.05 deg/s along

the three axis. These requirements are also met for both cases, see Figs. 4.15.e, 4.15.f, 4.16.e and 4.16.f.

These mission-oriented criteria enable to quantify the worst case of mission performance loss due to faults. Particularly, it can be concluded from Fig. 4.15.b and Fig. 4.16.b that the worst case correspond to stuck-closed faults that occur in thrusters 2,4,14 and 16. As shown in Fig. 4.15, the solution without the anti-windup strategy can no longer guarantee the capture of the target in the presence of faults. One can understand that the behaviour shown in Fig. 4.15, would be further degraded if noise was considered to affect the navigation unit. This was observed when comparing Fig. 4.7 and Fig. 4.11. On the other hand, the results obtained for case 2, see Fig. 4.16, proved that the capture performance requirements are met, no matter which thruster is faulty. Thus, it is argued that the proposed FTC strategy is promising since it is able to cover all faulty situations, i.e. when a thruster opens at its maximum rate until its maximum value and when it closes at its maximum rate, until it produces no thrust.

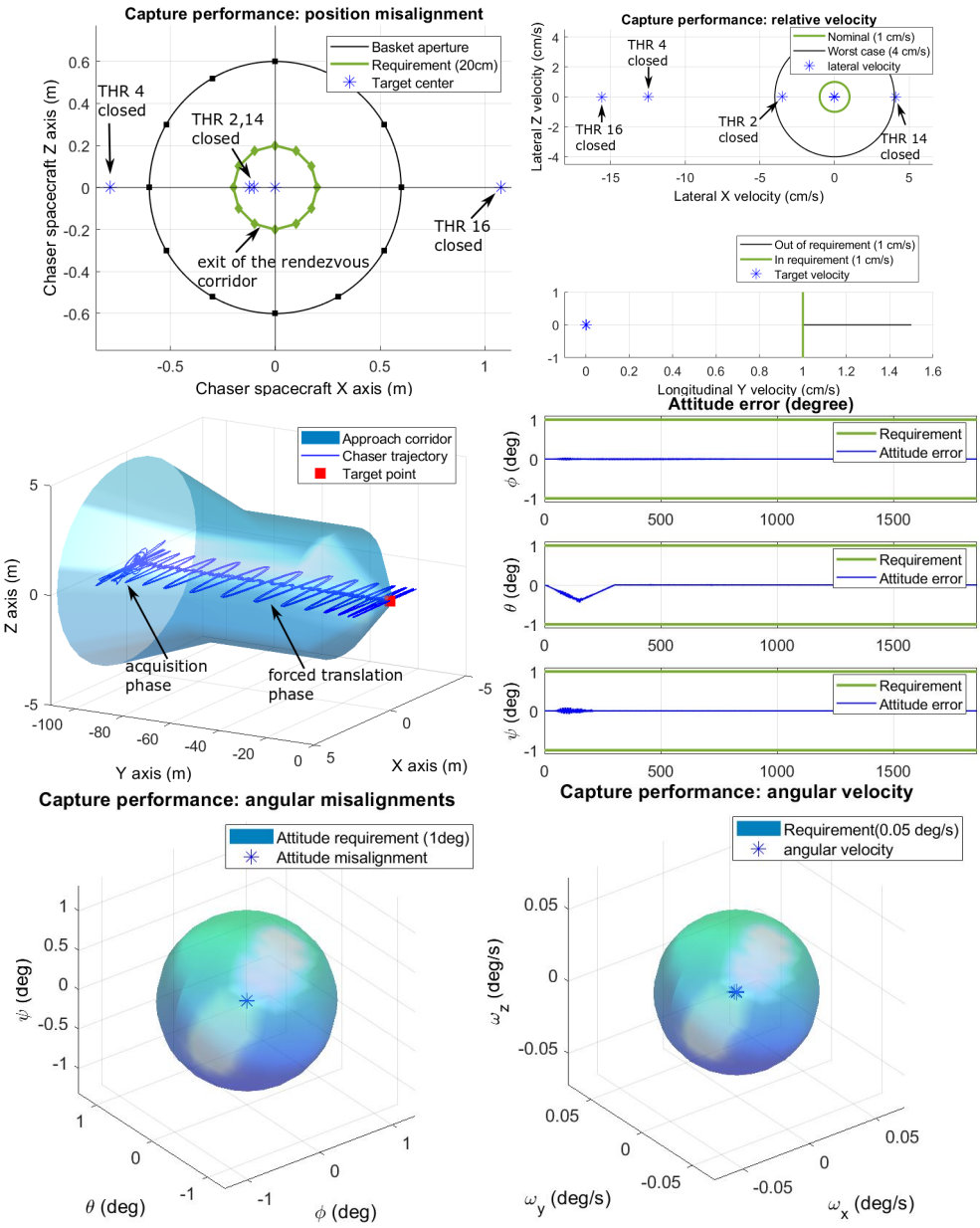

Figure 4.15: Simulation campaign with the FES without anti-windup strategy (48 faulty cases - faults occur at $t = 40s$): a) position misalignment and b) relative velocities at the capture point - c) relative position versus the rendezvous corridor - d) attitude error - e) attitude and f) angular velocity at the capture point.

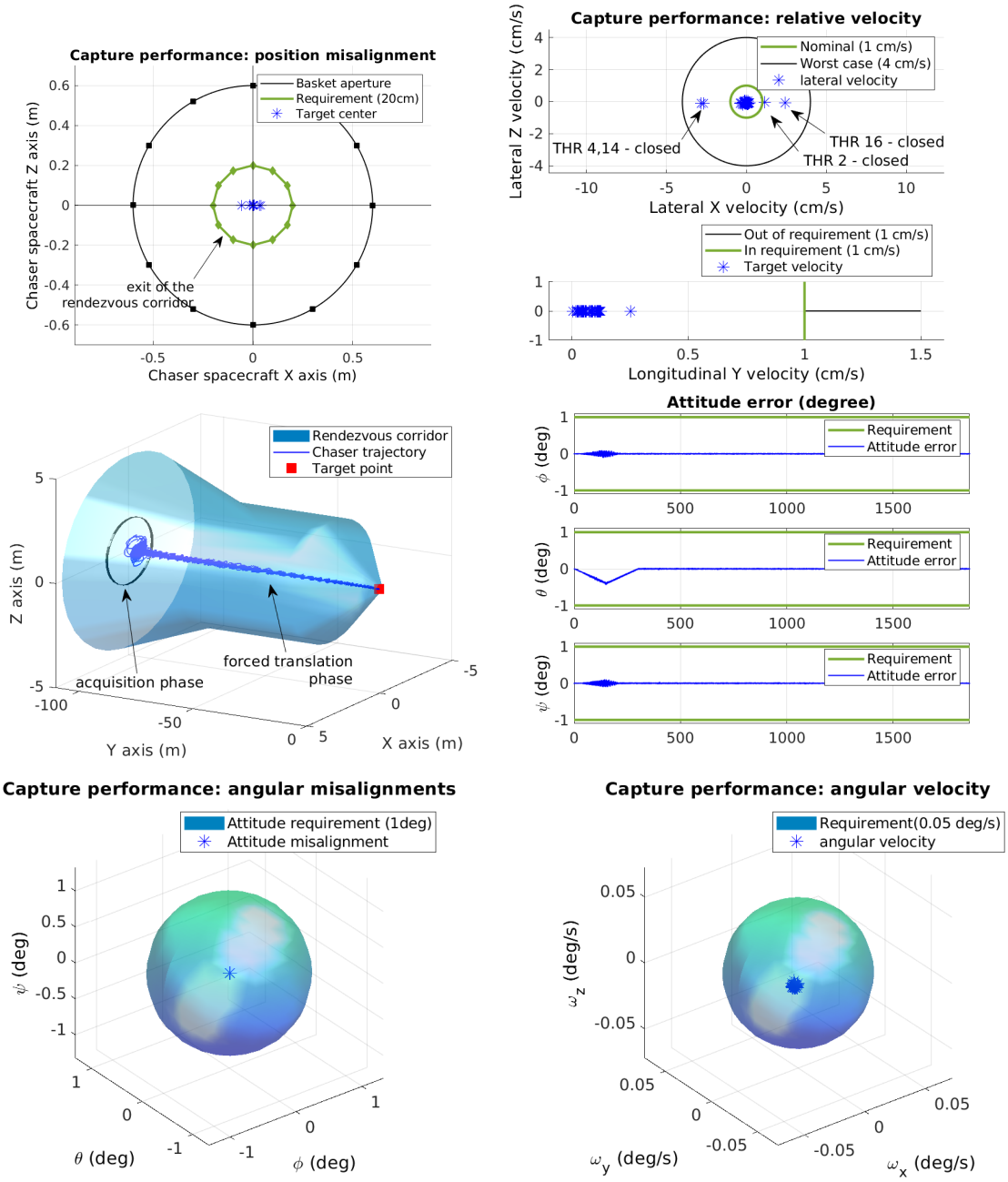

Figure 4.16: Simulation campaign with the FES with anti-windup strategy (48 faulty cases - faults occur at $t = 40s$): a) position misalignment and b) relative velocities at the capture point - c) relative position versus the rendezvous corridor - d) attitude error - e) attitude and f) angular velocity at the capture point.

4.7 Conclusions

In this chapter, a dual quaternion-based general super-twisting algorithm (GSTA) nested with a fault estimator is employed for achieving fault tolerance against thruster faults, during a rendezvous mission with a passive target on a circular orbit around Earth. The coupling effects between attitude and translation dynamics are taken into account, thanks to the dual quaternion formalism and to the GSTA theory, leading the approach to behave to the so-called six degree-of-freedom technique. Stability of the overall FTC is proved considering that the perturbations seen by the GSTA are state-dependent, and it is shown that the overall FTC scheme is asymptotically stable. An anti-windup strategy is joint to the GSTA, to prevent instability of the FTC scheme in case of

actuator saturation. The developed theory is verified through a simulation campaign in a functional engineering simulator that considers a realistic navigation unit, solar arrays flexible modes, propellant sloshing and the most dimensioning space disturbances, i.e. gravity gradient, magnetic filed and the atmospheric drag and J_2 effect. Mission-oriented criteria are analysed over 48 simulations under faulty situations and it is shown that the FTC strategy is able to accommodate thruster faults so that, the space mission is fulfilled, despite the loss of controllability of the faulty actuator.

5 Conclusions and Perspectives

In this thesis, the development of a robust control law with SMC techniques was firstly analyzed. The developments were applied to a rendezvous mission in a circular orbit with a passive target. This solution was further studied by considering the occurrence of faults. Consequently, fault tolerant capabilities of SMC were explored within the same aerospace mission. The perturbations caused by the solar arrays and the fuel tanks were considered, i.e. the flexible modes and the sloshing phenomena. In addition, the most dimensioning space disturbances (e.g. Earth gravity, the second zonal harmonic J_2, atmospheric drag and magnetic disturbances) were considered. Finally, the proposed solution is implemented in a high-fidelity benchmark, where the results obtained showed the potential of the proposed solution.

5.1 Conclusions

In Chapter 2, a brief introduction to the main concepts of SMC was done. The main properties of this technique were highlighted. In addition, the description of the different generations of SMC and their characteristics were mentioned. From this chapter, it is understood that in order to reduce the chattering effect, the implementation of a Higher Order SMC is needed. It was mentioned that, it is implicit that the higher the order of the SMC, the need of higher order derivatives of the sliding surface increases. It was then concluded that the best trade-off between the need of derivatives of the sliding surface and having a control signal with reduced chattering, was offered by the SOSMC.

An insight into the characteristics of the rendezvous mission studied in this work, was done in Chapter 3. The description of the modelling was developed separately for translational and rotational motions by neglecting the coupling effects. A first approach towards the development of a robust controller was developed based on the linearized approximation of the model. The control techniques employed were FOSMC and STA in a backstepping setup. Stability of both solutions was assessed with Lyapunov methods. Then, the linear control laws were implemented in a high-fidelity simulator that is based on the nonlinear equations, i.e. the coupling effect, space disturbances, sloshing phenomena and flexible modes are taken into account. The results obtained support the selection of the STA as robust controller, given that the advantages over the FOSMC, are clearly shown.

FTC capabilities of SMC techniques are explored in Chapter 4, by analyzing two faulty thruster cases: stuck open and stuck close. A new configuration of thrusters was specifically designed for this purpose. Unlike in Chapter 3, the new thruster structure has 24 thrusters with an actuation capacity of 2 N. Fault compensability criteria was analyzed given the new thruster structure. After this assessment, the design of a FTC solution is studied. The proposed solution consists of a GSTA controller nested with a nonlinear estimator. It was shown that in order to avoid thruster saturation, an anti-windup strategy was needed. With the intention of showing the efficiency and

limitations of the solution, simulations with different conditions were carried out. First, a perfect navigation unit was considered, i.e. the measurements provided by the navigation unit are nothing else but the states. The proposed solution had no major problems when dealing with faults. Then, a more realistic navigation unit was considered, i.e. noisy measurements. It was shown, that the proposed solution was capable of compensating faults despite of the corrupted measurements. Finally, two simulation campaigns, considering both types of faults, were conducted. The first simulation campaign did not consider measurement noise or the anti-windup strategy. Results showed that this solution can not guarantee a successful target capture, given that for some thruster failures, the chaser can no longer align its position with the target. The second simulation campaign, takes into account the noisy measurements and the anti-windup strategy. Results showed that the proposed FTC solution can overcome the considered type of faults leading to a successful capture of the target.

In addition, Chapter 4 presented a 6DoF model that allows the consideration of the coupling effects. Unlike what was considered in Chapter 3, the sloshing phenomena and the flexible modes are no longer treated as approximations, instead they are treated as state dependent. This lead to the selection of the GSTA controller, since as mentioned in Section 2.5.4, it is known for its capability of compensating state dependent perturbations. Furthermore, an anti-windup strategy was added to the GSTA solution to avoid saturation on the thrusters due to the control law. It was shown that this was necessary so that the chaser was capable of maintaining the tracking of the target, no matter which actuator was faulty.

Recalling the arguments expressed in Chapter 1, the main objective of this thesis was to explore the FTC capabilities of SMC techniques without the need of a FDI unit. As mentioned before, both active and passive approaches can be found in literature. Most active approaches can not guarantee stability of the closed loop given the assumption of the presence of a FDI unit. On the other hand, the limitations on the passive approaches relied on the fact that the faults considered were only loss of effectiveness. This thesis, successfully proposed a passive FTC solution with SMC, capable of compensating more serious failures, i.e. a stuck open and a stuck close fault, and with a realistic navigation unit.

5.2 Perspectives

In the following, a list of suggested future perspectives is stated:

- Robustness against sloshing phenomena and flexible modes was previously shown. It would be interesting to be able to extend the robustness property against variable or uncertain mass and inertia.
- It was previously considered that the target was a sphere. The problem would become more complex in the case where the target geometry affects the relative motion. Certainly, the complexity would increase when considering a tumbling target.
- Further analysis can be done with regards to less aggressive sliding mode techniques, which do not saturate the thrusters. Perhaps, this could be analyzed as an option to substitute the anti-windup strategy.
- The availability of the states can not be always guaranteed. Consider for example the case where no velocities are available. A solution to this problem can be analyzed.
- Although it is known that delays are present in every system, no delays were considered in this thesis. This can be further analyzed for example when considering delays in the thruster's response or in the navigation unit.

Appendix

A.1 Phase plane

Fig. 2.2 was obtained with Matlab, specifically with the use of pplane. The simulated system has the following form:

$$\begin{aligned} \dot{x} &= y \\ \dot{y} &= y - x + u \end{aligned} \tag{1}$$

where $u = 4x$ for the saddle point, and $u = -4x$ for the unstable focus at the origin.

A.2 Design Process of Sliding Mode Control in a Backstepping Setup for $r = 3$

Consider the following system in state space form:

$$\begin{bmatrix} \dot{x}_1 \\ \dot{x}_2 \\ \dot{x}_3 \end{bmatrix} = \begin{bmatrix} A_{11} & A_{12} & A_{13} \\ A_{21} & A_{22} & A_{23} \\ A_{31} & A_{32} & A_{33} \end{bmatrix} \begin{bmatrix} x_1 \\ x_2 \\ x_3 \end{bmatrix} + \begin{bmatrix} 0 \\ 0 \\ \mathcal{I}_m \end{bmatrix} (u + d) \tag{2}$$

Following the design process explained in Section 3.4.1, the tracking error is first defined as $e_{x_1} = x_{1c} - x_1$. Its derivative is expressed as:

$$\dot{e}_{x_1} = \dot{x}_{1c} - \dot{x}_1 = \dot{x}_{1c} - A_{11}x_1 - A_{12}x_2 - A_{13}x_3 \tag{3}$$

Given that x_2 is used as virtual controller, i.e. $x_2 \to \varepsilon_1$, the expression of the virtual controller is obtained from (3) as:

$$\varepsilon_1 = (A_{12})^{+} \left(\dot{x}_{1c} - A_{11}x_1 - A_{13}x_3 - \hat{A}_1 e_{x_1} \right) \tag{4}$$

where the term $\hat{A}_1 e_{x_1}$ is employed to guarantee the convergence of e_{x_1}. The second error is defined as $e_{x_2} = \varepsilon_1 - x_2$ and its derivative is expressed as:

$$\dot{e}_{x_2} = \dot{\varepsilon}_1 - \dot{x}_2 = \dot{\varepsilon}_1 - A_{21}x_1 - A_{22}x_2 - A_{23}x_3 \tag{5}$$

Now, x_3 is employed as virtual controller, i.e. $x_3 \to \varepsilon_2$. Then, the definition of ε_2 is obtained from (5) as:

$$\varepsilon_2 = (A_{23})^{+} \left(\dot{\varepsilon}_1 - A_{21}x_1 - A_{22}x_2 - \hat{A}_2 e_{x_2} + A_{12}^{\intercal} e_{x_1} \right) \tag{6}$$

Term $\hat{A}_2 e_{x_2}$ is used to guarantee the convergence of e_{x_2}. Furthermore, the term $A_{12}^{\intercal} e_{x_1}$ is included to eliminate crossed terms that are derived from further expressions, see (14)-(18). The last error is defined as $e_{x_3} = \varepsilon_2 - x_3$ and its derivative is defined as:

$$\dot{e}_{x_3} = \dot{\varepsilon}_2 - \dot{x}_3 = \dot{\varepsilon}_2 - A_{31}x_1 - A_{32}x_2 - A_{33}x_3 - u - d \tag{7}$$

To study the stability of the under-actuated dynamics a joint Lyapunov function is defined as :

$$V = V_1 + V_2 + V_3 = e_{x_1}^\intercal e_{x_2} + e_{x_2}^\intercal e_{x_2} + e_{x_3}^\intercal e_{x_3} \tag{8}$$

First, the derivative of V_1 is analyzed by employing the definition in (3) as follows:

$$\dot{V}_1 = e_{x_1}^\intercal \dot{e}_{x_1} = e_{x_1}^\intercal \left[\dot{x}_{1c} - A_{11}x_1 - A_{12}x_2 - A_{13}x_3\right] \tag{9}$$

From the definition of $e_{x_2} = \varepsilon_1 - x_2$, it is obtained that $x_2 = \varepsilon_1 - e_{x_2}$. By substituting it in (9) and employing the definition of ε_1 expressed in (4), it follows:

$$\begin{aligned}
\dot{V}_1 &= e_{x_1}^\intercal \left[\dot{x}_{1c} - A_{11}x_1 - A_{12}\{\varepsilon_1 - e_{x_2}\} - A_{13}x_3\right] \\
&= e_{x_1}^\intercal \left[\dot{x}_{1c} - A_{11}x_1 - A_{12}\left\{(A_{12})^+ \left(\dot{x}_{1c} - A_{11}x_1 - A_{13}x_3 - \hat{A}_1 e_{x_1}\right) - e_{x_2}\right\} - A_{13}x_3\right] \\
&= e_{x_1}^\intercal A_{12} e_{x_2} + e_{x_1}^\intercal \hat{A}_1 e_{x_1}
\end{aligned} \tag{10}$$

The next step is to analyze the derivative of V_2 by employing the definition of $\dot{e}_{x_2}$ in (5) as follows:

$$\dot{V}_2 = e_{x_2}^\intercal \dot{e}_{x_2} = e_{x_2}^\intercal \left[\dot{\varepsilon}_1 - A_{21}x_1 - A_{22}x_2 - A_{23}x_3\right] \tag{11}$$

It follows that, from the definition of $e_{x_3} = \varepsilon_2 - x_3$, it can be said that $x_3 = \varepsilon_2 - e_{x_3}$. By substituting it in (11) and employing the definition of ε_2 expressed in (6), it follows:

$$\begin{aligned}
\dot{V}_2 &= e_{x_2}^\intercal \left[\dot{\varepsilon}_1 - A_{21}x_1 - A_{22}x_2 - A_{23}\{\varepsilon_2 - e_{x_3}\}\right] \\
&= e_{x_2}^\intercal \left[\dot{\varepsilon}_1 - A_{21}x_1 - A_{22}x_2 - A_{23}\left\{(A_{23})^+ \left(\dot{\varepsilon}_1 - A_{21}x_1 - A_{22}x_2 - \hat{A}_2 e_{x_2} + A_{12}^\intercal e_{x_1}\right) - e_{x_3}\right\}\right] \\
&= e_{x_2}^\intercal \hat{A}_2 e_{x_2} - e_{x_2}^\intercal A_{12}^\intercal e_{x_1} + e_{x_2}^\intercal A_{23} e_{x_3}
\end{aligned} \tag{12}$$

Finally, by employing the definition of $\dot{e}_{x_3}$, expressed in (7), the derivative of V_3 is as follows:

$$\dot{V}_3 = e_{x_3}^\intercal \dot{e}_{x_3} = e_{x_3}^\intercal [\dot{\varepsilon}_2 - A_{31}x_1 - A_{32}x_2 - A_{33}x_3 - u - d] \tag{13}$$

By using the expressions obtained in (10),(12) and (13), the derivative of the joint Lyapunov function is:

$$\begin{aligned}
\dot{V} = \dot{V}_1 + \dot{V}_2 + \dot{V}_3 &= e_{x_1}^\intercal A_{12} e_{x_2} + e_{x_1}^\intercal \hat{A}_1 e_{x_1} + e_{x_2}^\intercal \hat{A}_2 e_{x_2} - e_{x_2}^\intercal A_{12}^\intercal e_{x_1} + e_{x_2}^\intercal A_{23} e_{x_3} \\
&+ e_{x_3}^\intercal [\dot{\varepsilon}_2 - A_{31}x_1 - A_{32}x_2 - A_{33}x_3 - u - d]
\end{aligned} \tag{14}$$

From (14), it can be seen that u has to have the following form:

$$u = \dot{\varepsilon}_2 - A_{31}x_1 - A_{32}x_2 - A_{33}x_3 + A_{23}^\intercal e_{x_2} - u_v \tag{15}$$

where u_v represent the discontinuous part of the controller, in this cases, the sliding mode controller. Then, by substituting (15) in (14) , it follows:

$$\begin{aligned}
\dot{V} = \dot{V}_1 + \dot{V}_2 + \dot{V}_3 &= e_{x_1}^\intercal A_{12} e_{x_2} + e_{x_1}^\intercal \hat{A}_1 e_{x_1} + e_{x_2}^\intercal \hat{A}_2 e_{x_2} - e_{x_2}^\intercal A_{12}^\intercal e_{x_1} + e_{x_2}^\intercal A_{23} e_{x_3} \\
&+ e_{x_3}^\intercal [\dot{\varepsilon}_2 - A_{31}x_1 - A_{32}x_2 - A_{33}x_3 - \left\{\dot{\varepsilon}_2 - A_{31}x_1 - A_{32}x_2 - A_{33}x_3 + A_{23}^\intercal e_{x_2} - u_v\right\} - d] \\
&= e_{x_1}^\intercal A_{12} e_{x_2} + e_{x_1}^\intercal \hat{A}_1 e_{x_1} + e_{x_2}^\intercal \hat{A}_2 e_{x_2} - e_{x_2}^\intercal A_{12}^\intercal e_{x_1} + e_{x_2}^\intercal A_{23} e_{x_3} - e_{x_3}^\intercal A_{23}^\intercal e_{x_2} + e_{x_3}^\intercal (u_v - d)
\end{aligned} \tag{16}$$

Consider the following properties:

$$\begin{aligned}
e_{x_1}^\intercal A_{12} e_{x_2} &= e_{x_2}^\intercal A_{12}^\intercal e_{x_1} \\
e_{x_2}^\intercal A_{23} e_{x_3} &= e_{x_3}^\intercal A_{23}^\intercal e_{x_2}
\end{aligned} \tag{17}$$

By employing (17) in (16), it follows:

$$\begin{aligned}
\dot{V} &= e_{x_1}^\intercal A_{12} e_{x_2} + e_{x_1}^\intercal \hat{A}_1 e_{x_1} + e_{x_2}^\intercal \hat{A}_2 e_{x_2} - e_{x_1}^\intercal A_{12} e_{x_2} + e_{x_2}^\intercal A_{23} e_{x_3} - e_{x_2}^\intercal A_{23} e_{x_3} + e_{x_3}^\intercal (u_v - d) \\
&= e_{x_1}^\intercal \hat{A}_1 e_{x_1} + e_{x_2}^\intercal \hat{A}_2 e_{x_2} + e_{x_3}^\intercal (u_v - d)
\end{aligned} \tag{18}$$

The convergence of $e_{x_1}^\intercal \hat{A}_1 e_{x_1}$ and $e_{x_2}^\intercal \hat{A}_2 e_{x_2}$ are guaranteed according to Remark 4, in Section (3.4.1). Convergence of e_{x_3} and the compensation against v is guaranteed by the selected sliding mode controller and the tunning of its gains.

A.3 Convex Polytopes

As stated in [HRGZ04], the following definitions are given:

- **Polytope**: A subset $P \subseteq \mathbb{R}^d$ that can be presented as a V-polytope or as an H-polytope.
- **V-Polytope**: The convex hull of a finite set $\mathbb{X} = \{x_1, \ldots, x_n\}$ of points in $\mathbb{R}^d$:

$$P = \text{conv}(\mathbb{X}) := \left\{ \sum_{i=1}^{n} \lambda_i x^i \;\middle|\; \lambda_i \geq 0, \sum_{i=1}^{n} \lambda = 1 \right\} \tag{19}$$

- **H-Polytope**: A bounded solution set of a finite system of linear inequalities:

$$P = P(A, b) := \left\{ x \in \mathbb{R}^d \;\middle|\; a_i^\intercal x \leq b_i \;\; \text{for} 1 \leq i \leq m \right\} \tag{20}$$

  where $A \in \mathbb{R}^{m \times d}$ is a real matrix with rows $a_i^\intercal$ and $b \in \mathbb{R}^m$ is a real vector with entries b_i. Here boundedness means that there is a constant N such that $\|x\| \leq N$ holds for all $x \in P$.

Theorem 4 (Polytope equivalence)**.** *The definitions of V-polytopes and of H-polytopes are equivalent. That is, every V-polytope has a description by a finite system of inequalities, and every H-polytope can be obtained as the convex hull of a finite set of points (its vertices).*

A.4 Quaternion product

Given two quaternions $\boldsymbol{p}$ and $\boldsymbol{q}$, it follows that:

$$\boldsymbol{p} = p_0 + ip_1 + jp_2 + kp_3 \quad \boldsymbol{q} = q_0 + iq_1 + jq_2 + kq_3 \tag{21}$$

where $p_0, p_1, p_2, p_3, q_0, q_1, q_2$ and q_3 are numerical values, while ijk represent imaginary components.

The basic operations between the imaginary components ijk are described as:

$$i^2 = j^2 = k^2 = ijk = -1 \tag{22}$$
$$ij = k = -ji \tag{23}$$
$$jk = i = -kj \tag{24}$$
$$ki = j = -ik \tag{25}$$

Then, the quaternion product between $\boldsymbol{p}$ and $\boldsymbol{q}$ is defined as:

$$\begin{aligned} \boldsymbol{p} \circ \boldsymbol{q} &= (p_0 + ip_1 + jp_2 + kp_3) \circ (q_0 + iq_1 + jq_2 + kq_3) \\ &= p_0q_0 + ip_1q_0 + jp_2q_0 + kp_3q_0 \\ &+ ip_0q_1 + i^2p_1q_1 + jip_2q_1 + kip_3q_1 \\ &+ jp_0q_2 + ijp_1q_2 + j^2p_2q_2 + kjp_3q_2 \\ &+ kp_0q_3 + ikp_1q_3 + jkp_2q_3 + k^2p_3q_3 \end{aligned} \tag{26}$$

By regrouping terms, (26) can be rewritten as:

$$\begin{aligned} \boldsymbol{p} \circ \boldsymbol{q} &= p_0q_0 - (p_1q_1 + p_2q_2 + p_3q_3) + p_0(iq_1 + jq_2 + kq_3) \\ &+ q_0(ip_1 + jp_2 + kp_3) + i(p_2q_3 - p_3q_2) \\ &+ j(p_3q_1 - p_1q_3) + k(p_1q_2 - p_2q_1) \end{aligned} \tag{27}$$

Consider the following definition:

$$\boldsymbol{p} \circ \boldsymbol{q} = \boldsymbol{r} = r_0 + ir_1 + jr_2 + kr_3 \tag{28}$$

It follows that (27) can be rewritten by considering (28) as:

$$\begin{aligned} r_0 &= p_0q_0 - p_1q_1 - p_2q_2 - p_3q_3 \\ r_1 &= p_0q_1 + p_1q_0 + p_2q_3 - p_3q_2 \\ r_2 &= p_0q_2 - p_1q_3 + p_2q_0 + p_3q_1 \\ r_3 &= p_0q_3 + p_1q_2 - p_2q_1 + p_3q_0 \end{aligned} \tag{29}$$

which can be rewritten in matrix form as:

$$\begin{bmatrix} r_0 \\ r_1 \\ r_2 \\ r_3 \end{bmatrix} = \left[\begin{array}{c|ccc} p_0 & -p_1 & -p_2 & -p_3 \\ \hline p_1 & p_0 & -p_3 & p_2 \\ p_2 & p_3 & p_0 & -p_1 \\ p_3 & -p_2 & p_1 & p_0 \end{array}\right] \circ \begin{bmatrix} q_0 \\ q_1 \\ q_2 \\ q_3 \end{bmatrix} = (\boldsymbol{p})^{+}\boldsymbol{q} = (\boldsymbol{q})^{-}\boldsymbol{p} \tag{30}$$

where $\boldsymbol{p}_v^{\intercal} = [p_1, p_2, p_3]$ and $\boldsymbol{q}_v^{\intercal} = [q_1, q_2, q_3]$, then the operators $(\boldsymbol{p})^{+}$ and $(\boldsymbol{q})^{-}$ are defined as:

$$(\boldsymbol{p})^{+} = \left[\begin{array}{c|c} p_0 & -\boldsymbol{p}_v^{\intercal} \\ \hline \boldsymbol{p}_v & p_0\mathcal{I} + \boldsymbol{C}(\boldsymbol{p}_v) \end{array}\right] \quad (\boldsymbol{q})^{-} = \left[\begin{array}{c|c} q_0 & -\boldsymbol{q}_v^{\intercal} \\ \hline \boldsymbol{q}_v & q_0\mathcal{I} - \boldsymbol{C}(\boldsymbol{q}_v) \end{array}\right] \tag{31}$$

$$\boldsymbol{C}(\boldsymbol{p}_v) = \begin{bmatrix} 0 & -p_3 & p_2 \\ p_3 & 0 & -p_1 \\ -p_2 & p_1 & 0 \end{bmatrix} \quad \boldsymbol{C}(\boldsymbol{q}_v) = \begin{bmatrix} 0 & -q_3 & q_2 \\ q_3 & 0 & -q_1 \\ -q_2 & q_1 & 0 \end{bmatrix} \tag{32}$$

Based on the previous definitions, the quaternion product of three arbitrary quaternions is defined as:

$$\boldsymbol{p} \circ \boldsymbol{q} \circ \boldsymbol{r} = (\boldsymbol{p})^{+}(\boldsymbol{r})^{-}\boldsymbol{q} = (\boldsymbol{r})^{-}(\boldsymbol{p})^{+}\boldsymbol{q} \tag{33}$$

Then, for a vector $\boldsymbol{r}_a = [x_a, y_a, z_a]^{\intercal}$ in coordinate frame A and $\boldsymbol{r}_b = [x_b, y_b, z_b]^{\intercal}$ in coordinate frame B, it follows:

$$\boldsymbol{r}_b = \mathbf{q}^{*} \circ \boldsymbol{r}_a \circ \mathbf{q} = (\mathbf{q}^{*})^{+}(\mathbf{q})^{-}\boldsymbol{r}_a \tag{34}$$

where $\mathbf{q}^{*} = [q_0, -\mathbf{q}_v^{\intercal}]^{\intercal}$. This is verified by using (32) as follows:

$$\underbrace{\begin{bmatrix} q_0 & q_1 & q_2 & q_3 \\ -q_1 & q_0 & q_3 & -q_2 \\ -q_2 & -q_3 & q_0 & q_1 \\ -q_3 & q_2 & -q_1 & q_0 \end{bmatrix}}_{(\mathbf{q}^{*})^{+}} \circ \underbrace{\begin{bmatrix} q_0 & -q_1 & -q_2 & -q_3 \\ q_1 & q_0 & q_3 & -q_2 \\ q_2 & -q_3 & q_0 & q_1 \\ q_3 & q_2 & -q_1 & q_0 \end{bmatrix}}_{(\mathbf{q})^{-}} = \underbrace{\begin{bmatrix} Q_{11} & Q_{12} & Q_{13} & Q_{14} \\ Q_{21} & Q_{22} & Q_{23} & Q_{24} \\ Q_{31} & Q_{32} & Q_{33} & Q_{34} \\ Q_{41} & Q_{42} & Q_{43} & Q_{44} \end{bmatrix}}_{\boldsymbol{Q}} \tag{35}$$

$$\begin{aligned} Q_{11} &= q_0q_0 + q_1q_1 + q_2q_2 + q_3q_3 & Q_{21} &= -q_1q_0 + q_0q_1 + q_3q_2 - q_2q_3 = 0 \\ Q_{12} &= -q_0q_1 + q_1q_0 - q_2q_3 + q_3q_2 = 0 & Q_{22} &= q_1q_1 + q_0q_0 - q_3q_3 - q_2q_2 \\ Q_{13} &= -q_0q_2 + q_1q_3 + q_2q_0 - q_3q_1 = 0 & Q_{23} &= q_1q_2 + q_0q_3 + q_3q_0 + q_2q_1 \\ Q_{14} &= -q_0q_3 - q_1q_2 + q_2q_1 + q_3q_0 & Q_{24} &= q_1q_3 - q_0q_2 + q_3q_1 - q_2q_0 \\ Q_{31} &= -q_2q_0 - q_3q_1 + q_0q_2 + q_1q_3 = 0 & Q_{41} &= -q_3q_0 + q_2q_1 - q_1q_2 + q_0q_3 = 0 \\ Q_{32} &= q_2q_1 - q_3q_0 - q_0q_3 + q_1q_2 & Q_{42} &= q_3q_1 + q_2q_0 + q_1q_3 + q_0q_2 \\ Q_{33} &= q_2q_2 - q_3q_3 + q_0q_0 - q_1q_1 & Q_{43} &= q_3q_2 + q_2q_3 - q_1q_0 - q_0q_1 \\ Q_{34} &= q_2q_3 + q_3q_2 + q_0q_1 + q_1q_0 & Q_{44} &= q_3q_3 - q_2q_2 - q_1q_1 + q_0q_0 \end{aligned}$$

Given that $\boldsymbol{r}_a$ can be written as a quaternion with scalar part zero and when multiplied by $\boldsymbol{Q}$, the scalar part is equal to zero, then $\boldsymbol{Q}$ can be factorized as:

$$\boldsymbol{Q} = \boldsymbol{C}_e = \mathbf{q}_v \cdot \mathbf{q}_v^{\intercal} + [q_0\mathcal{I} - \boldsymbol{C}(\mathbf{q}_v)]^2 \tag{36}$$

The property in (36) can be simply verified by:

$$\mathbf{q}_v \cdot \mathbf{q}_v^\intercal = \begin{bmatrix} q_1 \\ q_2 \\ q_3 \end{bmatrix} \cdot \begin{bmatrix} q_1 & q_2 & q_3 \end{bmatrix} = \begin{bmatrix} q_1 q_1 & q_1 q_2 & q_1 q_3 \\ q_2 q_1 & q_2 q_2 & q_2 q_3 \\ q_3 q_1 & q_3 q_2 & q_3 q_3 \end{bmatrix} \tag{37}$$

$$q_0 \mathcal{I} - \boldsymbol{C}(\mathbf{q}_v) = \begin{bmatrix} q_0 & 0 & 0 \\ 0 & q_0 & 0 \\ 0 & 0 & q_0 \end{bmatrix} - \begin{bmatrix} 0 & -q_3 & q_2 \\ q_3 & 0 & -q_1 \\ -q_2 & q_1 & 0 \end{bmatrix} = \begin{bmatrix} q_0 & q_3 & -q_2 \\ -q_3 & q_0 & q_1 \\ q_2 & -q_1 & q_0 \end{bmatrix} \tag{38}$$

$$[q_0 \mathcal{I} - \boldsymbol{C}(\mathbf{q}_v)]^2 = \begin{bmatrix} q_0 & q_3 & -q_2 \\ -q_3 & q_0 & q_1 \\ q_2 & -q_1 & q_0 \end{bmatrix} \begin{bmatrix} q_0 & q_3 & -q_2 \\ -q_3 & q_0 & q_1 \\ q_2 & -q_1 & q_0 \end{bmatrix} = \begin{bmatrix} d_{11} & d_{12} & d_{13} \\ d_{21} & d_{22} & d_{23} \\ d_{31} & d_{32} & d_{33} \end{bmatrix} \tag{39}$$

$$\begin{aligned}
d_{11} &= q_0 q_0 - q_3 q_3 - q_2 q_2 & d_{21} &= -q_3 q_0 - q_0 q_3 + q_1 q_2 & d_{31} &= q_2 q_0 + q_1 q_3 + q_0 q_2 \\
d_{12} &= q_0 q_3 + q_3 q_0 + q_2 q_1 & d_{22} &= -q_3 q_3 + q_0 q_0 - q_1 q_1 & d_{32} &= q_2 q_3 - q_1 q_0 - q_0 q_1 \\
d_{13} &= -q_0 q_2 + q_3 q_1 - q_2 q_0 & d_{23} &= q_3 q_2 + q_0 q_1 + q_1 q_0 & d_{33} &= -q_2 q_2 - q_1 q_1 + q_0 q_0
\end{aligned}$$

In the following (34) is substituted by (36).

A.5 Separation of the relative dynamics model

The relative dynamics equation in its dual form is defined as shown in (4.60):

$$\dot{\bar{\boldsymbol{\omega}}}_e^{(c)} = \underbrace{-\bar{\boldsymbol{M}}^{-1} \circ \left(\bar{\boldsymbol{\omega}}_c^{(c)} \times \bar{\boldsymbol{M}} \circ \bar{\boldsymbol{\omega}}_c^{(c)} \right)}_{a} + \underbrace{\bar{\boldsymbol{M}}^{-1} \circ \bar{\boldsymbol{f}}_c^{(c)}}_{b} - \underbrace{\hat{\mathbf{q}}_e^* \circ \dot{\bar{\boldsymbol{\omega}}}_t^{(t)} \circ \bar{\mathbf{q}}_e}_{d} + \underbrace{\bar{\boldsymbol{\omega}}_e^{(c)} \times \left(\bar{\mathbf{q}}_e^* \circ \bar{\boldsymbol{\omega}}_t^{(t)} \circ \bar{\mathbf{q}}_e \right)}_{c} \tag{40}$$

For convenience, the definitions employed for separating (40) are listed in the following:

$$\bar{\boldsymbol{M}} = m \frac{d}{d\varepsilon} \mathcal{I}_{3\times 3} + \varepsilon \boldsymbol{J} \tag{41}$$

$$\bar{\boldsymbol{M}}^{-1} = \boldsymbol{J}^{-1} \frac{d}{d\varepsilon} + \varepsilon \frac{1}{m} \mathcal{I}_{3\times 3} \tag{42}$$

$$\frac{d}{d\varepsilon}(\boldsymbol{a} + \varepsilon \boldsymbol{b}) = \frac{d}{d\varepsilon}\boldsymbol{a} + \frac{d}{d\varepsilon}\varepsilon \boldsymbol{b} = \boldsymbol{b} \tag{43}$$

$$\varepsilon^2 = 0 \tag{44}$$

$$\bar{\boldsymbol{\omega}}_c^{(c)} = \boldsymbol{\omega}_c^{(c)} + \varepsilon \boldsymbol{v}_c^{(c)} = \boldsymbol{\omega}_c^{(c)} + \varepsilon \left(\dot{\boldsymbol{r}}_c^{(c)} + \boldsymbol{\omega}_c^{(c)} \times \boldsymbol{r}_c^{(c)} \right) \tag{45}$$

$$\bar{\boldsymbol{\omega}}_t^{(t)} = \boldsymbol{\omega}_t^{(t)} + \varepsilon \boldsymbol{v}_t^{(t)} = \boldsymbol{\omega}_t^{(t)} + \varepsilon \left(\dot{\boldsymbol{r}}_t^{(t)} + \boldsymbol{\omega}_t^{(t)} \times \boldsymbol{r}_t^{(t)} \right) \tag{46}$$

$$\bar{\boldsymbol{\omega}}_e^{(c)} = \boldsymbol{\omega}_e^{(c)} + \varepsilon \boldsymbol{v}_e^{(c)} = \boldsymbol{\omega}_e^{(c)} + \varepsilon \left(\dot{\boldsymbol{r}}_e^{(c)} + \boldsymbol{\omega}_e^{(c)} \times \boldsymbol{r}_e^{(c)} \right) \tag{47}$$

$$\boldsymbol{\omega}_e^{(c)} = \boldsymbol{\omega}_c^{(c)} - \boldsymbol{C}_e \boldsymbol{\omega}_t^{(t)} \tag{48}$$

$$\boldsymbol{v}_e^{(c)} = \boldsymbol{v}_c^{(c)} - \boldsymbol{C}_e \boldsymbol{v}_t^{(t)} \tag{49}$$

$$\bar{\boldsymbol{f}}_{ct}^{(c)} = \boldsymbol{f}_{ct}^{(c)} + \varepsilon \boldsymbol{\tau}_{ct}^{(c)} \tag{50}$$

As mentioned in Section 4.4.5, given the particular geometry of the target and the capture mechanism, the problem is reduced to the model of the chaser, i.e. $\bar{\boldsymbol{\omega}}_t^{(t)} = \boldsymbol{\omega}_t^{(t)} + \varepsilon \boldsymbol{v}_t^{(t)} = 0$. This means that (40) is reduced to:

$$\dot{\bar{\boldsymbol{\omega}}}_e^{(c)} = \underbrace{-\bar{\boldsymbol{M}}^{-1} \circ \left(\bar{\boldsymbol{\omega}}_c^{(c)} \times \bar{\boldsymbol{M}} \circ \bar{\boldsymbol{\omega}}_c^{(c)} \right)}_{a} + \underbrace{\bar{\boldsymbol{M}}^{-1} \circ \bar{\boldsymbol{f}}_c^{(c)}}_{b} \tag{51}$$

Now that the properties are defined, the separation of (51) into real and dual parts, begins. First, the term (51).a is separated by employing the properties (41)-(45).

$$
\begin{aligned}
-\bar{\boldsymbol{M}}^{-1}\circ\left(\bar{\boldsymbol{\omega}}_c^{(c)}\times\bar{\boldsymbol{M}}\circ\bar{\boldsymbol{\omega}}_c^{(c)}\right) &= -\bar{\boldsymbol{M}}^{-1}\circ\left[\left(\boldsymbol{\omega}_c^{(c)}+\varepsilon\boldsymbol{v}_c^{(c)}\right)\times\left(m\frac{d}{d\varepsilon}\mathcal{I}_{3\times3}+\varepsilon\boldsymbol{J}\right)\circ\left(\boldsymbol{\omega}_c^{(c)}+\varepsilon\boldsymbol{v}_c^{(c)}\right)\right]\\
&= -\left(\boldsymbol{J}^{-1}\frac{d}{d\varepsilon}+\varepsilon\frac{1}{m}\mathcal{I}_{3\times3}\right)\circ\left[\left(\boldsymbol{\omega}_c^{(c)}+\varepsilon\boldsymbol{v}_c^{(c)}\right)\times\left(m\boldsymbol{v}_c^{(c)}+\varepsilon\boldsymbol{J}\boldsymbol{\omega}_c^{(c)}\right)\right]\\
&= -\left(\boldsymbol{J}^{-1}\frac{d}{d\varepsilon}+\varepsilon\frac{1}{m}\mathcal{I}_{3\times3}\right)\circ\left[\boldsymbol{\omega}_c^{(c)}\times m\boldsymbol{v}_c^{(c)}+\varepsilon\left(\boldsymbol{\omega}_c^{(c)}\times\boldsymbol{J}\boldsymbol{\omega}_c^{(c)}\right)\right]\\
&= \boxed{-\left(\boldsymbol{J}^{-1}(\boldsymbol{\omega}_c^{(c)}\times\boldsymbol{J}\boldsymbol{\omega}_c^{(c)})\right)-\varepsilon[\boldsymbol{\omega}_c^{(c)}\times\boldsymbol{v}_c^{(c)}]}
\end{aligned}
\tag{52}
$$

Now, the term (51).b is separated by employing (41)-(44) and (50) as follows:

$$
\bar{\boldsymbol{M}}^{-1}\circ\bar{\boldsymbol{f}}_{ct}^{(c)} = \left(\boldsymbol{J}^{-1}\frac{d}{d\varepsilon}+\varepsilon\frac{1}{m}\mathcal{I}_{3\times3}\right)\circ\left(\boldsymbol{f}_{ct}^{(c)}+\varepsilon\boldsymbol{\tau}_{ct}^{(c)}\right) = \boxed{\boldsymbol{J}^{-1}\boldsymbol{\tau}_{ct}^{(c)}+\varepsilon\frac{1}{m}\boldsymbol{f}_{ct}^{(c)}} \tag{53}
$$

Then, (51) is rewritten by separating (52) and (53) into real and dual parts, as follows:

- Real part

$$
\dot{\boldsymbol{\omega}}_e^{(c)} = -\left(\boldsymbol{J}^{-1}(\boldsymbol{\omega}_c^{(c)}\times\boldsymbol{J}\boldsymbol{\omega}_c^{(c)})\right)+\boldsymbol{J}^{-1}\boldsymbol{\tau}_c^{(c)} \tag{54}
$$

  which can also be rewritten by employing the real part of (48) in (54) and considering that $\boldsymbol{\omega}_t^{(t)}=0$, it follows:

$$
\boxed{\dot{\boldsymbol{\omega}}_e^{(c)} = -\boldsymbol{J}^{-1}\left(\boldsymbol{\omega}_e^{(c)}\times\boldsymbol{J}\boldsymbol{\omega}_e^{(c)}\right)+\boldsymbol{J}^{-1}\boldsymbol{\tau}_c^{(c)}} \tag{55}
$$

  where $\boldsymbol{\tau}_c^{(c)}=\boldsymbol{\tau}_{c_u}^{(c)}+\boldsymbol{\tau}_{ct_d}^{(c)}+\boldsymbol{\tau}_{c_f}^{(c)}$, as stated in (4.50).

- Dual part

$$
\ddot{\boldsymbol{r}}_e^{(c)} = \underbrace{-\boldsymbol{\omega}_c^{(c)}\times\boldsymbol{v}_c^{(c)}}_{a}+\frac{1}{m}\boldsymbol{f}_c^{(c)} \tag{56}
$$

  Following the definition (48) and (49), (56).a is rewritten as follows considering that $\boldsymbol{\omega}_t^{(t)}=\boldsymbol{v}_t^{(t)}=0$:

$$
-\boldsymbol{\omega}_c^{(c)}\times\boldsymbol{v}_c^{(c)} = -\boldsymbol{\omega}_e^{(c)}\times\boldsymbol{v}_e^{(c)} \tag{57}
$$

  From (47) it is known that $\boldsymbol{\omega}_e^{(c)}=\left(\dot{\boldsymbol{r}}_e^{(c)}+\boldsymbol{\omega}_e^{(c)}\times\boldsymbol{r}_e^{(c)}\right)$, then (56) is finally written as:

$$
\boxed{\ddot{\boldsymbol{r}}_e^{(c)} = -\boldsymbol{\omega}_e^{(c)}\times\dot{\boldsymbol{r}}_e^{(c)}-\boldsymbol{\omega}_e^{(c)}\times\boldsymbol{\omega}_e^{(c)}\times\boldsymbol{r}_e^{(c)}+\frac{1}{m}\boldsymbol{f}_c^{(c)}} \tag{58}
$$

  where $\boldsymbol{f}_c^{(c)}=\boldsymbol{f}_{c_u}^{(c)}+\boldsymbol{f}_{ct_d}^{(c)}+\boldsymbol{f}_{c_f}^{(c)}$ as stated in (4.50).

References

[AE08] Halim Alwi and Christopher Edwards. Fault tolerant control using sliding modes with on-line control allocation. *Automatica*, 44(7):1859–1866, 2008.

[AET11] Halim Alwi, Christopher Edwards, and Chee Pin Tan. Fault tolerant control and fault detection and isolation. In *Fault Detection and Fault-Tolerant Control Using Sliding Modes*, pages 7–27. Springer, 2011.

[Ank10] Finn Ankersen. *Guidance, navigation, control and relative dynamics for spacecraft proximity maneuvers*. 2010.

[AVG+09] Kyle Alfriend, Srinivas Rao Vadali, Pini Gurfil, Jonathan How, and Louis Breger. *Spacecraft formation flying: Dynamics, control and navigation*, volume 2. Elsevier, 2009.

[BBF+97] Frank Bauer, John Bristow, David Folta, Kathy Hartman, David Quinn, Jonathan How, Frank Bauer, John Bristow, David Folta, Kathy Hartman, et al. Satellite formation flying using an innovative autonomous control system (autocon) environment. In *Guidance, Navigation, and Control Conference*, page 3821, 1997.

[BKL+06] Mogens Blanke, Michel Kinnaert, Jan Lunze, Marcel Staroswiecki, and J Schröder. *Diagnosis and fault-tolerant control*, volume 691. Springer, 2006.

[BPZ04] Giorgio Bartolini, Elisabetta Punta, and Tullio Zolezzi. Simplex methods for nonlinear uncertain sliding-mode control. *IEEE Transactions on Automatic Control*, 49(6):922–933, 2004.

[BS99] V. Brodsky and M. Shoham. Dual numbers representation of rigid body dynamics. *Mechanism and Machine Theory*, 34:693–718, 1999.

[CAE19a] Lejun Chen, Halim Alwi, and Christopher Edwards. Development and evaluation of an integral sliding mode fault-tolerant control scheme on the reconfigure benchmark. *International Journal of Robust and Nonlinear Control*, 29(16):5314–5340, 2019.

[CAE19b] Lejun Chen, Halim Alwi, and Christopher Edwards. On the synthesis of an integrated active lpv ftc scheme using sliding modes. *Automatica*, 110:108536, 2019.

[CCD+17a] Jing Chang, Jérôme Cieslak, Jorge Dávila, Jun Zhou, Ali Zolghadri, and Zongyi Guo. A two-step approach for an enhanced quadrotor attitude estimation via imu data. *IEEE Transactions on Control Systems Technology*, 26(3):1140–1148, 2017.

[CCD+17b] Jing Chang, Jérôme Cieslak, Jorge Davila, Ali Zolghadri, and Jun Zhou. Analysis and design of second-order sliding-mode algorithms for quadrotor roll and pitch estimation. *ISA transactions*, 71:495–512, 2017.

[CEA19] L Chen, C Edwards, and H Alwi. Integral sliding mode fault-tolerant control allocation for a class of affine nonlinear system. *International Journal of Robust and Nonlinear Control*, 29(3):565–582, 2019.

[CEAS20] Lejun Chen, Christopher Edwards, Halim Alwi, and Masayuki Sato. Flight evaluation of a sliding mode online control allocation scheme for fault tolerant control. *Automatica*, 114:108829, 2020.

[CEH15] Jérôme Cieslak, Denis Efimov, and David Henry. Transient management of a supervisory fault-tolerant control scheme based on dwell-time conditions. *International Journal of Adaptive Control and Signal Processing*, 29(1):123–142, 2015.

[CFM18] Ismael Castillo, L Fridman, and Jaime A Moreno. Super-twisting algorithm in presence of time and state dependent perturbations. *International Journal of Control*, 91(11):2535–2548, 2018.

[CG10] Alessandro Casavola and Emanuele Garone. Fault-tolerant adaptive control allocation schemes for overactuated systems. *International Journal of Robust and Nonlinear Control*, 20(17):1958–1980, 2010.

[CH87] Thomas Carter and Mayer Humi. Fuel-optimal rendezvous near a point in general keplerian orbit. *Journal of Guidance, Control, and Dynamics*, 10(6):567–573, 1987.

[CJ14] Andrea Cristofaro and Tor Arne Johansen. Fault tolerant control allocation using unknown input observers. *Automatica*, 50(7):1891–1897, 2014.

[CJT15] Abbas Chamseddine, Cédric Join, and Didier Theilliol. Trajectory planning/replanning for satellite systems in rendezvous mission in the presence of actuator faults based on attainable efforts analysis. *International Journal of Systems Science*, 46(4):690–701, 2015.

[CKB13] Asif Chalanga, Shyam Kamal, and B Bandyopadhyay. Continuous integral sliding mode control: A chattering free approach. In *2013 IEEE International Symposium on Industrial Electronics*, pages 1–6. IEEE, 2013.

[Cli82] William Kingdon Clifford. *Mathematical papers*. Macmillan and Company, 1882.

[CMZL20] Zhenzhong Chu, Fei Meng, Daqi Zhu, and Chaomin Luo. Fault reconstruction using a terminal sliding mode observer for a class of second-order mimo uncertain nonlinear systems. *ISA transactions*, 97:67–75, 2020.

[CW60] W Clohessy and R Wiltshire. Terminal guidance system for satellite rendezvous. *SYSTEM*, 4(1), 1960.

[Dav13] Jorge Davila. Exact tracking using backstepping control design and high-order sliding modes. *IEEE Transactions on Automatic Control*, 58(8):2077–2081, 2013.

[DCH+16] Jorge Davila, Jérôme Cieslak, David Henry, Ali Zolghadri, and Francisco Javier Bejarano. A fault tolerant controller based on quasi-continuous high-order sliding mode technique. In *2016 American Control Conference (ACC)*, pages 7529–7534. IEEE, 2016.

[DCH19] Jorge Dávila, Jérôme Cieslak, and David Henry. Disturbance observer-based fault-tolerant control for a class of additive faults. In *New Trends in Observer-Based Control*, pages 337–355. Elsevier, 2019.

[DFPU09] Jorge Davila, Leonid Fridman, Alessandro Pisano, and Elio Usai. Finite-time state observation for non-linear uncertain systems via higher-order sliding modes. *International Journal of Control*, 82(8):1564–1574, 2009.

[DHFM17] Hongyang Dong, Qinglei Hu, Michael I Friswell, and Guangfu Ma. Dual-quaternion-based fault-tolerant control for spacecraft tracking with finite-time convergence. *IEEE Transactions on Control Systems Technology*, 25(4):1231–1242, 2017.

[DHM16] Hongyang Dong, Qinglei Hu, and Guangfu Ma. Dual-quaternion based fault-tolerant control for spacecraft formation flying with finite-time convergence. *ISA transactions*, 61:87–94, 2016.

[DILU90] S.V. Drakunov, D.B. Izosimov, A.G. Luk'yanov, and V.I. Utkin. Block control principle i. *Automation and Remote Control*, 51:601–609, 1990.

[DLCH+15] Alejandra Ferreira De Loza, Jérôme Cieslak, David Henry, Jorge Dávila, and Ali Zolghadri. Sensor fault diagnosis using a non-homogeneous high-order sliding mode observer with application to a transport aircraft. *IET Control Theory & Applications*, 9(4):598–607, 2015.

[DLJS17] Jingwei Dong, Chuanjiang Li, Boyan Jiang, and Yanchao Sun. Fixed-time nonsingular terminal sliding mode control for spacecraft rendezvous. In *Control And Decision Conference (CCDC), 2017 29th Chinese*, pages 5340–5345. IEEE, 2017.

[DP01] Yixin Diao and Kevin M Passino. Stable fault-tolerant adaptive fuzzy/neural control for a turbine engine. *IEEE Transactions on Control Systems Technology*, 9(3):494–509, 2001.

[EAH18] Christopher Edwards, Halim Alwi, and Mirza Tariq Hamayun. Fault tolerant control using integral sliding modes. In *Advances in Variable Structure Systems and Sliding Mode Control—Theory and Applications*, pages 305–338. Springer, 2018.

[ECH13] Denis Efimov, Jérome Cieslak, and David Henry. Supervisory fault-tolerant control with mutual performance optimization. *International Journal of Adaptive Control and Signal Processing*, 27(4):251–279, 2013.

[EEZ16] Denis Efimov, Christopher Edwards, and Ali Zolghadri. Enhancement of adaptive observer robustness applying sliding mode techniques. *Automatica*, 72:53–56, 2016.

[ELS+10] Christopher Edwards, Thomas Lombaerts, Hafid Smaili, et al. *Fault tolerant flight control*. Springer, 2010.

[Eme63] SV Emel'yanov. On pecularities of variables structure control systems with discontinuous switching functions. In *Doklady ANSSR*, volume 153, pages 776–778, 1963.

[Eme86] SV Emelyanov. Higher order sliding modes in the binary control systems. In *Sov. Phys. Dokl.*, volume 4, pages 291–293, 1986.

[Eme06] SV Emelyanov. Variable structure control systems. 1967, 2006.

[ES98] Christopher Edwards and Sarah Spurgeon. *Sliding mode control: theory and applications*. Crc Press, 1998.

[ESA] Satellite Missions, prisma prototype. https://earth.esa.int/web/eoportal/satellite-missions/p/prisma-prototype. Accessed: 2020-03-20.

[ESP00] Christopher Edwards, Sarah K Spurgeon, and Ron J Patton. Sliding mode observers for fault detection and isolation. *Automatica*, 36(4):541–553, 2000.

[EUT+70] SV Emelyanov, VI Utkin, VA Taran, et al. Theory of systems with variable structure. *Science, Moscow*, 1970.

[FdLCH+15] Alejandra Ferreira de Loza, Jérôme Cieslak, David Henry, Ali Zolghadri, and Leonid M Fridman. Output tracking of systems subjected to perturbations and a class of actuator faults based on hosm observation and identification. *Automatica*, 59:200–205, 2015.

[Feh03] Wigbert Fehse. *Automated rendezvous and docking of spacecraft*, volume 16. Cambridge university press, 2003.

[FIS20] Antonella Ferrara, Gian Paolo Incremona, and Bianca Sangiovanni. Sliding mode fault diagnosis with vision in the loop for robot manipulators. In *New Trends in Robot Control*, pages 81–105. Springer, 2020.

[FKB99] Christian W Frei, Frantisek J Kraus, and Mogens Blanket. Recoverability viewed as a system property. In *Control Conference (ECC), 1999 European*, pages 2197–2202. IEEE, 1999.

[FMB+15] Leonid Fridman, Jaime A Moreno, Bijnan Bandyopadhyay, Shyam Kamal, and Asif Chalanga. Continuous nested algorithms: The fifth generation of sliding mode controllers. In *Recent Advances in Sliding Modes: From Control to Intelligent Mechatronics*, pages 5–35. Springer, 2015.

[FNG96] David Folta, Lauri Newman, and Tom Gardner. Foundations of formation flying for mission to planet earth and new millennium. In *Astrodynamics Conference*, page 3645, 1996.

[Fol01] WM Folkner. Lisa orbit selection and stability. *Classical and Quantum Gravity*, 18(19):4053, 2001.

[Fon14] Robert Fonod. *Model-based Fault Diagnosis and Fault Accommodation for Space Missions: Application to the Rendezvous Phase of the MSR Mission.* PhD thesis, Bordeaux, 2014.

[FYH13] Yong Feng, Xinghuo Yu, and Fengling Han. On nonsingular terminal sliding-mode control of nonlinear systems. *Automatica*, 49(6):1715–1722, 2013.

[FYM02] Yong Feng, Xinghuo Yu, and Zhihong Man. Non-singular terminal sliding mode control of rigid manipulators. *Automatica*, 38(12):2159–2167, 2002.

[GBDB17] José Antonio González, Antonio Barreiro, Sebastián Dormido, and Alfonso Baños. Nonlinear adaptive sliding mode control with fast non-overshooting responses and chattering avoidance. *Journal of the Franklin Institute*, 354(7):2788–2815, 2017.

[GCTS09] BM Gonzalez-Contreras, Didier Theilliol, and Dominique Sauter. On-line reconfigurability evaluation for actuator faults using input/output data. *IFAC Proceedings Volumes*, 42(8):674–679, 2009.

[GdR17] Haichao Gui and Anton HJ de Ruiter. Adaptive fault-tolerant spacecraft pose tracking with control allocation. *IEEE Transactions on Control Systems Technology*, (99):1–16, 2017.

[GMF11] Tenoch Gonzalez, Jaime A Moreno, and Leonid Fridman. Variable gain super-twisting sliding mode control. *IEEE Transactions on Automatic Control*, 57(8):2100–2105, 2011.

[GS19] Eli Gershon and Uri Shaked. Robust switching-based fault-tolerant control. In *Advances in H∞ Control Theory*, pages 107–118. Springer, 2019.

[GV16] Haichao Gui and George Vukovich. Dual-quaternion-based adaptive motion tracking of spacecraft with reduced control effort. *Nonlinear Dynamics*, 83(1-2):597–614, 2016.

[Ham48] William Rowan Hamilton. Xi. on quaternions; or on a new system of imaginaries in algebra. *The London, Edinburgh, and Dublin Philosophical Magazine and Journal of Science*, 33(219):58–60, 1848.

[HBHS20] Riadh Hmidi, Ali Ben Brahim, Fayçal Ben Hmida, and Anis Sellami. Robust fault tolerant control design for nonlinear systems not satisfying matching and minimum phase conditions. *International Journal of Control, Automation and Systems*, pages 1–14, 2020.

[HCT+19] David Henry, Jérôme Cieslak, Jazmín Zenteno Torres, P Colmenarejo, J Branco, N Santos, P Serra, J Telaard, H Strauch, AM Giordano, M De Stefano, et al. Model-based fault diagnosis and tolerant control: the esa's e. deorbit mission. European Control Conference 2019, 2019.

[HEA11] Mirza Tariq Hamayun, Christopher Edwards, and Halim Alwi. Design and analysis of an integral sliding mode fault-tolerant control scheme. *IEEE Transactions on Automatic Control*, 57(7):1783–1789, 2011.

[HEA16] Mirza Tariq Hamayun, Christopher Edwards, and Halim Alwi. *Fault tolerant control schemes using integral sliding modes*. Springer, 2016.

[Hen08] D. Henry. Fault diagnosis of the MICROSCOPE satellite actuators using H_∞/H_- filters. *AIAA Journal of Guidance, Control, and Dynamics*, 31(3):699–711, 2008.

[Hen10] David Henry. A norm-based point of view for fault diagnosis. application to aerospace missions. In *8th European Workshop on Advanced Control and Diagnosis, Ferrara, Italy*, pages 4–16, 2010.

[HKC08] Ying-Jeh Huang, Tzu-Chun Kuo, and Shin-Hung Chang. Adaptive sliding-mode control for nonlinearsystems with uncertain parameters. *IEEE Transactions on Systems, Man, and Cybernetics, Part B (Cybernetics)*, 38(2):534–539, 2008.

[HLC12] Mohamed Harmouche, Salah Laghrouche, and Yacine Chitour. Robust and adaptive higher order sliding mode controllers. In *2012 IEEE 51st IEEE Conference on Decision and Control (CDC)*, pages 6436–6441. IEEE, 2012.

[HLPSA15] David Henry, Catherine Le Peuvédic, Luigi Strippoli, and Finn Ankersen. Robust model-based fault diagnosis of thruster faults in spacecraft. *IFAC-PapersOnLine*, 48(21):1078–1083, 2015.

[HMT+10] G. Herrmann, P. P. Menon, M. C. Turner, D. G. Bates, and I. Postlethwaite. Anti-windup synthesis for nonlinear dynamic inversion control schemes. *International Journal of Robust and Nonlinear Control*, 20(13):1465–1482, 2010.

[HRGZ04] Martin Henk, Jürgen Richter-Gebert, and Günter M Ziegler. 16 basic properties of convex polytopes. *Handbook of discrete and computational geometry*, pages 255–382, 2004.

[HTW+98] Jonathan How, Robert Twiggs, David Weidow, Kathy Hartman, and Frank Bauer. Orion-a low-cost demonstration of formation flying in space using gps. In *AIAA/AAS Astrodynamics Specialist Conference and Exhibit*, page 4398, 1998.

[HW03] RA Hess and SR Wells. Sliding mode control applied to reconfigurable flight control design. *Journal of Guidance, Control, and Dynamics*, 26(3):452–462, 2003.

[IB97] Rolf Isermann and Peter Balle. Trends in the application of model-based fault detection and diagnosis of technical processes. *Control engineering practice*, 5(5):709–719, 1997.

[Ise06] Rolf Isermann. *Fault-diagnosis systems: an introduction from fault detection to fault tolerance*. Springer Science & Business Media, 2006.

[IZG11] Hojjat A Izadi, Youmin Zhang, and Brandon W Gordon. Fault tolerant model predictive control of quad-rotor helicopters with actuator fault estimation. In *Proceedings of the 18th IFAC World Congress*, volume 18, pages 6343–6348, 2011.

[Jew17] Christopher Michael Jewison. *Guidance and control for multi-stage rendezvous and docking operations in the presence of uncertainty*. PhD thesis, Massachusetts Institute of Technology, 2017.

[Jia05] Jin Jiang. Fault-tolerant control systems-an introductory overview. *Acta Automatica Sinica*, 31(1):161–174, 2005.

[JKR08] Jaehyun Jin, Sangho Ko, and Chang-Kyung Ryoo. Fault tolerant control for satellites with four reaction wheels. *Control Engineering Practice*, 16(10):1250–1258, 2008.

[JS01] JL Junkins and H Schaub. Analytical mechanics of aerospace systems. *Texas A&M University*, 2001.

[JWD95] H.P. Jin, P. Wiktor, and D.B. DeBra. An optimal thruster configuration design and evaluation for quick step. *Control Engineering Practice*, 3(8):1113–1118, 1995.

[JY12a] Jin Jiang and Xiang Yu. Fault-tolerant control systems: A comparative study between active and passive approaches. *Annual Reviews in control*, 36(1):60–72, 2012.

[JY12b] Jin Jiang and Xiang Yu. Fault-tolerant control systems: A comparative study between active and passive approaches. *Annual Reviews in Control*, 36(1):60 – 72, 2012.

[KCB+15] Shyam Kamal, Asif Chalanga, B Bandyopadhyay, et al. Multivariable continuous integral sliding mode control. In *2015 International Workshop on Recent Advances in Sliding Modes (RASM)*, pages 1–5. IEEE, 2015.

[Law63] Derek F Lawden. *Optimal trajectories for space navigation*, volume 3. Butterworths, 1963.

[Lev87] A Levant. Higher order sliding modes and their application for controlling uncertain processes. *Institute for System Studiesof the USSR Acadamy of Science, Moskau, Diss*, 1987.

[Lev98] Arie Levant. Robust exact differentiation via sliding mode technique. *automatica*, 34(3):379–384, 1998.

[Lev01] Arie Levant. Universal single-input-single-output (siso) sliding-mode controllers with finite-time convergence. *IEEE transactions on Automatic Control*, 46(9):1447–1451, 2001.

[Lev03a] Arie Levant. Higher-order sliding modes, differentiation and output-feedback control. *International journal of Control*, 76(9-10):924–941, 2003.

[Lev03b] Arie Levant. Introduction to high-order sliding modes. *School of Mathematical Sciences, Israel*, 58(6):1, 2003.

[Lev07] Arie Levant. Principles of 2-sliding mode design. *automatica*, 43(4):576–586, 2007.

[LJPZ19] Chun Liu, Bin Jiang, Ron J Patton, and Ke Zhang. Decentralized output sliding-mode fault-tolerant control for heterogeneous multiagent systems. *IEEE Transactions on Cybernetics*, 2019.

[LJZ18] Chun Liu, Bin Jiang, and Ke Zhang. Adaptive fault-tolerant h-infinity output feedback control for lead-wing close formation flight. *IEEE Transactions on Systems, Man, and Cybernetics: Systems*, 2018.

[LLT18] Lei Liu, Yan-Jun Liu, and Shaocheng Tong. Neural networks-based adaptive finite-time fault-tolerant control for a class of strict-feedback switched nonlinear systems. *IEEE transactions on cybernetics*, 49(7):2536–2545, 2018.

[LP16] Jianglin Lan and Ron J Patton. A new strategy for integration of fault estimation within fault-tolerant control. *Automatica*, 69:48–59, 2016.

[LP17] Jianglin Lan and Ron J Patton. Integrated fault estimation and fault-tolerant control for uncertain lipschitz nonlinear systems. *International Journal of Robust and Nonlinear Control*, 27(5):761–780, 2017.

[LP18] Jianglin Lan and Ron J Patton. A decoupling approach to integrated fault-tolerant control for linear systems with unmatched non-differentiable faults. *Automatica*, 89:290–299, 2018.

[LSD12] Lijun Liu, Yi Shen, and Earl H Dowell. Integrated adaptive fault-tolerant h infinity output feedback control with adaptive fault identification. *Journal of Guidance, Control, and Dynamics*, 35(3):881–889, 2012.

[LY16] Xiao-Jian Li and Guang-Hong Yang. Neural-network-based adaptive decentralized fault-tolerant control for a class of interconnected nonlinear systems. *IEEE transactions on neural networks and learning systems*, 29(1):144–155, 2016.

[MG12] O. Montenbruck and E. Gill. *Satellite Orbits. Models, Methods, Applications (4th Ed.)*. Springer, 2012.

[MJ03] Jan Maciejowski and Colin Jones. Mpc fault-tolerant flight control case study: Flight 1862. Technical report, 2003.

[MJTC15] Yajie Ma, Bin Jiang, Gang Tao, and Yuehua Cheng. Uncertainty decomposition-based fault-tolerant adaptive control of flexible spacecraft. *IEEE Transactions on Aerospace and Electronic Systems*, 51(2):1053–1068, 2015.

[MNB15] Abdel-Razzak Merheb, Hassan Noura, and François Bateman. Design of passive fault-tolerant controllers of a quadrotor based on sliding mode theory. *International Journal of Applied Mathematics and Computer Science*, 25(3):561–576, 2015.

[MO12] Jaime A Moreno and Marisol Osorio. Strict lyapunov functions for the super-twisting algorithm. *IEEE transactions on automatic control*, 57(4):1035–1040, 2012.

[Mor09] Jaime A Moreno. A linear framework for the robust stability analysis of a generalized super-twisting algorithm. In *2009 6th International Conference on Electrical Engineering, Computing Science and Automatic Control (CCE)*, pages 1–6. IEEE, 2009.

[MV11] Monika Marwaha and John Valasek. Fault-tolerant control allocation for mars entry vehicle using adaptive control. *International Journal of Adaptive Control and Signal Processing*, 25(2):95–113, 2011.

[Nor] Northrop grumman's mev-1 servicer docks with intelsat satellite. https://spacenews.com/northrop-grummans-mev-1-servicer-docks-with-intelsat\-satellite/. Accessed: 2020-03-20.

[OH16] Adam Owczarkowski and Dariusz Horla. Robust lqr and lqi control with actuator failure of a 2dof unmanned bicycle robot stabilized by an inertial wheel. *International Journal of Applied Mathematics and Computer Science*, 26(2):325–334, 2016.

[PFH16] C. Pittet, A. Falcoz, and D. Henry. A model-based diagnosis method for transient and multiple faults of aocs thrusters. In *20th IFAC Symposium on Automatic Control in Aerospace ACA 2016*, volume 49, pages 82–87, Sherbrooke, Quebec, Canada, 2016. IFAC.

[QTHH16] Xin Qi, Didier Theilliol, Yuqing He, and Jianda Han. Recoverable set computation for post-fault/failure quadrotors based on sum of squares (sos). In *2016 3rd Conference on Control and Fault-Tolerant Systems (SysTol)*, pages 73–78. IEEE, 2016.

[RKFZ15] Héctor Ríos, Shyam Kamal, Leonid M Fridman, and Ali Zolghadri. Fault tolerant control allocation via continuous integral sliding-modes: a hosm-observer approach. *Automatica*, 51:318–325, 2015.

[RNP14] Damiano Rotondo, Fatiha Nejjari, and Vicenç Puig. A virtual actuator and sensor approach for fault tolerant control of lpv systems. *Journal of Process Control*, 24(3):203–222, 2014.

[Rou98] Alain Roux. Cluster regroups for relaunch. *Aerospace America*, 36(8):48–51, 1998.

[RTAS07] Mickael Rodrigues, Didier Theilliol, Samir Aberkane, and Dominique Sauter. Fault tolerant control design for polytopic lpv systems. *International Journal of Applied Mathematics and Computer Science*, 17(1):27–37, 2007.

[SB10] Marcel Staroswiecki and Denis Berdjag. A general fault tolerant linear quadratic control strategy under actuator outages. *International Journal of Systems Science*, 41(8):971–985, 2010.

[SBD18] Maria Cristina Vilela Salgado, Mischel Carmen Neyra Belderrain, and Tessaleno Campos Devezas. Space propulsion: A survey study about current and future technologies. *Journal of Aerospace Technology and Management*, 10, 2018.

[SEFL14] Yuri Shtessel, Christopher Edwards, Leonid Fridman, and Arie Levant. *Sliding mode control and observation*, volume 10. Springer, 2014.

[SG09] Shay Segal and Pini Gurfil. Effect of kinematic rotation-translation coupling on relative spacecraft translational dynamics. *Journal of Guidance, Control, and Dynamics*, 32(3):1045–1050, 2009.

[SH17] Richard Seeber and Martin Horn. Stability proof for a well-established super-twisting parameter setting. *Automatica*, 84:241–243, 2017.

[Sid97] Marcel J Sidi. *Spacecraft dynamics and control: a practical engineering approach*, volume 7. Cambridge university press, 1997.

[SJSL14] Qikun Shen, Bin Jiang, Peng Shi, and Cheng-Chew Lim. Novel neural networks-based fault tolerant control scheme with fault alarm. *IEEE transactions on cybernetics*, 44(11):2190–2201, 2014.

[SMP+10] Yuri B Shtessel, Jaime A Moreno, Franck Plestan, Leonid M Fridman, and Alexander S Poznyak. Super-twisting adaptive sliding mode control: A lyapunov design. In *49th IEEE conference on decision and control (CDC)*, pages 5109–5113. IEEE, 2010.

[Sta05] M Staroswiecki. Fault tolerant control using an admissible model matching approach. In *Decision and Control, 2005 and 2005 European Control Conference. CDC-ECC'05. 44th IEEE Conference on*, pages 2421–2426. IEEE, 2005.

[Stu91] Eduard Study. Von den bewegungen und umlegungen: I. und ii. abhandlung. *Mathematische Annalen*, 39:441–565, 1891.

[SWZP15] Q. Shen, D. Wang, S. Zhu, and E. K. Poh. Integral-type sliding mode fault-tolerant control for attitude stabilization of spacecraft. *IEEE Transactions on Control Systems Technology*, 23(3):1131–1138, May 2015.

[TLP13] Mohammed Taleb, Arie Levant, and Franck Plestan. Pneumatic actuator control: Solution based on adaptive twisting and experimentation. *Control Engineering Practice*, 21(5):727–736, 2013.

[Utk77] Vadim Utkin. Variable structure systems with sliding modes. *IEEE Transactions on Automatic control*, 22(2):212–222, 1977.

[Utk78] Vadim Ivanovich Utkin. Sliding modes and their applications in variable structure systems. *Mir, Moscow*, 1978.

[Utk13] Vadim I Utkin. *Sliding modes in control and optimization*. Springer Science & Business Media, 2013.

[VG93] ST Venkataraman and S Gulati. Control of nonlinear systems using terminal sliding modes. 1993.

[WHD+19] Qing Wang, Changhua Hu, Chaoyang Dong, et al. Eso-based fault-tolerant anti-disturbance control for air-breathing hypersonic vehicles with variable geometry inlet. *Nonlinear Dynamics*, 98(3):2293–2308, 2019.

[WHWH06] Yuanxin Wu, Xiaoping Hu, Meiping Wu, and Dewen Hu. Strapdown inertial navigation using dual quaternion algebra: error analysis. *IEEE Transactions on Aerospace and Electronic Systems*, 42(1):259–266, 2006.

[Wie98] B. Wied. *Space vehicle dynamics and control*. Reston, VA: American Institute of Aeronautics and Astronautics, 1998.

[WLS+12] Jianying Wang, Haizhao Liang, Zhaowei Sun, Shijie Zhang, and Ming Liu. Finite-time control for spacecraft formation with dual-number-based description. *Journal of Guidance, Control, and Dynamics*, 35(3):950–962, 2012.

[WLS13] Jianying Wang, Haizhao Liang, and Zhaowei Sun. Dual-quaternion-based finite-time control for spacecraft tracking in six degrees of freedom. *Proceedings of the Institution of Mechanical Engineers, Part G: Journal of Aerospace Engineering*, 227(3):528–545, 2013.

[WPC06] Zhengxin Weng, Ron Patton, and Ping Cui. Active fault-tolerant control of a double inverted pendulum. *IFAC Proceedings Volumes*, 39(13):1515–1520, 2006.

[WS12] Jianying Wang and Zhaowei Sun. 6-dof robust adaptive terminal sliding mode control for spacecraft formation flying. *Acta Astronautica*, 73:76–87, 2012.

[WZS00] N Eva Wu, Kemin Zhou, and Gregory Salomon. Control reconfigurability of linear time-invariant systems. *Automatica*, 36(11):1767–1771, 2000.

[XCW15] Sendren Sheng-Dong Xu, Chih-Chiang Chen, and Zheng-Lun Wu. Study of nonsingular fast terminal sliding-mode fault-tolerant control. *IEEE Transactions on Industrial Electronics*, 62(6):3906–3913, 2015.

[XYG17] Bing Xiao, Shen Yin, and Huijun Gao. Reconfigurable tolerant control of uncertain mechanical systems with actuator faults: A sliding mode observer-based approach. *IEEE Transactions on Control Systems Technology*, 26(4):1249–1258, 2017.

[YA02] Koji Yamanaka and Finn Ankersen. New state transition matrix for relative motion on an arbitrary elliptical orbit. *Journal of guidance, control, and dynamics*, 25(1):60–66, 2002.

[YE07] Xing-Gang Yan and Christopher Edwards. Nonlinear robust fault reconstruction and estimation using a sliding mode observer. *Automatica*, 43(9):1605–1614, 2007.

[YJ15] Xiang Yu and Jin Jiang. A survey of fault-tolerant controllers based on safety-related issues. *Annual Reviews in Control*, 39(Supplement C):46 – 57, 2015.

[YJS12] Hao Yang, Bin Jiang, and Marcel Staroswiecki. Fault recoverability analysis of switched systems. *International Journal of Systems Science*, 43(3):535–542, 2012.

[YJSZ15] Hao Yang, Bin Jiang, Marcel Staroswiecki, and Youmin Zhang. Fault recoverability and fault tolerant control for a class of interconnected nonlinear systems. *Automatica*, 54:49–55, 2015.

[YYK17] Shen Yin, Hongyan Yang, and Okyay Kaynak. Sliding mode observer-based ftc for markovian jump systems with actuator and sensor faults. *IEEE Transactions on Automatic Control*, 62(7):3551–3558, 2017.

[YZ02] Xinghuo Yu and Man Zhihong. Fast terminal sliding-mode control design for nonlinear dynamical systems. *IEEE Transactions on Circuits and Systems I: Fundamental Theory and Applications*, 49(2):261–264, 2002.

[YZMQ13] Bin Yu, Youmin Zhang, Ismael Minchala, and Yaohong Qu. Fault-tolerant control with linear quadratic and model predictive control techniques against actuator faults in a quadrotor uav. In *2013 Conference on Control and Fault-Tolerant Systems (SysTol)*, pages 661–666. IEEE, 2013.

[ZTCHD17] Jazmìn Zenteno Torres, Jérôme Cieslak, David Henry, and Jorge Davila. Fault compensability criteria with application to a rendezvous mission around mars. In *14th International Workshop on Advanced Control and Diagnosis*, 2017.

[ZWT+16] Meng Zhou, Zhenhua Wang, Didier Theilliol, Yi Shen, and Mickael Rodrigues. A self-healing control method for satellite attitude tracking based on simultaneous fault estimation and control design. In *2016 3rd Conference on Control and Fault-Tolerant Systems (SysTol)*, pages 349–354. IEEE, 2016.